DE GRUYTER

Andrey Beresnyak,
Alexander Lazarian

TURBULENCE IN MAGNETO-HYDRODYNAMICS

STUDIES IN MATHEMATICAL PHYSICS 12

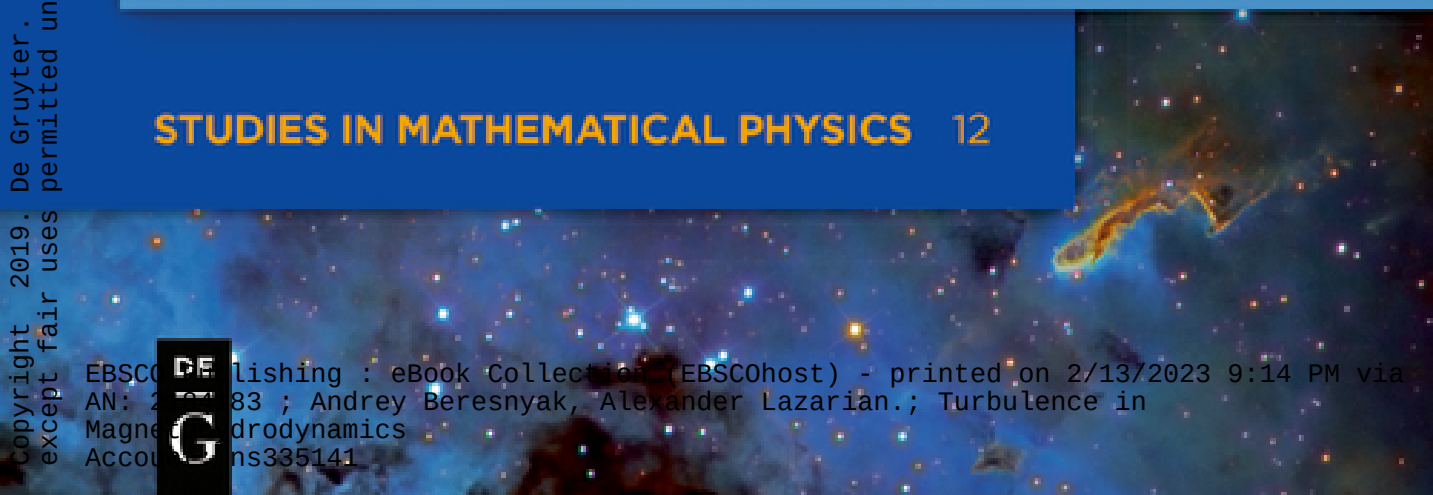

Andrey Beresnyak, Alexander Lazarian

Turbulence in Magnetohydrodynamics

De Gruyter Studies in Mathematical Physics

Volume 12

Andrey Beresnyak, Alexander Lazarian

Turbulence in Magnetohydrodynamics

DE GRUYTER

Physics and Astronomy Classification Scheme 2010
Primary: 95.30.Qd, 94.05.Lk, 52.30.Cv; Secondary: 52.65.Kj, 52.35.Ra

Authors
Dr Andrey Beresnyak
Naval Research Laboratory
Plasma Physics Division, Code 6720
4555 Overlook Av., S.W.
Washington, D.C. 20375
USA
andrey.at.astro@gmail.com

Prof. Alexander Lazarian
University of Wisconsin-Madison
Department of Astronomy
475 N. Charter Street
Madison, WI 56726
USA
alazarian@facstaff.wisc.edu

ISBN 978-3-11-026290-2
e-ISBN (PDF) 978-3-11-026328-2
e-ISBN (EPUB) 978-3-11-039224-1
ISSN 2194-3532

Bibliographic information published by the Deutsche Nationalbibliothek
The Deutsche Nationalbibliothek lists this publication in the Deutsche Nationalbibliografie; detailed bibliographic data are available on the Internet at http://dnb.dnb.de.

Typesetting: VTeX UAB, Lithuania
Printing and binding: CPI books GmbH, Leck

www.degruyter.com

Preface

Historically, most of the turbulence studies were concerned with nonconductive fluids, described by the Navier–Stokes equations. This is because most fluids present on Earth are nonconductive. In the context of a larger Cosmos, this situation is not a rule but rather an exception. Indeed, space is filled with ionizing radiation and only the protection of our atmosphere, which is very dense by astronomical standards, allows us to have a big volumes of insulating fluids, such as the atmosphere and the oceans. In contrast, most of the ordinary matter in the universe is ionised, that is, in a state of plasma. The description of ionized, well-conductive fluids must include magnetic Lorentz force and the induction equation for the magnetic field. As it turned out, turbulent conductive fluids tend to quickly generate their own magnetic fields in the process known as dynamo. On the other hand, the presence of the dynamically important magnetic field could be considered an observational fact. In spiral galaxies, the magnetic field has a regular component, usually along the arms and a random turbulent component of the same order. The value of the magnetic field, around 5 μG, roughly suggests equipartition between magnetic and kinetic forces. The excitation of magnetic turbulence is thought to be the main cause of accretion, because hydrodynamic thin disks are stable. Accretion onto black holes is estimated to be the most potent source of energy in Cosmos, exceeding thermonuclear burning in stars. Closely related to this problem are widely observed astrophysical jets, which are highly collimated flows perpendicular to the accretion disks in which the magnetic field plays an important role in collimation and energy transfer. Understanding shear-driven dynamo and its nonlinear evolution is of high astrophysical importance. Direct observation of magnetic turbulence is the interstellar medium, galaxy clusters, solar wind have confirmed earlier claims that turbulence is inevitable in high-Reynolds' number flows, even though astrophysical flows are characterized by fairly small number densities. Through the book we mention various examples of astrophysical turbulence as well as turbulence in our solar system, the heliosphere, while the observational techniques to study, specifically, astrophysical turbulence are reviewed in the last chapter.

Observations of magnetized turbulence in the interstellar medium, galaxy clusters and the solar wind have confirmed that turbulence is indeed ubiquitous in astrophysical flows and has been detected in almost all astrophysical and space environments; see, e. g., [173, 11, 76]. The Reynolds' numbers of astrophysical turbulence are, typically, very high, owing to astrophysical scales which are enormous compared to dissipative scales. Recent years have been marked by a new understanding of the key role that turbulence plays in a number of astrophysical processes [90, 129]. Most notably, turbulence has drastically changed the paradigms of interstellar medium and molecular cloud evolution [408, 343, 431]; see also [311]. While small scale, kinetic turbulence has been probed by a variety of approaches such as gyrokinetics, Hall MHD and electron MHD [196, 381, 84], this book is mostly concerned with so-called mag-

https://doi.org/10.1515/9783110263282-201

netohydrodynamics of MHD, which is a simple one-fluid description, similar to the Navier–Stokes equation. It could be thought as a 2nd Newton's law for conductive fluid and also could be derived systematically from kinetic theory. The conventional condition of the applicability of the fluid approach, namely that a mean-free path of the particle due to particle-particle collisions must be much smaller than gradient scales of the problem (the so-called Knudsen number much smaller than unity) seems to be too restrictive in most plasmas, especially astrophysical plasmas. Indeed, plasmas are often collisionless, i. e., the effects of collisions could be neglected compared to collective effects, as charged particles are capable of long-range interactions. In many cases, such as the star's interiors, plasma could be considered highly collisional. In other environments, such as solar wind or galaxy clusters, pair collisions will be inefficient and collective interactions must play their own dissipative role. The observations of inertial range fluctuations way below pair collision mean-free path in the solar wind support this idea. Although this book is mostly focused on standard nonrelativistic MHD, in Chapter 5 we mention some relativistic MHD studies, which are relevant for relativistic astrophysical sources such as gamma-ray bursts and active galactic nuclei (AGN) jets. Relativistic force-free MHD is an important limit applicable to relativistic electron-positron jets close to the central engine of AGN, where the energy density of matter is negligible compared to electromagnetic energy density.

Turbulence is a common phenomenon, a time-dependent, quasi-stochastic flow, associated with nonlinearities present in fluid equations. Dissipation in fluids is often associated with microscopic phenomena and dissipation scales are typically much smaller than the scales of the problem. Physically, the development of turbulence could be seen as exciting many degrees of freedom present in a fluid system. Turbulence has been observed since long time ago, as evidenced by Leonardo sketches. A major role in turbulence research is played by invariants of the "ideal" equations free of dissipation, examples of which are energy conservation or the circulation of velocity frozen into a fluid. The way these invariants are broken by turbulence could be insightful for understanding observable physical phenomena. Some of the conserved quantities form a "cascade" through scales, which could be understood quantitatively by scaling arguments. In the context of magnetized fluids turbulence breaks an ideal frozen-in condition for magnetic field lines and facilitates magnetic reconnection. As stochastic phenomenon turbulence is best studied with statistical methods, the quantities averaged over ensemble play a major role. These include power spectra and structure functions. Turbulence theory produced a number of analytically derived relations for certain structure functions, which allows for cross-checks for consistency with observation and experiment.

Lately, the theory and experiment has been complemented by a new method, numerical simulations that we often call "numerics" in this book. One example of the type of numerical simulations, direct numerical simulations (DNS), are prominently presented in this book. DNS refers to a "fully resolved" numerical experiment, where numerics faithfully reproduce properties of the original equations of fluid dynamics.

An opposite of DNS, Implicit Large Eddy Simulations (ILES), are also very common in astrophysics. These are not attempting to archive high accuracy at all scales, but instead aim to reproduce large-scale and intermediate-scale dynamics correctly. Numerics stand in between theory and experiment. On one hand, numerics solve MHD equations directly, without regard to doubt whether MHD is applicable. The simulation setup is often abstract, such as using a periodic box, attempting to emulate infinite space and/or statistically homogeneous turbulence. In nature, e. g., in the solar wind, homogeneity is rather an exception. In this aspect, numerics are close to theory. On the other hand, numerics are often called a "numerical experiment," as it measures the relevant physical quantities of the phenomena without invoking much of the theoretical assumptions or prerequisites. Compared to a real-life experiment, in numerics it is easier to study statistically homogeneous or statistically stationary state cases and it is possible to measure statistical quantities very well, in principle with arbitrary precision. Progress in computing allowed us to use grid sizes of around 4000^3 nowadays, and Reynolds' numbers in these experiments started approaching those encountered in space physics.

Chapter 2 overviews the origin of astrophysical magnetic fields, a problem which is known as turbulent dynamo. This problem can be roughly subdivided into the so-called large-scale dynamo, a generation of magnetic fields on scales larger than the outer scale of turbulence and small-scale dynamo, which generates small-scale turbulent magnetic perturbations. On some level, MHD equations seem to suggest that magnetic field is "frozen" into well-conducting fluids, and as it is being carried around by the fluid magnetic field it is amplified by stretching and folding. This process has been extensively studied since the 1960s. In this book, we decided that it would be impossible to cover such a broad topic as turbulent dynamo; instead, we wrote Chapter 2 intending to demonstrate that turbulent dynamo is generic, i. e., given kinetic motions dominate over magnetic stress the dynamo will continue to increase magnetic energy. We restrict ourselves to small-scale dynamo, which is more generic. Also we discuss mostly "nonlinear dynamo," the situation in which magnetic forces cannot be ignored, albeit often on fairly small scales, which is universally applicable to most observed objects.

Similar to hydrodynamic turbulence, most of the theoretical progress on MHD turbulence has been made in the so-called incompressible limit, which is covered in Chapter 3. The physical justification of this limit in hydrodynamics was the fact that sound waves could often be ignored in turbulent dynamics and the solenoidal turbulent motions have their own dynamics, which are well-described by incompressible equations, at least on small scales. Similar notion is used in MHD where it is often possible to assume that the MHD fast mode splits from an incompressible cascade of Alfvenic and slow modes. It turns out that another split is possible due to the extreme anisotropy in the inertial range of MHD turbulence when the slow mode becomes passive and does not contribute to essential nonlinearity, its cascade being slaved to the

Alfvenic mode. The cascade of Alfvenic mode is often called Alfvenic turbulence or reduced MHD and contains all necessary statistical properties of small-scale MHD turbulence. It turns out that this MHD turbulence in a strong mean field (strong local B_0 compared to perturbations) is essentially three-dimensional, and not two-dimensional as was thought before.

Iroshnikov and Kraichnan first pointed out that the magnetic field cannot be excluded by the choice of reference frame, therefore, in every parcel of the fluid a mean magnetic field will remain, which would be much stronger than small-scale perturbations. This naturally lead to further studies which took into account anisotropy of MHD turbulence in a strong mean field namely the work of Goldreich and Sridhar which used an uncertainty relation between the wave frequency and the cascade timescale to formulate the so-called "critical balance." Later we show how this picture is connected to the modern view of MHD turbulence. Chapter 3 describes a special case of MHD turbulence without cross-helicity. Physically, this means that the amount of perturbations propagating in one direction along mean magnetic field is perfectly statistically balanced by perturbations moving in the opposite direction; this case being called "balanced turbulence." However, in real systems, MHD turbulence is often imbalanced, because there are sources and sinks of energy and these are rarely homogeneous in space. Also, due to fluctuations of all quantities in time, conceptually, one will have to understand the most general imbalanced case in order to create a theory for the specific balanced case. Unlike hydrodynamics, where the introduction of fluctuations of dissipation rate ϵ in the theory was rather obvious, e. g., Kolmogorov–Obukhov extension of the Kolmogorov model or the She–Leveque model, in MHD the introduction of imbalance significantly complexifies theory. In Chapter 4, we discuss some new ideas which lead to creation of imbalanced turbulence models and their numerical testing.

Chapter 5 is devoted to compressible MHD turbulence and various approaches in the weakly compressible, as well as supersonic limit. In MHD, the decomposition into four basic linear modes has been insightful for describing strongly compressible turbulence. The study of supersonic ISM turbulence is important for understanding the structure of molecular clouds and subsequent star formation. In this respect, the studies of density scalings and thermal instability in DNS have become commonplace. The solar wind, a MHD flow emitted from the sun at speeds 400–800 km/s is also compressible and its properties and the transition to dispersive regime at small scales is a large part of MHD turbulence now, due to availability of in-situ measurements.

Contents

1 Introduction into MHD turbulence

Our goal in this section is to highlight various directions in MHD turbulence research, which will be explored in more detail later in the book. We also discuss the relevance of these studies to space physics and astrophysics in general.

1.1 Turbulence around us

We live in a turbulent world. Air in the atmosphere, jets of water from a tap, even our blood in the large arteries is turbulent. Observations of magnetized turbulence in the interstellar medium, galaxy clusters and the solar wind have confirmed that turbulence is indeed ubiquitous in astrophysical flows and has been detected in almost all astrophysical and space environments; see, e. g., [173, 11] (see Figure 1.1).

Turbulence is a direct consequence of large-scale fluid motions experiencing low friction. To characterize the relative influence of viscosity, we use a dimensionless Reynolds number, $\mathrm{Re} = LV/\nu$, where L is the scale of the flow, e. g., the diameter of a jet, V is its velocity, and ν is fluid kinematic viscosity. Flows with $\mathrm{Re} \gg 1$ are typically turbulent, with the degree of chaos increasing with the increase of Re.

The Reynolds' numbers are usually very large in astrophysical flows, because the scales and velocities are large, determined by the size and the motions of astronomical objects, whereas viscosity and magnetic diffusivity are defined by microphysics.[1] For instance, Re numbers of 10^{10} and larger are common for astrophysics. For so large Re, the inner degrees of fluid motion get excited, and a complex pattern of motion develops.

The notion of turbulence is associated with chaos and unpredictability; however, turbulence has its order. It is a sort of "ordered chaos" that allows for a remarkably simple statistical description (see, e. g., [324]). If the injections and sinks of the energy are correctly identified, we can try to describe turbulence statistically for *arbitrary* Re. The range of scales between the injection scale and the dissipation scale is called the inertial range. Turbulence often allows a simplified statistical treatment over its inertial range. For instance, the spatial variations of any physical variable, $X(\mathbf{r})$, is related to the difference of X between points separated by a distance $\mathbf{l}$. If averaged over different realizations of the process or, in practice, averaged over the entire turbulent volume, this provides a valuable measure of X variation with $\mathbf{l}$. The result can also be given in

1 Often one can express kinematic viscosity as proportional to vl, where v is the microscopic, e. g., thermal velocity and l is the collisional mean-free path, also a microscopic quantity. We discuss how this simple picture is modified in the so-called collisionless plasmas in Section 2.2.1.

https://doi.org/10.1515/9783110263282-001

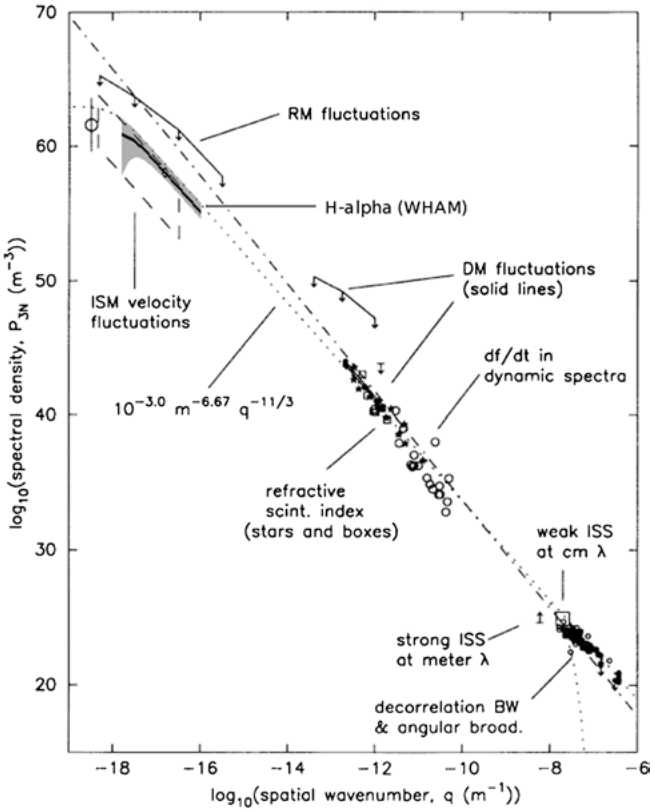

Figure 1.1: Big power law in the sky from [11] extended to scale of parsecs using WHAM data from [76]. Reproduced from [76] with permission of AAS.

terms of the Fourier transform of this average, with the displacement $\mathbf{l}$ being replaced by the wavenumber $\mathbf{k}$ parallel to $\mathbf{l}$ and $|\mathbf{k}| = 1/|\mathbf{l}|$. For example, for the isotropic hydrodynamic turbulence kinetic energy spectrum, $E(k)dk$, describes how much energy resides at the interval $k, k + dk$. At large scale L (i. e., small k), one expects to observe features reflecting energy injection. At small scales, energy dissipation takes place. Between these two scales, one expects to see a power-law scaling reflecting the self-similar process of nonlinear energy transfer.

In other words, in spite of its complexity, the turbulent cascade is self-similar over its inertial range and allows a rather simple description, which is very advantageous for many applications. For this range, the physical variables are proportional to the power of the eddy size over a range of scales, leading to scaling laws expressing the dependence of certain nondimensional combinations of physical variables on the eddy size. The scaling relations can predict turbulent properties on the whole range of scales, including those, that are out of reach of large-scale numerical simulations.

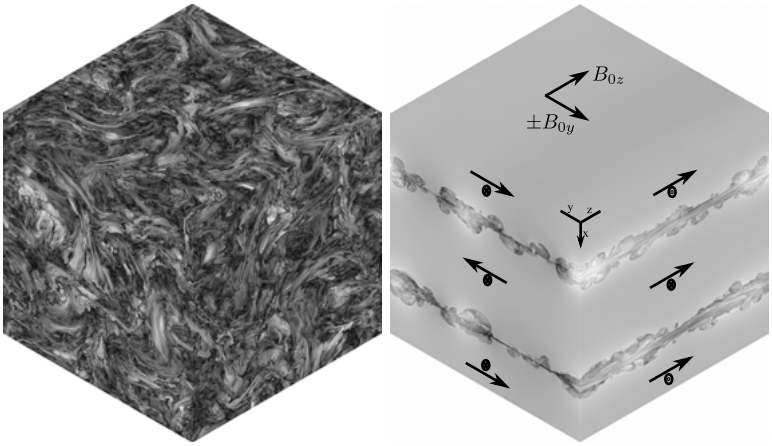

Figure 1.2: Simulated MHD turbulence visualized by magnetic field magnitude shown in grayscale. Left: statistically homogeneous and isotropic turbulence with zero net flux through the volume, driven by volumetric force. Right: MHD turbulence driven by the instability in the current layer from [27]. Reproduced from [27] with permission of AAS.

These scaling relations are very valuable for obtaining an insight of the processes at the inertial range.

Turbulence can be driven by the variety of mechanisms. Simulated turbulence is often driven by applied volumetric force; see the left side of Figure 1.2. Turbulence can also be driven by cosmological flows, as we discuss, see Section 2.2. One interesting source of turbulent energy release is the instability of the thin current sheet; see the right side of Figure 1.2, which is an example of the self-driven reconnection that we discuss in Section 8.4. Another generic way to induce turbulence and convert gravitational energy into heating and particle acceleration is the so-called magnetorotational instability (MRI). Astrophysical flows have a relatively large Reynolds' number, and since hydrodynamic Keplerian flows are stable, this presents a problem for explaining astrophysical accretion. If magnetic fields are sufficiently weak, they can induce MRI the essence of which is easy to understand—consider perturbations of the toroidal field within a thin Keplerian highly conductive disk. The magnetic field line perturbed in the plane of the disk will be subject to further instabilities. Indeed, the plasmas that get closer to the gravitational source are going to get larger angular velocity, while a more distant part is going to get a smaller velocity. The tension of the magnetic field that connects these two parcels of plasmas is going to increase the angular momentum of the more distant parcel and decrease the angular momentum of the closer to the center parcel. As a result, the perturbation is the magnetic field is going to grow, inducing angular momentum transport.

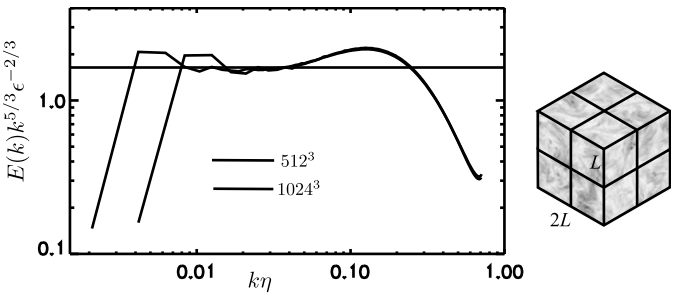

Figure 1.3: Left: Spectrum of hydrodynamic turbulence compensated by Kolmogorov scaling to give approximate constant function versus wavenumber. Right: The conceptual subdivision of a large datacube into 8 smaller cubes having similar statistics as the large cube but missing largest scale perturbations. From [21].

1.2 Kolmogorov scaling

Turbulent spectrum has a beginning and the end. Outer scale or integral scale L is the scale where most energy resides,[2] usually this is also a scale where energy is injected.[3]

The energy "cascades" down to smaller scales until it hits the so-called Kolmogorov scale, where dissipative processes overcome nonlinear transfer of energy.

The Kolmogorov scale can be expressed as a combination of viscosity/diffusivity and energy dissipation rate, which gives a unit of length,

$$\eta = \left(\nu_n^3/\epsilon\right)^{1/3(n+i+1)}, \tag{1.1}$$

where n is the order of the diffusivities, e. g., 2 for classic diffusivity, i is the spectral index, e. g., $-5/3$ in case of classic Kolmogorov theory, ν_n is viscosity or magnetic diffusivity, so that the dissipation operator looks like $-\nu_n(-\nabla^2)^{n/2}$ and ϵ is the energy dissipation rate.

Dimensionless ratio L/η could serve as a "length of the spectrum."

In hydrodynamic turbulence, a popular starting point is the Kolmogorov model, which assumes a self-similar cascade of energy through scales [224]. Cascade means that the energy is being transferred from one scale to another locally in scale without dissipation so that the energy rate is constant for all scales:

$$\epsilon \approx u_l^2/t_{\text{cas}} = \epsilon, \tag{1.2}$$

where u_l is a characteristic velocity and t_{cas} is the cascading timescale. For the hydrodynamic cascade, [224] assumes $t_{\text{cas}} \approx l/u_l$, which results in

$$\epsilon \approx u_l^3/l = \epsilon. \tag{1.3}$$

2 Can be defined formally through integral over the spectrum, e. g., $L = 3\pi/4E \int_0^\infty k^{-1}E(k)\,dk$.

3 Inverse cascade in two-dimensional hydrodynamic turbulence is one counterexample of this.

Going further and formally defining u_l through structure functions (see Section 3.8), and assuming that all structure functions are "self-similar," this model predicts that the spacial power spectrum of turbulence, $E(k)$, will be a power-law function of wavenumber,

$$E(k) = C_K \epsilon^{2/3} k^{-5/3}, \tag{1.4}$$

where C_K is a Kolmogorov constant. The limitations of this formula are well known and typically corrected by the "intermittency correction" $(kL)^{\alpha}$, where L is an outer scale and α is a small number, around 0.035 [392]. In simulations or measurements with small inertial range, this correction can often be neglected. In particular, a compilation of experimental results for hydrodynamic turbulence [404] suggests that a Kolmogorov constant is universal for a wide variety of flows. High-resolution numerical simulations of isotropic incompressible hydrodynamic turbulence [179] suggest the same value for the Kolmogorov constant, around 1.6. See also Figure 1.3 which represents statistically homogeneous, isotropic simulations with two different Reynolds numbers indicating how "inertial range" of $k^{-5/3}$ scaling broaden with Re. Once we subscribe to the notion of self-similarity, simulation with higher numerical resolution can be considered both as a simulation resolving smaller physical scales and as a simulation of a larger volume of turbulence and containing many turbulent realizations. The statistics will be similar in cases with small or large Re; see Figures 1.3, 3.8.

Total energy dissipation in turbulence can be empirically expressed as

$$\epsilon = C_K' \delta v^3 / L, \tag{1.5}$$

which resembles Equation (1.3) written for the outer scale. This relation has been known as the zeroth law of turbulence and can be experimentally or numerically validated by changing viscosity, the scale of the system or perturbation velocity while keeping the structure of the turbulence approximately the same. For example, one can study grid-generated turbulence with different fluids and vary the scale of the system as well as flow speed. The same type of turbulent flow results in approximately the same dimensionless coefficient C_K'. This expression represents a connection between outer scale L which feature almost inviscid flow that injects energy and the dissipative scales, which actually dissipate this injected energy. More detailed statistical studies of turbulence benefits from using such quantities as spectra, correlation functions, and structure functions.

Turbulence is neither completely homogeneous nor exactly self-similar. It features "structures," i. e., spacial locations where the fluctuations are enhanced compared to their surroundings. This, in particular, can result in places where the energy release is enhanced. Unlike the Kolmogorov description of the two-point correlations, so far we do not have a similar accepted theory of intermittency even in the case of hydrodynamic incompressible turbulence, not to speak about MHD turbulence theory.

In the book, we analyze some results related to the structure of the intermittent turbulent flows, and analyze higher order statistics of fluctuations. This part of the book has less rigorous physics-based justification, but it reflects the state of the field as we see it.

1.3 Compressible MHD equations and simulated turbulence

Ideal MHD equations describe the dynamics of ideally conducting inviscid fluid with the magnetic field and can be written in Heaviside units, redefining the electric charge with a factor of $1/4\pi$ getting rid of 4π factors in Maxwell's equations as

$$\partial_t \rho + \nabla \cdot (\rho \mathbf{v}) = 0, \tag{1.6}$$

$$\rho(\partial_t + \mathbf{v} \cdot \nabla)\mathbf{v} = -\nabla P + \mathbf{j} \times \mathbf{B}, \tag{1.7}$$

$$\nabla \cdot \mathbf{B} = 0, \tag{1.8}$$

$$\partial_t \mathbf{B} = \nabla \times (\mathbf{v} \times \mathbf{B}), \tag{1.9}$$

$$P = P(\rho, s) \tag{1.10}$$

with current $\mathbf{j} = \nabla \times \mathbf{B}$ and vorticity $\boldsymbol{\omega} = \nabla \times \mathbf{v}$, $P(\rho, s)$ is an equation of state. Introducing sound speed $c_s^2 = \partial P / \partial \rho$, linearized MHD equations reveal four perturbation modes:

1) Alfvén mode – transverse waves with v and B perturbations along $\mathbf{k} \times \mathbf{B}$ and dispersion relation $\omega = (\mathbf{v_A} \cdot \mathbf{k})$, where $\mathbf{v_A} = \mathbf{B}/\sqrt{4\pi\rho}$, so-called Alfvén velocity = magnetic field $\mathbf{B}$ in velocity units introduced earlier. The phase velocity of Alfvén mode is

$$u_A = \omega/k = \pm(\mathbf{v_A} \cdot \hat{\mathbf{k}}) = \pm v_A \cos\theta, \tag{1.11}$$

while its group velocity $\partial\omega/\partial\mathbf{k} = \pm\mathbf{v_A}$, hence the term Alfvén velocity.

2,3) Fast and slow modes – compressible waves with perturbations in the $\mathbf{k}, \mathbf{B}$ plane propagating correspondingly faster and slower than v_A, with the dispersion relation

$$u_{f,s}^2 = \omega^2/k^2 = \frac{1}{2}\left[(v_A^2 + c_s^2) \pm \sqrt{(v_A^2 + c_s^2)^2 - 4v_A^2 c_s^2 \cos^2\theta}\right]. \tag{1.12}$$

4) Entropy mode – non-propagating passive scalar perturbations of specific entropy [251, 44].

In this book, we use several tools related to numerical computations, among them compressible and incompressible MHD codes. We use pseudospectral code [33, 32] for the incompressible calculations and the so-called finite volume codes for compressible cases. The pseudospectral code solves above equations as an ordinary differential equation in time for each spacial Fourier harmonic, the "pseudo" coming from the fact that nonlinear term is calculated in real space, and then converted back to Fourier space. Unlike finite difference schemes, the pseudospectral scheme does not

suffer from either dispersion of dissipation errors. The dissipation is explicit, and the divergence-free condition for velocity and magnetic field are done with simple algebraic operations in Fourier space. For time integration, we use leapfrog which is time-reversible and numerical dissipation is absent, since the nonlinear term, calculated in this manner, preserve both energy and cross-helicity. These simulations are "fully resolved," i. e., the viscosity and magnetic diffusivities are explicit, and all scales of interests are represented in these highly precise calculations. This comes at a limitation of relatively low Re.

1.4 How MHD cascade is different from hydro cascade?

An initially unmagnetized well-conductive turbulent fluid generates its own magnetic field, which becomes dynamically important on almost all relevant scales. The presence of the large-scale field, however, is qualitatively different from the presence of large-scale flows in hydrodynamics. The large-scale flow can be eliminated by the proper choice of a reference frame, but magnetic field cannot be eliminated like this. The inertial range motions of MHD turbulence, therefore, exist on the background of the large-scale mean magnetic field. This is known as a "strong field limit." Initial investigations of the strong field limit by Iroshnikov and Kraichnan [201, 236] concluded that inertial-range MHD turbulence has to be weak turbulence. However, the subsequent analytic work [158] demonstrated that MHD turbulence tends to become stronger and not weaker during the cascade. In fact, similar arguments lead Goldreich and Sridhar [172] (thereafter GS95) to the conclusion that there is a different regime of turbulence, strong MHD turbulence, which is associated with the so-called strong critically-balanced anisotropic cascade.

The properties of the anisotropic cascade can be rigorously argued to be governed by the Alfvenic part of MHD perturbations. This regime has been dubbed Alfvenic turbulence. The Alfvenic component evolves according to the so-called reduced MHD; see, e. g., [206], which has been known in plasma physics for a long time and can be justified based on plasma drift approximation alone, without resorting to collisions; see, e. g., [382]. The incompressible case has only the Alfven and pseudo-Alfven modes. The latter is the incompressible limit of the usual slow MHD modes. Both modes exhibit the same relations between the parallel and perpendicular scales of the turbulent perturbations. The full compressible MHD also includes fast mode cascade [83], which develops independently of the Alfven and slow modes. Reduced MHD has an inherent scaling symmetry, similar to the symmetry of hydrodynamic equations, which allows building a model of self-similar turbulence with the power-law scalings of spectra. This is only possible in the so-called strong mean field limit and strong anisotropy limit; however, this does not seems to be a big limitation, because in turbulence with large inertial range these conditions are always satisfied in the middle of the inertial range; see, e. g., [22].

The theory of strong turbulence formulated in [172] predicts the Kolmogorov scaling in terms of the dominant perpendicular motions, i. e., $E(k) \sim k^{-5/3}$ and the scale-dependent anisotropy with the perpendicular scales $l_\perp$ and the parallel scales $l_\parallel$ related through the critical balance condition $l_\parallel \sim l_\perp^{2/3}$, which testifies that the smaller eddies are significantly more elongated than their large-scale counterparts. We use $l_\perp$ and $l_\parallel$ as these are quantities defined in respect to the local direction of magnetic field. This is paramount for our understanding of this parallel spectrum and considered in great detail in Chapter 3. While [172] suggested a closure model predicting the $k_\parallel \sim k_\perp^{2/3}$ anisotropy in the frame associated with the global mean field, it was not observed in first numerical simulations of strong three-dimensional MHD turbulence in [92]. Instead, this anisotropy was observed in the structure function measurement performed in the frame associated with the local magnetic field. Similarly, space physics measurements in the solar wind [195] observed the $k_\parallel^{-2}$ parallel scaling using the wavelet technique and associating parallel direction to the direction of the local field. Given the importance of the parallel spectrum for a variety of phenomena, e. g., resonant scattering of solar energetic particles, the measurements and theories of the parallel spectrum and anisotropy attracted considerable attention; see, e. g., [342, 443, 300]. In this book, we also strongly argue in favor of the scale-dependent anisotropy in the local frame. We show that it can be obtained not only through phenomenological hand-waving critical balance argument, but also by considering the Lagrangian frequency spectrum of the Alfven wave propagating along the field line [26]. In this case, the famous $k_\parallel \sim k_\perp^{2/3}$ anisotropy is the result of the interplay between Eulerian perpendicular spectrum and Lagrangian parallel spectrum.

The precise value of the spectral slope of the perpendicular spectrum was a matter of debate. As earlier simulations [303, 330] reported slopes shallower than the standard GS95's $-5/3$, some adjustments have been proposed to accommodate this difference [159, 48, 170]. A model with the so-called "dynamic alignment" [48, 49] got a lot of publicity. In the book, we will provide arguments suggesting that the discrepancy between the GS95 expectations and the results of low-resolution MHD turbulence simulations can arise from MHD turbulence being less local compared to the hydrodynamic turbulence [32]. Indeed, the higher resolution simulations [25, 26] show consistency with the GS95 spectral slope and the anisotropy scalings. Additional facts, e. g., the difference in kinetic and magnetic energies in the strong field limit, with, is also problematic to explain in the framework of a completely local cascade. The reader has a chance to study these arguments in more detail in Sections 3.10 and 3.11 .

Another layer of complexity is added to the MHD turbulence theory when we remember that MHD has more invariants than hydrodynamics. Apart from energy, there is also energy-like pseudoscalar named cross helicity. In the incompressible case, this creates two independent energy cascades. Basically, the amount of perturbations propagating in one direction along mean magnetic field is different from the amount of perturbations in the opposite direction. This "imbalanced turbulence" is prominently known in the solar wind community as cross-helical turbulence. Not

surprisingly, there are more perturbations propagating away from the sun than propagating toward the sun in the solar wind. Imbalance makes GS95 theory inapplicable, and in Chapter 4, we argue that the critical balance must be completely abandoned for the strongest wave component for the theory to make any sense. The anisotropy for this component has to be argued based on a new principle [30].

Compressible MHD turbulence is even more complicated. Weakly compressible turbulence can be considered along the same lines as incompressible, and fast mode its own separate cascade [293, 82]. Numerical studies of weakly compressible as well as incompressible cases include [81, 82, 37, 231, 239]. We return to the issue of compressible turbulence in Chapter 5.

1.5 Turbulent dynamo

When turbulence takes place in conducting fluids, and the magnetic energy is less than the kinetic energy of turbulent motions, the turbulence induces magnetic field generation, which is frequently referred to as "turbulent dynamo." This process has been studied both analytically and numerically. One can distinguish two distinct regimes: (1) the magnetic energy is less than the kinetic energy of driving eddies at **all** scales down to the dissipation scale and (2) the kinetic and magnetic energies come to the equipartition at some scale. The first regime is called "kinematic" or "linear" dynamo, referring to the induction equation being linear with respect to the magnetic field. The kinematic dynamo, which ignores magnetic field back-reaction is of little astrophysical importance, because it takes incredibly short time, by astrophysical standards to generate sufficiently strong fields violating this condition (for specific estimates refer to Section 2.2.1). The second regime, when the magnetic back-reaction is important on **some** scale is termed "nonlinear dynamo." Despite that kinematic dynamo studies were favored due to their simplicity, it turns out that nonlinear dynamo can often be described statistically by very basic means. The lessons that we learned in turbulence theory, and in particular, the concept of the scale-local cascade of energy can be applied to dynamo as well, which will result in a surprisingly simple description. One broad conclusion from such a theory, which we describe in Section 2.1, is that a certain constant fraction of the kinetic energy around 6 % is being converted into magnetic energy.

1.6 Magnetohydrodynamics and reconnection

Magnetized turbulence involves both the motion of the fluid and magnetic fields. The magnetic fields embedded in a highly conductive fluid retain their topology due to the magnetic fields being frozen-in. This notion is based on the Alfven theorem [7]. This concept of frozen-in magnetic fields is a basis of many theories, e. g., presented

in the textbooks theory of star formation in the magnetized interstellar medium. However, this notion of flux freezing is somewhat difficult to reconcile with the picture of freely moving turbulent eddies. In fact, in the absence of means of changing magnetic field topology, one may expect the development of the very chaotic felt-like structure of the magnetic field. In the book, we show that this is not what is happening in the real world as magnetic fields in turbulent fluids do not obey the Alfven theorem and demonstrate the ability to change their topology and connectivity due to the process of magnetic reconnection [278, 232, 143, 142, 267]. The corresponding process of turbulent reconnection dramatically changes many astrophysical phenomena and has many implications that we briefly discuss in Chapter 9. We show that turbulent reconnection is a natural ingredient of turbulent motions in the magnetized fluid.

1.7 Observing MHD turbulence

Significant progress has been achieved in understanding MHD turbulence due to the advances of numerical computations. In particular, some earlier studies of magnetized turbulence were guided mostly by observations of magnetic fluctuation of the outer heliosphere and solar wind [462]. Controlled experiments, in this case, were not easy, which resulted in theories of MHD turbulence which were not confirmed by subsequent numerical simulations. The synergetic use of numerical simulations and observational data is advantageous, however.

A significant progress in theoretical understanding of what information about turbulence can be obtained from observing Doppler-broadened spectral lines originating in turbulent volumes [271, 272, 258, 274] as well as synchrotron-emitting turbulent volumes [276] provides new ways of utilizing the observational data for obtaining turbulence spectra (see [269, 74, 465, 290, 212]). The understanding of the anisotropies induced by Alfven, slow and fast modes provide a new way of studying these modes using spectroscopic [208] and synchrotron data [275, 276], while the fundamental fact that turbulent eddies are aligned with the direction of magnetic field opened a new way of tracing magnetic field with spectroscopic data [174, 460, 286] as well as synchrotron data [286]. We cover this topic in Chapter 10.

1.8 Applications of MHD turbulent theory

While the statistical theory of MHD turbulence is an exciting research avenue by itself, the interest of a broad astrophysical community to the theory arises from its astrophysical implications. As the MHD turbulence is ubiquitous in astrophysical environments, it modifies, if not radically changes most of the astrophysical processes. For instance, the presence of a magnetic field makes MHD turbulence anisotropic [325, 393, 194, 172]. As we will show below, the relative importance of inertia and magnetic force changes

with scale, so the anisotropy of MHD turbulence changes as well. Many astrophysical processes, e. g., related to the dynamics of dust, scattering, and acceleration of energetic particles, thermal conduction, can be obtained if the turbulence spectrum and its anisotropy are known. Also, important insights can be obtained if we know turbulence intermittency, e. g., related to the concentration of energy in the spatially distinct region; see, e. g. [264, 36].

As charged particles are bound to follow magnetic field lines, the famous theorem by Alfven [7] mathematically proving the concept of flux freezing seems very natural. This concept states that plasma and magnetic fields are well coupled. This served as the foundation for many astrophysical theories, from the theory of star formation and evolution of accretion disks [408, 343, 431]; see also the review [311] to the theories of heat transfer in magnetized plasmas. However, as we mentioned in Section 1.6 the classical flux freezing is only valid in laminar conductive fluids and is grossly violated in turbulent ones. This calls for significant modifications of the textbook theories, in particular, the star formation theory. For the latter theory, the concept of "reconnection diffusion" was introduced by the improved understanding of MHD turbulence and turbulent reconnection [256, 281, 262]. The star formation driven by reconnection was explored in [377, 376, 288].

Similarly, magnetic field wondering that naturally happens in turbulent constantly reconnecting magnetic field lines changes dramatically the heat transport of the particles moving along these magnetic field lines [336, 257]. This process competes with the heat transport by the eddies that are induced reconnection diffusion of plasmas of different temperatures. Depending on the turbulence parameters, one or the other process dominates [257].

1.9 Cosmic ray transport and acceleration

Cosmic rays are charged energetic particles, and they are expected to follow magnetic field lines. Turbulent perturbations of the magnetic field lines were expected to produce scattering of cosmic rays. Nevertheless, an ad hoc approach to treating turbulence present serious problems when the expectations are confronted with observations. The most dramatic of them is related to the transport of cosmic rays perpendicular to mean magnetic field. Even the maximum scattering of particles that corresponds to the scattering every period is producing perpendicular diffusion that is many orders of magnitude less than the one required by the galactic cosmic ray observations. [204, 399] suggested the approach to handling this problem, and it is related to magnetic field line wandering.

Another problem of the energetic particle dynamics is related to the efficiency of scattering by MHD turbulence. The theoretical calculations based on the assumed isotropic theory of magnetic turbulence were inconsistent with available observational data and this induced the appearance of ad hoc models consisting of slab waves

that scatter particles and rather esoteric 2D perturbations, which are inefficient in the scattering of particles. More recent studies in [453, 454] identified fast MHD modes as the primary scattering agent within galactic MHD turbulence while demonstrating that the contribution of Alfvenic and slow modes for scattering is significantly reduced [70, 453, 41]. As the turbulence scattering is associated with stochastic acceleration of cosmic rays, the fast modes happen to be effective in inducing such an acceleration. A similar conclusion was obtained in [58]. The efficiency of such acceleration increases if MHD turbulence decreases cosmic ray mean-free path.

Turbulent acceleration of energetic particles is an example of the stochastic or second-order Fermi acceleration. The energy gain in such acceleration is relatively inefficient as it is proportional to $(v/c)^2$, where v is the turbulent velocity at the scale that interacts with cosmic rays and c is the speed of light. A much more efficient process is happening in shocks, where the energy gain is proportional to $V_{\rm shock}/c$ [241, 18, 45]. The turbulent dynamo in the shock precursor was identified in [28] as a promising way of enhancing of the magnetic field in front of shocks. This, in its turn, makes it possible to accelerate protons to energies to 10^{15} eV, which is higher than the shock acceleration in the traditional treatment can provide.

Another process of the first-order Fermi acceleration happens within regions of turbulent reconnection [111]. Shrinking of the magnetic field lines within the extended current sheets associated with the reconnection in turbulent fluids provide the acceleration that the cosmic ray constantly gain energy as quantitatively discussed in [38].

2 Astrophysical dynamo

One of the main questions of MHD dynamics is how conductive fluid generates its magnetic field, a process known broadly as "dynamo." Turbulent dynamo is known as "large-scale/mean-field dynamo" and "small-scale/fluctuation dynamo," in the first case magnetic fields are amplified on scales larger than the outer scale of turbulence in the seconds on smaller scales.

Although several "no-dynamo" theorems have been proven for flows with symmetries, a common turbulence, which possesses no exact symmetries, was expected to amplify magnetic field by stretching, due to the particle separation in a turbulent flow. For the large-scale dynamo, a "twist-stretch-fold" mechanism was introduced [428]. If the turbulent flow has exact statistical isotropy, it cannot generate a large-scale field, so the observed large-scale fields, such as fields in the disk galaxies, are generated when statistical symmetries of turbulence are broken by large-scale asymmetries of the system. These asymmetries may include stratification, rotation, and shear; see, e. g., [435, 215]. One can study large-scale dynamo using the so-called mean field theory (see, e. g. [238]), where the magnetic and velocity fields are decomposed into mean and fluctuating part. The equations for the mean field are closed using statistical or volume averaging over the fluctuating part. The traditional theories of mean field dynamo, however, often fail due to issues related to magnetic helicity [435, 437]. The study of the large-scale dynamo is complex due to the variety of conditions in astrophysical flows in different objects. One ambitious goal of large-scale dynamo theory is to explain the solar cycle. In this book, we do not consider large-scale dynamo, instead referring the reader to the review [56]. In this chapter, we concentrate on the small-scale dynamo as it is more universal, generic, and crucial to understand the level of magnetization in astrophysical environments. Small scale dynamo often generates magnetic fields with an energy of the order of the kinetic energy, the so-called equipartition. Magnetic perturbations can subsequently be ordered by slower large-scale dynamo and produce large-scale magnetic fields. Some objects, such as galaxy clusters, are dominated by the small-scale dynamo, however.

The kinematic regime of small-scale dynamo was historically the most studied. It ignores the backreaction of the magnetic field [217, 235, 245]. However, from these models, it was not clear whether magnetic energy will continue to grow after the end of the kinematic regime. In astrophysical objects with very large Re, it becomes inapplicable very quickly. Also, the magnetic spectrum of the kinematic dynamo, possessing positive spectral index, typically 3/2, is incompatible with observations in galaxy clusters [248]; see Figure 2.1. These observations indicate a steep spectrum with a negative power index at small scales. In fact, from a theoretical viewpoint, kinematic dynamo is inapplicable in most astrophysical environments because the Alfvén speed is typically many orders of magnitude higher than the Kolmogorov velocity (Section 1.2).

https://doi.org/10.1515/9783110263282-002

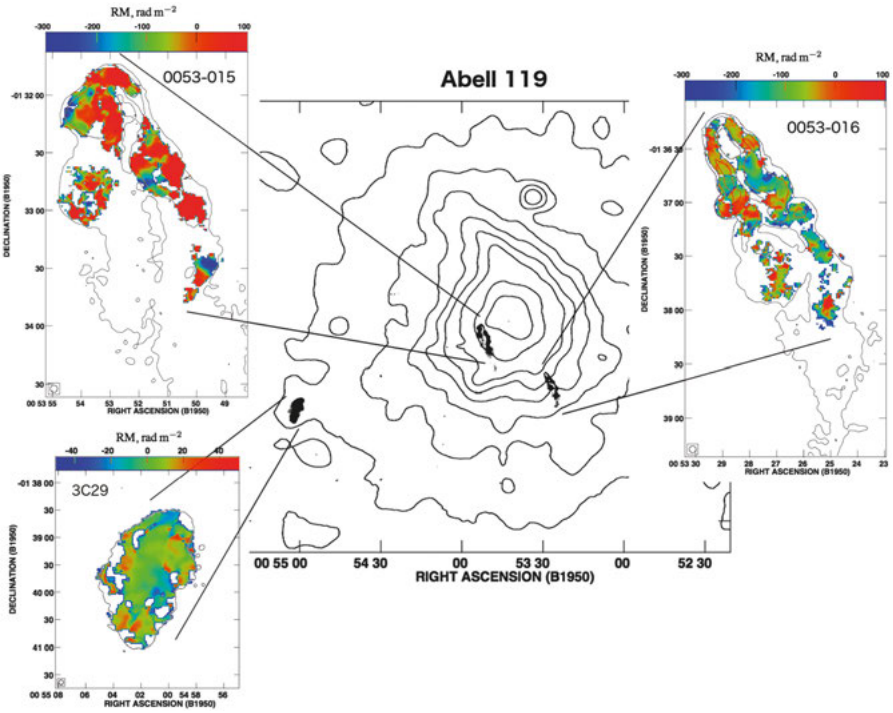

Figure 2.1: Evidence of small-scale dynamo action in clusters of galaxies. The figure shows the Faraday rotation measure maps of radio sources within a galaxy cluster from [150, 118]. The cluster electrons act as a foreground for the radio source. These maps indicate magnetic fields in the cluster on scales of 10–40 kpc and strength of several μG.

2.1 Nonlinear small-scale dynamo

2.1.1 Linear growth stage

Nonlinear small-scale dynamo models developed slowly and were influenced by analytical studies of kinematic regime. It was believed for some time that after going nonlinear, the small-scale dynamo will saturate. If we agree to this proposition and assume that the magnetic energy indeed saturates as soon as the dynamo becomes nonlinear, then the saturation level, in this case, will be of order $\rho v_\eta^2/2$, where v_η is a Kolmogorov velocity scale. This is a factor of $\mathrm{Re}^{-1/2}$ smaller than the kinetic energy density and will be completely dynamically unimportant in high Re astrophysical environments. In fact, observations clearly indicate the opposite—a sizable energy density of the magnetic field in large-scale systems; see Figure 2.1 (for the estimate of Re in galaxy cluster environments see the subsequent subsection). Understanding the nonlinear regime which is dominant in astrophysical environments was, therefore, very important. The early work by Schlüter and Bierman [387] suggested that the dynamo will not stop and will continue to grow, saturating on each subsequent scale after a dynamical time. Recently, small-scale dynamo underwent revival due to the availability

of direct numerical simulations. Simulations of the dynamo saturated state produced steep spectra and significant outer-scale fields. The saturated state was only weakly dependent on Re and Pr as long as Re was large; see, e. g., [188]. Furthermore, it was suggested in [381, 93, 373, 28, 23] that there is a linear growth stage. In subsequent sections, we will follow the argumentation of [23], which supplied analytical and numerical arguments in favor of the universality of the nonlinear small-scale dynamo.

We will assume that the magnetic and kinetic spectra at a particular moment of time are similar to what is presented in Figure 2.2. Magnetic and kinetic spectra cross at some "equipartition" scale $1/k^*$, below which both spectra are steep due to MHD cascade [172, 21]. This assumption is suggested by both numerical evidence [32, 93] and observations of magnetic fields in clusters of galaxies [248]. Starting with very small magnetic energy and following standard kinematic dynamo calculations, e. g., [245], the magnetic energy will grow exponentially until the magnetic spectrum intersect kinetic spectrum at the viscous scales (assuming Pr = 1). This will roughly correspond to the beginning of the nonlinear regime with equipartition scale equal to the dissipation scale.

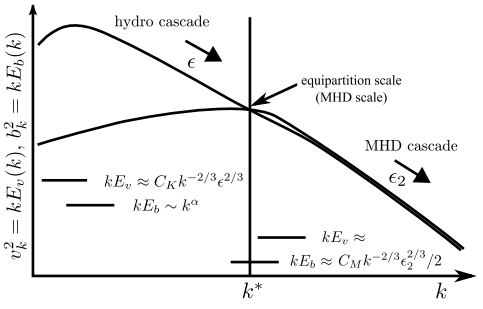

Figure 2.2: A cartoon of kinetic and magnetic spectra in small-scale dynamo, at a particular moment of time when equipartition wavenumber is k^*. From [23].

At large scales, the magnetic spectrum is shallow, k^α, $\alpha > 0$, while the kinetic spectrum is steep due to the hydrodynamic cascade. Most of the magnetic energy is contained at the scale of $1/k^*$. We designate C_K and C_M as Kolmogorov constants of hydro and MHD, respectively. The hydrodynamic cascade rate is ϵ and the MHD cascade rate as ϵ_2. Due to the conservation of energy in the inertial range, magnetic energy will grow at a rate $\epsilon - \epsilon_2$. We will designate $C_E = (\epsilon - \epsilon_2)/\epsilon$ as an "efficiency of the small-scale dynamo" and will argue that this is a true constant since (a) turbulent dynamics is local in scale in the inertial range; (b) ideal MHD or Euler equations do not contain any scale explicitly. Magnetic energy will grow linearly with time if ϵ = const. The equipartition scale $1/k^*$ will grow with time as $t^{3/2}$ [28]. Alternatively, one can say that small-scale dynamo saturates at several dynamical times at scale $1/k^*$ and proceeds to a twice larger scale [381]. If magnetic energy grows approximately until equipartition [188, 93], the whole process will take around several outer timescales of the system, or more quantitatively, $(C_K^{3/2}/C_E)(L/v_L)$.

2.1.2 Locality of the small-scale dynamo

We will use the "smooth filtering" approach with dyadic-wide filter in k-space [9]. We designate a filtered vector quantity as $\mathbf{a}^{[k]}$ where k is a center of a dyadic Fourier filter in the range of wave numbers $[k/2, 2k]$. The actual logarithmic width of this filter is irrelevant to further argumentation, as long as it is not very small. We will assume that the vector field $\mathbf{a}$ is Hölder-continuous, i. e., $|\mathbf{a}(\mathbf{x}) - \mathbf{a}(\mathbf{y})| < |\mathbf{x}-\mathbf{y}|^{\mathbf{h}}$ with exponent $0 < h < 1$ and designate $a_k = \langle|\mathbf{a}^{[k]}|^3\rangle^{1/3}$ (angle brackets are averages over ensemble), which is expected to scale as $a_k \sim k^{\sigma_3}$, e. g., $k^{-1/3}$ for velocity in Kolmogorov turbulence. The energy cascade rate is $\epsilon = C_K^{-3/2} k v_k^3$, where we defined Kolmogorov constant C_K by third order, rather than second-order quantities. We will keep this designation, assuming that traditional Kolmogorov constant could be used instead. We use spectral shell energy transfer functions such as $T_{vv}(p,k) = -\langle \mathbf{v}^{[k]}(\mathbf{v}\cdot\nabla)\mathbf{v}^{[p]}\rangle$, $T_{w^+w^+}(p,k) = -\langle \mathbf{w}^{+[k]}(\mathbf{w}^-\cdot\nabla)\mathbf{w}^{+[p]}\rangle$ [6], applicable to incompressible ideal MHD equations, where $w^\pm$ are Elsässer variables and v, b, and $w^\pm$ are measured in the same Alfvénic units. Using central frequency k and studying "infrared" (IR) transfers from $p \ll k$, and "ultraviolet" (UV) transfers, from $q \gg k$, we will provide absolute bounds on $|T|$, in units of the energy transfer rate as in [9, 138], and *relative* volume-averaged bounds which are divided by the actual energy rate and are dimensionless. We will consider three main k intervals presented in Figure 2.2: $k \ll k^*$ ("hydro cascade"), $k \sim k^*$ ("dynamo"), and $k \gg k^*$ ("MHD cascade").

MHD cascade, $k \gg k^*$ The only energy cascades here are Elsässer cascades and, by the design of our problem, w^+ and w^- have the same statistics so that we will drop $\pm$. For an exchange with the $p \ll k$ band, for $|T_{ww}|$, using Hölder inequality and wavenumber conservation, we get an upper bound of $p w_p w_k^2$ and for the $q \gg k$ band, it is $k w_q^2 w_k$; these bounds are asymptotically small. For the full list of transfers and limits, refer to Table 2.1. This bound is relative to $C_M^{-3/2} k w_k^3$, where C_M is a Kolmogorov constant for MHD, from which we get that most of the energy transfer with the $[k]$ band should come from the $[kC_M^{-9/4}, kC_M^{9/4}]$ band; see [21]. The global transfers between kinetic and magnetic energy must average out in this regime. Nevertheless, the pointwise IR and UV transfers can be bounded by $p b_p v_k b_k$ and $k b_q^2 v_k$ and are small [138].

Table 2.1: Transfers and upper limits.

Transfers			$p \ll k$	$q \gg k$
$T_{vv}(p,k)$	=	$-\langle \mathbf{v}^{[k]}(\mathbf{v}\cdot\nabla)\mathbf{v}^{[p]}\rangle$	$p v_p v_k^2$	$k v_k v_q^2$
$T_{bb}(p,k)$	=	$-\langle \mathbf{b}^{[k]}(\mathbf{v}\cdot\nabla)\mathbf{b}^{[p]}\rangle$	$p b_p v_k b_k$	$k b_k v_q b_q$
$T_{vb}(p,k)$	=	$\langle \mathbf{b}^{[k]}(\mathbf{b}\cdot\nabla)\mathbf{v}^{[p]}\rangle$	$p v_p b_k^2$	$k b_k v_q b_q$
$T_{bv}(p,k)$	=	$\langle \mathbf{v}^{[k]}(\mathbf{b}\cdot\nabla)\mathbf{b}^{[p]}\rangle$	$p b_p v_k b_k$	$k v_k b_q^2$
$T_{w^+w^+}(p,k)$	=	$-\langle \mathbf{w}^{+[k]}(\mathbf{w}^-\cdot\nabla)\mathbf{w}^{+[p]}\rangle$	$p w_p w_k^2$	$k w_k w_q^2$

Hydro cascade, $k \ll k^*$ Despite having some magnetic energy at these scales, most of the energy transfer is dominated by the velocity field. Indeed, $|T_{vv}|$ is bounded by $pv_pv_k^2$ for $p \ll k$ and by $kv_q^2v_k$ for $q \gg k$. Compared to these, $|T_{bv}|$ transfers are negligible: $pb_pv_kb_k$ and $kb_q^2v_k$. For magnetic energy in the $p \ll k$ case, we have $|T_{vb}|$ and $|T_{bb}|$ transfers bounded by $pv_pb_k^2$, $pb_pv_kb_k$, and for the $q \gg k$ case, $|T_{vb}|$ and $|T_{bb}|$ are bounded by $kb_kv_qb_q$. Out of these three expressions, the first two go to zero, while the third goes to zero if $\alpha - 2/3 < 0$ or have a maximum at $q = k^*$ if $\alpha - 2/3 > 0$. This means that for the transfer to magnetic energy we have IR locality, but not necessarily UV locality. Note that magnetic energy for $k \ll k^*$ is small compared to the total, which is dominated by $k = k^*$. We will assume that $\alpha - 2/3 > 0$ and that the spectrum of b_k for $k < k^*$ is formed by nonlocal $|T_{vb}|$ and $|T_{bb}|$ transfers from k^*, namely magnetic structures at k are formed by stretching of magnetic field at k^* by velocity field at k. Magnetic spectrum before k^* is, therefore, nonlocal and might not be a power-law, but our further argumentation will only require that $b_k < v_k$ for $k < k^*$.

Dynamo cascade $k = k^*$ In this transitional regime, our estimates of Elsässer UV transfer and kinetic IR transfer from two previous sections will hold. We are interested how these two are coupled together and produce observed magnetic energy growth. IR $p \ll k^*$ $|T_{vb}|$ and $|T_{bb}|$ transfers will be bounded by $pv_pb_{k^*}^2$ and $pb_pv_{k^*}b_{k^*}$, which go to zero, so there is a good IR locality. Ultraviolet transfers will be bounded by $k^*b_{k^*}b_qv_q$. This quantity also goes to zero as q increases, so there is an UV locality for this regime as well. Let us come up with bounds of relative locality. Indeed, the actual growth of magnetic energy was defined as $\epsilon_B = \epsilon - \epsilon_2 = C_EC_K^{-3/2}kv_k^3$. So, the $p \ll k^*$ IR bound is $k^*C_E^{3/2}C_K^{-9/4}$ and the UV bound is $k^*C_E^{-3/2}C_M^{9/4}$. We conclude that most of the interaction, which results in magnetic energy growth, must reside in the wavevector interval of $k^*[C_E^{3/2}C_K^{-9/4}, C_E^{-3/2}C_M^{9/4}]$. Numerically, if we substitute $C_K = 1.6$, $C_M = 4.2$, $C_E = 0.05$, we get the interval of $k^*[0.004, 2000]$. So, despite being asymptotically local, small-scale dynamo can be fairly nonlocal in practice.

Summarizing, the kinetic cascade at large scales and the MHD cascade at small scales are dominated by local interactions. The transition between the kinetic cascade and the MHD cascade is also dominated by local interactions, and since ideal MHD equations do not contain any scale explicitly, the efficiency of small-scale dynamo C_E is a truly universal constant. Note that C_E relates energy fluxes, not energies, so this claim is unaffected by the presence of intermittency. Magnetic spectrum at $k \ll k^*$ is dominated by nonlocal triads that reprocess magnetic energy from $k = k^*$, but since this part of the spectrum contains negligible magnetic energy, our universality claim is unaffected by this nonlocality.

2.1.3 Numerical results

Numerical simulations of statistically homogeneous isotropic small-scale dynamo in [23] were performed by solving MHD equations with stochastic non-helical driving and

explicit dissipation with $\mathrm{Pr}_m = 1$. We ran several statistically independent simulations in each group and obtained growth rates and errors from sample averages. The energy injection rate was controlled. Figure 2.3 shows the sample-averaged time evolution of magnetic energy. Growth is initially exponential and smoothly transitions into the linear stage. Note that scatter is initially small, but grows with time, which is consistent with the picture of the magnetic field growing at progressively larger scales and having progressively less independent realizations in a single datacube.

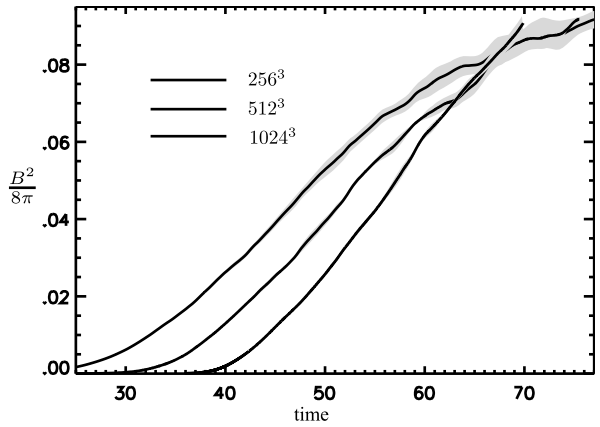

Figure 2.3: Magnetic energy growth versus time in code units, observed in simulations with $\mathrm{Re}_m = 1000$ ($\tau_\eta = 0.091$ in code units), $\mathrm{Re}_m = 2600$ ($\tau_\eta = 0.057$), and $\mathrm{Re}_m = 6600$ ($\tau_\eta = 0.036$). We used sample averages which greatly reduced fluctuations and allowed us to measure C_E with sufficient precision. From [23].

2.1.4 Efficiency of nonlinear dynamo

Our C_E is much smaller than unity. One would expect a quantity of order unity because this is a universal number, determined only by strong interaction on equipartition scale. If we refer to the ideal incompressible MHD equations, written in terms of Elsässer variables, $\partial_t \mathbf{w}^\pm + \hat{S}(\mathbf{w}^\mp \cdot \nabla)\mathbf{w}^\pm = 0$, the dynamo could be understood as decorrelation of $\mathbf{w}^\pm$, which are originally equal to each other in the hydrodynamic cascade. In our case, this decorrelation is happening at the equipartition scale $1/k^*$. Being time-dependent, it propagates upscale, while, ordinarily, energy cascade goes downscale. The small value of C_E might be due to this. As opposed to picture with multiple reversals and dissipation due to microscopic diffusivity, typical for the kinematic case, in our picture we appeal to *turbulent diffusion* which helps to create the large-scale field. Both stretching and diffusion depend on turbulence at the same designated scale $1/k^*$, so, in the asymptotic regime of large Re, one of these processes must dominate. As C_E is small, stretching and diffusion are close to canceling each other.

A better studied and understood kinematic dynamo might shed some light on the problem of small C_E. In the kinematic regime, when we neglect Lorentz force in the MHD equation, the growth is exponential, and the rate is expected to come from the fastest shearing rate of smallest turbulent eddies. Observed rates, however, are smaller which was interpreted as a competition between stretching and turbulent mixing [139]. In our simulations, in the kinematic regime of M7-9, we observed growth rate $\gamma\tau_\eta = 0.0326$, where $\tau_\eta = (\nu/\epsilon)^{1/2}$ is a Kolmogorov timescale, which is consistent with [188, 384]. In terms of a minimum timescale, $\tau_{\min} \approx 9\tau_\eta$, $\gamma\tau_{\min} = 0.3$, which is still small. The Kazantsev–Kraichnan model [217, 245] predicts $\gamma\tau_{\min} \sim 1$. This model, however, uses ad hoc delta-correlated velocity, which does not correspond to any dynamic turbulence and its statistics are time-reversible, as opposed to time-irreversible real turbulence. Time irreversibility of hydro turbulence mandates that fluid particles separate faster backward in time, since $\langle v_{\|l}^3 \rangle = -4/5\epsilon l$ is negative.

In [23], the interplay of stretching and diffusion was studied by simulations of kinematic dynamo forward and backward in time. The backward dynamo was faster by a factor of 2.0 ± 0.1, which is roughly consistent with the ratio of particle diffusion forward and backward in time. This result hints that the dynamo is a result of competing mechanisms of turbulent stretching and turbulent diffusion and the outcome depends on statistics of velocity other than just velocity spectrum.

2.1.5 Dynamo simulations with intermittent driving

We have extended the study of statistically homogeneous isotropic small-scale dynamo simulations in [23] with a series of simulations with intermittent energy injection into the velocity field, with the period 1, 2, 4, and 8 self-correlation timescales of velocity, τ_c. All simulations have a magnetic Prandtl number $\mathrm{Pr}_m = 1$. We limited driving to lower harmonics in Fourier space, $|k| < 2.5$. We started each MHD simulation by seeding the low-level white noise magnetic field into the dataset obtained from the driven hydrodynamic simulation which reached a statistically stationary state. This dataset was further evolved by full incompressible MHD equations. Figure 2.4 shows the evolution of magnetic energy in time. The previously measured normalized growth rate $C_E = 0.05$ is roughly consistent with most of the data. An important prediction of [23] was also that the magnetic outer scale is proportional to v_A^3/ϵ and grows in time as $t^{3/2}$. We are using this conjecture to estimate the outer scale of cluster magnetic fields, and we plotted the v_A^3/ϵ versus the magnetic outer scale, which we determined from the peak of the magnetic spectrum. The simulation with constant driving, the upper panel of Figure 2.4, showed good agreement with the proposed scaling and we have determined the dimensionless coefficient c_l in the relation $L_B = c_l v_A^3/\epsilon$ around 0.2, with best fit 0.18. The intermittently driven simulation have demonstrated large scatter, which is because turbulence spectra do not depend instantaneously on the energy injection rate, but have a memory spanning around about one dynamical time.

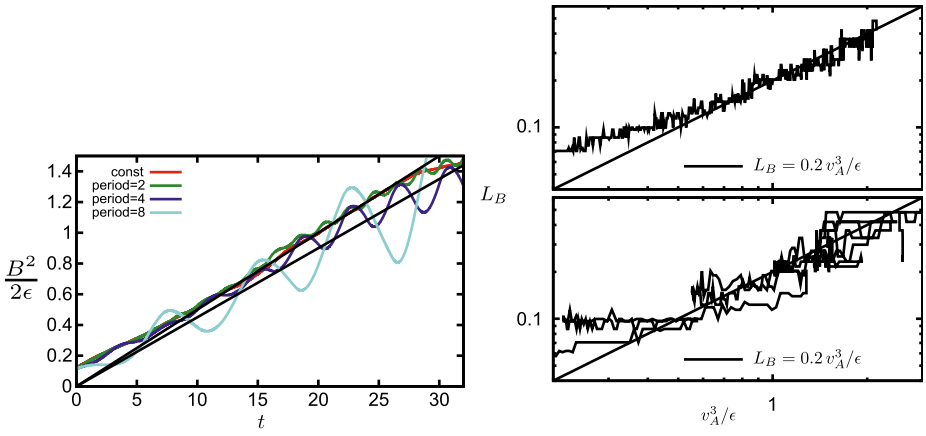

Figure 2.4: Left: The magnetic energy in Alfvén units, divided by the energy driving rate, ϵ, resulting in $B^2/2\epsilon$ (simulation time units) versus time (simulation time units), similar to results reported in [23]. Different curves correspond to intermittent driving with the period of driving varied from 1 to 8 τ_c. The half of the period the driving was on, while the other half it was off. We also put a simulation with constant driving for comparison. Two thin lines correspond to the efficiencies of nonlinear dynamo C_E of 0.045 and 0.05 (dimensionless). Right: The relation between magnetic energy and the outer scale during the time evolution in the simulation of the nonlinear small-scale dynamo. The upper plot corresponds to the case with constant driving, reported earlier in [23], while the lower plot has been produced in an otherwise similar simulation with intermittent driving with the period of $8\tau_c$. In the case of intermittent driving, we used the dissipation rate ϵ averaged over $2\tau_c$ like the analysis of cluster data. We determined outer scale of magnetic field by its peak wavenumber of the spectrum $L_B = 2\pi/k_{\max}$. The best fit corresponds to the coefficient $c_l \approx 0.18$ in Equation (2.5). Reproduced from [39] with permission of AAS.

Also, the cascade rate at the equipartition scale is delayed compared to the injection rate. We found that averaging cascade rate over $2\tau_c$ and introducing phase delay of $\pi/2$ will work the best to reproduce the L_B relation and we presented the plot of such constructed L_B–v_A^3/ϵ on the lower panel of Figure 2.4. The scatter was significantly reduced and the derived c_l coefficient is also the same as for the constant driving case.

2.2 Dynamo in galaxy clusters

2.2.1 Physical conditions in galaxy clusters

Galaxy clusters (GC) are filled with hot intracluster medium (ICM), which is known to be magnetized from radio observations. These observations reveal both the occurrence of Faraday rotation effect on polarized radiation from background quasars [98, 99] and of diffuse synchrotron emission [152] from the ICM. The magnetic field estimated based on these observations range between a fraction and several μG. Measurements on the structural and spectral features are sparse and more difficult but

indicate steep power-laws below few tens of kpc [248, 242]. For massive clusters, turbulence in the ICM is mainly driven by structure formation [338, 373, 433, 319, 320]. The most important magnetic field amplification mechanism in the ICM is the small-scale or fluctuation dynamo (SSD), which operates on scales smaller than the turbulence outer scale (see Section 2.1). In kinematic regime, the magnetic energy grows exponentially, until the approximation breaks down, roughly in a dynamical time multiplied by $\mathrm{Re}^{-1/2}$, where Re is an effective Reynolds' number. The extremely hot and rarefied plasma of the cluster have very large collisional mean-free paths, around

$$\lambda \approx 10^3\,\mathrm{pc}(n/3\times10^{-3}\,\mathrm{cm}^{-3})^{-1}(T/10\,\mathrm{keV})^{3/2}, \tag{2.1}$$

at the same time, given that the observed magnetic field is around 3 μG, the Larmor radius is smaller by many orders of magnitudes:

$$r_L \approx 10^{-9}\,\mathrm{pc}(T/10\,\mathrm{keV})(B/3\,\mu\mathrm{G})^{-1}. \tag{2.2}$$

Collisional transport, described by Braginsky viscosity and magnetic diffusivity does not terminate turbulent cascade before plasma scales d_i and r_L and the cascade continues as plasma turbulence, which is evidenced in another case of tenuous and magnetized plasma—the solar wind [289]. This is called collisionless plasma. It is challenging to understand from the theoretical viewpoint since nonlinear plasma effects are dominating the transport. This has been known since early laboratory plasma experiments when it became clear that collisional "classic transport" is grossly insufficient to explain cross-field diffusion [155]. Normally, the effective parallel mean-free path is smaller than the one obtained by collisional formula but larger than the Bohm estimate ($\lambda_{\mathrm{eff}} \sim r_L$). The search for this "mesoscale" for cluster conditions resulted in estimates for the mean-free path of the proton in the ICM of around 10^{-3}–10^{-6} pc [380, 29, 383, 60]. From these estimates, we expect clusters to be turbulent with Reynolds' numbers Re exceeding 10^{12}. If we combine this estimate with the above estimate of the kinematic SSD growth rate, for a dynamical time ~ eddy turnover time ~ 1 Gyr [319], the exponentiation timescale is smaller than 1 Gyr $(\mathrm{Re})^{-1/2} \approx 1$ kyr.

The kinematic approximation of small-scale dynamo breaks down very quickly, and the dynamo spends most of the time in the nonlinear regime. In this regime, the magnetic energy continues to grow as it reaches equipartition with the turbulent kinetic energy cascade at progressively larger scales [387]. At this stage, the magnetic energy is characterized by a steep spectrum and an outer scale, L_B, a small fraction of the kinetic energy outer scale. This picture has been advocated for any high-Re flow, with the argument relying on the locality of energy transfer functions (Section 2.1). It also follows that the magnetic energy growth rate corresponds to a certain fraction of the turbulent dissipation rate, with this fraction being a universal dimensionless number around 0.05, and that the magnetic outer scale L_B grows with time as $L_B \approx t^{3/2}$ [23]. Magnetic energy finally saturates when L_B is a substantial fraction of the outer scale of the turbulence. However, this may never happen in galaxy clusters, as we show below.

2.2.2 Limitation of dynamo simulations

An important consequence of the above picture is that the memory of the initial seed field is quickly lost. We expect magnetic field in clusters to depend only on the cluster turbulent history. While this theoretical insight was certainly useful, its applications to cluster formation was not immediately realized. There are two main reasons for this. First, despite considerable progress in modeling of structure formation and GCs, the dynamic range of spatial scales achieved so far was considerably below the threshold necessary for the turbulent dynamo to operate efficiently. Second, given the current understanding of MHD dynamo (Section 2.1), lack of detailed knowledge about the ICM turbulence precludes accurate estimates of both magnetic energy, and in particular, the outer scale of the magnetic spectrum. MHD numerical models of GCs often report rather weak magnetic field amplification roughly by factors $\lesssim 30$ [321, 117, 126, 432], this including sizable contribution from compression, see Figure 2.5. As alluded above, the reason is the low Re of the simulated flows. The kinematic growth rate is $\gamma \approx \mathrm{Re}^{1/2}/30\tau_L$ [188, 384, 23], where τ_L is the turnover time of the largest eddy. So even with Re $\sim$ several $\times 10^2$, typical for cluster simulations, the dynamo will be stuck for several dynamical times in a kinematic regime, i. e., several Gyr, while in nature this stage will be many orders of magnitude quicker than the dynamical time (see Section 2.2.1). Figure 2.6 demonstrates the difference between the magnetic energy growth between the case with huge Re (straight line) and Re that are available with current numeric capabilities (actual growth obtained in simulations with Re = 1000 and 3300). The growth observed in simulations is delayed due to the grossly prolonged kinematic stage. Figure 2.7 shows structure functions from MHD simulations of clusters in fully cosmological context. From this figure we see that magnetic and kinetic energies are close on equipartition scales on dissipation scales or below, which is the evidence that the transition to fully nonlinear dynamo have not yet happened, therefore these simulations were under-resolved, as far as dynamo is concerned. Given the above argumentation, fully resolving dynamo would require much higher effective Re.

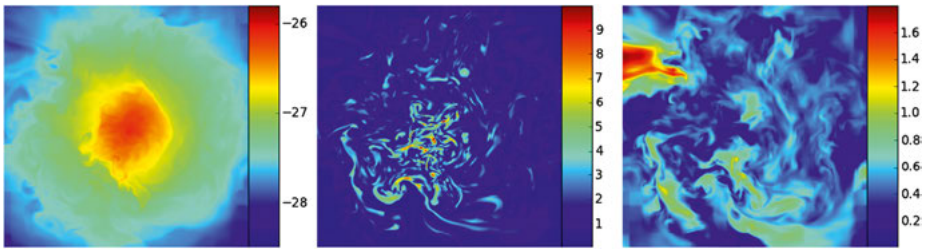

Figure 2.5: Cluster simulated in a fully cosmological context: a slice through the center (3 Mpc across) – log density $\log_{10}(\rho\,\mathrm{g}^{-1}\,\mathrm{cm}^3)$ (left), RMS magnetic field, μG (middle) and RMS velocity, 10^8 cm/s (right). Typical sound speed $c_s \sim 10^8$ cm/s, typical Alfven speed $v_A \sim 10^7$ cm/s. Reproduced from [40] with permission of AAS.

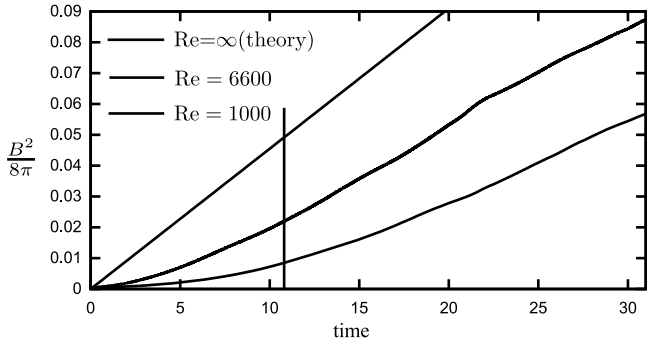

Figure 2.6: The growth of dynamo can be significantly delayed in simulations, compared with the actual high-Re flows. We compare magnetic energy growth from 4×10^{-4} below equipartition in $\mathrm{Re} = 10^3$ and $\mathrm{Re} = 6.6 \times 10^3$ simulations (solid) from [23] and the hypothetical $\mathrm{Re} = \infty$ case, which is represented by linear growth $C_E \epsilon t$ (dashed). If we stop simulation around the dashed line, which roughly corresponds to the duration of cosmological simulation $\sim$ 11 dynamical times, magnetic energy will be grossly underestimated. Its value will depend on the seed field as well as the effective Reynolds' number of the simulation. From [39].

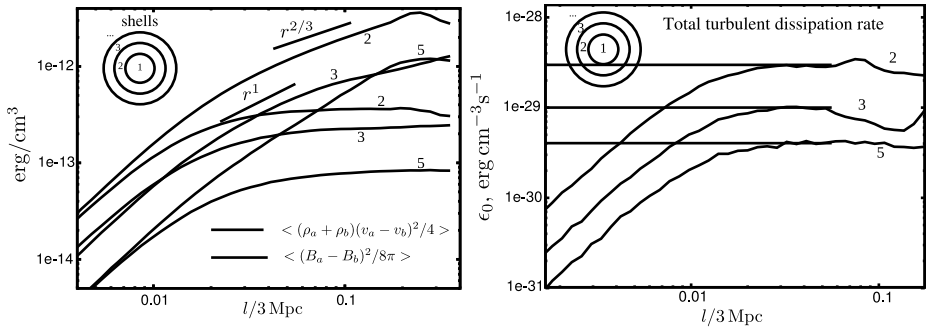

Figure 2.7: Left: Second-order structure functions, characterizing kinetic (solid), and magnetic (dashed) energy density in a simulated cluster. Here, ρ_a, ρ_b, v_a, v_b, B_a, B_b are the quantities taken at points a and b, separated by the distance l. Middle point between a and b lies within a shell, whose number is indicated on the plot. The radius of nth shell is $n \cdot 300$ kpc. We used structure functions to calculate these quantities in shells around the cluster center because all quantities depend strongly on the distance to the center. Right: Dissipation/cascade rate in the cluster, calculated by the third-order SFs in three shells. This allows estimating dynamic lifetime of turbulence in cluster, which is $3 \cdot 10^9$ years in shells 2–3 and $8 \cdot 10^9$ years in shell 5. Reproduced from [40] with permission of AAS.

Below we report on the progress with the approach which is different from direct approach of cosmological MHD simulation, which given the present state of our numerical capabilities, as we argued above is completely inadequate. We have recently employed a novel technique to model the formation of a massive GC with sufficient resolution to resolve the turbulent cascade [319, 320]. We have extracted the time-dependent properties of the turbulence and used this information in combination with indepen-

dent results on turbulent dynamo obtained from high-resolution periodic box simulations. The novelty and advantage of our approach is that the turbulence is self-consistently estimated through a numerical hydrodynamic model of structure formation, while the magnetic field evolution is estimated based on theory, which was confirmed in large-scale homogeneous dynamo simulations, robustly tested by studying low Re effects in a scaling study. Importantly enough, such dynamo simulations, unlike cosmological cluster models, are not limited in the number of dynamical times one can simulate.

2.2.3 Analysis of cluster simulations

Details of the cluster simulation called the Matryoshka run can be found in [225, 319, 320].

Between 60 and 90 % of the kinetic energy of the cluster turbulence is in the solenoidal component [320]. This is the relevant component for the discussed small-scale dynamo mechanism, and the key question is whether it resembles homogeneous isotropic turbulence in the inertial range.

We checked statistical isotropy of the cluster turbulence by comparing the longitudinal velocity SF with the analytical expression that presumes statistical isotropy: $\langle(\delta v_{\parallel l})^2\rangle = (2/l^2)\int_0^l \langle(\delta v_{\perp x})^2\rangle x dx$. Statistical isotropy seems to be satisfied quite well [40]. A more critical test is provided by the relation between structure functions of different orders. For example, the dimensionless ratio $-\langle(\delta v_l)^2\rangle^{3/2}/\langle(\delta v_{\parallel l})^3\rangle$ is of interest to relate the energy cascade rate with the energy content of the cascade. We looked at this ratio in the cluster simulation and the homogeneous incompressible driven turbulence [40]. For the latter, we used data from fully resolved direct numerical simulation of incompressible hydrodynamic driven turbulence in a periodic box. From the comparison, we concluded that the second-order structure function of the cluster simulations in the range of scales 0.14–0.4 Mpc could be reliably used to estimate the turbulent dissipation rate, $\epsilon_{\rm turb}$, associated with the incompressible velocity component and necessary to evaluate dynamo action in the ICM. The turbulence dissipation rate is then estimated as follows:

$$\epsilon_{\rm turb} = (c_1/c_2)(5/4)\left\langle(\delta v_l)^2\right\rangle^{3/2}/l, \tag{2.3}$$

where $c_2 \approx 27$ is the ratio of the structure functions (second order to 1.5 power and third order, see above) and $c_1 \approx 1.17$ is a factor to correct for dissipation effects, as in our finite Re simulations the Kolmogorov's $-4/5$ normalization slightly underestimates the turbulent dissipation rate.

As expected, at a given time $\epsilon_{\rm turb}$ is a rather constant function of l within the inertial range. The observed deviation was used to estimate the error of the measurement of $\epsilon_{\rm turb}$. We plotted the dissipation rate determined in this manner on the top panel of

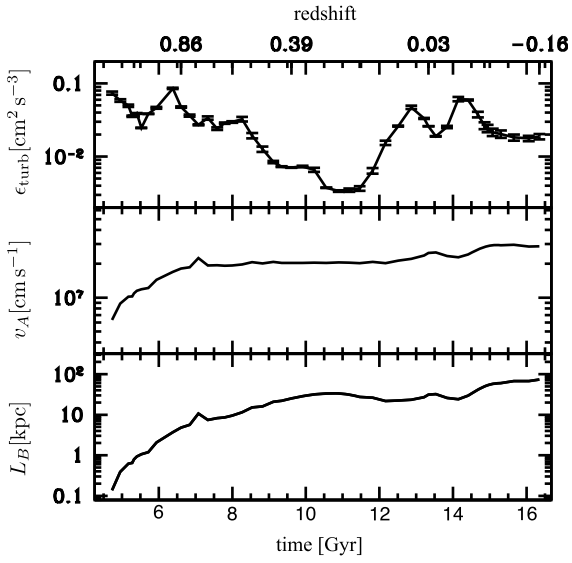

Figure 2.8: The evolution of the turbulent dissipation rate (upper plot), Alfvén speed (middle), and the outer scale of the magnetic field (bottom) inferred from the cosmological cluster simulation by using self-similar laws for turbulence and dynamo tested and normalized in well-resolved high-Re DNS. In obtaining v_A, we divided the magnetic energy E_B from Equation (2.4) to the average density within 1/3 of the virial radius. Reproduced from [39] with permission of AAS.

Figure 2.8. We used the velocity structure function calculated within 1/3 of the virial radius of the simulated cluster for each data-cube. As we see from this figure, the dissipation rate varies nonmonotonically over roughly an order of magnitude in scale over the lifetime of the cluster. The errorbars defined above indicate the deviation from Kolmogorov's self-similarity and were rather small, except for the time intervals where the rate was changing rapidly, i. e., the cluster was either relaxing of experiencing a fresh injection of kinetic energy.

We then estimated magnetic energy density as [23]

$$E_B = \int_0^t C_E \rho \epsilon_{\rm turb} dt \tag{2.4}$$

with $C_E = 0.05$. This equation originally described average magnetic energy density in a statistically homogeneous case, as in simulations from Section 2.1.3. When we apply it to the cluster simulation, we have to take into account that both ρ and ϵ depend on the distance to the cluster center (radius) and on time. As we found, ϵ have only modest dependence on the radius, however, ρ is highly peaked around the center, so E_B will exhibit similar behavior. The cluster's density profile is almost invariant in time if expressed in virial units, i. e., $\rho(r,t) = \rho(t) f(r/R_{\rm vir})$ and the radial dependence can be pulled in front of the time integral in Equation (2.4). If at any given time, we are interested only in Alfvén speed $v_A = (2E_B/\rho)^{1/2}$, this quantity will have only weak dependence on radius and may well be characterized by the average within the radius of $R_{\rm vir}/3$. We plotted such averaged Alfvén velocity on the middle panel of Figure 2.8. Furthermore, as was shown in [23], for statistically stationary turbulence the magnetic

energy containing scale could be estimated as

$$L_B = c_l v_A^3 / \epsilon_{\rm turb}, \tag{2.5}$$

where $c_l \approx 0.18$ is a universal coefficient, which could be determined in DNS; see Figure 2.4. Our cluster turbulence was rather nonstationary, however, as discussed in Section 2.1.5, the estimate Equation (2.5) can also be applied to non-stationary driven turbulence as long as the dissipation rate is averaged over a timescale around one dynamical time; see below. This is because hydrodynamic cascade has a memory over around one dynamical time and the changes in the driving rate do not instantaneously affect turbulent rate on small scales (Section 2.1.5). So, in using Equation (2.5) we used the $\epsilon_{\rm turb}$ averaged over 2 Gyr, which approximately corresponds to two dynamical times.

The middle and bottom panels of Figure 2.8 show time evolution of the average RMS Alfvén speed, $v_A = (2E_B/\rho)^{1/2}$ and the magnetic outer scale L_B. Note that while v_A grows monotonically, L_B can decrease somewhat during a prolonged increase of the turbulent activity, such as during several major mergers.

Our estimates for $z \sim 0$ characteristic values of Alfvénic speed $v_A \sim 10^7$ cm/s and the outer scales $L_B \sim$ 30–50 kpc, are consistent with the observed values reported in the literature [313, 128, 50, 181, 180]. This indicates that the type of nonlinear dynamo described in [23] is consistent with what we observe in clusters, irrespective of the initial conditions. On the other hand, kinematic models, as well as ad hoc MHD simulations with limited Re, e. g., [14], would require fine-tuning of initial conditions to achieve this.

One interesting conclusion from our results on Figure 2.8 is that the outer scale of the magnetic field grows relatively quickly after the beginning of the simulation. This is different from the direct MHD cluster simulations where we had mostly kinematic growth with a magnetic spectrum peaked on numerical dissipation scale, e. g., [447]. Note that the scale of the magnetic field plays a crucial role in cosmic ray escape times, therefore correctly estimating magnetic outer scale is essential for models of particle acceleration in clusters [58, 59, 40, 320].

2.2.4 Cluster magnetic fields

Similar idea based on post-processing of hydrodynamic data was also employed in [373], but with substantial differences. The turbulence in these early calculations was not as resolved as in ours, and the growth of magnetic energy and Alfvén scale were not estimated from the turbulent dissipation rate and the precise estimate of C_E, as we did here.

One of the differences between cluster turbulence and the statistically stationary turbulence studied in [23] was the strong variations of the cascade rate over timescales of 1–2 dynamical timescales of the cluster. Our estimates of the efficiency in the case of

intermittent driving from this work are roughly compatible with $C_E = 0.05$ and further work with higher Re is expected to clarify whether the differences between constant and intermitted driving are significant. We concluded that the effects of intermittent driving could probably be ignored at the level of precision of the $\epsilon_{\rm turb}$ measurement. Note that although Section 2.1.5 simulations were insightful in understanding basic physics behind high-Re small-scale dynamo, we did not use them directly as a subgrid model for Section 2.2.3 simulations. Instead, we used Equation (2.4), which is a closer approximation for the astrophysical cases with Re $> 10^{12}$, this difference being especially critical for the cluster case, which had only several dynamical times to evolve (see Figure 2.5 and corresponding discussion).

All basic properties of the cluster, such as its mass, size, and thermal energy continue to grow along with its magnetic energy and magnetic outer scale. The detailed comparison between thermal, turbulent, and magnetic energy components of the cluster has been performed in [318]. There it is found that the fraction of the thermal energy arising from the turbulent dissipation rate changes relatively little over the cosmological time and the turbulent Mach number is also rather stable. Since the magnetic energy is also a fraction of the accumulated turbulent dissipation rate, the plasma β in our cluster fluctuates around a constant value ~ 40 for the past 10 Gyr [318].

The treatment of cluster turbulence with ILES, as well modeling the evolution of the magnetic energy with the model from [23] relies on the assumption that the Reynolds numbers in clusters are high. For example, our comparison of the cluster simulation and the DNS leads to an estimate of an effective Kolmogorov (dissipation) scale for the cluster simulation of $\eta \approx 2.7$ kpc, corresponding to an effective Re around 3000. We expect clusters to have higher Re, as briefly discussed in Section 2.2.1, due to the collective microscopic scattering in the high-β ICM plasma [380, 263, 383, 60]. An important observational test to the problem of the ICM viscosity are the measurements of Faraday rotation in AGN sources located in clusters, which allowed to probe subkiloparsec scales due to the relatively high resolution of radio maps [242, 248, 180]. The inferred magnetic spectrum in these measurements is negative and steep, typically around Kolmogorov in the range of scales below five kpcs and down to the resolution limit. Such a magnetic spectrum is expected from MHD turbulence with small dissipation scales. It would be grossly inconsistent with magnetic spectra obtained in either kinematic dynamo models, due to their positive spectral indexes, or with MHD models using Spitzer viscosity, which would typically give a rather shallow spectrum with the index around –1; see, e. g., [88]. Complementary to this observational constraint is the theoretical estimates leading to the "mesoscale," i. e., the scale above which one can apply ordinary MHD. We discussed these estimates in the Introduction. However, some additional explanation may be in order. The estimates mentioned above assume that plasma is already magnetized to some degree (not necessarily strongly, e. g., a ~ 1 nG field still gives $r_L \sim 10^{-6}$ pc $\ll \lambda$ and the instability mechanisms should

still work). The most agnostic and practical approach to this bootstrap problem is saying that ICM could obtain this tiny initial field through a variety of mechanisms, such as plasma turbulence, primordial field compressed into ICM, or the AGN fields being mixed by turbulence. A more minimalistic approach is to rely on plasma turbulence alone in the various mechanisms of plasma dynamo. One estimate [380] suggests that the plasma dynamo grows on timescales of ~1 year. Similar work on small-scale dynamos based on closures for pressure-anisotropic plasma was done in [229, 374, 146] and also indicates fast growth. Once the magnetic field reaches the values such that Alfven speed is comparable to the turbulent velocity perturbation on the mesoscale, the more generic and simple mechanism of nonlinear local MHD dynamo described in [23] will start taking place. The outer scale of the magnetic field will start growing from mesoscale up to the approximate values we derive in this chapter. For example, if the mesoscale is 10^{-4} pc, and the density is 10^{-3} cm^{-3}, such an initial field is around three nG. The particular mechanism of the bootstrap makes little difference as far as our calculations are concerned, because either the timescale of 1 year predicted by the above plasma dynamo theories or the estimate for the maximum kinematic growth timescale of 1 kyr we mentioned in the Introduction, all could be considered essentially zero, i. e., the bootstrap happens "instantly," as far as cosmological timescales are concerned. From either observations alone or theory alone, the effective viscosity seems not to be large enough to affect magnetic spectrum above 1 kpc. Therefore, we expect the Re in clusters to be at least 10^4 and likely much higher. Our calculations relied on this fact and the results, grossly consistent with the current observational properties of clusters, provide another support for the picture of a turbulent ICM, as opposed to an earlier view of a viscous and laminar ICM.

3 Incompressible MHD turbulence

In this chapter, we will consider the inertial range of incompressible MHD turbulence with zero cross helicity. The relation between studies of compressible and incompressible regimes is complex. The key issues in the study of the compressible case are: (a) a phenomenon of shocks, (b) the inherently compressible mode (the fast mode in MHD), and (c) a new dimensionless number $M_s = \delta v/c_s$, the Mach number. The latter number could be considered scale dependent by introducing $M_{s,l} = \delta v_l/c_s$. Since δv_l rapidly decay with l, we might consider the motion "subsonic" on small scales. The phenomena (a)–(b), however, can be manifested on any scale.

The most general compressible case, therefore, can be simplified assuming no shocks, this is called the weakly compressible case, or also getting rid of essentially compressible mode—fast mode and assuming that velocity field is purely solenoidal (vortical). These simplifications are similar to one proposed in hydrodynamics and are motivated by a low Mach number on small scales and the relative absence of the interaction between sound waves and turbulence. Likewise, we are motivated by the relatively minor interaction of fast mode and the rest of MHD turbulence. The latter will be further quantified in Chapter 5.

The motivation behind working with the incompressible case is that in most useful cases it can be shown to be free of the characteristic length scale, velocity scale, and time scale. This makes general qualitative and dimensional arguments traditionally used in turbulence theory especially powerful.

The critical difference between incompressible hydrodynamics and incompressible magnetohydrodynamics is that the latter indeed has a designated velocity scale. Local Alfvénic velocity $v_A = B/\sqrt{4\pi\rho}$ can play a role of such a velocity scale, and it seemingly complicates the theory leading to the dimensionless number called' Alfven Mach number $M_A = \delta v/v_A$. Later in this chapter, however, we will show that the inertial range of incompressible MHD turbulence corresponds to the limit of $M_A \to 0$ and can be described using two sets of equations—reduced MHD and the mixing of the slow mode which, as it turns out, no longer possesses designated velocity scale and possesses the same symmetry as incompressible magnetohydrodynamics.

The key to understanding the inertial range of MHD turbulence lies in a fact that turbulent perturbations of v and B will be much smaller (in proper units) than the local mean B field, e. g., $M_{A,l} \sim l^{1/3}$ if we use Kolmogorov scaling. Also, local mean field cannot be excluded by choice of reference frame. This makes local mean field to dominate the dynamics, which was realized by [201, 236]. This dominant contribution, however, is just a wave propagation and hopefully can be trivially described. It is worth noting that most astrophysical environments are indeed somewhat strongly magnetized, typically with $M_A \sim 1$ on the outer scale. This is a consequence of small-scale dynamo being always fast as we showed in Section 2.1. Also, on cosmological timescales, large-scale dynamo will be able to operate in such objects as spiral galax-

https://doi.org/10.1515/9783110263282-003

ies and rotating stars and provides the mean field with scales much larger than turbulent outer scales.

In other words, in all cases of astrophysical turbulence that we know, including turbulence driven by MRI, the large-scale field will be dominant compared to fluctuations. This limit is also known as "strong mean field case." As we will show below, the dynamics in this regime is dominated be Alfven mode. Thus it is often called "Alfvenic turbulence."

We will delay the discussion of the compressible modes and perturbations of density until Section 5 only saying that it is often that dominant Alfven mode provides shearing that often also govern some of the aspects of the dynamics of density, e. g., [37].

The interaction of wavepackets, propagating in a strong mean field is unusual due to a dispersion relation of the type $\omega = k_\parallel v_A$, where $k_\parallel$ is a wavevector parallel to the mean magnetic field. Such a highly anisotropic dispersion relation results in an anisotropic turbulence. Qualitatively, this has been pointed out in [325, 393, 194] and has been an improvement compared to the isotropic Iroshnikov–Kraichnan picture. The quantitative picture did not arrive until much later. As we will show below, an important robust prediction of theory is that in the case of weak interaction mean field turbulence creates "perpendicular cascade," with the perpendicular wavenumber $k_\perp$ increasing while $k_\parallel$ staying constant. This enhances the nonlinearity, described by $\xi = \delta v k_\perp / v_A k_\parallel$, which is the ratio of the mean-field term to the nonlinear term. When turbulence becomes marginally strong, $\xi \sim 1$, the nonlinear timescales become close to the dynamical timescales $\tau_{\rm casc} \sim \tau_{\rm dyn} = 1/wk_\perp$.

In this situation, a "critical balance" of $\xi \sim 1$ has been suggested by Goldreich and Sridhar [172] as a condition which is statistically maintained in the further marginally strong cascade. Since "critical balance" eliminates the dimensionless number ξ from the theory, the cascading model becomes the Kolmogorov model. It is worth noting that "critical balance" works well only in a "balanced" case with a single amplitude of perturbation and a single parameter ξ. In a more complex imbalanced case, an extra argument needs to be in place to close the theory, namely the influence of directional uncertainty of the $\mathbf{v}_A$, first described in [30], which we will return to in Chapter 4.

An important experimental verification of MHD turbulence theories is provided by the solar wind—tenuous magnetized plasma emitted from the sun and propagating outwards, this region of magnetized plasma is also called heliosphere. Ion counters and magnetometers provided measurements of the solar wind parameters roughly from 0.3 to 5 AU distance to the sun. These in-situ measurements are valuable because they lack uncertainties of astrophysical measurements associated with projection on the line of sight. Solar wind density and speed widely vary depending on the flow angle with respect to ecliptic; see Figure 3.1. Solar wind fluctuations measured by a single spacecraft represent time-sequence, which can be analyzed with Fourier series. These time sequences demonstrate fluctuations on timescales from days to seconds.

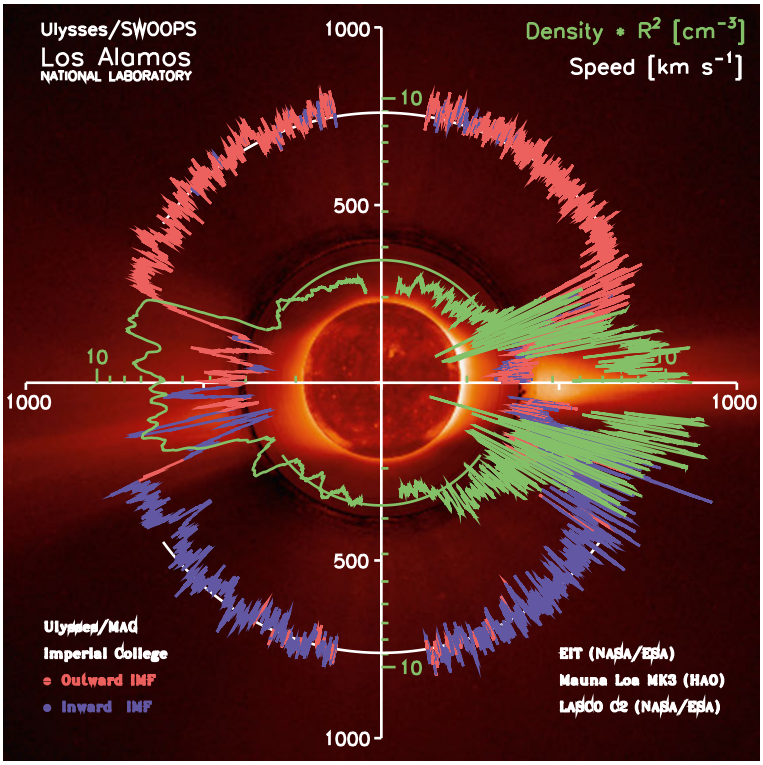

Figure 3.1: Density and speed of the solar wind recorded by ULYSSES/SWOOPS from [310]. Reproduced from [310] with permission of Wiley.

Given that velocity of the solar wind, 300–800 km/s, is much larger compared to typical Alfvén speed of 30 km/s, this is interpreted as the spectrum of spacial fluctuations with scales from 1 AU to hundreds of km. Figure 3.2 shows characteristic spectra obtained by Helios 2 spacecraft. The f^{-1} part of the spectrum corresponds to perturbations with the shot-noise statistics emitted by the sun, while the $f^{-5/3}$ part corresponds to the perturbations that were well-evolved dynamically, i. e., their own characteristic timescales are much shorter than the flight-time from the sun to the observer-satellite. Recently, multi-spacecraft measurements (see, e. g., [342]) have improved the measurements further by allowing better coverage of wavenumber space, as well as quantifying the time evolution of perturbations in the frame of the flow.

3.1 Equations of incompressible MHD and conservation laws

Ideal MHD equations introduced in 1.3 can be simplified into their incompressible form, assuming velocity is purely solenoidal, $\nabla \cdot \mathbf{v} = 0$. This makes the density equation and the equation of state irrelevant and only dynamical equations for velocity

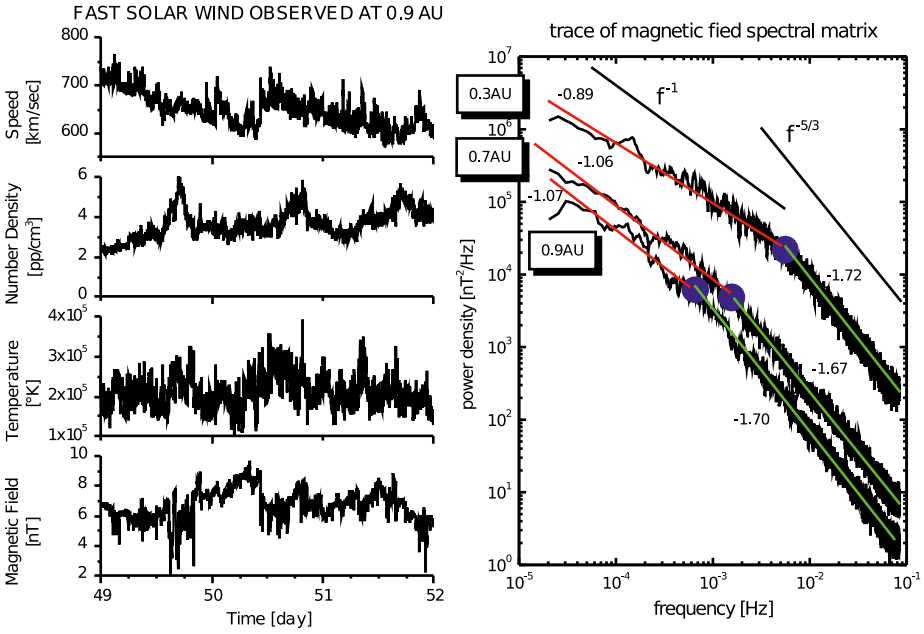

Figure 3.2: Left: A sample of fast solar wind at distance 0.9 AU measured by the Helios 2 spacecraft. Right: Power density spectra of magnetic field fluctuations observed by Helios 2 between 0.3 and 1 AU. The spectral break shown by each spectrum, moves to the lower frequency as the distance from the sun increases from [61]. Reproduced from [61] with permission of authors.

and magnetic field remain:

$$\partial_t \mathbf{v} = -\nabla P/\rho - \boldsymbol{\omega} \times \mathbf{v} + \mathbf{j} \times \mathbf{b}, \tag{3.1}$$

$$\partial_t \mathbf{b} = \nabla \times (\mathbf{v} \times \mathbf{b}), \tag{3.2}$$

$$\nabla \cdot \mathbf{v} = 0, \tag{3.3}$$

$$\nabla \cdot \mathbf{b} = 0, \tag{3.4}$$

note how we define current $\mathbf{j} = \nabla \times \mathbf{B}$ and vorticity $\boldsymbol{\omega} = \nabla \times \mathbf{v}$ in the $c = 1$ units. We also got rid of density completely by expressing magnetic field to velocity units $\mathbf{b} = \mathbf{B}/\rho^{1/2}$ (the absence of 4π is due to Heaviside units).

In these equations, the pressure term $-\nabla P/\rho$ acts only to impose the $\nabla \cdot \mathbf{v} = 0$ constraint, i. e., P is not a dynamic variable. This could be further made clearer by introducing solenoidal projection operator $\hat{S} = (1 - \nabla\Delta^{-1}\nabla)$ and rewriting equations without explicit constraints as

$$\partial_t \mathbf{v} = \hat{S}(-\boldsymbol{\omega} \times \mathbf{v} + \mathbf{j} \times \mathbf{b}), \tag{3.5}$$

$$\partial_t \mathbf{b} = \nabla \times (\mathbf{v} \times \mathbf{b}). \tag{3.6}$$

Now if the initial conditions for $\mathbf{v}$ and $\mathbf{b}$ satisfy divergence-free condition the further evolution will preserve this constraint. We will use these two equations until the end of the next chapter.

We also introduce Elsässer variables $\mathbf{w}^{\pm} = \mathbf{v} \pm \mathbf{b}$ so that equations above can be rewritten as

$$\partial_t \mathbf{w}^{\pm} + \hat{S}(\mathbf{w}^{\mp} \cdot \nabla)\mathbf{w}^{\pm} = 0. \tag{3.7}$$

This pair of equations resembles incompressible Euler's equation, which is not surprising since hydrodynamics is a case of $b = 0$ when $\mathbf{w}^{+} = \mathbf{w}^{-}$. The deeper analogy, however, is missing because $\mathbf{w}^{\pm}$ are not transformed similar to $\mathbf{v}$. Nevertheless, the strong mean field case in the weak turbulence regime ($\xi \ll 1$) certainly benefits from this approximate analogy between $\mathbf{v}$ and $\mathbf{b}$ as will follow below.

It is now easy to see that the general conservation laws of ideal MHD (see Section 1.3) are now being reduced only to energy, $1/2 \int v^2 + b^2 d\mathbf{r}$ and cross-helicity $\int \mathbf{v} \cdot \mathbf{b} d\mathbf{r}$ conservation in this incompressible formulation. By taking the sum and difference of these quantities, we obtain Elsasser energies $1/2 \int (w^{\pm})^2 d\mathbf{r}$ conservation.

Before proceeding further, a comment is necessary regarding the analogy between vorticity and magnetic field. As we saw above, the magnetic field and velocity field play a similar dynamical role. However, their dynamical equations are somewhat different. On the other hand, the vorticity and magnetic field are evolved by the same dynamical equation. If at some initial point of time, the weak magnetic field is aligned with vorticity everywhere, its evolution will be precisely described by vorticity. From a physical standpoint, there is no reason to expect such a peculiar initial condition, however.

3.2 From weak to strong turbulence

Let us explicitly write down the local mean field as $\mathbf{v_A}$, and perturbations $\delta\mathbf{w}^{\pm} = \mathbf{w} \pm \mathbf{v}_A$:

$$\partial_t \delta\mathbf{w}^{\pm} \mp (\mathbf{v_A} \cdot \nabla)\delta\mathbf{w}^{\pm} + \hat{S}(\delta\mathbf{w}^{\mp} \cdot \nabla)\delta\mathbf{w}^{\pm} = 0. \tag{3.8}$$

Note that $(\mathbf{v_A} \cdot \nabla)\delta\mathbf{w}^{\pm}$ are divergent-free. From now on, we denote $\parallel$ and $\perp$ as directions parallel and perpendicular to $\mathbf{v}_A$ and the subscript to the vector means projection to $\mathbf{v}_A$ or the perpendicular plane, respectively.

In the limit of small δw's, they represent perturbations, propagating along $\mathbf{B}$ or in the opposite direction, with the nonlinear term describing their interaction. Note that "self-interaction" of δw^{+} or δw^{-} is absent, both being an exact solution in the absence of another. The largest nonzero contribution to nonlinear interaction is a three-wave process, with one opposite wave; however, $\omega = k_{\parallel} v_A$ dispersion relation results in the degeneracy of the two conservation laws

$$\pm\omega_1 = \pm\omega_2 \pm \omega_3, \tag{3.9}$$

$$k_{\parallel 1} = k_{\parallel 2} + k_{\parallel 3}, \tag{3.10}$$

and dictates that one of the frequencies and parallel wavenumbers have to be zero. Thus the interaction is mediated by the evanescent zero-frequency wave, and the absolute magnitudes of the parallel wavenumbers must be equal. This is known as frequency resonance and results in a cascade that increases only $k_\perp$.

Furthermore, the cascading rate $\delta w k_\perp$, the inverse of cascade time, will be reduced by a factor of ξ, weakness of interaction, that we introduced before. Finally, applying cascade phenomenology, we can write for the energy cascade rate, which is expected to be constant through scales:

$$\epsilon = \delta w^2 \delta w k_\perp \frac{\delta w k_\perp}{v_A k_\parallel} = \text{const.} \tag{3.11}$$

Note $k_\parallel$ here is constant, so the phenomenological cascade spectrum is determined by $\delta w^2 \sim k_\perp^{-1}$, which corresponds to a one-dimensional perpendicular spectrum $E(k_\perp) \sim \delta w^2 k_\perp^{-1} \sim k_\perp^{-2}$. This argument can be supplanted by the rigorous perturbation collision integral approach, used in wave turbulence and solved exactly by Zakharov transformation, which was done in [158].

One interesting consequence of this exact solution is that turbulence quickly grows very anisotropic, with $k_\perp/k_\parallel \sim k_\perp$. Even more interesting is that this weak wave turbulence becomes stronger and not weaker on smaller scales—quite the opposite to the Iroshnikov–Kraichnan picture. Indeed, in the Iroshnikov–Kraichnan picture, the artificially introduced isotropy, i. e., $k_\perp/k_\parallel \sim 1$ results in the interaction strength

$$\xi = \frac{\delta w k_\perp}{v_A k_\parallel} \sim \delta w \sim k^{-1/4} \xrightarrow[k\to\infty]{} 0, \tag{3.12}$$

while the correct theory, maintaining $k_\parallel$ constant will result in

$$\xi = \frac{\delta w k_\perp}{v_A k_\parallel} \sim k_\perp^{1/2} \xrightarrow[k_\perp\to\infty]{} \infty. \tag{3.13}$$

Two lessons that we learn from this simple perturbation study is that (1) the resonance condition of Alfvénic perturbations result in "perpendicular cascade," quickly making MHD turbulence more anisotropic with eddies elongated along the mean field. The anisotropy of MHD turbulence has been known since long time ago empirically from tokamak experiments and has been a motivation for the so-called reduced MHD approximation [206, 409], which will be considered in the next subsection.

The second lesson is that the "perpendicular cascade" tends to become strong with $\xi \sim 1$. Does the situation with $\xi \ll 1$, e. g., weak MHD turbulence, ever realized in nature? It is certainly possible in strongly magnetized cases with weak driving, e. g., magnetospheres of stars, planets, neutron stars, etc. The experimental evidence for the weak MHD turbulence is still lacking, however. Typically, in the ISM the perturbations δw are of the same order as the mean field v_A and $\xi \sim 1$ to begin with. This results in MHD turbulence being strong to begin with and it remains such along the cascade.

3.3 Reduced MHD approximation

Further simplifications to Equation (3.8) are possible when taking into account anisotropy $k_\perp \gg k_\parallel$ and the fact that $\delta w \ll v_A$. This could be done by neglecting parallel gradients in the nonlinear term. Indeed, taking these conditions into account, the mean field term $(v_A\nabla_\parallel)\delta w^\pm$ is always much larger than similar contribution from the nonlinear term, $(\delta w_\parallel^\mp\nabla_\parallel)\delta w^\pm$ and the latter could be ignored. This will result in three components of Equation (3.8) being split into interdependent equations for the scalar $\delta w_\parallel^\pm$ and vector $\delta\mathbf{w}_\perp^\pm$:

$$\partial_t\delta\mathbf{w}_\parallel^\pm \mp (\mathbf{v_A}\cdot\nabla_\parallel)\delta\mathbf{w}_\parallel^\pm + \hat{S}(\delta\mathbf{w}_\perp^\mp\cdot\nabla_\perp)\delta\mathbf{w}_\parallel^\pm = 0, \tag{3.14}$$

$$\partial_t\delta\mathbf{w}_\perp^\pm \mp (\mathbf{v_A}\cdot\nabla_\parallel)\delta\mathbf{w}_\perp^\pm + \hat{S}(\delta\mathbf{w}_\perp^\mp\cdot\nabla_\perp)\delta\mathbf{w}_\perp^\pm = 0. \tag{3.15}$$

Note that Equation (3.14) depends on Equation (3.15), but not vice versa. Strong mean field limit with $\delta w \ll v_A$ and, possibly marginal, anisotropy with $k_\perp \geq k_\parallel$ is enough to make this approximation.

Since Equation (3.14) represent passive dynamics and does not have essential nonlinearity, the nonlinear cascade is completely governed by Equation (3.15). This latter equation is known as reduced MHD.

We have to note that the in the anisotropic limit the $\delta\mathbf{w}_\perp^\pm$ is purely the Alfvén mode and $\delta w_\parallel^\pm$ is the amplitude of the slow mode. The turbulent dynamics resulting from reduced MHD is also called Alfvénic turbulence for obvious reasons.

Slow mode has an interesting passive dynamics, with $\delta w_\parallel^+$ being a passive scalar to $\delta\mathbf{w}_\perp^-$ motions and $\delta w_\parallel^-$ is a passive scalar to $\delta\mathbf{w}_\perp^+$ motions. For practical purposes, it is sufficient to study Alfvénic dynamics. The slow mode will have the same statistics. The amplitude of slow mode is not determined in this ansatz, so the Kolmogorov constant for Alfvénic component may in principle be determined numerically, while the total Kolmogorov constant will depend on a slow mode content. Later in the book, we will show that in some important idealized cases, such as statistically isotropic MHD turbulence, the slow mode content can be determined from numerical simulations.

Finally, it is worth noting that reduced MHD may be applied beyond the incompressible MHD description of this chapter. The truth is that Alfvénic perturbations are transverse and rely only on the tension of the magnetic field line as a restoring force, not requiring pressure support. The charged particles tied to this magnetic field line in a strongly magnetized case provide inertia. The $[\mathbf{E}\times\mathbf{B}]$ drift waves with wavelengths much smaller than the ion skin depth are indeed just Alfvén waves, and they exist regardless of the collisionality of the plasma [382]. One important application of reduced MHD is the description of the dynamics in the solar wind, which is almost completely collisionless.

The reduced MHD or RMHD has a remarkable two-parametric symmetry: $\mathbf{w} \to \mathbf{w}A$, $\lambda \to \lambda B$, $t \to tB/A$, $\Lambda \to \Lambda B/A$. Here, λ is a perpendicular scale, Λ is a parallel scale, A and B are arbitrary parameters of the transformation. This is exactly the

symmetry of the Euler equation except for the parallel scale Λ transforms similar to time, not to length. As we will show below, such property is not coincidental and lead to several deep analogies between dynamics in time and parallel structure in space. This symmetry as we alleged above hints to the absence of designated length- and time-scale, and can be used to furnish Kolmogorov-style [224] arguments and expect power-law spectra. In nature, this regime for MHD can be achieved deeply within the inertial range where $\delta w^{\pm} \ll v_A$. In numerical simulations, it would be challenging to reach these universal dynamics by driving turbulence strongly on the outer scale. Instead, one can directly solve RMHD equations, with symmetry already built in. As practice shows, the statistics from the full MHD with $\delta w^{\pm} \sim 0.1 v_A$ is very close to RMHD; see [33].

Another, not dynamical, symmetry is present in RMHD—it is related to the value of the v_A, which is a parameter in the equation. Indeed equations are unchanged under transformation $v_A \to v_A A,\ \Lambda \to \Lambda A$, i. e., parallel scale and the Alfvén speed can be rescaled simultaneously without changing the dynamics.

3.4 Strong turbulence: phenomenology

As we showed in the two sections above, the dynamics naturally leads to strong turbulence, where ξ will try to increase by the perpendicular cascade. Goldreich and Sridhar [172] suggested that this process will be limited by the uncertainty relation between the cascading timescale and the wave-packet frequency $\tau_{\rm casc}\omega > 1$. While $\tau_{\rm casc}$ is not immediately known, it can be taken as a dynamical timescale $\delta w^{-1} k_\perp^{-1}$, in which case the above condition turns into $\xi < 1$. Since ξ wants to increase along perpendicular cascade, the competing processes will lead to $\xi \sim 1$, introduced by Goldreich and Sridhar as "critical balance." From the cascade viewpoint, we can now regard turbulence as "strong" and apply standard Kolmogorov phenomenology assuming local-in-scale energy transfer. Now we have two Elsasser energies as conserved variables, and the cascade timescale is determined by the shear rate of the opposite wave:

$$\epsilon^+ = \frac{(\delta w_\lambda^+)^2 \delta w_\lambda^-}{\lambda}, \quad \epsilon^- = \frac{(\delta w_\lambda^-)^2 \delta w_\lambda^+}{\lambda}. \tag{3.16}$$

We designated $\epsilon^{\pm}$ as an energy flux of each of the Elsässer variables; these fluxes do not interchange energy in the ideal case. $\delta w_\lambda^{\pm}$ is a characteristic perturbation amplitude on a perpendicular scale λ. This is a real-space analog of Fourier wavepacket with a central wavenumber of $2\pi/\lambda$ and of wavenumber width around the same quantity.

Such a theory is valid only in a balanced case with both w's around the same, which was properly noted in [172]. In the imbalanced case, such theory would break down due to the absence of resonantly interacting eddies and will come to a contradiction, which will be explained in detail in the chapter dedicated to imbalanced.

In the balanced case, we assume $\delta w_\lambda^+ = \delta w_\lambda^-$ and one of Equations (3.16) is sufficient. This gives scaling $\delta w \sim \lambda^{1/3}$ or, in terms of energy spectrum $E(k)$,

$$E(k) = C_K \epsilon^{2/3} k_\perp^{-5/3}, \tag{3.17}$$

where C_K is a Kolmogorov constant.

3.4.1 Dissipation scales

So far, we dealt with the ideal MHD equations. The cascade picture, however, implicitly assumes that the cascade terminates at a certain scale. In astrophysical settings, these scales are usually minuscule. In numerical simulations and experiments, Reynolds' numbers are not that high, however. We will need dissipation scales later in this chapter for the method of scaling study, which allows for precise estimation of power scaling and other quantities. Here, we will derive dissipation scales corresponding to scalar diffusivities, keeping in mind that (a) the actual break in the spectrum may be a constant factor away from this scale and (b) astrophysical fluids rarely have scalar diffusivities; so in real plasmas, one should include more physics to obtain break of the fluid spectrum.

Here, we introduce an scalar dissipation term to the RHS of Equation (3.7) as $-\nu_n(-\nabla^2)^{n/2}\mathbf{w}^\pm$, where n is an order of viscosity, e. g., $n = 2$ corresponds to normal Newtonian viscosity, while for $n > 2$ it is usually called hyperviscosity. The dissipation scale for the GS95 model is the same as the one for Kolmogorov model, i. e.,

$$\eta = \left(\frac{\nu_n^3}{\epsilon}\right)^{1/(3n-2)}. \tag{3.18}$$

This could be obtained with phenomenological argumentation, such as local Re $\sim$ 1, or from dimensional argument: it is easy to check that the above expression is a unique combination of ν_n and ϵ that of units of length. Since we know that $\epsilon \sim v^3/L$, we can derive for the length of the inertial range:

$$L/\eta = \left(\frac{L^{n-1}v}{\nu_n}\right)^{3/(3n-2)} = \mathrm{Re}_n^{3/(3n-2)}, \tag{3.19}$$

where $\mathrm{Re}_n = L^{n-1}v/\nu_n$ is a generalization of the Reynolds' number for the arbitrary order of diffusivity.

3.4.2 Anisotropy from phenomenological viewpoint

Our assumption of critical balance $\xi = 1$ allow us to directly estimate anisotropy of the perturbations. A different measure of anisotropy is possible, one of the easiest

and descriptive is called "wavevector anisotropy." It relates two wavevectors at which the one-dimensional spectrum along the field and perpendicular to the field have the same power. Likewise, the same measurement can be done with second-order structure functions and the relation obtained between parallel and perpendicular scales. These relations will be identical as long as we convert the perpendicular scale to perpendicular wave numbers as $k_\perp = 2\pi/\lambda$ and parallel scales to parallel wave numbers as $k_\parallel = 2\pi/\Lambda$. This comes from the duality of one-dimensional power spectra and second-order structure function.

Using $\xi = 1$, from Kolmogorov scaling $\delta w \sim \lambda^{1/3}$, we obtain $k_\parallel \sim k_\perp^{2/3}$, which is known as GS95 anisotropy. This result, however, is deeper than just phenomenology, as we will show in subsequent chapters.

This can be obtained dimensionally from the $\Lambda \sim v_A$ symmetry of RMHD we demonstrated in Section 3.3. Indeed, the only sensible law respecting RMHD v_A symmetry must have $\Lambda \sim v_A$. The rest of the expression must have units of time, which is uniquely obtained from λ and ϵ as $\lambda^{2/3}\epsilon^{-1/3}$:

$$\Lambda = C_A v_A \lambda^{2/3} \epsilon^{-1/3}, \tag{3.20}$$

where we introduced a dimensionless "anisotropy constant" C_A. Here, we of course assumed that turbulence is local in scale, e. g., the dynamics of each given scale have no knowledge of other distant scales, but only of the local dissipation rate ϵ. The intermittency-corrected model will have this corrected by a particular power of Re, which explicitly contains outer scale and dissipation coefficients.

We designate the value of the structure function along the λ axis as the perpendicular structure function. The perpendicular second-order structure function which correspond to $k_\perp^{-5/3}$ spectrum will have the scaling

$$\mathrm{SF}_\perp \sim \lambda^{-1+5/3} = \lambda^{2/3}. \tag{3.21}$$

From the definition of wave-vector anisotropy, the same value should appear at the Λ axis when $\Lambda \sim \lambda^{2/3}$, i. e., the parallel structure function will be expressed as

$$\mathrm{SF}_\parallel \sim \lambda^{2/3} \sim \Lambda. \tag{3.22}$$

The parallel spectrum, which corresponds to such SF is $E(k_\parallel) \sim k_\parallel^{-2}$ and from dimensional arguments, we can also recover the prefactor as

$$E(k_\parallel) = C_\parallel \epsilon v_A^{-1} k_\parallel^{-2}, \tag{3.23}$$

where we introduced the dimensionless $C_\parallel$ – parallel Kolmogorov constant. Such a spectrum was indeed found in observations of the solar wind turbulence; see, e. g., [195] and Section 3.7.

Equations (3.17) and (3.20) (or, alternatively (3.23)) roughly describe the spectrum and anisotropy of MHD turbulence, which may be corrected for intermittency. The correction to power slope is usually negative due to three facts: (a) the pure intermittency-free measure is of third order (see exact scaling laws for the inertial range of MHD turbulence), (b) the power spectrum is of lower, second order, and (c) power-law exponents of different order are a concave function of their order [153]. The correction for hydrodynamic turbulence was found around –0.03. We will show below that MHD numerics converges to approximately the same number. This deviation is rather small and maybe not relevant even in astrophysical context.

3.4.3 Modifications of GS95

A more radical modification which leads to a shallower and not steeper spectrum was proposed by Boldyrev (2005, [48], 2006 [49], henceforth B06) who suggested that the original GS95 scalings can be modified by a scale-dependent factor that decreases the strength of the interaction, so that the RHS of Equation (3.16) is effectively multiplied by a factor of $(\lambda/L)^{1/4}$, where L is an outer scale. Different arguments to the same effect were proposed by Gogoberidze [170]. In this case, the spectrum will be expressed as $E(k) = C_{K2}\epsilon^{2/3}k^{-3/2}L^{1/6}$. The nonlinear strength ξ in their argument is modified by the same factor of $k_\perp^{-1/4}L$, so that anisotropy follows modified critical balance with $k_\parallel \sim k_\perp^{1/2}$. The dissipation scale of B06 model is different from that of the GS95 model and can be expressed as $\eta' = (\nu_n^3/\epsilon)^{1/(3n-1.5)}L^{0.5/(3n-1.5)}$. We will show below that numerics disfavor –3/2 spectra and 1/2 anisotropy scalings.

3.5 Anisotropy from Lagrangian viewpoint

The studies of hydrodynamic turbulence have benefitted from Lagrangian measurements: measurements that are performed by following a fluid element. Often, the Lagrangian viewpoint offers a simpler conceptual picture than the Eulerian viewpoint. The example of this is Lagrangian frequency spectrum, which statistically evaluates the properties of the velocity of a given fluid element.

The Kolmogorov theory is conceptually simpler in Lagrangian formulation. The Euler's equation using Lagrangian derivative is simply a third Newton's law for the fluid element:

$$\frac{d\mathbf{v}}{dt} = -\frac{\nabla P}{\rho}. \tag{3.24}$$

The work per unit mass, done upon a fluid element by pressure of surrounding fluid elements will be expressed, therefore, as $\mathbf{v}\cdot d\mathbf{v}/dt$. The Kolmogorov theory would therefore assume that, given a characteristic time interval τ, the work done per unit

mass upon a fluid element during this interval, $\delta\mathbf{v}_\tau \cdot \delta\mathbf{v}_\tau/\tau$, will be constant when τ corresponds to inertial-range timescales and equal to the turbulence energy cascade rate per unit mass ϵ.

More formally, in stationary turbulence the second-order Lagrangian structure function of velocity should satisfy:

$$SF(\tau) = \left\langle \left(\mathbf{v}(t+\tau) - \mathbf{v}(t)\right)^2 \right\rangle \approx \epsilon\tau \tag{3.25}$$

in the inertial range, where $\mathbf{v}(t)$ is a velocity as a function of time for a given fluid element. Likewise, the time structure function will correspond to the frequency spectrum of

$$E(\omega) = C_L \epsilon \omega^{-2}, \tag{3.26}$$

which was first noted soon after the publication of Kolmogorov theory and appeared in [250] (see also [101, 422]). The remarkable properties of this spectrum is a simple power scaling (–2 versus –5/3) and the fact that it is proportional to the first power of ϵ, i. e., the energy *spectrum* is proportional to *energy injection rate* and it probably does not need intermittency correction.

This spectrum has a dissipation *timescale* associated with the lifetime of critically damped eddies, also called the Kolmogorov timescale:

$$\tau_\eta = (\nu/\epsilon)^{1/2}. \tag{3.27}$$

It is easy to see that while the break of Eulerian spectrum behaves like $\eta \sim \nu^{3/4}$, the break in Lagrangian spectrum $\tau_\eta \sim \nu^{1/2}$.

In MHD, the Lagrangian formulation becomes more involved since there are now several local propagating wave characteristics. Following a fluid element, we will find oscillations associated with the wave-train that propagates through, which would make the classic Lagrangian measurement of limited value.

In the incompressible MHD, the Lagrangian evolution becomes somewhat simpler, as all modes propagate in the same direction with the same speed, modulo, the sign of the speed. Namely, the Elsässer components propagate either along or against the local magnetic direction, i. e., along the magnetic field line. Such propagation will be described by the functional form $f(s \mp v_A t)$, where s is a distance along the field line. The nonlinear interaction will contribute to a slower time evolution of f and the trajectory $s = \pm v_A t$ will be analogous to following hydrodynamic fluid element.

The ersatz of the following wave characteristic of $\mathbf{w}^+$ and $\mathbf{w}^-$ would be recording the data along the field line in fixed time. The positive direction s will be equivalent to the following evolution of $\mathbf{w}^+$ backward in time and $\mathbf{w}^-$ forward in time. This is related to the discussion of field line diffusion [24] which we will return to in Chapter 7. In measuring the frequency spectrum, the sign of time is unimportant. So the measurement of the power spectrum along the field line will be analogous to the Lagrangian

frequency spectrum with frequency ω replaced by the wavenumber $k_\parallel = \omega/v_A$ [25]:

$$E(k_\parallel) = E(\omega)\frac{d\omega}{dk_\parallel} = C_L\epsilon(v_A k_\parallel)^{-2}v_A = C_L\epsilon v_A^{-1}k_\parallel^{-2} \tag{3.28}$$

This is the same expression as obtained in Section 3.4.2 from phenomenological considerations, assuming $C_L = C_\parallel$. Likewise, the parallel structure function will be expressed as

$$SF_\parallel(l) = \epsilon l v_A^{-1}. \tag{3.29}$$

The dimensional argument involving Alfvén symmetry of reduced MHD arrive at the same result [23]. Indeed, the symmetry allows only dependence on the combination $k_\parallel v_A$, so, one must keep energy $E(k_\parallel)dk_\parallel$ constant under such transformation, which requires that $E(k_\parallel) \sim v_A^{-1}$. The rest is due to units of ϵ and k giving the dimension of the wavevector power spectrum. This parallel second-order spectrum scales linearly with ϵ, similarly to the *third-order* Eulerian scaling.

3.6 Parallel spectrum: numerics

Full MHD has no exact Alfvén symmetry, which reduced MHD has. Using Alfvén symmetry in the inertial range, however, can be argued based on the high anisotropy and small amplitude of the perturbation as we demonstrated above (see also [23]). Below we will check if the parallel spectrum still follows Equation (3.23) not only in Alfvénic MHD but in the general MHD case as well. Especially interesting is the case with a zero mean magnetic field, where the v_A will be determined only by local fluctuations.

The numerical data is from DNS of strong reduced MHD turbulence [25], which are the well-resolved driven statistically stationary simulations intended to precisely calculate averaged quantities.[1]

See RMHD simulation parameters in code units in Table 3.1 under rows M1–3 and M1H–3H. The only difference between M1–3 and M1H–3H was that the latter were performed with higher order diffusivities.

For comparison, we performed simulations with zero mean field described in rows MHD1–2. We have calculated the spectra along the magnetic field line, and for the reduced MHD cases we additionally have calculated the one-dimensional spectra along the x direction, which was the global mean field direction.

Three-dimensional numerics are affected by the finite Re effects, so the use of the rigorous scaling study method, described in more detail in Section 3.9, is warranted. It is fairly common in the analysis of experimental data and DNS [404, 179, 213, 22, 25], which compares spectra from simulations with several different Re values on the same

1 Reduced MHD, as we demonstrated above, describe Alfvén dynamics, which does not depend on plasma parameters, such as the ratio of plasma pressure magnetic pressure β.

Table 3.1: Three-dimensional MHD and RMHD simulations.

Run	N^3	Dissipation	v_A	ϵ	η	$k_{\max}\eta$	$v_A\tau_\eta$
MHD1	1536^3	$-5\cdot10^{-10}k^4$	0.73	0.091	0.0021	1.08	0.026
MHD2	1536^3	$-6.2\cdot10^{-10}k^4$	1.53	0.728	0.0018	0.92	0.025
M1	1024^3	$-1.75\cdot10^{-4}k^2$	1	0.06	0.0031	1.05	0.044
M2	2048^3	$-7\cdot10^{-5}k^2$	1	0.06	0.00155	1.06	0.028
M3	4096^3	$-2.78\cdot10^{-5}k^2$	1	0.06	0.00077	1.06	0.017
M1H	1024^3	$-1.6\cdot10^{-9}k^4$	1	0.06	0.0030	1.04	0.045
M2H	2048^3	$-1.6\cdot10^{-10}k^4$	1	0.06	0.00152	1.04	0.029
M3H	4096^3	$-1.6\cdot10^{-11}k^4$	1	0.06	0.00076	1.04	0.018

plot with dimensionless axes. The parallel spectrum was plotted versus dimensionless wavenumber $kv_A\tau_\eta$ and compensated by $k^2\epsilon^{-1}v_A$ to see how the scaling is consistent with (3.23). This measurement is presented in Figure 3.4. For the reduced MHD case, the spectra collapsed on the dissipation scale, corresponding to an overall scaling of k^{-2}.

Reduced MHD can be performed with a choice of the mean field strength, which implies a particular choice of ϵ to generate strong turbulence from the outer scale. The precise Alfven symmetry ensures precise linear scaling with ϵ in Equation (3.23). However, statistically isotropic MHD simulations with zero mean field MHD1–2, for which Alfvén symmetry is absent, and the inertial range scaling (3.23) cannot be rigorously argued based on units, can be used to verify this scaling.

This is based on an idea introduced by [201, 236] that the RMS magnetic field can play the role of the local mean field and this could still be regarded as the *strong mean field* limit. Our test of Equation (3.23) will, therefore, test not only the Lagrangian spectrum idea itself, but also the hypothesis mentioned above. In the MHD case, we used simulations with different ϵ and substituted the RMS field instead of v_A in Equation (3.23). Figure 3.4 demonstrates that there is an inertial range convergence to k^{-2} even in this zero mean field case. The linear scaling with ϵ, not $\epsilon^{2/3}$, which would be Eulerian spectrum scaling, is also confirmed.

Based on this evidence, we can reasonably argue that even MHD turbulence that lacks mean or background field behaves similar to the MHD turbulence with the strong mean field in the inertial range.

Another possible spectral measurement is with respect to the global mean field. We do not expect such scalings to deviate significantly from the perpendicular scalings for the following reason: Alfvén waves propagate along the local field direction which deviates by an angle of $\delta B_L/B_0$ from $\mathbf{B}_0$, while the angular anisotropy in this frame is $\delta B_l/B_0$, with inertial range values of δB_l much smaller than the outer scale value of δB_L. It follows that the anisotropy will be washed out. Figure 3.5 presents a measurement of the spectrum along the x – global mean field direction. It is grossly consistent with –5/3, i. e., the perpendicular spectral scaling observed in [25].

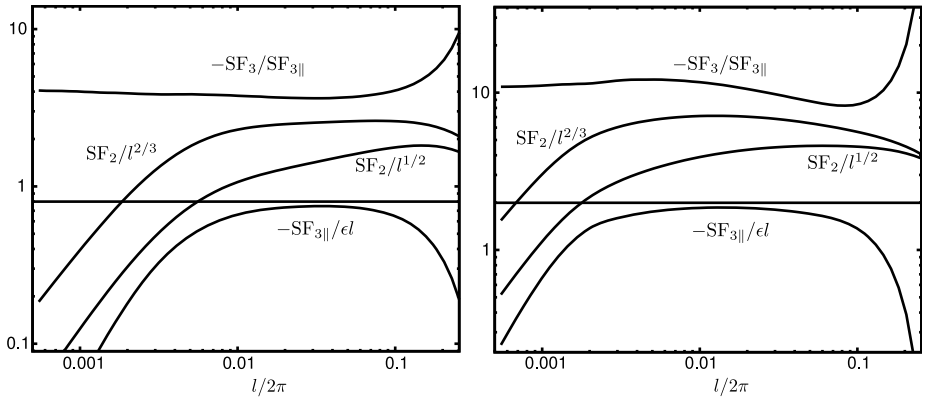

Figure 3.3: Different structure functions versus the distance l, measured in hydrodynamic (left) and MHD (right) simulations. Solid lines show $-SF_{3\|}/l\epsilon$. The influence of driving and dissipation is minimized in the point where $-SF_{3\|}/l\epsilon$ is closer to its theoretical value. The dashed line indicates the ratio of the third-order SF, defined in the text to the parallel third-order SF. This ratio is a test for turbulence self-similarity, as long as this ratio is constant, the turbulence is well self-similar. Finally, dotted and dash-dotted lines indicate the same second-order structure functions, compensated by $l^{1/2}$ and $l^{2/3}$ correspondingly, in arbitrary units. Here, $l^{2/3}$ is the Richardson–Kolmogorov scaling and $l^{1/2}$ is the scaling that appears in Kraichnan DIA model for hydrodynamics, Iroshnikov–Kraichnan model for MHD and B06 model. From [36].

3.7 Parallel spectrum observations versus numerics

Critical balance refers to the interaction parameter $\xi = \delta v \lambda_\| / v_A \lambda_\perp$ being around unity in strong MHD turbulence. It has been argued as an uncertainty relation between the wave frequency and the cascade timescale in [172]. This was useful in the qualitative understanding of strong turbulence, but the generality of this argument results in apparent paradoxes in cases with pure propagating solutions with $\xi \gg 1$, i. e., strong Alfvénic waves. This is because the decorrelation argument does not explicitly refer to nonlinear interaction.

More importantly, the application of the uncertainty relation argument fails in the imbalanced turbulence, where it predicts that the anisotropy of the stronger Elsässer component should be higher than the anisotropy of the weaker component, while in reality, the opposite is true (see Section 4 and [30, 33]). The Lagrangian argument, more rigorous and mature, circumvents this problem. We notice that the energy cascade is manifested both in space and time domains, with the parallel direction is equivalent to the time domain. It follows then that the anisotropy relation $k_\| \sim k_\perp^{2/3}$ is the correspondence between space domain (Eulerian) and frequency domain (Lagrangian) spectra. While the critical balance argument requires that the average ξ must be close to unity, the new argument only requires that the average ξ is a scale-independent quantity, a dimensionless constant derived from scale-free nonlinear dynamics.

Observational data from the solar wind points to the k^{-2} parallel spectrum, e. g., [195] used a wavelet technique to follow the local field direction, Figure 3.6. This has been further improved in [443] and compared with the global Fourier spectra. [359] obtained similar results with wavelets and demonstrated scale-dependent anisotropy. [300] used the structure function measurement and observed the same scaling. Multi-spacecraft measurements in [342] allowed better coverage of k-space and also pointed to k^{-2}. Some of the earlier measurements, however, reported scale-independent anisotropy these measurements in the global frame (e. g., [306]), as we argued above, are not indicative of contradiction with the k^{-2} result, due to these spectra being dominated by contamination from perpendicular spectrum due to field-wandering effect (Section 3.6). Numerical studies overwhelmingly support k^{-2}, as long as the measurements were along the local field direction (see, e. g., [92, 303, 33, 32, 22]), while the measurements in the global frame usually demonstrate scale-independent anisotropy; see, e. g., [183] or our Figure 3.5. Lagrangian frequency spectrum has been measured in hydrodynamic simulations (see, e. g., [456]) and showed correspondence with the theoretical ω^{-2}, while the measurement in statistically isotropic MHD turbulence [65] also tentatively confirmed ω^{-2}.

From the convergence study in Figure 3.4, we found scaling of k^{-2}. The deviation in visible slope of around 0.1 is evident on this figure and an example of a long-range finite-Re effect. These deviations were discussed in detail in [32, 21, 23]. The devia-

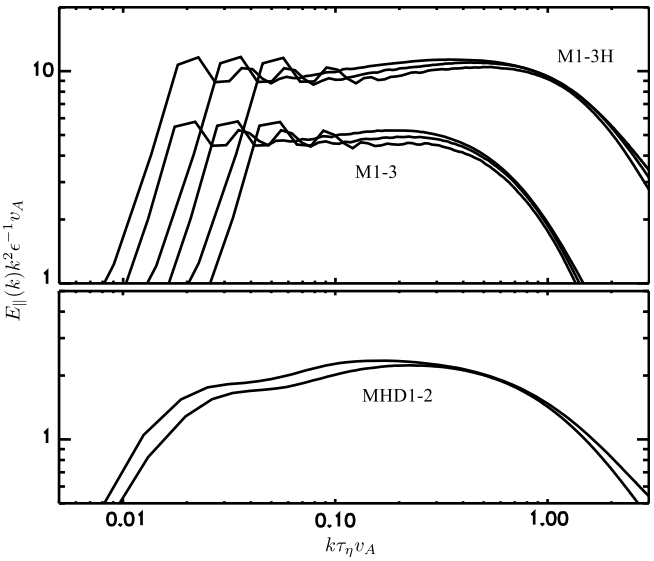

Figure 3.4: Energy spectrum along the magnetic field line compensated by the theoretical scaling $\epsilon k_\parallel^{-2}$ (3.23). Solid, dashed, and dash-dotted are spectra from 4096^3, 2048^3, and 1024^3 simulation correspondingly on the upper plot. The M1–3H has been multiplied by a factor of two to separate the curves. On the lower plot, dashed and solid are MHD1 and MHD2, correspondingly. Reproduced from [26] with permission of AAS.

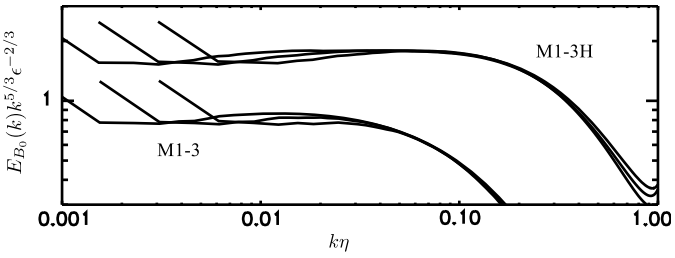

Figure 3.5: The spectra along the global mean field in M1–3, M1–3H. The M1–3H spectra have been multiplied by a factor of two. This plot demonstrates that this energy spectrum scaling is consistent with −5/3, i. e., the same as the perpendicular scaling. Reproduced from [26] with permission of AAS.

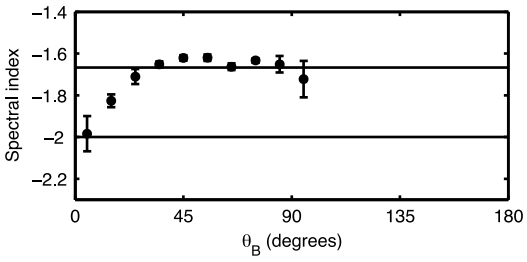

Figure 3.6: Slopes of the spectra of fluctuations at different angles with respect to the local magnetic field measured in the solar wind from [195]. Reproduced from [195] with permission of APS.

tion from the expected perpendicular –1.7 slope is around ∼ 0.2 in the intermediate scales but disappeared when higher Re are achieved. Normally, the deviations had been observed within around an order of magnitude in scale from the driving scale. Further solar wind measurements or larger scale numerics will help to rectify the problem.

3.8 Statistical indicators of turbulence

Statistical measurement normally involves averaging over many realizations of the same random process, i. e., statistical averaging. Turbulence is often seen as a volume-filling and persistent process, so its statistical measurements may be replaced with averaging over volume and time, using so-called ergodic hypothesis. While theory usually relies on ensemble averaging, numerical experiment uses volume and time averaging. In the course of this book, we use averaging signs <> for both statistical and volume averaging. A good overview of statistical measures can be found in [324]. Among most popular measures, structure and correlation functions of various orders have been used in turbulence research for some time. Below we denote structure function as SF. While in theory, these are quantities statistically averaged over ensemble in numerics, the averaging is usually over time and volume using homogeneity and stationarity.

In isotropic hydrodynamics, we often use isotropic second-order structure function of velocity:

$$SF^2(l) = \left\langle \left(v(\mathbf{r}-\mathbf{l}) - v(\mathbf{r})\right)^2 \right\rangle_{\mathbf{r}}. \tag{3.30}$$

This is a difference in velocity between two points separated by the vector $\mathbf{l}$, squared and averaged over the volume, i. e., the vector $\mathbf{r}$. This quantity could be represented by the sum of the longitudinal and transverse components with velocity decomposed into a direction perpendicular and parallel to $\mathbf{l}$. The longitudinal structure function is important in experimental research of hydrodynamic turbulence because this is the primary quantity measured by the heated wire technique.

MHD turbulence is not isotropic, however, so there is a wider variety of structure functions that one can possibly measure. However, in the reduced MHD limit, there is a particular structure function, which plays the similar role as the isotropic SF in hydrodynamics, the perpendicular SF

$$SF_{\perp}^2(l) = \left\langle \left(w^{\pm}(\mathbf{r}-l\mathbf{n}) - w^{\pm}(\mathbf{r})\right)^2 \right\rangle_{\mathbf{r}}, \tag{3.31}$$

where $\mathbf{n}$ is a vector perpendicular to the magnetic field. Power spectra, on the other hand, are produced by obtaining a Fourier transform $\hat{\mathbf{v}}(\mathbf{k})$ of original quantity $\mathbf{v}(\mathbf{r})$ and taking the product $\frac{1}{2}\mathbf{v_i}(\mathbf{k})\mathbf{v_i^*}(\mathbf{k})$, where $*$ is a complex conjugate. Spectra and structure functions have one-to-one correspondence by various Fourier transforms; see [324].

Some exact relations for structure functions in turbulence are known both for hydro and MHD; see, e. g., [44]. The famous Kolmogorov $-4/5$ law relates a parallel signed structure function for velocity in the inertial range with the dissipation rate:

$$SF_{3\|h}(l) = \left\langle \left(\delta v_{l\|}\right)^3 \right\rangle = -\frac{4}{5}\epsilon l. \tag{3.32}$$

Another exact relation, similar to the Yaglom's $-4/3$ law for incompressible hydro exists for axially symmetric MHD turbulence:

$$SF_{3\|}(l) = \left\langle \delta w_{l\|}^{\mp} \left(\delta w_l^{\pm}\right)^2 \right\rangle = -2\epsilon l, \tag{3.33}$$

where l is taken perpendicular to the axis of statistical symmetry—the direction of the mean magnetic field $\mathbf{B}$ [360]. One can measure SFs above and argue about influence of dissipation and driving in each particular simulation. Figure 3.3 shows several structure functions, compensated by various powers of l and the ratio of parallel third-order structure function and full third-order SF, $SF_3 = \langle |v(\mathbf{r}-\mathbf{l}) - v(\mathbf{r})|^3 \rangle$.

The inertial range in a simulation is often defined as a range of scales where $-SF_{3\|}/l$ is closest to its theoretical value, i. e., where the influence of energy injection from driving and energy dissipation from viscous term is minimized. Turbulence self-similarity can be tested by the ratio of different structure functions. If this ratio is dimensionless, it is supposed to be constant through scales. For example, we can take

the ratio of the unsigned and signed third-order SFs. This ratio must be constant as long as turbulence is self-similar. Figure 3.3 shows that hydrodynamic turbulence is rather self-similar at the same time the scaling of the second-order structure function in the inertial range is around $l^{0.7}$, i. e., close to the Kolmogorov scaling.

In the MHD simulation in Figure 3.3, the self-similarity is not so good. One can argue, however, that the scaling is closer to the $l^{2/3}$ in the point where $-SF_{3\parallel}/l\epsilon$ is closest to its theoretical value of 2. Using these arguments, however, have a great deal of subjectivity to them. A better, more rigorous method, which tests self-similarity as well as derives asymptotic scalings is described in the next section, it is called scaling convergence study, and it is based on a convergence or a comparison of simulations or experiments, which have a different value of the outer scale, e. g., simulations may be presented in a series with varying Reynolds' number.

Power spectra are the measures complementary to second-order structure functions. In particular, so-called one-dimensional power spectrum P_k is a Fourier transform of the SF_2.

This particular measure is popular in the satellite measurements of the solar wind turbulence, where the quantity of interest, e. g., $\mathbf{v}$ or $\mathbf{B}$ is measured as a function of time. It is then interpreted as a measurement in space as if turbulence was frozen during satellite fly by. This is known as Taylor hypothesis and is generally applicable if the fly by speed is much higher than evolution speed of the turbulence, e. g., group velocities of the perturbations involved. Each measurement is obtained along a line in a turbulent realization. The power spectra from many samples like this are averaged to obtain P_k for either velocity or magnetic field. Another experimental measure is the so-called parallel power spectrum $P_{\parallel k}$. It is obtained in the measurements of hydrodynamic turbulence by a heated wire technique. A scalar quantity is measured in this technique, which is the velocity perturbation parallel to the average flow velocity. Similarly, this is interpreted as a measurement in space by using Taylor frozen flow hypothesis. The third type of power spectrum, which is favored by numerics is a three-dimensional spectrum $E(k)$. This spectrum is calculated from a full three-dimensional power spectrum $\frac{1}{2}\mathbf{v}(\mathbf{k})\cdot\mathbf{v}^*(\mathbf{k})$ by integrating over the solid angle in $\mathbf{k}$ space, so that $E(k)$ is only a function of scalar k. In statistically isotropic turbulence, the integration is in spherical shells, while in reduced MHD, the parallel wavenumber is infinitely small compared to other wavenumbers, so the integration is, effectively, along all $k_\parallel$ and the circle in $\mathbf{k}_\perp$ space so that the isotropic spectrum is equivalent to the perpendicular spectrum. Three spectra, $P(k)$, $P_\parallel(k)$, and $E(k)$, of the solenoidal vector field are related by the following expressions (see, e. g., [324]):

$$P(k) = \int_k^\infty E(k_1)\frac{dk_1}{k_1}, \tag{3.34}$$

$$P_\parallel(k) = \int_k^\infty E(k_1)\left(1-\frac{k^2}{k_1^2}\right)\frac{dk_1}{k_1}. \tag{3.35}$$

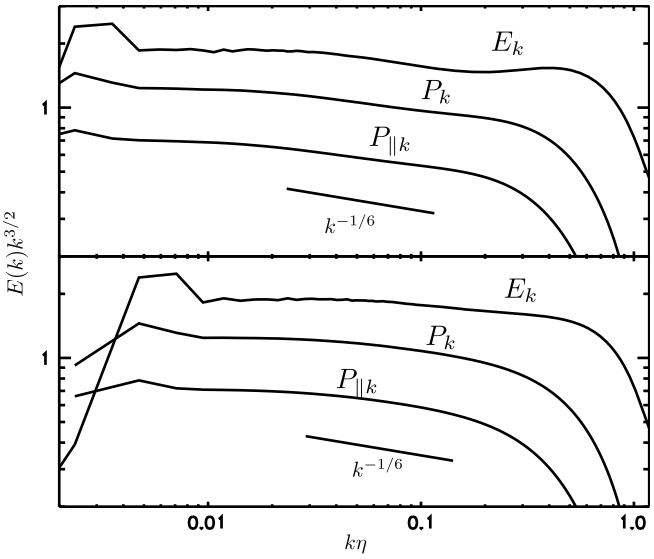

Figure 3.7: Three types of spectra from a numerical simulations R1, R4. E_k – solid, P_k – dashed, $P_{\|k}$ – dash-dotted. In a simulation with limited resolution, all three spectra have different shapes. From [36].

From these relations, it is clear that power law in one of the spectra will be the same power-law in others. However, in practice spectra are never exact power laws over all range of scales, so the shape of different spectra may be different. Figure 3.7 shows three types of spectra from a simulation. The primary spectrum here was E_k, and the two other spectra were calculated by the above formula.

Interesting to note that three spectra have different shapes. This gets us back to the discussion of the subjectivity of the power law exponent: if one would want to claim a particular scaling by estimating the scaling from the numerical spectrum, the estimate will likely depend on the type of the spectrum and the range of k used for fitting the exponent. Visually, based on Figure 3.7 one can claim any spectral slope between –5/3 and –1.4. This reinforces the need for rigorous quantitative measurement based on scaling convergence, presented in the next section.

3.9 The scaling convergence argument

Turbulence with a very long range of scales is common in astrophysics. Three-dimensional numerics, on the contrary, is unable to reproduce such range, and struggles to obtain a good inertial range. In this situation, rigorous quantitative arguments were invented to investigate asymptotic scaling.

Imagine we performed several simulations with different Reynolds' numbers. If we believe that turbulence is universal, and the separation of scales between forcing scale and dissipation scale is large enough, the properties of small scales should not

depend on how turbulence was driven and also on the scale separation itself. This is because MHD or hydrodynamic equations do not explicitly contain any designated scale, so the simulation with a smaller dissipation scale could be considered, because of the symmetry from equations, as a simulation with the same dissipation scale, but larger driving scale.

For example, the small-scale statistics in a 1024^3 simulation will look similar to small-scale statistics in 512^3 simulation, if we keep physical sizes of the grid cell and the dissipation scale the same.

Figure 3.8 shows convergence of many turbulence experiments as well as numerical experiments onto the same curve after the scale and the power spectrum were made dimensionless using the Kolmogorov scale and Kolmogorov velocity scale.

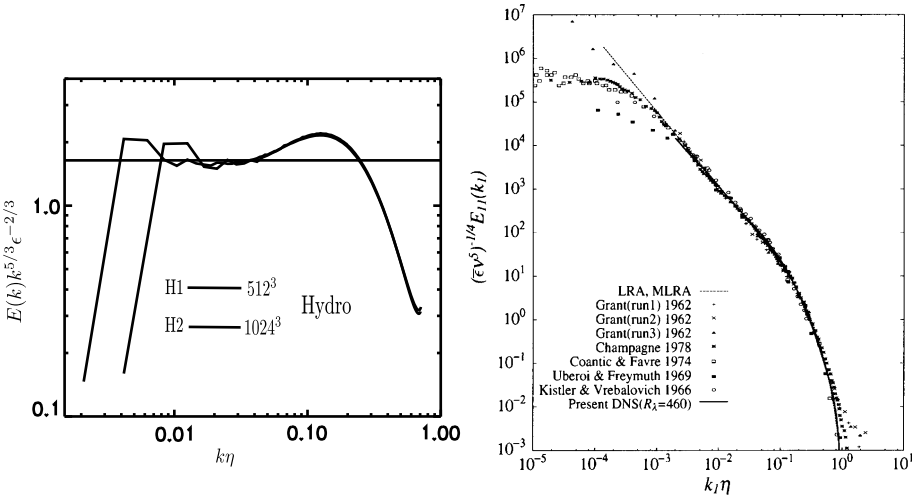

Figure 3.8: Left: The spectra from hydrodynamic simulations illustrate the numerical scaling argument. As long as turbulence is scale-local, simulations with different Re will exhibit similar statistics, as evident from the convergence of dimensionless spectra. Right: Similar convergence study with experimental data points on top of the simulation (solid line) from [179]. Reproduced from [179] with permission of AIP.

The scaling argument in numerics in practice require that not only the geometry of the elementary cells are the same but the actual numerical scheme used to solve the equations is the same. The numerical formulations should not contain any scale explicitly as well, which is typically satisfied.

It is interesting that in the case of numerics the scaling argument does not require that discretized formulation exactly follows continuous formulation on grid scales, e. g., it does not require numerical results to be well resolved and precise of grid scale, but as long as the grid scale is the fixed fraction of the dissipation (Kolmogorov) scale, it would still work. This is because the statistics on small scales is similar in two sim-

ulations as long as numerical effects are the same, which is the case when numerical effects are the same on the dissipation scale. At the same time, the influence of the changing outer scale should be small by the assumption of turbulence locality.

In practice, the scaling argument or a resolution study is done in the following way: the spectra from two or more simulations are expressed in dimensionless units corresponding to the expected scaling, e. g., a $E(k)k^{5/3}\epsilon^{-2/3}$ is used for hydrodynamics, and plotted versus the dimensionless wavenumber $k\eta$, where dissipation scale η corresponds to the same model of dissipation scales, e. g., $\eta = (\nu^3/\epsilon)^{1/4}$ is used for scalar second-order viscosity ν and Kolmogorov phenomenology. On the plot, the two spectra should collapse onto the same curve on the viscous scales; see, e. g., Figure 3.8. The method has been used in hydrodynamics since a while ago, e. g., in references [457, 179, 213]. For hydrodynamics, good convergence on the dissipation scale has been observed starting with rather moderate resolutions indicating that hydrodynamic cascade is very local in scale.

While experimental data suffer from systematic uncertainties on small scales, high-resolution numerical simulations allow to collect tremendously large and precise statistics on small scales, driving statistical error virtually to zero. The scaling study based on numerics, when done properly, allows for a very precise measurement in scaling, e. g., in simulations in reference [213], which had a resolution up to 4096^3 and even the intermittency correction to the Kolmogorov scaling has been captured. This correction is only around 0.04 in the spectral slope.

3.10 Numerical studies of the spectral slope

We add to the RHS of Equation (3.15) an explicit dissipation term of n-th order $-\nu_n(-\nabla^2)^{n/2}\mathbf{w}^{\pm}$ and forcing term $\mathbf{f}$. Diffusive terms with $n = 2$ are referred to as normal viscosity and with $n > 2$ are referred to as hyperviscosity. We solve these equations by pseudospectral dealiased code [33, 32, 34, 21, 22].

The seminal paper by Kolmogorov [224] suggested that if strong turbulence is universal and its scaling is only determined by the dissipation rate and viscosity, the dissipative range would have certain spacial-, velocity- and time-scales, known as Kolmogorov scales. This has been tested with a number of experimental and/or numerical data being expressed in units of these scales and presented on the same plot; see, e. g., [404, 179]. This method shows remarkable collapse of all data on the same curve (see Figure 3.8), validating Kolmogorov's conjecture. Technically, the scaling study investigates the scaling of the Kolmogorov dissipation scale and velocity scale with Reynolds' number. For example, in the presence of normal viscosity, the Kolmogorov velocity should scale as $\mathrm{Re}^{-1/4}$ for the –5/3 power law, while for the –3/2 model it will scale as $\mathrm{Re}^{-3/8}$. The scaling study method becomes especially powerful in numerics, where all the data are available at all times for averaging.

Given a characteristic eddy scale l, the number of eddies in a datacube goes as l^{-3}, while the number of correlation timescales for strong turbulence goes as $l^{-2/3}$, so the statistical error due to volume and time-averaging goes as $l^{-11/6}$, which is about a factor of 10^{-4} between outer scale eddies and viscously damped eddies in highest resolution simulations. The dissipation scale, therefore, is not only the most separated from the driving scale and the least affected by driving, but also has the smallest statistical error. In combination with the very low numerical error of the pseudospectral method (see below), the Kolmogorov amplitude of spectra is one of the most robust and best-measured quantities in numerics. In particular [213], using a simulation group up to 4096^3 resolution, has been able to estimate the power slope of hydrodynamic turbulence within tiny error and differentiate between $-5/3 \approx -1.667$ slope and intermittency-corrected -1.7. We aim to distinguish between the $-3/2$ and $-5/3$ slope, which are different by ≈ 0.167, much higher than the precision of the method, ≈ 0.02. This is much better than using subjectively perceived flatness of the spectra to determine the asymptotic scaling, as it could easily fail, e. g., due to the transitional scalings that look subjectively flat.

Checking the hypothesis that the Kolmogorov scale and the Kolmogorov velocity scale correctly with the Reynolds' number requires plotting the spectrum in Kolmogorov units, i. e., making the x and y axes dimensionless. The x axis is expressed in $k\eta$, where η is not necessarily the classic Kolmogorov scale, corresponding to $-5/3$ slope, but defined by Equation (1.1), i. e., different for each spectral slope. The y axis is usually expressed in units of $E(k)k^{5/3+\alpha}L^{\alpha}\epsilon^{-2/3}$, where α is the correction to the $-5/3$ slope and L is an outer scale, which is normally kept constant in a scaling study. This is, in fact, the only dimensionless expression for the spectrum that does not contain η explicitly. If one wants to multiply the above expression by some power of (L/η), or the Reynolds' number, this would introduce explicit η dependence and would violate the so-called zeroth law of turbulence that claims that large-scale properties are largely independent of viscosity. We also note that the scaling study works perfectly well not only with spectra but with other measures. In particular, we reproduced the results reported below by using the second-order perpendicular structure function.

Two series of reduced MHD driven simulations are described in Table 3.1 as M1–3 and M1–3H. These are simulations with a strong mean field that we denote B_0, RMS fields $v_{\rm rms} \approx B_{\rm rms} \approx 1$, perpendicular box size of 2π and parallel box size of $2\pi B_0$. The driving was correspondingly anisotropic with anisotropy $B_0/B_{\rm rms}$, so that turbulence starts being strong from the outer scale. Technically, B_0 is arbitrary. However, the RMHD limit is only applicable to very large B_0 [22]. Our previous simulations showed a rapid decrease of parallel correlation length right after the driving scale, which indicates the efficiency of nonlinear interaction and the regime of strong turbulence. The correlation timescale for v and B was around $\tau \approx 0.97$, so the box contained roughly 6.5 parallel correlation lengths in the parallel direction and about 3–5 in the perpendicular direction. Each simulation was started from long-evolved low-resolution simulation and was subsequently evolved for $\Delta t = 13.5$ in high resolution. We used the

last 7 dynamical times for averaging. In our previous work [21, 22], we found that averaging over ∼ 7 correlation timescales give a reasonably good statistic on outer scale and excellent statistics on smaller scales. Numerically, we used $k_{\max}\eta > 1$ resolution criterion, with η being classic Kolmogorov scale. For the hyperdiffusive series, we used the same criterion. Additionally, we checked the numerical precision of the spectra by performing a resolution study on lower resolutions. In particular, we saw spectral error lower than 8×10^{-3}, up to $k\eta = 0.5$ when increasing resolution from 576^3 to 960^3 and the spectral error lower than 3×10^{-3} when we increased parallel resolution in a 1152^3 simulation by a factor of two. We did not use any data above $k\eta = 0.5$ for fitting as the spectrum sharply declines after this point and contains negligible energy. We conclude that for our purposes, using $k_{\max}\eta = 1$ is sufficient, and using cubic resolution, i. e., parallel resolution equal to perpendicular resolution is also sufficient or even somewhat excessive. Note that increasing resolution while keeping $k_{\max}\eta > 1$ with η corresponding to –5/3 slope is a conservative choice for all types of turbulence with slope shallower than –5/3, including the –3/2 model.

Figure 3.9 presents a convergence test for the –5/3 model, and the convergence is reasonable, while the best convergence is reached at the –1.7 scaling. Figure 3.10 has a test for the –3/2 model and the convergence is poor in either low or high wavenumbers. The former is due to the scaling being actually quite shallower than –1.5 at low wavenumbers. Figure 3.11 shows a convergence study for the residual energy spec-

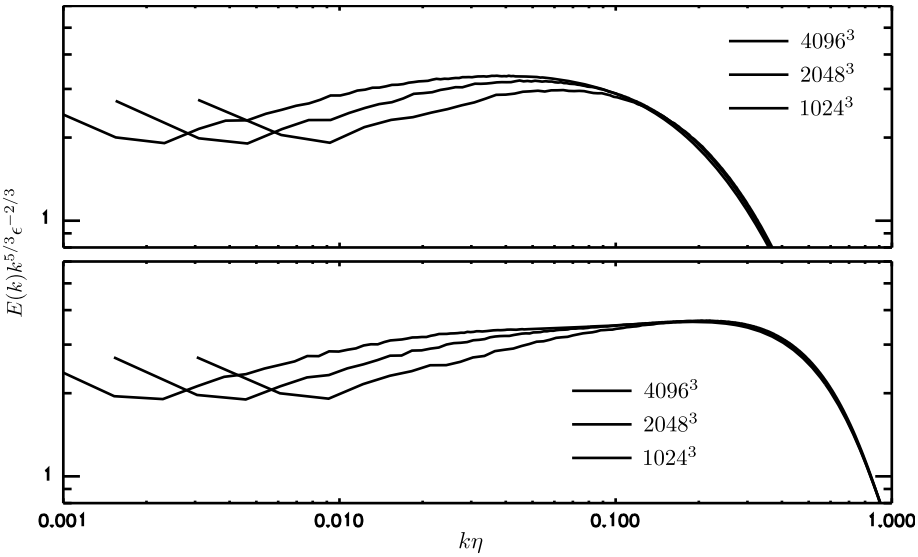

Figure 3.9: Checking –5/3 hypothesis with the scaling study. Solid, dashed, and dash-dotted are spectra from 4096^3, 2048^3, and 1024^3 simulation, correspondingly. The upper plot shows normal diffusion M1-3 simulations, and the lower plot shows hyperdiffusive M1–3H simulations. The convergence is reasonable around the dissipation scale. The scaling that achieves the best convergence is ≈ –1.70 [21]. From [25].

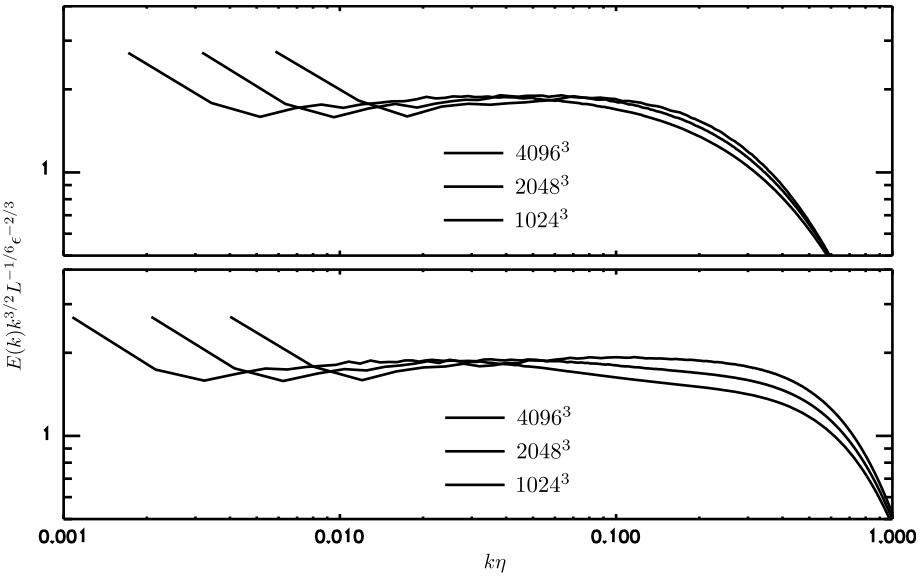

Figure 3.10: Checking −3/2 hypothesis with the scaling study. The convergence is poor. Convergence is not visible at the dissipation scales, meaning that Kolmogorov scales defined by −3/2 model are inconsistent with the measurement. From [25].

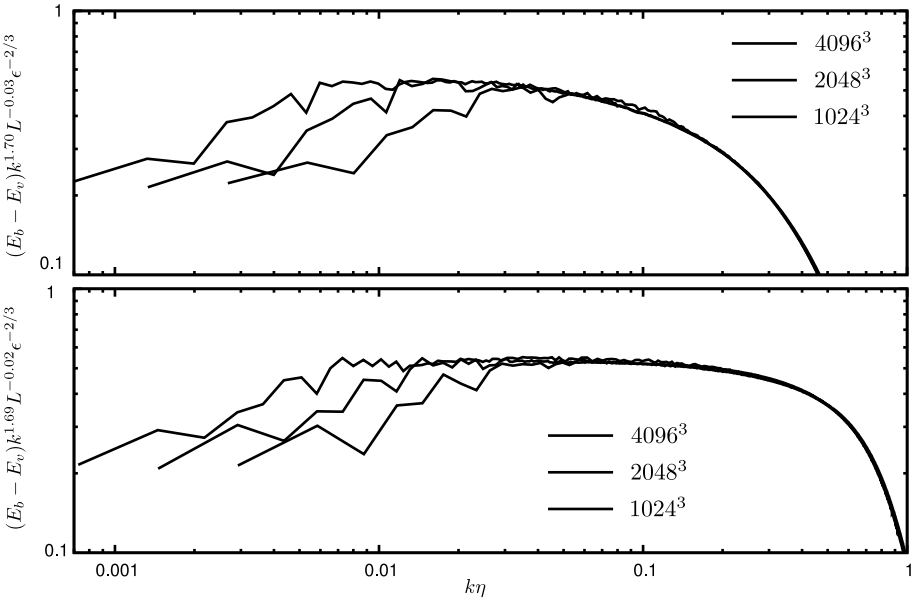

Figure 3.11: Residual energy convergence. Best convergence is $k^{-1.70}$ scaling for M1–3 and $k^{-1.69}$ scaling for M1–3H. From [25].

trum (magnetic energy minus kinetic energy). The best convergence is, again, near –1.7 slope. Note that in all three cases the convergence or the lack of convergence is consistent across two simulation groups with different dissipation prescriptions, M1–3 and M1–3h. This is expected as different dissipation schemes only affect the shape of the dissipation range, while the nature of the convergence argument has nothing to do with a particular shape of the dissipation range.

The flat part of the normalized spectrum was used to obtain Kolmogorov constant of $C_{KA} = 3.3 \pm 0.1$, which was reported in [21]. The total Kolmogorov constant for both Alfvén and slow mode in the above paper was estimated as $C_K = 4.2 \pm 0.2$ for isotropically driven turbulence with a zero mean field. This was obtained using empirical energy ratio between a slow and Alfvén mode, C_s which is between 1 and 1.3. This larger value of Kolmogorov constant, $C_K = C_{KA}(1 + C_s)^{1/3}$ is due to slow mode being passively advected and not contributing to nonlinearity. The measurement of C_{KA} had relied on the assumption that the region around $k\eta \approx 0.07$ represents an asymptotic regime. We performed simulations with resolution up to 4096^3, which also confirmed the –5/3 spectrum [25]. It was also obtained from these simulations that the residual energy, $E_B - E_v$ have the same spectral slope as the total energy, i. e., there is a constant fraction of residual energy in the inertial range. This fraction was measured in [25] to be around 0.15. Previously, the most popular model [330] suggested that the spectrum of the residual energy follows k^{-2} scaling, which is problematic both conceptually and theoretically. We confirmed that the residual energy is a fraction of the total energy in the inertial range and made explanations suggesting different scalings for magnetic and kinetic energies unnecessary.

Our results suggest that the residual energy scales as the total energy and is simply a constant fraction of the total energy. Our best estimate for this fraction is $\sigma_r = 0.15 \pm 0.03$. More commonly used in the solar wind community, the Alfven ratio is $r_A = E_v/E_B = (1 - \sigma_r)/(1 + \sigma_r) \approx 0.74$. The discussion of the fraction of the residual energy and its scale-dependence dates back a couple of decades and has recently been connected to other dimensionless measures called alignment measures in simulations [32] and in solar wind measurements [445, 73]. Explaining previously reported –2 scaling [330] for the residual energy is challenging from the theoretical standpoint. Indeed, if we assume a particular residual energy fraction on the outer scale, and the –2 scaling its value will depend on the separation from the outer scale, which will suggest nonlocal dynamics of this quantity. Our simulations, confirming that the residual energy is likely to be just a fraction of the total energy in the asymptotic regime, resolve this conceptual difficulty and make theories suggesting different scalings for magnetic and kinetic energies obsolete. The solar wind spectra often feature different kinetic and magnetic scalings; see Figure 3.12. Furthermore, the amount of residual energy is not stable from measurement to measurement and is different for the fast and the slow solar wind [445, 73]. Such deviations from idealized numerical experiments will be investigated in the future. While we believe that reduced MHD is a good description for low-frequency solar wind fluctuations, the mismatch between simulations and the

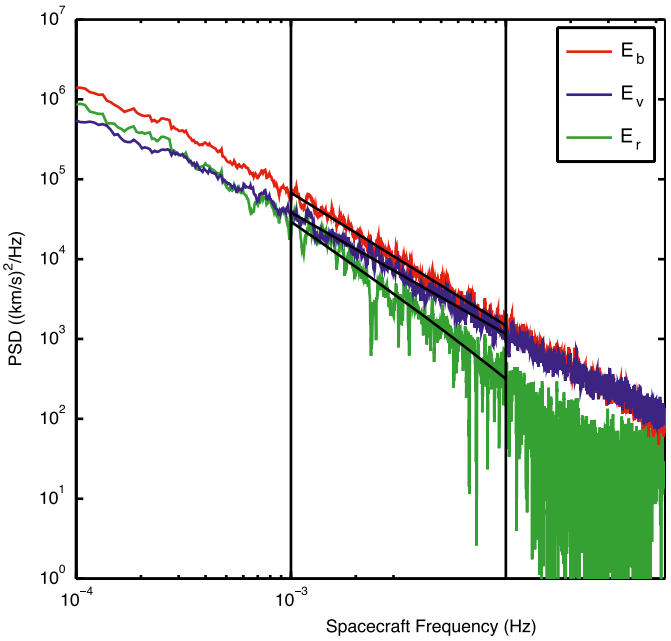

Figure 3.12: Power spectra of magnetic field, velocity, and residual energy measured in the solar wind. Alfven ratio was strongly fluctuating, and the average was around 0.71 from [73]. Reproduced from [73] with permission of AAS.

solar wind could be due to the latter having significant deviations from homogeneity, anisotropy with respect to the sunward direction [184], the presence of large amounts of discontinuities [53], or the fact that, unlike simulations, solar wind may be driven on various scales.

To summarize, the highest resolution MHD simulations to date, with Re up to 36000 exhibit asymptotic spectral scaling of around –1.7, slightly steeper than Kolmogorov. The residual energy and also kinetic and magnetic energies separately exhibit the same scaling.

3.11 Dynamic alignment models

Having sizable number of degrees of freedom, MHD turbulence can, in principle, have nontrivial scalings of dimensionless quantities in the inertial range. One of these quantities, Alfven ratio, has been discussed in the previous section and had been found, within errors of our measurement, not scale-dependent.

Another important dimensional quantity is the MHD turbulence *imbalance*, i. e., the ratio of upward and downward propagating waves, which will be considered in Chapter 4.

Recently, some models have been suggesting that various local alignment effects, i. e., local variations of dimensionless combinations of **B** and **v** will result in a gross modification of the energy cascade itself, due to the systematic scale-dependent weakening of nonlinear interaction [48], [170]. For example, in [48] it was proposed that $\mathbf{w}^+$ and $\mathbf{w}^-$ eddies are scale-dependently aligned and, therefore, the GS95 model should be modified.

A sizable confusion ensued, however to which alignment measure represent the interaction weakening more accurately. The original [48] idea was analyzed in [29] and no significant alignment was found for the averaged angle between $\mathbf{w}^+$ and $\mathbf{w}^-$, $AA = \langle|\delta\mathbf{w}^+_\lambda \times \delta\mathbf{w}^-_\lambda|/|\delta\mathbf{w}^+_\lambda||\delta\mathbf{w}^-_\lambda|\rangle$, but when this angle was weighted with the amplitude $PI = \langle|\delta\mathbf{w}^+_\lambda \times \delta\mathbf{w}^-_\lambda|\rangle/\langle|\delta\mathbf{w}^+_\lambda||\delta\mathbf{w}^-_\lambda|\rangle$, some alignment was found.

Later [49] proposed the alignment between **v** and **b**, and subsequently [304] suggested a particular amplitude-weighted measure, $DA = \langle|\delta\mathbf{v}_\lambda \times \delta\mathbf{b}_\lambda|\rangle/\langle|\delta\mathbf{v}_\lambda||\delta\mathbf{b}_\lambda|\rangle$, that was claimed to depend of perpendicular scale as $\lambda^{1/4}$. In a sense, *DA* is very similar to *PI* but uses **B** and **v** instead of $\mathbf{w}^\pm$.

The measure for local imbalance can be introduced as $IM = \langle|\delta(w^+_\lambda)^2 - \delta(w^-_\lambda)^2|\rangle/\langle\delta(w^+_\lambda)^2 + \delta(w^-_\lambda)^2\rangle$, [32].

Our analysis has shown that the numerical claims of *DA* scale dependency have been ill-founded. More importantly, as we will show below: (a) the choice of *DA* as a measure exclusively responsible for interaction weakening is arbitrary and not founded in theory, and (b) the explanation of *DA* scale-dependency from [49] are at odds with the symmetries of MHD equations as well as empirical evidence.

Figure 3.13 studies scale-dependency of *DA* and *IM* by the method of scaling study. The asymptotic scale-dependency slope for *DA* is around 0.06, which is comparable to intermittency corrections and way below 1/4 suggested in [49].

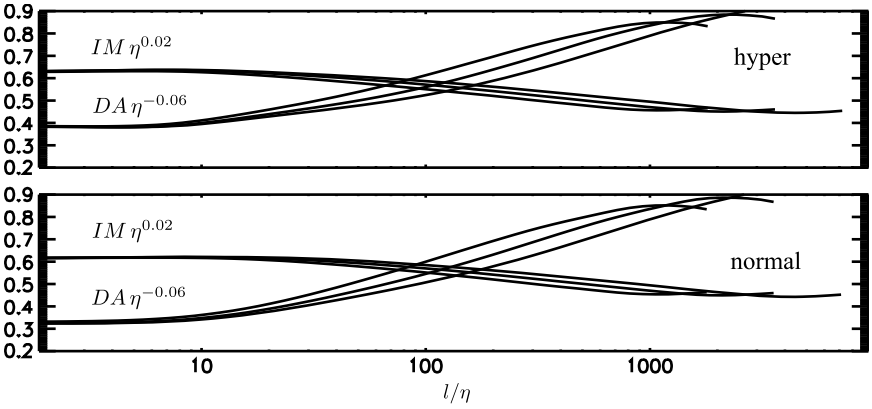

Figure 3.13: Scaling study of alignment measures $DA = \langle|\delta\mathbf{v}\times\delta\mathbf{b}|\rangle/\langle|\delta v\delta b|\rangle$ and $IM = \langle|\delta(w^+)^2 - \delta(w^-)^2|\rangle/\langle\delta(w^+)^2 + \delta(w^-)^2\rangle$ from M1–3H (top) and M1–3 (bottom). The alignment slopes converge to relatively small values, e. g., 0.06 for *DA* which is smaller than 0.25, predicted by [49]; see also [32, 21, 22]. Reproduced from [26] with permission of AAS.

Let us critically review physical argumentation why alignment should be a power-law of scale in [49]. The argument is that *DA* will tend to increase, but will be bounded by field wandering, i. e., the alignment on each scale will be created independently of other scales and will be proportional to the relative perturbation amplitude $\delta B/B_0$. But this violates Alfvén symmetry of RMHD equations (see Section 3.3), which suggests that B_0 can be factored out. A perfectly aligned state, e. g., with $\delta \mathbf{w}^- = 0$ is a precise solution of MHD equations and it is not destroyed by its field wandering. Empirically, the alignment measured in simulations of strong MHD turbulence with different values of $\delta B_L/B_0$ showed very little or no dependence on this parameter [32].

Scale-dependency of *DA* seems to be tied to the outer scale, i. e., nonuniversal and related to the fact that MHD turbulence is less local than hydro turbulence [32, 34, 21], and that the driving used in most simulations MHD turbulence is statistically different than perturbations in the inertial range. Namely, the perfect randomness of the driving scale has to transition to the asymptotic alignment of the inertial range about a factor of 0.5. This transition takes about 1.3 orders of magnitude in scale. An analytical upper bound on the cascade locality suggests that the width of the energy transfer window can be as large as $C_K^{9/4}$ [23]. The observation of [32] that MHD simulations normally lack bottleneck effect, even with high-order dissipation, while hydrodynamic simulations always have the bottleneck, which is especially dramatic with high-order dissipation is consistent with MHD being less local than hydro (by a factor of $\sim (3.3/1.6)^{9/4} \approx 5$).

The papers [49, 304] and subsequent papers assert that the particular measure of alignment, *DA* in our notation, is weakening interaction scale-dependently, so that the energy spectral slope is modified. In particular, the above papers claim that if $DA \sim \lambda^\alpha$, then the spectrum $E(k) \sim k^{-5/3+2/3\alpha}$ which, in the case of $\alpha = 1/4$ will result in $E(k) \sim k^{-3/2}$. Let us critically examine the claim $E(k) \sim k^{-5/3+2/3\alpha}$ from the theoretical viewpoint. The exact relation describing energy flux through scales is given by Equation (3.33). Let us analyze this statistical average for a "+" component at a particular value of l: $\langle \delta w_{l\|}^- (\delta w_l^+)^2 \rangle$. Indeed, it appears that the anticorrelation of δw_l^- and δw_l^+ could result in a reduction of the above statistical average. *DA*, however, does not describe such an anticorrelation. Furthermore, *DA* is based on a second-order measure, while $\langle \delta w_{l\|}^- (\delta w_l^+)^2 \rangle$ is third order. Most importantly, no rigorous argumentation could suggest that the discussed anticorrelation necessarily reduces the above statistical average. Indeed, the $\delta w_{l\|}^-$ is a signed quantity, and so is the whole expression under the statistical average. Therefore, the value of the statistical average is not necessarily related to the RMS values of the expression, but rather depend on the *skewness* of the PDF of the expression. This is most obviously indicated by Figure 3.3, where the ratio of unsigned to signed statistical average is about 10. This ratio can be arbitrarily large, e. g., in weak MHD turbulence, where taking larger B_0 will result in decreased energy rates, the above PDF becoming closer to Gaussian and its skewness going to zero. It is only the Kolmogorov similarity hypothesis for the case of strong MHD turbulence that asserts that the skewness is independent on scale, and allows us to derive the $k^{-5/3}$ spectrum. When one wants to explore different similarity relations, it is necessary to

argue in favor of the new scale-independent skewness based on a different argument. This so far has not been accomplished. To summarize, the assertion that the *DA* factor weakens the interaction is not theoretical but rather heuristic is based on empirical scalings in a backward logic type of connection.

3.12 Anisotropy scaling study

In the theoretical sections, we alluded that anisotropy should be universal in the inertial range due to the connection between Lagrangian spectrum and parallel spectrum. The relation between parallel and perpendicular scales is expected to have a form $\Lambda = C_A v_A \lambda^{2/3} \epsilon^{-1/3}$, where C_A is an anisotropy constant to be determined from the numerical experiment or observation. Note that both Alfvénic and slow modes should have the same anisotropy. This is because they have the same ratio of propagation to nonlinear timescales. It is interesting to repeat the convergence argument now for anisotropy relation, which is what we did in Figure 3.14. We used the so-called minimum parallel structure function, described in detail in [33]. From this scaling study, we obtained $C_A = 0.63$. Note, that the conventional definition of critical balance involves the amplitude, rather than $(\epsilon\lambda)^{1/3}$, so the constant in this classical formulation will be $C_A C_K^{1/2} \approx 1.1$, which is closer to unity. Together with energy spectrum, this is a full description of the universal axisymmetric two-dimensional spectrum of MHD turbulence in the inertial range.

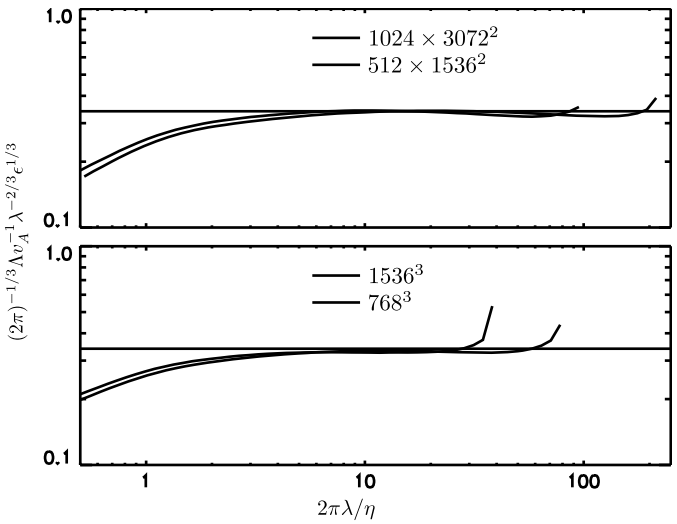

Figure 3.14: The scaling study for anisotropy shows moderately good convergence to a universal anisotropy $\Lambda = C_A v_A \lambda^{2/3} \epsilon^{-1/3}$ with anisotropy constant C_A of around 0.63. From [22].

3.13 Summary of balanced driven MHD turbulence

In this chapter, we argued that the properties of Alfvén and slow components of incompressible MHD turbulence in the inertial range will be determined only by the Alfvén speed v_A, dissipation rate ϵ, and the scale of interest λ. The energy spectrum and anisotropy of Alfvén mode will be expressed as

$$E(k) = C_K \epsilon^{2/3} k^{-5/3}, \tag{3.36}$$

$$\Lambda/\lambda = C_A v_A (\lambda\epsilon)^{-1/3}, \tag{3.37}$$

with $C_K = 3.3$ and $C_A = 0.63$ (modulo small intermittency corrections to power indexes). If the slow mode is present, its anisotropy will be the same, and it will contribute to both energy and dissipation rate. Assuming the ratio of slow to Alfvén energies between 1 and 1.3, the latter was observed in statistically isotropic high-resolution MHD simulation with zero mean field, we can use $C_K = 4.2$ for the total energy spectrum [21].

Furthermore, we argued theoretically and found numerically that the ratio of kinetic to magnetic energies in the inertial range is constant, $r_A = E_v/E_B \approx 0.74$, consistent with the latest measurements in the solar wind [73].

Anisotropy of MHD turbulence is an important property that affects such processes as interaction with cosmic rays. Since cosmic ray pressure in our galaxy is of the same order as dynamic pressure, their importance should not be underestimated.

Fully compressible MHD equations contain extra degrees of freedom, which, in a weakly compressible case, entails the additional cascade of the fast MHD mode, possibly of weak nature. This is the subject of Chapter 5.

3.14 Turbulence driven by external current

Cosmic rays (CRs) contribute significantly to the overall energetics of the ISM. While being produced in supernova remnants, CRs stream around interacting with the ISM magnetic fields creating CR-induced turbulence. One of the simplest approaches is to treat CRs as an external current acting on the dynamic MHD fluid. In this section, we will study MHD turbulence driven in such a way and derive basic scaling laws.

This problem is also related to the issue of acceleration of CRs themselves, namely that to be accelerated efficiently, CRs must self-scatter, i. e., induced MHD perturbations that result in their own scattering. Furthermore, to guarantee acceleration to the observed "Knee" of the spectrum at 10^{15} eV, this also must be a dynamo process, in which average magnetic field is significantly increased. Evidence of field amplification has been found in the Cassiopeia A SNR [434] and in Tycho's SNR [69].

The reader should keep in mind that the simplified approach, assuming that cosmic rays are acting on MHD plasma as an external current and that the bending of

cosmic rays is small, is essentially a limit of infinite energy of CRs and is certainly not applicable to realistic SNRs. The discussion of this simple problem, well described within the realm of MHD theory and numerics, can be a good starting point in the search for a more realistic particle-MHD dynamo.

3.14.1 MHD equations with external current and conservation laws

The portion of the Lorentz force, associated with the cosmic ray current should be subtracted from the total Lorentz force, as this portion is not applied directly to the fluid. The induction equation, however, is unchanged, as it is the consequence of the Ohm's law. The resulting equations are MHD equations with an external current, which we call Bell-MHD equations after [19]. Again we are using Heaviside–Alfvén units with $\mathbf{j} = \nabla \times \mathbf{B}$, which helps to avoid having factors of $\sqrt{4\pi}$, ρ and c in the MHD equations and also expresses the magnetic field in velocity units, as the density assumed to be unity. It is easy to go back to CGS units remembering that energy density in Heaviside–Alfven units is $\rho(B^2 + v^2)/2$. Also, the current density $j = (j_{\mathrm{CGS}}/c)(4\pi/\rho)^{1/2}$,

$$(\partial_t + \mathbf{v} \cdot \nabla)\mathbf{v} = -\nabla P + \mathbf{j} \times \mathbf{B} - \mathbf{j_e} \times \mathbf{B}, \tag{3.38}$$

$$\partial_t \mathbf{B} = \nabla \times (\mathbf{v} \times \mathbf{B}). \tag{3.39}$$

The equations above are basically MHD equations with an extra "force" $-\mathbf{j_e} \times \mathbf{B}$. Physically, this extra term means that the MHD fluid has external current embedded in it, which has an electric connection with a fluid but does not apply any force to the fluid.

A certain insight into the dynamics could be obtained by reviewing conservation laws for the above system. Originally, MHD equations have five basic conservation laws for scalar or pseudoscalar quantities: mass m, momentum p, energy E, cross-helicity H_c, and magnetic helicity H_M. As the continuity equation is unchanged, conservation of mass still holds. Furthermore, as induction equation is unchanged, the magnetic helicity conservation still holds and multiplying Equation (3.38) by $\mathbf{B}$ one can verify that cross-helicity is also conserved. The energy and momentum conservation are the two conservation laws that are broken by the Bell-MHD system. The average extra momentum per unit time is related to the average magnetic field $\mathbf{B_0}$ as $-\mathbf{j_e} \times \mathbf{B_0}$. This extra momentum has to be provided by external current. In the case of supernova remnants, the amount of momentum carried by high-energy cosmic rays is small compared to the inflowing fluid momentum, therefore, the component of external currents which is perpendicular to $\mathbf{B_0}$ will be suppressed in one gyration for the current-carrying cosmic rays. Keeping in mind of this, we will consider only the case when $\mathbf{j_e} \| \mathbf{B_0}$ and the global momentum conservation holds true. Multiplying Equation (3.38) by $\mathbf{v}$, we see that the extra energy per unit time is $-\mathbf{v} \cdot (\mathbf{j_e} \times \mathbf{B}) = \mathbf{j_e} \cdot (\mathbf{v} \times \mathbf{B})$,

i. e., it is associated with the electromotive force (EMF) of the fluid, $\mathcal{E} = \mathbf{v} \times \mathbf{B}$, applied to the external current. As we will see below for the unstable modes, MHD fluid applies such an EMF as to extract energy from the external current. Obviously, this results in the energy loss in the loop of the external current. In the case of the external current provided by cosmic rays, they are being slowed down by MHD fluid's EMF. We can also write down Equation (3.38) in Fourier space and investigate energy injection as a function of scale. In order to do this, the equations for the time derivative of the Fourier-transformed velocity $\hat{\mathbf{v}}_k$ have to be multiplied to $\hat{\mathbf{v}}_k^*$, a complex conjugate. The result is the energy injection with the rate of $\mathbf{j_e} \cdot (\mathbf{v_k} \times \mathbf{B_k^*})$, or $\mathbf{j_e} \cdot \mathcal{E}_\mathbf{k}$, where $\mathcal{E}_\mathbf{k}$ is the power spectrum of EMF, $\mathbf{v_k} \times \mathbf{B_k^*}$.

3.14.2 Linear and nonlinear stages

The linear phase of Bell's instability can be investigated by applying small perturbations to the initial state $\mathbf{B} = \mathbf{B}_0$. This initial state corresponds to plasma current completely canceling out the external current, i. e., the total current of zero. The mutual repulsion of external and plasma current results in an unstable situation which will grow exponentially from small perturbations of $\mathbf{B}_1$ and $\mathbf{v}_1$. Using linear analysis of the equations above, one can verify that the fastest growing mode has a wavenumber $k_d = j_e/2B_0$ parallel to $\mathbf{B}_0$, while the perturbations $\mathbf{B}_1$ and $\mathbf{v}_1$ are perpendicular to $\mathbf{B}_0$ and have a certain sign of circular polarization, corresponding to the sign of current helicity $\mathbf{j}_e \cdot \mathbf{B}_0$ [19]. Energy is equipartitioned between v and B. The fastest growing mode of field perturbations grows at the rate[2] of $j_e/2$, while the energy grows at a rate j_e. It is also worth noting that in the presence of scalar viscosity ν and magnetic diffusivity ν_m this growth rate will be decreased by $-(\nu + \nu_m)j_e^2/4B_0^2$.

The nonlinear stage takes over when nonlinear terms of Equations (3.38)–(3.39) become comparable with linear terms. This will happen when energy density exceeds characteristic initial energy density $B_0^2/2$. Note that in the limit of ideal incompressible MHD statistically homogeneous system described by Equations (3.38)–(3.39) has a single characteristic energy density scale, B_0^2, timescale $1/j_e$, which corresponds to the linear growth rate, and length scale B_0/j_e, which corresponds to the wavelength of the most unstable mode. If we conjecture that B_0 will become unimportant later in the nonlinear evolution, the system will only have a characteristic timescale $1/j_e$. It also turns out that dissipative effects can be neglected as long as B_0/j_e is above all dissipative scales.

Suppose at some moment of time during nonlinear evolution the spectrum of perturbations has an integral (outer) scale L. We will argue that perturbations on this scale will be able to freely expand due to the Lorentz force, just like an unstable helical

2 In CGS units, $k_d(\mathrm{CGS}) = 4\pi j_e(\mathrm{CGS})/(2B_0 c)$ and the growth rate is $(j_e(\mathrm{CGS})/2c)(4\pi/\rho)^{1/2}$.

mode in the linear regime. We will also conjecture, by analogy with linear stage, that the product $\mathbf{j_e} \cdot (\mathbf{v} \times \mathbf{B})$, i. e., the work of external current onto the fluid, will be proportional to energy. The difference with the linear stage is that the EMF spectrum will no longer be proportional to the energy spectrum, rather it will peak at the integral scale. The result will be the growth of energy at the integral scale, the growth of the integral scale itself and the direct energy cascade on scales below integral scale. From here on, we introduce two dimensionless constants that describe this process: the ratio of EMF to total energy (which conventionally have the same Heaviside–Alfven units) C_E and the fraction of energy that goes into the direct cascade C_D. We expect C_E and C_D to be below unity. The whole spectrum of perturbations at any moment of time will be determined only by the total energy E and the integral scale L. The time evolution for these will be determined by

$$\frac{dE}{dt} = (1 - C_D) C_E j_e E. \tag{3.40}$$

At the same time, at the sufficiently high Reynolds' numbers, the dissipation will only depend on large-scale quantities, as is typical for turbulence. This is satisfied as long as the dissipation scales are much smaller than all relevant scales of the problem, including $1/k_d = B_0/j_e$. It is possible to verify that if the linear instability is growing, i. e., $\nu, \nu_m < B_0^2/j_e$, the dissipation scale will be smaller than $1/k_d (B_0/B)^{1/2}$, so this condition is always satisfied as long as there is a growth of instability. For the dissipation rate, we can take a classic large-scale expression $\delta v^3/L$:

$$\frac{E^{3/2}}{L} = C_K C_D C_E j_e E. \tag{3.41}$$

Here, we have introduced Kolmogorov constant C_K. This will eventually give us the relation between the integral scale and the energy density:

$$L = E^{3/2}/(C_K C_D C_E j_e E) = E^{1/2}/(C_K C_D C_E j_e). \tag{3.42}$$

We expect approximate equipartition between magnetic and kinetic energies and Equation (3.42) has a simple physical meaning. Since $E^{1/2} \sim B$, the fluctuations of the magnetic field are such that the fluctuations of the total current density (plasma plus external) are of the order of the external current density itself, on the outer scale of turbulence. In other words, collisions of expanding spirals from Bell instability almost fully randomizes total current, but its RMS value always stays around j_e.

The scalings above could be verified in numerics, in particular, we observe that the energy density continues to grow exponentially in the nonlinear stage, Figure 3.15. And the outer scale L indeed follows the above scaling (see Figure 3.17). We can also directly verify that EMF drives turbulence mostly on the integral scale.

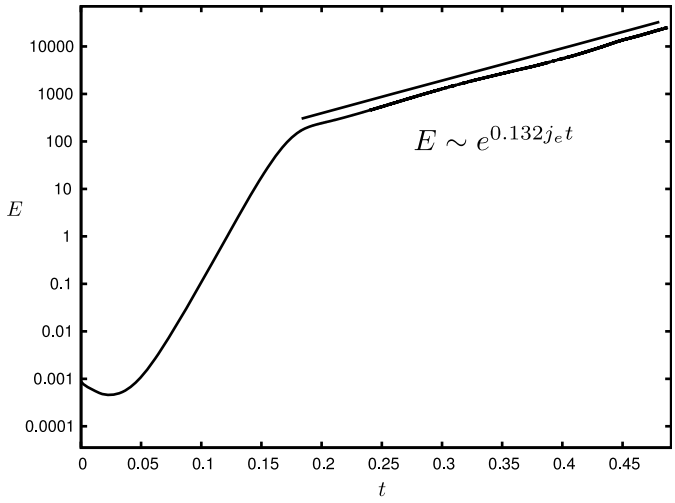

Figure 3.15: Energy grows exponentially in both linear and nonlinear regime of Bell's instability. While the linear growth rate is, approximately, j_e, the nonlinear growth rate is reduced by a factor of 0.132. From [35].

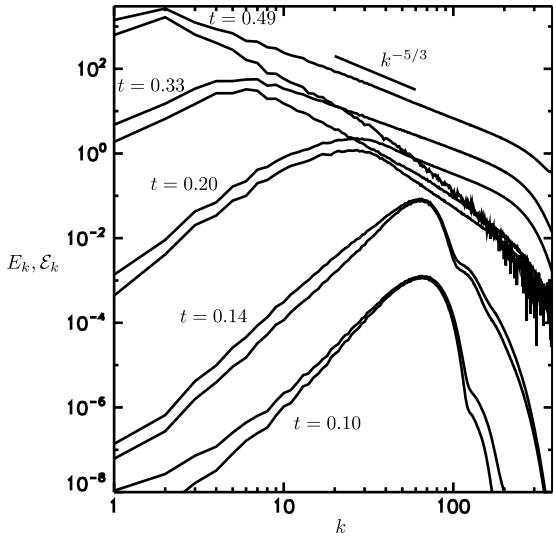

Figure 3.16: Energy spectra (solid) and EMF spectra (dashed) at several moments of simulation time. We only take the vector component of EMF, which is parallel to j_e, therefore the dashed spectrum is also the energy injection spectrum. The first two spectra feature linear mode growth with EMF spectrum proportional to the energy spectrum. Later, nonlinear stages show EMF driving dominant at the largest, energy containing scale of the spectrum. Below energy-containing scale the energy injection becomes negligible and the spectrum exhibiting an "inertial range" $k^{-5/3}$ scaling. Reproduced from [35] with permission of AAS.

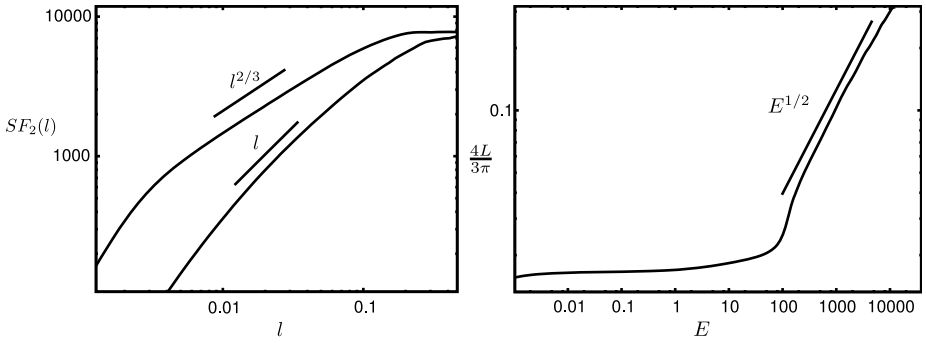

Figure 3.17: Left: Anisotropy of Bell-MHD turbulence below the energy containing scale at $t = 0.49$. In this plot, we show second-order structure functions of density parallel (dashed) and perpendicular (solid) to the local mean magnetic field. The scalings of l^1 and $l^{2/3}$ are expected from inertial range of strong MHD turbulence [172]. Our measurement is grossly consistent with the Goldreich–Sridhar anisotropy. Right: The dependence of energy containing scale L on energy density E. The linear growth regime features constant L, corresponding to the wavelength of the fastest growing mode. The nonlinear regime is characterized by the $l \sim E^{1/2}$ law, with both E and l growing exponentially in time. Reproduced from [35] with permission of AAS.

3.14.3 Empirical findings

We performed a series of six incompressible numerical experiments changing the value of initial magnetic field B_0 between values of 0.5, 1.0, and 2.0 and changing current between 40 and 20. Due to the symmetries of the dynamical equations, we expected simulations with the same j_e/B_0 ratio to exhibit the same behavior, assuming that the timescale was appropriately rescaled to $1/j_e$. This was indeed the case. Also, as long as the scale $1/k_d$ was well separated from both dissipation scale and the cube size scale, the behavior was similar for all simulations, assuming the same rescaling. Since incompressible MHD is scale-free, the only true physical parameter of the problem is j_e, and since it has units of $1/s$, it simply designates the only available timescale for the problem. In other words, the evolution is expected to be universal as long as the dissipation coefficients are small and the box size is large enough.

Keeping this in mind, we performed a single 1152^3 large-scale simulation to verify the scaling in Equation (3.42). In this simulation, we chose $j_e = 120$, $B_0 = 1$, so that $k_d = 60$ and is well separated from the dissipation scale at around $k = 300$. Figures present measurements from this simulation. The total energy evolution is presented in Figure 3.15, while spectra of total energy and the EMF along $\mathbf{j_e}$ are presented in Figure 3.16. The nonlinear regime exhibits a pure exponential growth, over at least a couple of the order of magnitude in energy, which is fully consistent with our model and implicitly verifies that the external current density j_e determines the only relevant timescale of the problem. The coefficient of reduction of the growth rate, 0.132, that we conjectured to be equal to the $(1 - C_D)C_E$ product indeed seems to be universal among

several simulations with different j_e, B_0, and numerical resolutions. We observe the transition to nonlinear stage at the level of $B_{\rm rms}/B_0 \sim 10$ similar to previous research, e. g., [371].

Furthermore, the spectra of energy and EMF, Figure 3.16, seem to support our conjectures about the scales at which the Bell-MHD turbulence is driven. For the linear growth regime, represented in Figure 3.16 by spectra at $t = 0.1$ and $t = 0.14$, the driving EMF spectrum is basically proportional to the energy spectrum, while for nonlinear growth regime at $t = 0.2$, 0.33, and 0.49 the EMF is peaked on the outer scale, supporting our conjecture about large-scale driving. In fact, to be important on smaller scales l, and to interfere with the energy cascade through scales, the EMF has to be at least scale-independent or to grow with smaller scales, which is clearly not the case. From the reduced ratio of EMF to energy in the nonlinear regime, we derive $C_E \approx 0.58$ and using $(1 - C_D)C_E = 0.132$ we have the fraction of energy captured by the direct cascade and dissipated as $C_D = 0.77$.

It is also interesting to study the statistical properties of the nonlinear Bell-MHD turbulence and see if they are similar to the ordinary direct-cascade MHD turbulence driven on large scales. We measured second-order structure function $SF(l)$ parallel and perpendicular to the local magnetic field, which is supposed to scale as l and $l^{2/3}$ correspondingly, according to the standard model of strong MHD turbulence by [172]. We found that the structure function measurement grossly consistent with the theory; see Figure 3.17. One of the important consequences of this is that due to local anisotropy, the Bell-generated turbulence will be inefficient at scattering particles with gyroradii much smaller than the outer scale L, similar to the driven MHD turbulence.

As the instability enters the nonlinear stage, the outer scale also quickly grows, in fact, exponentially in time. Figure 3.17 investigates the dependence of the outer scale on the mean energy density and finds that indeed outer scale grows as the square root of energy density as Equation (3.42) suggests. We found that $L \approx 0.97E^{1/2}/j_e$. Assuming equipartition between magnetic and kinetic energies, which is indeed approximately satisfied, and going back to CGS units in the above relation, we obtain $B_{\rm rms}({\rm CGS}) \approx 4\pi j_e({\rm CGS})L({\rm CGS})/c$.

3.14.4 Applications of current driven turbulence to astrophysical systems

The key properties of the Bell-MHD turbulence we have uncovered, such as Equation (3.42) suggests that, when considering including the feedback on cosmic rays and making conjectures about their possible roles in cosmic ray acceleration, one has to be very careful in adopting the spectrum and amplitude of such turbulence. This is because this turbulence will strongly affect the properties of lower-energy CRs, i. e., the same particles that mostly contribute to current. Another source of uncertainty would be understanding possible effects of compressible turbulence. Our picture of growing magnetic helixes on the outer scale L due to interaction with local external current

does not explicitly depend on fluid pressure, however, and the zeroth law of turbulence. Equation (3.41), to the best of our knowledge, is supposed to be correct even in supersonic turbulence. Furthermore, since our results indicate that the C_D fraction of total energy goes into the direct cascade and dissipates into heat, the sonic Mach number of Bell-MHD turbulence can be estimated as $M_s \approx \sqrt{(1 - C_D)/2C_D} \approx 0.4$. Although qualitatively the picture of nonlinear stage is not supposed to change, we might expect the coefficients C_D, C_E, and C_K to somewhat vary in the compressible case.

Our results are applicable not only to supernova remnants problem but to any conductive fluid with external current, e. g., plasma with rigid wires embedded in it and the current driven by an external voltage. The quick exponential growth of both energy and fluid EMF suggests that external energy source will only be able to maintain such current for a limited amount of time.

Several pathways are available to study back-reaction to cosmic rays. One of the approaches is the bottom-up plasma simulations, e. g., by [370]. Another alternative is the study of nonlinear streaming instability [113] and long wavelength dynamics [66, 371]. A different way to generate turbulence is by cosmic ray pressure, turbulence driven on large scales by interaction of density gradients and nonbarotropic cosmic ray pressure generating vorticity by baroclinic term, which was suggested in [28]. Magnetic energy density E_B is bound on energetic grounds, and also constrained by observations [434, 69, 440], so we can compare the outer scale growth as a function of magnetic energy density E_B and find $L \sim E_B^{1/2}$ dependence for the Bell's mechanism, while the small-scale dynamo has $L \sim E_B^{3/2}$ dependence. For these two mechanisms, the product of LB, which determines the scattering of highest energy particles, will behave as E_B^1 and E_B^2, correspondingly. More accurate estimates involving conditions in the supernova remnants seem to indicate that dynamo mechanism is more important for particle scattering [28].

4 Imbalanced MHD turbulence

While hydrodynamic turbulence have only one energy cascade, the incompressible MHD turbulence has two, due to the exact conservation of the Elsässer (oppositely going wave packets') "energies." This can be also formulated as the conservation of total energy and cross-helicity.[1] The situation of zero total cross-helicity, which we considered in previous sections has been called "balanced" turbulence as the amount of oppositely moving wavepackets balance each other, the alternative being "imbalanced" turbulence. Most of the above studies concentrated on the balanced case, and without exception, the GS95 model, which is the strong cascading model with critical balance, can only be kept self-consistent assuming balanced case.

The real MHD turbulence, however, is often imbalanced, such as in situations when the mean magnetic field is present and we have a strong localized source of perturbations. The perfect example is the solar wind, where satellite measurements discovered strong correlations between $\mathbf{v}$ and $\mathbf{B}$ since long time ago. These correlations actually correspond to the imbalanced turbulence with the dominant component propagating away from the sun; see Figure 4.2. If the mean magnetic field of the Parker spiral is directed locally outwards, the sun then the dominant component will be $\mathbf{w}^-$, otherwise it will be $\mathbf{w}^+$.

Certainly, we expect similar phenomena to happen in the active galactic nuclei (AGN), where the jet has a strong large mean magnetic field component and the perturbations will propagate primarily away from the central engine. Another example is the interstellar medium (ISM) turbulence in spiral galaxies. Indeed, in spiral galaxies, due to the action of the large-scale dynamo there is a average component of the mag-

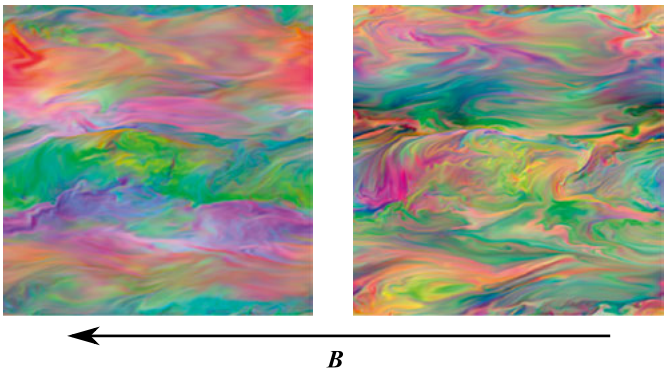

Figure 4.1: The slices of $\mathbf{w}^+ = \mathbf{v} + \mathbf{B}/\sqrt{4\pi\rho}$ (left) and $\mathbf{w}^- = \mathbf{v} - \mathbf{B}/\sqrt{4\pi\rho}$ (right) from the three-dimensional MHD simulation with strong mean magnetic field and imbalance. From [36].

1 The latter, $\int \mathbf{v}\cdot\mathbf{B}\, d^3x$ is a quantity conserved in the absence of dissipation.

https://doi.org/10.1515/9783110263282-004

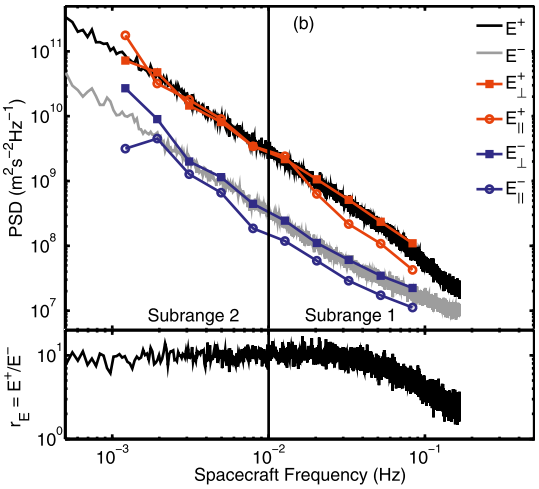

Figure 4.2: Spectra of imbalanced turbulence measured in the solar wind. Trace of the Fourier and wavelet power spectra of $(w^+)^2$ (black line and red symbols) and $(w^-)^2$ (gray line and blue symbols) parallel and perpendicular to the local magnetic field. The bottom panel shows the ratio $(w^+/w^-)^2$ from [444]. Reproduced from [444] with permission of APS.

netic field, spanning the radius of the disk itself. The ISM turbulence, however, is inhomogeneous, due to the energy sources for turbulence (supernovas and stellar winds) distributed unevenly in the disk. This will create imbalanced turbulence, which might have properties different from the balanced one, which has implications for ISM heating, cosmic ray propagation, and many other physical processes in the ISM.

Finally, from the theoretical viewpoint, it is impossible to fully understand balanced turbulence by itself, if the more general imbalanced case is not treated. This is due to the fact that turbulence is a stochastic phenomena with all quantities fluctuating and every piece of turbulence at any given time can have imbalance in it. In this respect, while the mean-field Kolmogorov model can be expanded to include fluctuations of the dissipation rate in the volume, the mean field GS95 model cannot.

Imbalanced turbulence or "turbulence with nonzero cross-helicity" has been discussed long ago by a number of authors [116, 309, 182, 362]. This work testified that the nonzero cross-helicity modifies the turbulence. Although these studies correctly reproduced separate cascades for energy and cross-helicity, they were based on then-popular models of MHD turbulence and later it became evident that these are problematic. For example, the closure theory of isotropic MHD turbulence [361], which reproduced Iroshnikov–Kraichnan model can be criticized on the basis that the ad hoc term for "relaxation of triple correlations," happen to be larger than real physical nonlinear interaction and makes MHD turbulence, effectively, isotropic. Numerics, however, show that strong MHD turbulence is locally anisotropic, as we demonstrated in previous sections. Another class of models were based on the so-called two-dimensional

MHD turbulence that, as we demonstrated in previous sections, is unable to reproduce basic properties of the real three-dimensional turbulence, such as strong interaction and critical balance. Figure 4.1 visualizes Elsassër variables in a 3D simulation with strong mean field.

4.1 Theoretical considerations

As we explained in the previous sections, the MHD cascade is primarily perpendicular and as it proceeds to small scales, the applicability of weak interaction breaks down, and Alfvénic turbulence becomes strong. In this situation, GS95 assumed that the frequency of the wavepacket cannot be smaller than the inverse lifetime of the wavepacket, estimated from nonlinear interaction. In the GS95 closure model, there is an explicit ad hoc term that allows for the increase of the wave frequency. Unlike previous models, this term is scale-dependent and is based on the assumption of turbulence locality, i. e., that there is one characteristic amplitude of perturbation pertaining to each scale and that this perturbation determines the strength of the interaction and finally renormalization of frequencies. However, as was realized as early as in the original GS95 paper in the imbalanced case we have two characteristic amplitudes, w^+, w^-, and the choice for frequency renormalization becomes unclear.[2] Any theory of strong imbalanced turbulence must deal with this difficulty.

Let us first demonstrate that a straightforward generalization of GS95 for the imbalanced case does not work. If we assume that the frequency renormalization for one wavepacket is determined by the shear rate of the oppositely moving wavepacket, the wave with small amplitude (say, w^-) may only weakly perturb large amplitude wave w^+ and the frequency of cascaded w^+ will conserve. On the other hand, w^+ may strongly perturb w^- and w^-'s frequency will be determined as w_l^+/l.[3] This mismatch in frequencies creates an inconsistency in the paradigm of scale-local cascade where both wavepackets must have both parallel and perpendicular wavenumbers comparable. As the cascade proceeds to smaller scales, this mismatch only increases, making the cascade nonlocal and inefficient. Such shutdown of the cascade on small scales is self-contradictory, since in the stationary case it must carry a constant energy flux for both components. In order to deal with this fundamental difficulty, one must assume something extra to the original GS95 critical balance.

2 We assume that imbalanced turbulence is "strong" as long as the applicability of weak Alfvénic turbulence breaks down. This requires that at least one component is perturbed strongly. In the imbalanced turbulence, the amplitude of the dominant component is larger, so that in the transition to strong regime the applicability of weak cascading of the subdominant component breaks down first.
3 Throughout this book, we assume that w^+ is the larger-amplitude wave. This choice, however, is purely arbitrary and corresponds to the choice of positive versus negative total cross-helicity.

Currently, there were several propositions how to deal with strong anisotropic imbalanced MHD turbulence. In [295], which we designate below as LGS07, the authors proposed that the parallel scale for both components is determined by the shear rate of the stronger component. This model predicts the same anisotropy for both components. In [30], which we designate below as BL08, the authors proposed a new formulation for critical balance for the stronger component. In [71], which we designate below as C08, an advection-diffusion model of cascading was adopted, where advection was describing perpendicular cascade and diffusion was describing the increase of frequencies. These three models clearly state the difficulty described above and try to resolve it with the new physical argumentation that goes beyond the original GS95 critical balance. These three models smoothly transition to the balanced theory of GS95 in the limit of small imbalance. Several other models have been suggested, advocating a different picture, in particular the influence of so-called dynamic alignment. In [356], which we designate below as PB09, the authors argued that the dynamic alignment will effectively lead to the same nonlinear timescale for both components. This has been criticized as grossly inconsistent with numerics [33, 34] and having no meaningful physical limit for large imbalances.

4.1.1 Lithwick, Goldreich, and Sridhar (2007) model, [295] LGS07

LGS07 argue that the strong wave w^+ is also cascaded strongly and its frequency is equal to the frequency of the weak wave, i. e., the critical balance for strong wave uses the amplitude of the strong wave itself ($w^+\Lambda = v_A\lambda$). In this case, the anisotropies of the waves are identical. The formulas for energy cascading are strong cascading formulas, i. e.,

$$\epsilon^{\mp} = \frac{(w^{\mp}(\lambda))^2 w^{\pm}(\lambda)}{\lambda}. \tag{4.1}$$

This lead to the prediction $w^+/w^- = \epsilon^+/\epsilon^-$. In terms of energy spectra, the model predicts

$$E_k^{\pm} = C_K(\epsilon^{\pm})^{4/3}(\epsilon^{\mp})^{-2/3}k^{5/3}, \tag{4.2}$$

where the Kolmogorov constant C_K must be the same for the theory to have a limit of standard balanced MHD turbulence.

4.1.2 Beresnyak and Lazarian (2008) model, [30] BL08

BL08 relaxes the assumption of local cascading for the strong component w^+, while saying the w^- is cascaded in a GS95-like way. In the BL08 picture, the waves have different anisotropies (see Figure 4.3) and the w^+ wave actually have smaller anisotropy than w^-, which is opposite to what a naive application of critical balance would pre-

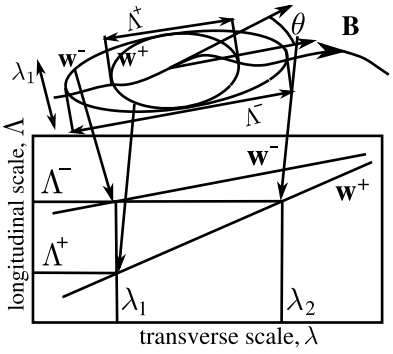

Figure 4.3: Upper: a $\mathbf{w}^+$ wavepacket, produced by cascading by $\mathbf{w}^-$ wavepacket is aligned with respect to $\mathbf{w}^-$ wavepacket, but misaligned with respect to the local mean field on scale λ_1, by the angle θ. Lower: the longitudinal scale Λ of the wavepackets, as a function of their transverse scale, λ; Λ^+, Λ^-, λ_1, λ_2 are the notation used in this book from the Beresnyak and Lazarian model [30]. Reproduced from [30] with permission of AAS.

dict. The anisotropies of the waves are determined by

$$w^+(\lambda_1)\Lambda^-(\lambda_1) = v_A\lambda_1, \tag{4.3}$$

$$w^+(\lambda_2)\Lambda^+(\lambda^*) = v_A\lambda_1, \tag{4.4}$$

where $\lambda^* = \sqrt{\lambda_1\lambda_2}$, and the energy cascading is determined by weak cascading of the dominant wave and strong cascading of the subdominant wave:

$$\epsilon^+ = \frac{(w^+(\lambda_2))^2 w^-(\lambda_1)}{\lambda_1} \cdot \frac{w^-(\lambda_1)\Lambda^-(\lambda_1)}{v_A\lambda_1} \cdot f(\lambda_1/\lambda_2), \tag{4.5}$$

$$\epsilon^- = \frac{(w^-(\lambda_1))^2 w^+(\lambda_1)}{\lambda_1}. \tag{4.6}$$

One of the interesting properties of the BL08 model is that, unlike LGS07 and C08, it does not produce self-similar (power-law) solutions when turbulence is driven with the same anisotropy for w^+ and w^- on the outer scale. BL08, however, claim that, on sufficiently small scales, the initial nonpower-law solution will transit into asymptotic power law solution that has $\Lambda_0^-/\Lambda_0^+ = \epsilon^+/\epsilon^-$ and $\lambda_2/\lambda_1 = (\epsilon^+/\epsilon^-)^{3/2}$. The range of scales for the transition region was not specified by BL08, but it was assumed that larger imbalance will require larger transition region.

4.1.3 Perez and Boldyrev (2009) model, [356] PB09

Unlike the models described above, PB09 employs dynamic alignment, which decreases without limit to smaller scales as $l^{1/4}$ and claims the 3/2 spectral slope for both components. In this respect, it is similar to [48, 49]. It is, however, a big step beyond these papers by claiming that alignment will effectively result in the same nonlinear timescales for both components, which effectively lead to $(w^+)^2/(w^-)^2 = \epsilon^+/\epsilon^-$. It could be rephrased that PB09 predicts turbulent viscosity, which is equal for both components. It is not clear, however, how this could be made consistent with the limit of large imbalances, where the weak component will not be able to produce any sizable turbulent viscosity.

4.2 Empirical study in MHD simulations with stochastic driving

The sub-Alfvénic turbulence, where the perturbation strengths $w^{\pm}$ are smaller that v_A is either weak or strong but anisotropic. The critical anisotropy is determined by the breakdown of the applicability of weak MHD turbulence which happens when $k_{\parallel} v_A / k_{\perp} \delta v \sim 1$; see Chapter 3. In most of our simulations, we drive turbulence on outer scale with the same anisotropy for both wave species, so this breakdown is determined by δv of the strong wave. We drive turbulence on outer scale in such a manner that the strong interaction establishes on the outer scale. Also, we provided driving for $k = 2..3.5$, which means that the maximum eddy size is several times smaller that the box. This is to ensure that the first turbulent scales $k \approx 4$ have more than enough space in parallel direction in case that we did not estimate the transition into strong interaction regime correctly and the parallel scale of the cascaded eddies is longer than we expected. The results from Chapter 3, however, suggest that our choice was correct, with the largest coherent eddy size being around 1/4 of the box size in both parallel and perpendicular directions. We used fully predetermined stochastic driving in both Elsasser variables[4] with a certain amplitude of the force ($f^{\pm}$, see Table 4.1), so the energy input was not strictly controlled by the forcing, but rather was calculated during the simulation. In addition, we developed a driving which ensures constant energy input for both components, these tests confirm properties of the imbalanced turbulence that were obtained with fully stochastic driving. We used the latter for most of our simulations.

In studying sub-Alfvénic turbulence, we adopted the approach to increase v_A by increasing B_0 and increase the parallel physical size of the box L by the same factor $1/M_A$ without changing the equilibrium value of δv, so that strong interaction timescale $\lambda/\delta v$ stays constant, and similarly the eddy transverse time Λ/v_A also stays constant. Alternatively, one can keep B_0 constant, but decrease δv, but in this case the timescales of sub- and trans-Alfvénic turbulence will be different. Also it is harder to tune the equilibrium δv, rather than B_0 and L. Note, that one can naively assume that due to GS95 anisotropy one needs lower numerical resolution in the parallel direction, approximately by the ratio of the anisotropies on the driving scale and on the dissipation scale, which is $(k_{\perp \mathrm{diss}}/k_{\perp \mathrm{driv}})^{1/3}$ in the GS95 model, and can be a number between

4 Elsasser driving is a preferred way to study inertial range of sub-Alfvenic turbulence as it simulates the supply of Elsasser energies from larger eddies of a realistic turbulence. It is important to remember that kinetic and magnetic energies are not separately conserved by MHD equations. So when one has a pure velocity driving in a simulation with mean field, he will generate approximately as much magnetic perturbations due to the Alfven effect, the result being two Alfven or pseudo-Alfven waves propagating in opposite directions. These waves, however, would have an artificial correlation (reflected by the fact that at $t = 0$ $\mathbf{b} = \mathbf{0}$). In order to use all degrees of freedom and have better stochasticity, one has to drive $\mathbf{w}^{+}$ and $\mathbf{w}^{-}$ independently. The mechanisms by which the outer scales of a realistic, say, ISM turbulence are driven are discussed in Chapter 5.

Table 4.1: MHD simulations of strong sub-Alfvénic ($B_0 = 10$) and trans-Alfvénic ($B_0 = 1$) turbulent flows with fully stochastic driving. Δt_0 is the duration of prior low resolution run in code units, Δt is the duration of the high resolution run, interval Δt_1 in the end of high-resolution run was used for data analysis.

Run	$n_x \cdot n_y \cdot n_z$	x:y:z	B_0	f^+	f^-	Δt_0	Δt	Δt_1	ϵ^+/ϵ^-	$(w^+)^2/(w^-)^2$
A1	$512 \cdot 768^2$	10:1:1	10	0.4	0.4	186	10	4.0	1	1
A2	768^3	1:1:1	1	0.44	0.44	186	10	4.0	1	1
A3	768^3	10:1:1	10	0.34	0.255	500	26	8.0	2.0	5.5 ± 1.0
A4	768^3	1:1:1	1	0.4	0.3	180	22	8.0	1.7	3.9 ± 0.3
A5	768^3	10:1:1	10	0.16	0.08	154	33	12.0	7.4	145 ± 10
A6	768^3	1:1:1	1	0.19	0.095	40	33	12.0	5.4	90 ± 10
A7	768^3	10:1:1	10	0.06	0.02	204	63	21.0	16	1150 ± 100
A8	768^3	1:1:1	1	0.075	0.025	160	63	21.0	12	1100 ± 100

2 and 4 in a high resolution MHD simulation. On the second thought, this approach is not evident, since the highest values of $k_\parallel$ in the *global reference frame* will be determined by field wandering on the outer scale. In other words, the anisotropy in the global frame will be approximately scale-independent and the ratios of $k_{\perp\mathrm{diss}}/k_{\perp\mathrm{driv}}$ and $k_{\parallel\mathrm{diss}}/k_{\parallel\mathrm{driv}}$ will be almost equal, which necessitates the use of NxNxN numerical resolution, i. e., cubes, for both elongated ($M_A < 1$) and cubic ($M_A \approx 1$) physical boxes.

We confirmed this by plotting the parallel and perpendicular spectra in the global frame and saw that the parallel spectrum protrude to almost as far as $k_{\perp\max}/M_A$. Figure 4.4 shows how energy is distributed on the two-dimensional $k_\parallel$, $k_\perp$ plane (global reference frame). We see that while most of the energy is in a GS95 cone, and there is also plenty of energy outside of it, especially in the upper right corner which correspond to maximum space frequencies in both parallel and perpendicular direction. If

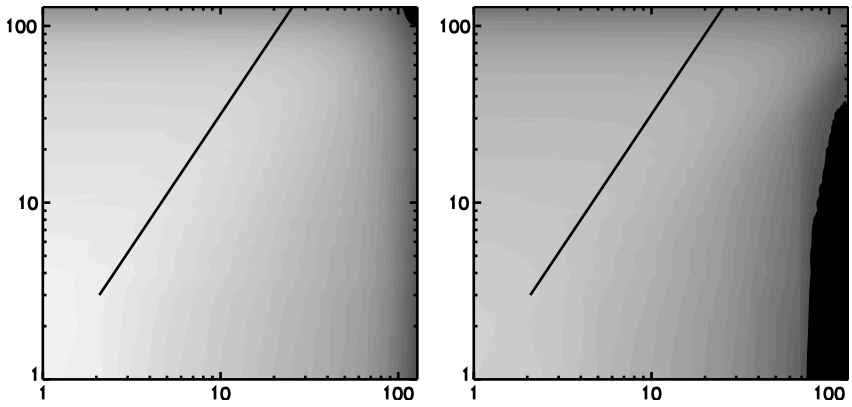

Figure 4.4: Two-dimensional energy spectrum in sub-Alfvénic and trans-Alfvénic case. For the sub-Alfvénic case, the abscissa k_x is scaled with a $1/M_A$ factor. The dashed line indicates GS95 $k_\parallel \sim k_\perp^{2/3}$ anisotropy. Reproduced from [33] with permission of AAS.

one decides to significantly cut the numerical resolution in parallel direction he/she would incorrectly describe the dynamics on small scales. In only one of our simulations, A1 (see Table 4.1), we were able to cut parallel resolution by a moderate factor of 1.5 without sacrificing small parallel scales, due to the relative lack of energy in a parallel direction in this particular *balanced sub-Alfvénic* case. In all other simulations, such a reduction was not possible because most of the k-space was filled with energy.

For all simulations A1–A8, we used hyperviscosity and hyperdiffusivity of 6th order (k^6). This choice was necessitated by the nature of imbalanced turbulence which has shorter inertial range for dominant wave due to fairly large cascading timescale of this wave (see Section 4.2.1). With currently available numerical resolutions, one cannot see an inertial interval of the strong wave in a simulation with large imbalance and real (k^2) diffusivity. Unfortunately, due to the bottleneck effect, hyperdiffusion have affected spectral slopes, although the effect on anisotropy was much less. We refer to [32] for a comparison of turbulent simulations with normal and hyperviscosity. Due to hyperviscosity, the dissipation scale was fairly small, the dissipation cutoff was around $k = 200$ (with Nyquist frequency of 384) for balanced simulations and about the same for weak component in imbalanced simulations. The strong component for the most imbalanced simulations A7 and A8 had a cutoff around $k = 100$ (Figure 4.10). Due to hyperviscosity, we cannot uniquely define a Reynolds' number of our simulations, however, viscous simulations with $\mathrm{Re} = \mathrm{Re}_m \approx 6000$ could provide turbulence inertial ranges that are similar to ours.

Once we have chosen the geometry of our simulation and figured out the extend of the perturbations on the spectral plane, the choice of timestep becomes evident. On one hand, for the dissipation term we use the integration technique [92, 303], and since we do not worry too much about the precision of the dissipation term, it does not limit the timestep. On the other hand, the general nonlinear term, containing both B_0 and δv can be seen as the sum of linear advection term with velocity v_A and nonlinear advection with δv, δb, etc. In turbulence, that is driven to be strong on the outer scale, these terms will be of the same order if we refer to the outer scale, i. e., the terms will be $v_A \delta v k_{\parallel \mathrm{driv}}$ and $\delta v \delta v k_{\perp \mathrm{driv}}$. On the dissipation scale, these terms will be determined by $v_A \delta v k_{\parallel \mathrm{diss}}$ and $\delta v \delta v k_{\perp \mathrm{diss}}$, which are, by the argument in the above paragraph, again of the same order. So we can just use linear advection behavior to estimate the timestep. This behavior in k-space is, essentially, a rotation of the phase of the wave, in a manner of $\exp(i k_\parallel v_A t)$. In order to reproduce this rotation numerically, we need $k_{\parallel \max} v_A \delta t$ to be smaller than unity, such as around 0.1, so that the code stays stable, since we do not need good precision beyond the dissipation scale where there is no energy.

The average dissipation rates $\epsilon^\pm$ reported in Table 4.1 were calculated using a sum of the work done to the Elsasser fields, i. e., we summed $(\mathbf{w}^\pm + \mathbf{f}^\pm dt) \cdot \mathbf{f}^\pm dt$ at every timestep. As our code (its nonlinear part) was energy conserving, we assume that the same amount of energy was, on average, lost to the dissipation term.

4.2.1 Establishment of the stationary state

One of the goals of this section is to demonstrate that a stationary state exists for imbalanced turbulence with rather high degree of imbalance. Note that the local model of weak Alfvénic turbulence work for imbalances of no more than $\epsilon^+/\epsilon^- = 2$ [158, 294], and the model of strong imbalance turbulence of C08 also requires similar limitation.

The highest imbalance we attempted in our simulation of $\epsilon^+/\epsilon^- = 16$ was essentially limited by the long times of establishment of the stationary state. Note that according to BL08 the dominant wave is cascaded weakly and its cascading times could be very large. Figure 4.5 shows the total energy evolution for both modes for the $\epsilon^+/\epsilon^- = 16$ case.[5] The full relaxation toward stationary state required around 300 Alfvén times or 50 crossing times.

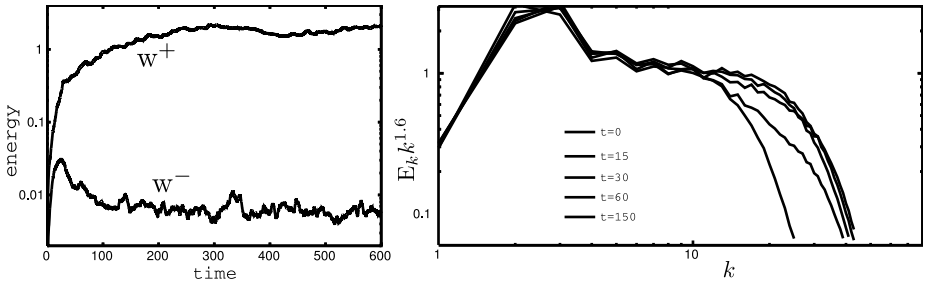

Figure 4.5: Left: energy relaxation toward stationary state for $\epsilon^+/\epsilon^- = 12$. Right: spectrum relaxation toward stationary state. The resolution of the experiment was increased from 128^3 to 256^3. Only the spectrum of the dominant wave is shown. The lines corresponds to $t = 15, 30, 60, 150$. Reproduced from [33] with permission of AAS.

As high imbalanced simulations proved to be so computationally expensive, we made a second experiment, which was to take the initial state that was already stationary and to increase the numerical resolution, which allows the spectrum to extend to larger wavenumbers. Note, that our forcing, although stochastic, was predetermined for each particular simulation and did not depend on numerical resolution. Now the question was how fast the spectra will relax to their stationary states. It turned out that the spectrum of the subdominant wave relaxed almost instantly, in a one dynamical time, which is consistent with BL08, while for the dominant wave the relaxation time was long. Note the dynamic (kinetic) timescale l/v for this region of k-space for the strong wave was rather small, around 0.3. The relaxation process is shown on Figure 4.5. It took $\delta t \approx 60$ to get reasonably close to the stationary state. We considered

5 Time was measured in Alfvénic units, but the size of the box was 2π, thus 2π was the time for an eddy to cross the box. The time for the largest turbulent eddy to cross itself, and also the largest eddy dynamical time (L/v) was around unity, because the size of the largest eddy was a fraction of around 0.2 or 0.3 of the cube size (see Figures 4.8 and 4.9).

this experiment a success and used the technique of increasing resolution to save computational time.

We also studied long-term evolution of nearly-balanced case when we allowed the low-resolution version of A3 to evolve for 500 time units. We did not notice any long-term trends either in the three-dimensional spectrum or in any other quantities during this run.

4.2.2 Parallel structure function

Unlike perpendicular structure function which is largely insensitive to the direction of the local field, the definition of the local field strongly affect the parallel structure function, which, in turn, determines the shape of the turbulent eddy. Since the latter is the major object of study in this section, we feel that the proper explanation of this point is due.

The simplest way to define parallel structure function, $\mathrm{SF}_\parallel$, is to take samples along the *global mean field*. This definition is, however, fairly bad, as it does not take into account field wandering. We expect $\mathrm{SF}_\parallel$, defined in such way, along with perpendicular structure function to reflect the anisotropy in the *global frame*, which, by the effects of field wandering, as we argued in Chapter 3, will be similar to the outer scale anisotropy. Therefore, such definition will effectively erase *scale-dependent anisotropy* which is the property of GS95-type models.

Another way is to define local magnetic field by averaging over some scale λ. In this way, the parallel structure function become a function of two scales, such as

$$\mathrm{SF}_\parallel^2(w^\pm, \Lambda, \lambda) = \left\langle \left(w^\pm(\mathbf{r} - \Lambda \mathbf{b}_\lambda / b_\lambda) - w^\pm(\mathbf{r})\right)^2 \right\rangle_{\mathbf{r}},$$

where $\mathbf{b}_\lambda$ is the magnetic field averaged over scale λ. We use Gaussian averaging defined as $\mathbf{b}_\lambda = 1/\lambda\sqrt{2\pi} \int \mathbf{b}(\mathbf{r} - \mathbf{R}) \exp(-R^2/2\lambda^2)\, d\mathbf{R}$. In order to reduce such a SF to a function of only Λ one can introduce a dependence between Λ and λ, and plug in the $\lambda = f(\Lambda)$ in the above equation. This definition of $\mathrm{SF}_\parallel$ will be a *model-dependent* though,

$$\mathrm{SF}_{\parallel\mathrm{model}}^2(w^\pm, \Lambda) = \mathrm{SF}_\parallel^2(w^\pm, \Lambda, f(\Lambda)).$$

For the balanced turbulence, the anisotropy was measured to be close to the one predicted by GS95, i. e., $\Lambda \sim \lambda^{2/3}$. One can, therefore, introduce a *reasonable* model-dependent $\mathrm{SF}_\parallel$ as taking $f(x) = \mathrm{const} \cdot x^{3/2}$, where the constant depend on the outer scale of the simulation. As we show below, this definition is almost perfect for balanced turbulence, but the question is whether it does equally well for the imbalanced case.

Let us consider some *model-independent* ways to determine $\mathrm{SF}_\parallel$. Apparently, the first definition using global field is model-independent, but fairly bad, it correspond

to taking averaging $\lambda = \infty$. One can also take $\lambda = 0$, i. e., always use local field without any averaging. An interesting model-independent method was used in [303], where two points were chosen to lie on the same magnetic field line. The distance Λ was also calculated along the line.

When we look for anisotropy, we normally want to obtain lower values of $\mathrm{SF}_\parallel$. According to the eddy ansatz, outlined in Section 4.1, we receive *lower* values of $|\mathbf{w}^\pm(\mathbf{r} - \Lambda\mathbf{n}(\mathbf{r})) - \mathbf{w}^\pm(\mathbf{r})|$, where $\mathbf{n}$ is a unit vector along the eddy. Therefore, the averaging of the field that provides *minimum* values of $\mathrm{SF}_\parallel$ approximates the direction of the eddy alignment better, provided that there is a connection between the field direction and eddy alignment (if there is no such connection, there will be no dependence on the averaging scale λ).

So, another model independent way to define $\mathrm{SF}_\parallel$ will be

$$\mathrm{SF}^2_{\parallel\min}(w^\pm, \Lambda) = \min_\lambda \mathrm{SF}^2_\parallel(w^\pm, \Lambda, \lambda).$$

This definition not only provides us with the value of $\mathrm{SF}_\parallel$, but, giving λ at which minimum is achieved, gives us a hint to how eddies are aligned with respect to the magnetic field.

Figure 4.6 shows a comparison between different methods to calculate parallel SF. We plotted them relative to $\mathrm{SF}^2_{\parallel\min}$. In the balanced case, the three methods, "minimal", "following the field line" and "model-dependent" work very well, while the "global field" method does not work. The latter confirms that turbulent eddies are aligned with respect to local field, not the global field (Cho and Vishniac (2000)). In the imbalanced case, the situation is more complicated. For the weak component, all three "good" methods work very well, while for the strong wave there is a systematic error for all methods, except "minimal." This is due to the fact that in the imbalanced turbulence the strong component (w^+) eddies are aligned with respect to much larger scales of the magnetic field (see Section 4.2). Since most magnetic field perturbation is provided by the strong wave, it follows that the strong field eddies are aligned with their own field on a larger scale. This directly confirms the prediction of BL08 model. On the bottom panel of Figure 4.6 the "field line" method gives values that are smaller than "minimal" method. This is due to the fact that in the field line method we measured the distance along magnetic field, and the physical distance was actually shorter, this allowed for smaller than $\mathrm{SF}^2_{\parallel\min}$ values on the outer scale where the difference between straight-line distance and along-the-field-line distance is significant.

It turns out (Figure 4.7) that the averaging scale at which minimum of parallel structure is reached for weak wave approximately corresponded to its anisotropy, which is consistent with strong cascading hypothesis. But for a strong wave, this averaging scale is *larger* than the perpendicular scale dictated by anisotropy. In other words, the eddies of the strong wave are aligned with respect to the magnetic field which is averaged on *larger scale* than the eddy's own perpendicular scale. This is consistent with the BL08 model.

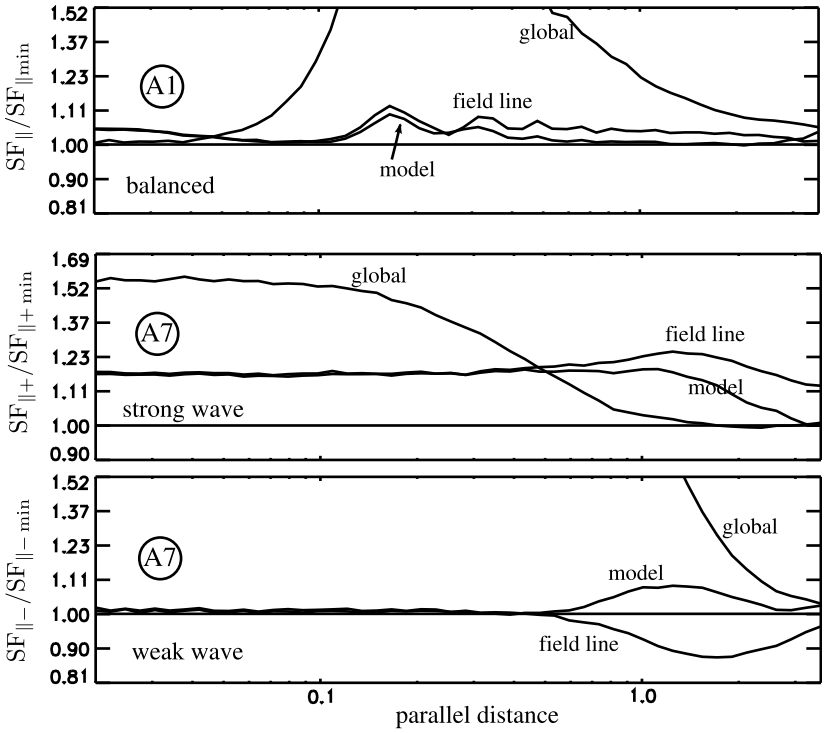

Figure 4.6: The ratio between parallel SFs calculated with different definition of the local field. Upper plot is for balanced simulation, while two lower plots are for strongly imbalanced simulation. The reference SF is "minimum" one described in the text. The dotted line is "model-dependent" SF, dashed line is for "following a field line" method, and the dotted-dashed line is for constant global mean field. Reproduced from [33] with permission of AAS.

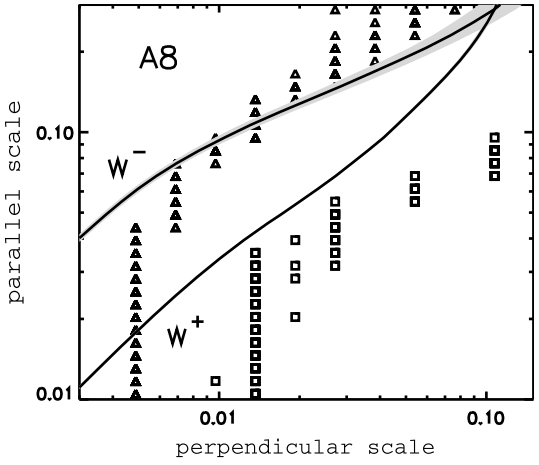

Figure 4.7: This plot shows values of λ_{avr} at which the minimum of the parallel structure function is reached. Triangles show perpendicular scales λ_{avr} at which the minimum of $SF^2_{\parallel}(w^-, \Lambda)$ is reached, while squares show perpendicular averaging scales at which the minimum of $SF^2_{\parallel}(w^+, \Lambda)$ is reached. Solid and dotted lines indicate w^+ and w^- eddies' anisotropy which are defined in Section 4.2.2 and presented in Figure 4.12. Reproduced from [33] with permission of AAS.

4.2.3 Spectra and anisotropies

We calculated two-dimensional (depending on parallel and perpendicular distances) second-order structure functions with respect to the local field using "model dependent" definition of the local field from previous section. Although this method slightly underestimates anisotropy, according to Figure 4.6, it works fairly well. The structure functions were calculated using all available "stationary state" datacubes, i. e., were averaged over time. The contours of these SFs for balanced simulations A1 and A2 are presented in Figure 4.8 and for imbalanced simulation A7 in Figure 4.9. Figure 4.8

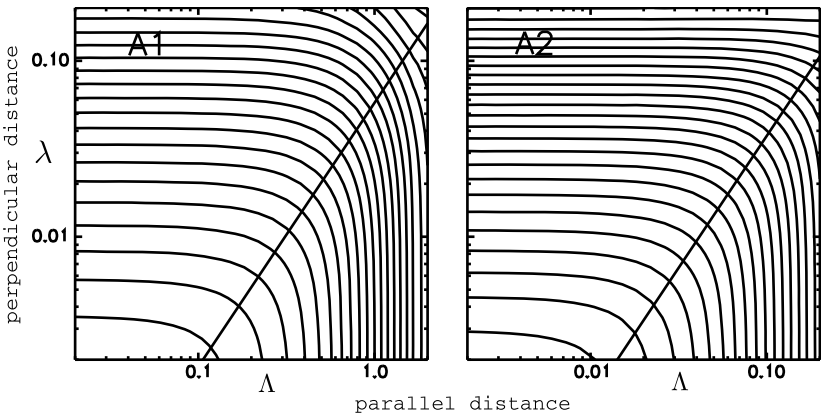

Figure 4.8: Comparison of the SFs from trans-Alfvénic (left) and sub-Alfvénic (right) balanced simulations. Note the difference in the x axis between two plots which indicates that A1 is approximately 10 times more anisotropic. Contours indicate SF levels, solid line is a demonstration of GS95 $\Lambda \sim \lambda^{2/3}$ law. Reproduced from [33] with permission of AAS.

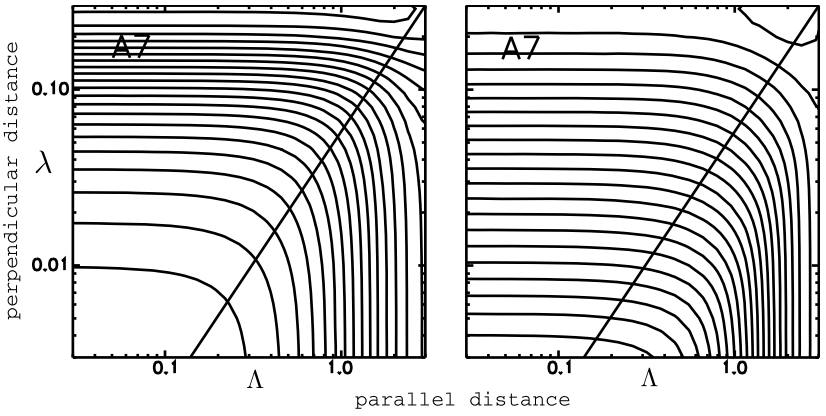

Figure 4.9: Comparison of the SFs from dominant (left) and subdominant (right) Alfvénic waves from $\epsilon^+/\epsilon^- = 16$ imbalanced simulations. The anisotropies of components are notably different. The solid line is the GS95 $\Lambda \sim \lambda^{2/3}$ law. Reproduced from [33] with permission of AAS.

shows SFs for total energy, i. e., it is summed over w^+ and w^-. These figures basically validate our assumptions from Section 4.2 regarding physical and computational dimensions of the box. We see that, according to expectations, trans-Alfvénic A2 is almost isotropic on the outer scale but becomes progressively anisotropic toward small scales, while, as we expected, sub-Alfvénic A1 has approximately 10:1 anisotropy on outer scale, and increases toward small scales. If we decrease anisotropy of A1 by a factor of 10 by rescaling the x-axis, we almost reproduce A2, the difference is mostly being on the outer scale (this difference is easier to see in Figure 4.11). Figure 4.9 shows SFs for two separate components w^+ and w^- in the strongly imbalanced case of A7. The anisotropy on outer scale is approximately 10:1 for both components, which validates our choice of computational box. This anisotropy increases toward small scale, but in a different fashion for each component. We see the anisotropy of strong wave is almost 5 times smaller on dissipation scales.

Figure 4.10 shows the so-called three-dimensional angle-summed spectra for both components in all simulations. These spectra are obtained by summation of spectra over solid angle for all wavevectors with the same magnitude k. It can be related to three-dimensional angle-averaged spectra by dividing by k^2. In the sub-Alfvénic cases A1, A3, A5, and A7, this spectrum is almost identical to the so-called perpendicular spectrum, which takes into account only structures perpendicular to the magnetic field and is the main target of prediction of the GS95 model. As they are almost identical, we did not have to plot perpendicular spectrum separately. Another definition of spectrum which depend only on the magnitude of the wavevector is the so-called one-dimensional spectrum (see, e. g., [324]). This spectrum is less sensitive to the bottleneck effect. We refer to [32] for a more thorough comparison between one-dimensional and 3D spectra and discussion on bottleneck effect.

In Figure 4.10, the two bottom plots have relatively large variation (gray areas) on the end of the w^+ spectra. This is due to the fact that in A7 and A8 we barely reached stationary state (for more discussion, see Figure 4.5 and Section 4.2.1) in the high-resolution run.

Figure 4.10 shows spectral slopes between –1.12 and –1.93 with balanced simulations having slopes as flat as –1.37.[6] The GS95 prediction is Kolmogorov's $-5/3 \approx -1.67$, while Boldyrev 2006 prediction is –1.5. The flat slopes observed in real data are most certainly due to rather strong bottleneck effect seen in simulations with hyperviscosity. In the imbalanced case, the predictions are following: LGS07 predicts –1.67 slopes for all 8 cases; C08 predicts –1.67 for balanced cases A1 and A2, A5–A8 are outside of the applicability of his model, A3 and A4 must show very different slopes-approximately –1 for weak component and –3 for strong component, also C08 predicts

6 The slopes for one-dimensional spectra are steeper, with a balanced slope of –1.45 and the most imbalanced slopes –1.97 for strong wave and –1.22 for a weak wave.

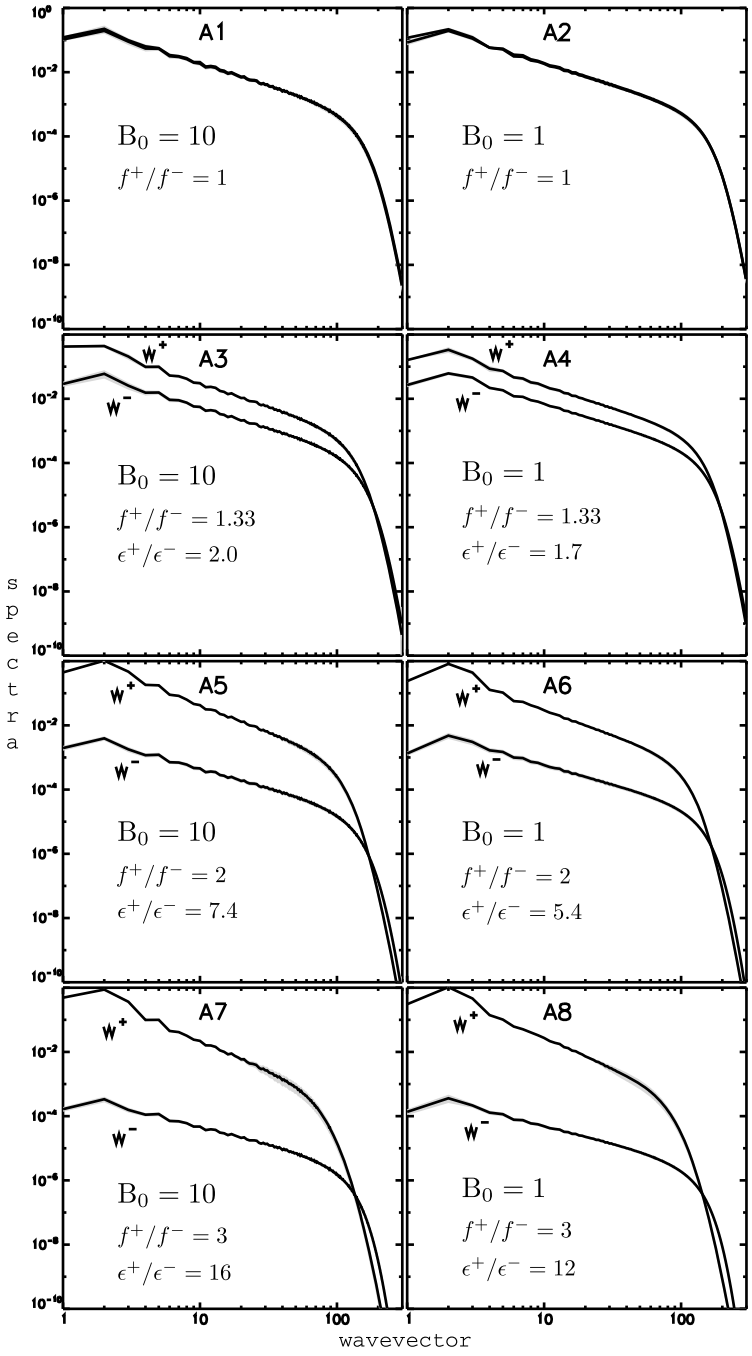

Figure 4.10: Spectra for all data, gray shows mean-square fluctuations in time. Reproduced from [33] with permission of AAS.

pinning on dissipation scales, i. e., spectra should converge on dissipation scale.[7] The ratios of the total energies (see Table 4.1) are predicted as following: C08 – A5–A8 are outside of applicability of his model, A3 and A4 should have a very large imbalance $(w^+)^2/(w^-)^2$ of at least a 1000, while 4–6 is actually observed; LGS07 predicted/observed – A3: 4/5.5, A4: 3/3.9, A5: 55/145, A6: 30/90, A7: 260/1150, A8: 144/1100. We see that in this respect deviations from LSG07 predictions are small for small imbalances but fairly large for large imbalances. BL08 argues that if one drives turbulence with the same anisotropy on outer scale (as in these simulations) the anisotropies of the components will diverge toward small scales, and this solution will not be self-similar (and not power-law). However, BL08 makes predictions regarding *local* slopes even in this case. This can be seen from (1), which is a classic critical balance between weak wave anisotropy and strong wave amplitude and (4), which is strong cascading of the weak wave. We do not expect relations between slopes based on (4) to hold, because it is strongly influenced by bottleneck effect (BL08 also predicts –1.67 slopes for balanced case). However, there is some dependence between energy slope and anisotropy slope, similar to what BL08 predicts. Namely, it follows from (1) that shallower anisotropy slope for w^- means steeper spectral slope for w^+, which is observed. Also, from (4), steeper spectral slope for w^+ also means shallower spectral slope for w^-, which is also observed.

The anisotropy was measured in the following manner. First, the parallel and perpendicular second-order structure functions were calculated, then we found equal values of parallel and perpendicular SFs and in this way the mapping or function between independent variables, parallel or perpendicular scales were created. This function is plotted on Figures 4.11, 4.12 with shades of gray indicating RMS fluctuations in time. This definition of $\Lambda(\lambda)$ mapping can be understood from two-dimensional plot of SF, e. g., Figure 4.8, when one follows a contour of SF and finds which parallel scale corresponds to a particular perpendicular scale. We see that for the imbalanced case anisotropy curves have different slopes and diverge from outer scale where they are equal (this is dictated by driving) to smaller scales where they are different.

We devoted Section 4.2.2 to the discussion of the measurements of the parallel structure function, which was used in the above definition of the anisotropy curves. Although it might appear that each and every definition produce a different anisotropy curve, the major difference is between global and local definition of the field direction, while all local methods ("field line," "model-dependent," and "minimal"), also dubbed "good" in Section 4.2, give very similar results. In fact, these is no perceivable qualitative difference between anisotropy curves obtained by either local methods. This could be explained by Figure 4.6 middle and bottom panels where the quantita-

7 LGS07 does not discuss transition to viscous scales, but as a model of local cascading, it must have pinning on viscous scale. The pinning, however, is impossible within the framework of LGS07, as the latter predicts $w^+/w^- = \epsilon^+/\epsilon^-$.

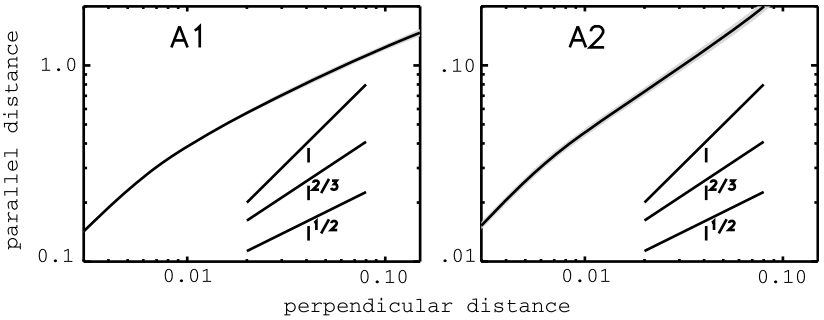

Figure 4.11: Anisotropies for balanced simulations. Reproduced from [33] with permission of AAS.

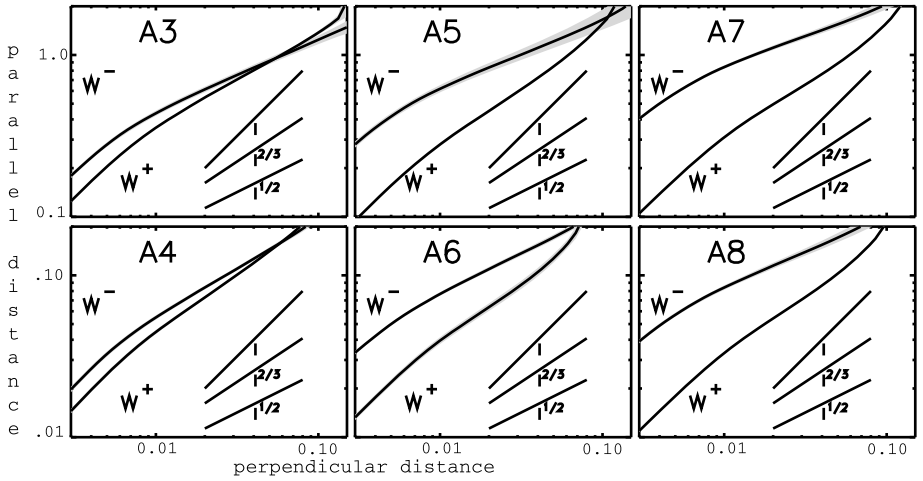

Figure 4.12: Anisotropies for imbalanced simulations. The mapping of $\Lambda(\lambda)$ is explained in Section 4.2.2. The difference in anisotropy between w^+ and w^- increases with increasing imbalance. Reproduced from [33] with permission of AAS.

tive differences between methods are small, but on the other hand, the dependence of $\mathrm{SF}_\parallel$ on scale is strong ($\sim l_\parallel$). Also, in the middle panel, the difference is mostly by a constant, which will only give a slight shift of the anisotropy plot. All in all, the claim that anisotropy curves will diverge by a factor of 3 to 4 in strongly imbalanced simulations stay true regardless of the "local" method used. We rejected the "global field" method as it does not reveal scale dependent anisotropy—a groundbase of the GS95 model. It is worth noting that LGS07, C08, and BL08 use GS95 as a basis and smoothly transit to GS95 in the balanced limit. There is a wealth of theoretical arguments why the SFs have to be measured with respect to the local field ([92, 303], etc.). We also would like to note that aside from driven simulations described in this section we also

observed a significant difference in w^+ and w^- anisotropies in a *decaying* imbalanced simulations.

C08 and LGS07 both predict identical GS95 anisotropy for both modes, which is inconsistent with simulations. BL08 predicts diverging anisotropy, most notably, with a stronger wave having smaller anisotropy, which is consistent with simulations. The value of the differences, however, do not reach the asymptotic value of ϵ^+/ϵ^- which may be attributed to the short inertial range.

4.2.4 Comparison with models

Numerics can only tentatively confirm a model, however, numerics is able to reject some models if the numerical quantity is robust, e. g., does not depend that much on Re. Although a theory can make a wide variety of predictions, only few of those can be effectively addressed by numerics. One of the quantities that is notoriously hard to measure in DNS is the spectral slope of turbulence. A difference between the $-3/2$ slope and $-5/3$ can be masked by a variety of effects such as bottleneck effect, driving, and so on. In contrast, the quantities such as Kolmogorov constant are fairly easy to obtain and quickly converge with increasing resolution. In fact, modest resolutions such as 128^3 give reasonably precise estimates of this constant. This is due to the fact that the *total energy* and the *total dissipation rate* are easy to measure, to get a statistical average, and also are free of uncertainties of interpretation. What sort of models can be judged on the basis of these quantities? Such are the models of *local cascading* where the cascade rate depends only on the characteristic quantities of, say, $w_l^\pm$ on a particular scale l (and, possibly, weakly depend on the spectral slope). In this case, numerics only have to reproduce a one or two steps of such cascading to obtain a reasonable dissipation rate based on a particular total energy. In this sense, our testing does fairly well, as we mostly consider models of local cascading (LGS07, C08, PB09, [359]), and at the same time, with 768^3 numerical resolution we reproduce five to six binary steps in k-space.

Our numerical data strongly contradict to three models of imbalanced turbulence, namely LGS07, C08, and PB09. In particular, two of these models, C08 and PB09, show gross inconsistencies between observed and predicted energy ratios versus dissipation ratios. Indeed, C08 must have a huge energy ratio (of around a 1000) in simulations with ϵ^+/ϵ^- close to two (A3 and A4), while a modest ratios of 4 and 6 are observed. PB09 does extremely bad in cases with large imbalances. A7 and A8 have energy ratios of around a 1000, while predicted quantities are 16 and 12. LGS07 does a much better job on energy ratios, but still fails the A7 and A8 (large imbalance) tests; see Figure 4.13.

Furthermore, LGS07 and C08 have predictions regarding eddy anisotropies. Both of these models predict equal anisotropies for w^+ and w^- while different anisotropies are observed. Aside from these inconsistencies, we also note that C08 predicts pinning

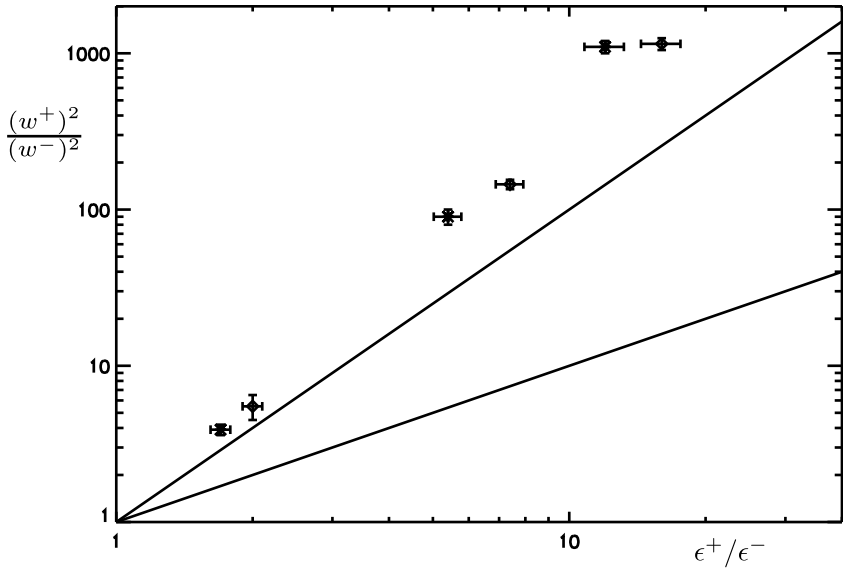

Figure 4.13: Total energy ratio versus dissipation rate ratio (see also Table 4.1). Diamonds: sub-Alvénic simulations, stars: trans-Alvénic simulations, solid line: LGS07 prediction, dashed line: PB09 prediction. There is no simple formula for the C08 model, but the energy ratio is expected to become very large when the dissipation rate ratio approaches the critical value of around two. Reproduced from [33] with permission of AAS.

at the dissipation scale, which is not observed. C08 also predicts that the strong wave has to have steeper spectral slope than the weak wave. This corresponds to numerics qualitatively, but not quantitatively, indeed, according to C08; A3 and A4 must have a huge slope difference of around 2, while the real difference is around 0.12.

Although it is harder to confirm a model rather than to reject a model by direct numerical simulations, we see that there is a qualitative agreement between BL08 and numerics. Most of the features predicted by BL08 are observed in simulations, namely (a) the anisotropies of the waves are different and strong wave anisotropy is smaller, (b) while the weak wave eddies are aligned with respect to the local field on the same scale as the eddy, the strong wave eddies are aligned with respect to a larger-scale field (Figure 4.7), (c) the energy imbalance is higher than in the case when both waves are cascaded strongly (Table 4.1), which suggest that the strong wave is cascaded weakly, (d) the dissipation scales for the weak and the strong waves are different, namely the inertial range for weak wave is longer (Figure 4.10), which is what predicted by BL08, and (e) there is no "pinning" at the dissipation scale, which suggests nonlocal cascading.

We note that there is no quantitative agreement between the difference in anisotropies in the "asymptotic power-law solutions" of BL08 and simulations (cf. Section 4.2 and Figure 4.12). This is probably due to the fact that asymptotic power-law solutions have not been established within our inertial range.

4.3 Empirical study in reduced MHD simulations with energy-controlled driving

Table 4.2 summarizes our reduced MHD simulations with imbalanced driving. In these simulations, we kept energy injection rate constant. All experiments were evolved to stationary state. We started our high-resolution simulations with earlier lower-resolution runs that were evolved for a long time, typically hundreds of Alfvénic times and reached stationary state. The imbalanced runs were evolved for longer times, up to 40 dynamical times, due to longer cascading timescales for the stronger component.

Table 4.2: Three-dimensional RMHD imbalanced simulations.

Run	Resolution	f	Dissipation	ϵ^+/ϵ^-	$(w^+)^2/(w^-)^2$
I1	$512 \cdot 1024^2$	$w^\pm$	$-1.9 \cdot 10^{-4} k^2$	1.187	1.35 ± 0.04
I2	768^3	$w^\pm$	$-6.8 \cdot 10^{-14} k^6$	1.187	1.42 ± 0.04
I3	$512 \cdot 1024^2$	$w^\pm$	$-1.9 \cdot 10^{-4} k^2$	1.412	1.88 ± 0.04
I4	768^3	$w^\pm$	$-6.8 \cdot 10^{-14} k^6$	1.412	1.98 ± 0.03
I5	$1024 \cdot 1536^2$	$w^\pm$	$-1.5 \cdot 10^{-15} k^6$	2	5.57 ± 0.08
I6	$1024 \cdot 1536^2$	$w^\pm$	$-1.5 \cdot 10^{-15} k^6$	4.5	45.2 ± 1.5

4.3.1 Nonlinear cascading and dissipation rate

Compared to spectral slopes, dissipation rates are robust quantities that require much smaller dynamical range and resolution to converge. Figure 4.14 shows energy imbalance $(w^+)^2/(w^-)^2$ versus dissipation rate imbalance ϵ^+/ϵ^- for simulations I2, I4, I5, and I6. We also use two data points from our earlier simulations with large imbalances, A7 and A5 from Section 4.2. I1 and I3 are simulations with normal viscosity similar to I2 and I4. They show slightly less energy imbalances than I2 and I4. We see that most data points are above the prediction of LGS07, which is consistent with BL08. In other words, numerics strongly suggest that

$$\frac{(w^+)^2}{(w^-)^2} \geq \left(\frac{\epsilon^+}{\epsilon^-}\right)^2. \tag{4.7}$$

Although there is a tentative correspondence between LGS07 and the data for small degrees of imbalance, the deviations for large imbalances are significant. The important lesson, however, that in the case of small imbalances the cascading smoothly transition to the balanced case, i. e., the prediction of GS95 model. This is an important verification that the exactly balanced case is not a special case, in a sense.

In the case of strong imbalance, it suggests that the strong component cascading rate is smaller than what is expected from strong cascading. As to the PB09 prediction, it is inconsistent with data for all degrees of imbalance including those with small imbalance and normal viscosity, i. e., I1 and I3.

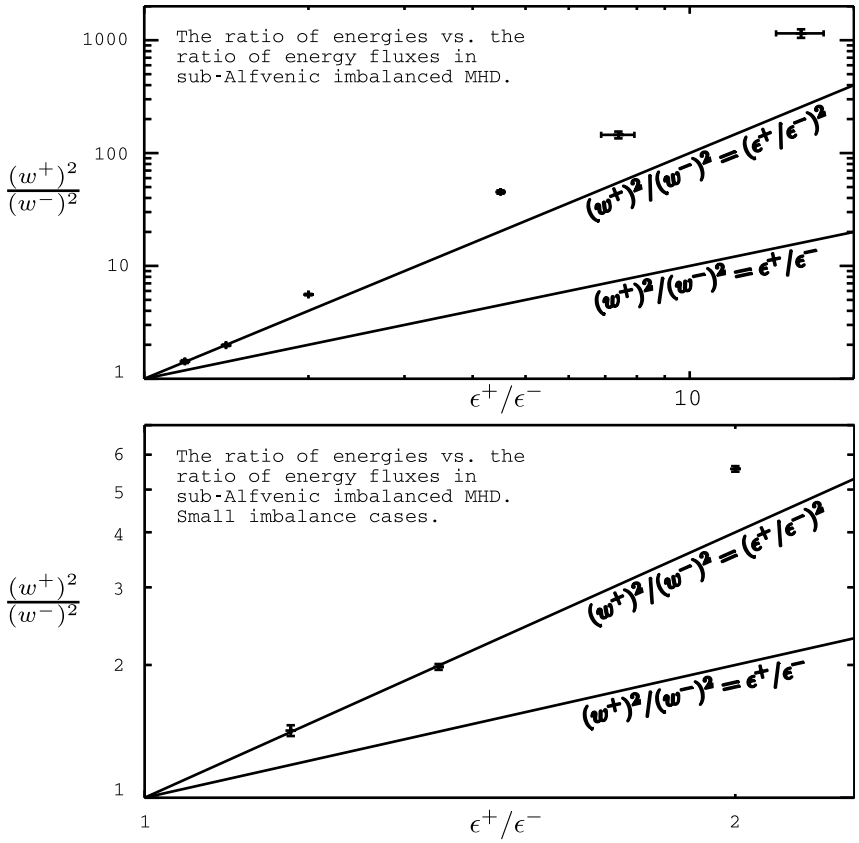

Figure 4.14: Energy imbalances versus dissipation rate imbalance. Lower panel shows a magnified portion of the upper panel. Solid line: LGS07 prediction, dashed line: a formula from PB09, this also is a prediction for purely viscous dissipation. The point indicates measurements from simulations, where error bars indicate fluctuation in time. I1 and I3 are simulations with normal viscosity, which have a slightly lower energy imbalance than I2 and I4. This is an indication that in these simulations viscosity was affecting outer scales. Two high imbalance points are taken from [33]. For a fixed dissipation ratio, the energy imbalance has a tendency to only *increase* with resolution. Reproduced from [34] with permission of AAS.

4.3.2 Imbalanced spectra

Figure 4.15 shows spectra from low-imbalance simulation I2, compensated by the predictions of PB09 and LGS07. We see that the collapse of two curves for w^+ and w^- is much better for the LGS07 model; the perceived deviation of spectral slope from $-5/3$ as we discussed extensively in Chapter 3.

Figure 4.16 shows spectra from all I1-6 simulations, compensated by the prediction of LGS07. For lower imbalances, the collapse is reasonably good and becomes progressively worse for larger imbalances. This deviation, however, does not fully follow the prediction of the asymptotic power-law solutions from BL08, which will predict that

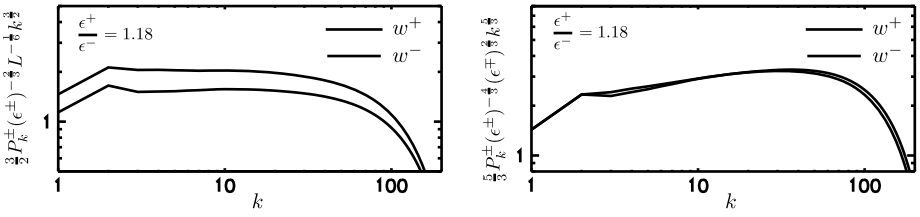

Figure 4.15: Energy spectra for w^+ (solid) and w^- (dashed) from simulation I2, compensated by factors that correspond to PB09 (left) and LGS07 (right). For this low-imbalanced case, spectra are consistent with LGS07 but grossly inconsistent with PB09. From [36].

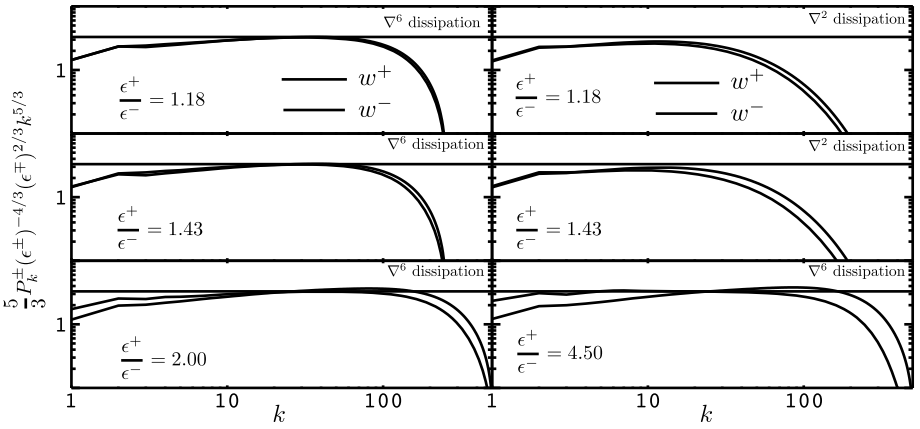

Figure 4.16: Energy spectra for w^+ (solid) and w^- (dashed) for simulations I1–I6, compensated by factors that correspond to LGS07. The thin solid line corresponds to Kolmogorov constant for Alfvénic turbulence $C_{KA} = 3.27$. The factor 5/3 is introduced due to the difference between P_k and E_k. From [36].

the solid curve will go above C_{KA} and the dashed curve—below it. This is possibly explained by the fact that asymptotic power law solutions were not reached in these limited resolution experiments; this is also observed for anisotropies which we consider in the next section.

4.3.3 Imbalanced anisotropies

We measured parallel and perpendicular structure functions in simulations I1–I6 in order to quantify anisotropies of eddies. The perpendicular structure function was defined in a conventional way. In the RMHD case which physically corresponds to the case of infinitely strong mean field, the perpendicular structure function is calculated with respect to this mean field. The same does not hold true for the parallel

structure function. Indeed, measuring parallel SF with respect to the global field will destroy scale-dependent anisotropy, even in the case of a very strong field. If we have $\delta B_L/B_0 \ll 1$, the field line wandering will be of the order of $B_0/\delta B_L$, while the GS95 anisotropy on the scale l will be much higher, $\sim B_0/\delta B_l$, by a factor of B_L/B_l. The direction of the mean field will deviate from the direction of the local field by the angle, which is much larger than the angle of GS95 anisotropy. This will result in an incorrect estimation of the parallel structure function, which will be contaminated by contribution from perpendicular direction.

For the parallel structure function, we will use the model-independent method suggested Section 4.2 or "minimum method." It turns out that this method gives very close results to the previously suggested methods of choosing the local mean field, most prominently in the balanced case. We choose this method as it does not contain any arbitrary assumptions as previous methods.

As long as we know, both parallel and perpendicular structure functions, the mapping $\Lambda(\lambda)$ is obtained from the equation $\mathrm{SF}^2_\parallel(w^\pm, \Lambda) = \mathrm{SF}^2_\perp(w^\pm, \lambda)$. Physically, this correspond to measurement of the parallel eddy size Λ, whose energy is concentrated on scales λ.

Figure 4.17 shows anisotropies for I1–6 simulations. All simulations were driven by the same anisotropies on the outer scale, which is unfavorable for obtaining the asymptotic power law solutions of BL08, which have an anisotropy ratio which is con-

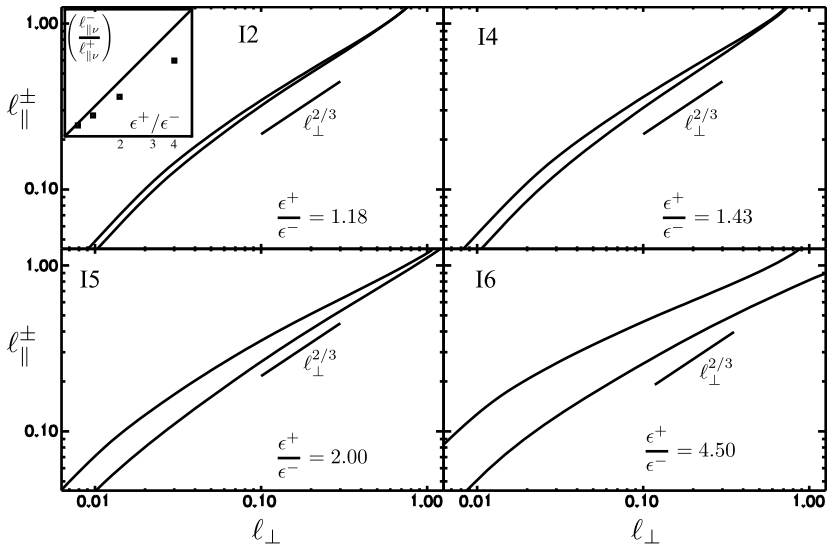

Figure 4.17: Anisotropies for w^+ (solid) and w^- (dashed), simulations I1–I6. The relation between parallel scale Λ and perpendicular scale λ is obtained by second-order structure functions, as explained in the text. The small upper inset shows the ratio of anisotropies on smallest scales versus the prediction of BL08 for the asymptotic power-law solution, which is ϵ^+/ϵ^-. From [36].

stant through scales and equal to ϵ^+/ϵ^-. It is, however, favorable to the LGS07 model, which predicts the same w^+ and w^- anisotropies for all scales. Therefore, these simulations are a sensitive test between LGS07 and BL08 models, both of which are roughly consistent in terms of energy ratios and spectra for small imbalances. If LGS07 was true, starting with the same anisotropies on outer scale, this should be preserved by the cascade on smaller scales, but this is not what is observed in Figure 4.17, where anisotropies start to diverge on smaller scales. The ratio of anisotropies is roughly consistent with BL08 asymptotic power-law solutions for small imbalances and falls short for larger imbalances. This is explained by the fact that it is harder to get to the asymptotic power-law solutions for larger imbalances, as was also observed for the case of power spectra. Our overall conclusion is that the anisotropy test is the experimentum crucis to differentiate between LGS07 and BL08 and based on Figure 4.17 this experiment clearly favors BL08.

5 Compressibility in MHD turbulence

Our discussion so far was centered at the incompressible MHD turbulence. Real astrophysical fluids are compressible. This poses a question to what extend our earlier description survives in realistic set ups and what additional properties are gained by compressible MHD turbulence. Historically, astrophysicists usually considered theories of incompressible turbulence to be something very academic and not relevant. We will show that there is a deep connection between the compressible and incompressible MHD turbulence.

Kolmogorov turbulence is applicable to realistically compressible nonmagnetized fluids, e. g., to turbulence in the Earth's atmosphere. Therefore, one should expect that some properties of GS95 model should be relevant at least for low Mach number magnetic turbulence. At the same time, additional compressible modes are excited in MHD in the presence of compressibility. In particular, while MHD turbulence in the incompressible limit can be decomposed into Alfvén and pseudo-Alfvén modes, in the case of compressible MHD turbulence, three modes, namely, Alfvén, slow and fast are excited. The pseudo-Alfvén modes are a limiting case of the slow modes in a situation of vanishing compressibility, the fast modes are a new type of motion intrinsic for compressible media.[1]

5.1 Decomposition into fundamental modes

To study the fundamental modes one has to decompose turbulence into Alfven, slow and fast modes. The original procedure of decomposition of MHD simulations into different modes proposed by Cho and Lazarian ([81, 82] henceforth CL02, CL03, respectively) was elaborated further in Kowal & Lazarian [231] where wavelets rather than Fourier modes were used. Unlike earlier studies which dealt with small perturbations (see [116]) the aforementioned papers demonstrated the decomposition of the trans-Alfvénic turbulence, i. e., the turbulence with substantial amplitudes. Decomposition is performed in the Fourier space by a simple projection of the velocity Fourier components $\hat{\mathbf{u}}$ on the direction of the displacement vector for each mode (see Figure 5.1). The directions of the displacement vectors $\hat{\boldsymbol{\xi}}_s$, $\hat{\boldsymbol{\xi}}_f$, and $\hat{\boldsymbol{\xi}}_A$ corresponding to the slow mode, fast and Alfvén modes, respectively, are defined by the unit vectors,

$$\hat{\boldsymbol{\xi}}_s \propto (-1+\alpha-\sqrt{D})k_\parallel\hat{\mathbf{k}}_\parallel + (1+\alpha-\sqrt{D})k_\perp\hat{\mathbf{k}}_\perp, \tag{5.1}$$

$$\hat{\boldsymbol{\xi}}_f \propto (-1+\alpha+\sqrt{D})k_\parallel\hat{\mathbf{k}}_\parallel + (1+\alpha+\sqrt{D})k_\perp\hat{\mathbf{k}}_\perp, \tag{5.2}$$

$$\hat{\boldsymbol{\xi}}_A = -\hat{\boldsymbol{\varphi}} = \hat{\mathbf{k}}_\perp \times \hat{\mathbf{k}}_\parallel, \tag{5.3}$$

1 In the limiting case of zero compressibility, the fast modes are sound waves propagating with infinite velocities.

https://doi.org/10.1515/9783110263282-005

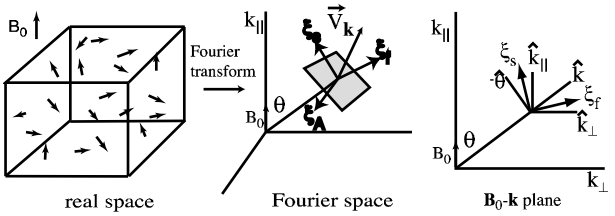

Figure 5.1: Schematic representation of the mode separation technique. The Alfvén, slow and fast modes are separated by the projection of the velocity Fourier component $\mathbf{v}_k$ on the bases $\hat{\boldsymbol{\xi}}_A$, $\hat{\boldsymbol{\xi}}_S$, and $\hat{\boldsymbol{\xi}}_f$ of the fundamental modes from CL03. Reproduced from Figure 1 from [82].

where $\mathbf{k}_\parallel$ and $\mathbf{k}_\perp$ are, respectively, the parallel and perpendicular to $\mathbf{B}_{\rm ext}$ components of wave vector; $D = (1+\alpha)^2 - 4\alpha\cos^2\theta$, $\alpha = a^2/V_A^2$. In addition, θ is the angle between $\mathbf{k}$ and $\mathbf{B}_{\rm ext}$, and $\hat{\boldsymbol{\varphi}}$ is the azimuthal basis in the spherical polar coordinate system. The Fourier components of each mode can be used to calculate spectra. To obtain other measures, such as structure functions, transforms back to the real space were used.

The results of CL02 and CL03 revealed important properties of compressible MHD turbulence. In particular, they revealed that GS95 scaling is valid for *Alfvén modes*:

$$\text{Alfvén: } E^A(k) \propto k^{-5/3}, \quad k_\parallel \propto k_\perp^{2/3}.$$

Slow modes also follow the GS95 model for both plasma pressure dominated media, i. e., high β, and mildly supersonic magnetic pressure dominated media, i. e., low β, cases:

$$\text{Slow:} \quad E^S(k) \propto k^{-5/3}, \quad k_\parallel \propto k_\perp^{2/3}.$$

For the highly supersonic low β case, the kinetic energy spectrum of slow modes becomes steeper, which is indicative of the formation of shocks.

Fast mode spectra were suggested in CL03 to be compatible with acoustic turbulence scaling relations:

$$\text{Fast:} \quad E^f(k) \propto k^{-3/2}, \quad \text{isotropic spectrum.}$$

Steeper spectrum $\sim k^{-2}$ was reported in [231] for fast modes with a different set of simulations obtained with a different code. Therefore, while the isotropy of the fast modes has been established, the exact value of the spectrum is still somewhat controversial. This calls for more research with higher resolution simulations.

For super-Alfvénic turbulence, the picture above is applicable at scales $l < l_A = LM_A^{-3}$. The scale l_A can be considered as the scale of the trans-Alfvenic turbulence injection.

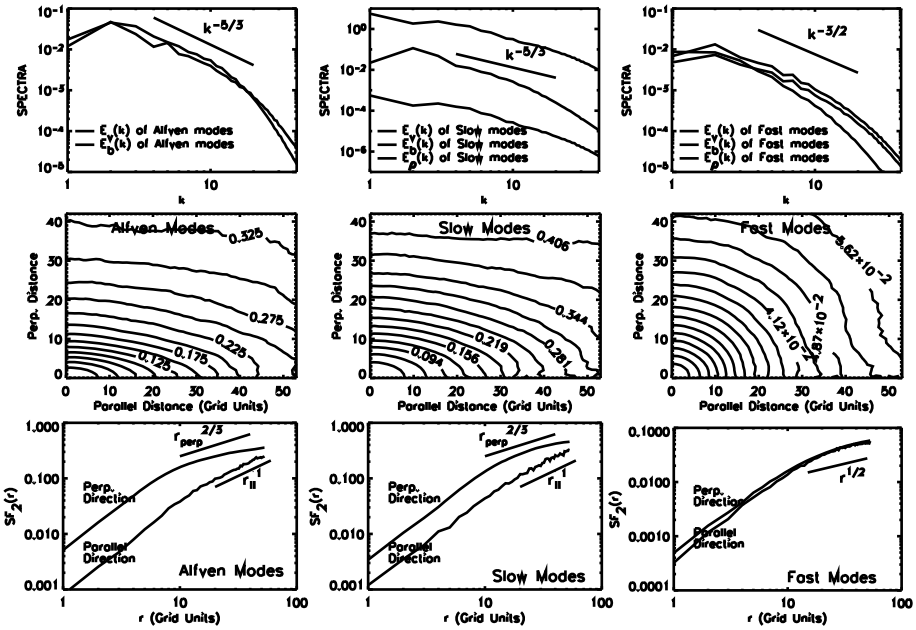

Figure 5.2: Highly supersonic low β ($\beta \sim 0.02$ and $M_s \sim 7$). $V_A \equiv B_0/\sqrt{4\pi\rho} = 1$. a (sound speed) $= 0.1$. $\delta V \sim 0.7$. Alfvén modes follow the GS95 scalings. Slow modes follow the GS95 anisotropy. Fast modes exhibit isotropy. Reproduced from Figure 3 from [82].

Figure 5.2 illustrates the fact that even in highly supersonic regime, the decomposition reveals a regular structure of MHD modes that corresponds to the expectation of the compressible extension of the GS95 theory. The customary claim that the modes in compressible MHD are completely blended and strongly interact is not right.

One can wonder whether the adopted statistical technique is reliable. That is, we separate each MHD mode with respect to the *mean* magnetic field $\mathbf{B}_0$. This procedure is affected by the wandering of large scale magnetic field lines, as well as density inhomogeneities. Nevertheless, CL03 demonstrated that the technique provided statistically correct results. For instance, in low β regime, the velocity of a slow mode is known to be nearly parallel to the *local* direction of magnetic field. Therefore, for low β plasmas, it is possible to obtain velocity statistics for slow modes in real space. To do this, one first should define the direction of the *local* mean magnetic field. Then the calculations of the second-order structure function for slow modes can be done: $\mathrm{vSF}_2(\mathbf{r}) = \langle |(\mathbf{v}(\mathbf{x}+\mathbf{r}) - \mathbf{v}(\mathbf{x})) \cdot \hat{\mathbf{B}}_l|^2 \rangle$, where $\hat{\mathbf{B}}_l$ is the unit vector along the *local* mean field.

Figure 5.3(a) presents the contours obtained by the method for the high sonic Mach number run. Figure 5.3(b) presents the result obtained the aforementioned way (dashed lines) and using the CL03 technique. A similar plot for the mildly supersonic case is presented in Figure 5.3(c).

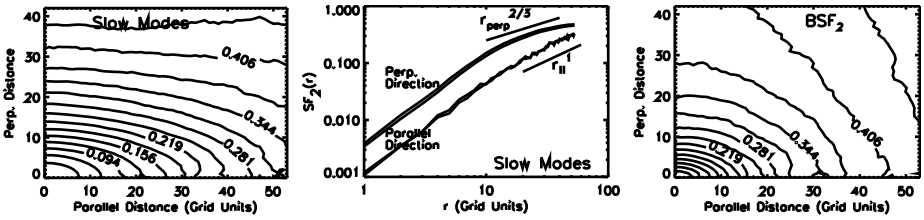

Figure 5.3: Comparison between Fourier space method and real space method of obtaining slow modes. (a) *left:* From real space calculation. $M_s \sim 7$. (b) *middle:* Solid: Fourier space. Dashed: real space. $M_s \sim 7$. (c) *right:* Similar plot for $M_s \sim 2.3$. From [232].

If the coupling between the modes were strong in MHD turbulence, one would not be able to talk about three different energy cascades. However, this is not true and one may wonder why the interactions are not strong.

A remarkable feature of the GS95 model is that Alfvén perturbations cascade to from one scale to a smaller one over just one wave period, while the other nonlinear interactions require more time. Therefore, one might expect that the nonlinear interactions with other types of waves only marginally affect Alfvénic cascade. Besides this, being incompressible, Alfvén modes do not depend on the sonic Mach number.

How much energy in compressible motions is drained from Alfvénic cascade is an important question the answer to which makes a lot of difference for various astrophysical problems. The question was discussed earlier for hydro turbulence. According to closure calculations [462], the energy in compressible modes in *hydrodynamic* turbulence scales as squared sonic Mach number, i. e., $\sim M_s^2$ if $M_s < 1$. CL03 extended this relation can be extended to MHD turbulence by using $\sim (\delta V)_A^2/(c_s^2 + V_A^2)$ instead of M_s^2. Note, that in the expression above the Alfven velocity is defined as $V_A \equiv B_0/\sqrt{4\pi\rho}$, where B_0 is the mean magnetic field strength. Since the Alfvén modes are anisotropic, CL03 introduced an additional factor. Indeed, it is known that the compressible modes are generated inside the so-called GS95 cone, which takes up $\sim (\delta V)_A/V_A$ of the wave vector space. The ratio of compressible to Alfvénic energy inside this cone is the ratio given above. If the fast modes are isotropic (see below), the diffusion or, "isotropization" of the fast wave energy in the wave vector space increase their energy by a factor $\sim V_A/(\delta V)_A$. This results in

$$\frac{\delta E_{\rm comp}}{\delta E_{\rm Alf}} \approx \frac{\delta V_A V_A}{V_A^2 + c_s^2}, \tag{5.4}$$

where $\delta E_{\rm comp}$ and $\delta E_{\rm Alf}$ are energy of compressible and Alfvén modes, respectively.

An important feature of Equation (5.4) suggests that the drain of energy from Alfvénic cascade is marginal when the amplitudes of perturbations are weak, i. e., $(\delta V)_A \ll V_A$. Numerical calculations in CL02 support these theoretical considerations. This justifies our treating modes separately. We note that a strongly entrenched claim that a strong coupling of incompressible and compressible motions is required

to explain simulations that show fast decay of MHD turbulence is wrong. Indeed, the incompressible motions decay themselves in just one Alfvén crossing time.

5.2 Other ways of decomposition into fundamental modes

Kowal and Lazarian (2010, [231] henceforth KL10) extended the CL03 decomposition into modes by introducing an additional step before the Fourier separation, in which we decompose each component of the velocity field into orthogonal wavelets using discrete wavelet transform:

$$\mathbf{U}(a, \mathbf{w}_{lmn}) = a^{-N/2} \sum_{\mathbf{x}_{ijk}} \psi\left(\frac{\mathbf{x}_{ijk} - \mathbf{w}_{lmn}}{a}\right) \mathbf{u}(\mathbf{x}_{ijk}) \Delta^N \mathbf{x}, \tag{5.5}$$

where $\mathbf{x}_{ijk}$ and $\mathbf{w}_{lnm}$ are N-dimensional position and translation vectors, respectively, while a is the scaling parameter. In addition, $\mathbf{u}(\mathbf{x}_{ijk})$ is the velocity vector field in the real space, $\mathbf{U}(\mathbf{x}_{ijk})$ is the velocity vector field in the wavelet space, and ψ is the orthogonal analyzing function called wavelet. The sum is taken over all position indices. KL10 uses the Daubechies wavelet as an analyzing function and fast discrete version of the wavelet transform and they obtained a finite number of wavelet coefficients. After the wavelet transform of the velocity, the Fourier representation of each wavelet coefficient was calculated. The separation into the MHD modes was performed in the Fourier space using the CL03 method and then iteration procedure for the Fourier coefficient was performed.

After KL06 obtained a Fourier representation of the Alfvén, slow and fast waves the final step was the inverse Fourier transform all wave components.

This more elaborate approach improves the original CL03 technique, namely, it allows for the local definition of the mean magnetic field and density used to calculate α and D coefficients. Due to the fact that the individual wavelets are defined locally both in the real and Fourier spaces, the averaging of the mean field and density is done only within the space of each wavelet. The utility of this approach is particularly obvious when the magnetic fluctuations are of high amplitude and, therefore, the direction of the local magnetic field varies significantly about the direction of the mean magnetic field.

The wavelet-based study in KL10 provided results consistent with that in CL03. For instance, Figure 5.4 shows the anisotropy for sub-Alfvénic turbulence which agrees well with that obtained in CL03.

Another way to decompose into modes using structure functions has been recently proposed and tested by one of the authors (AB). In this method, the separation vector $\vec{l}$ of the structure function plays the role of the wavenumber, because there is a correspondence relation between one-dimensional structure function along the certain line and the power spectrum along the same line. Figure 5.5 shows the contours of the structure function corresponding to each mode obtained in datacubes

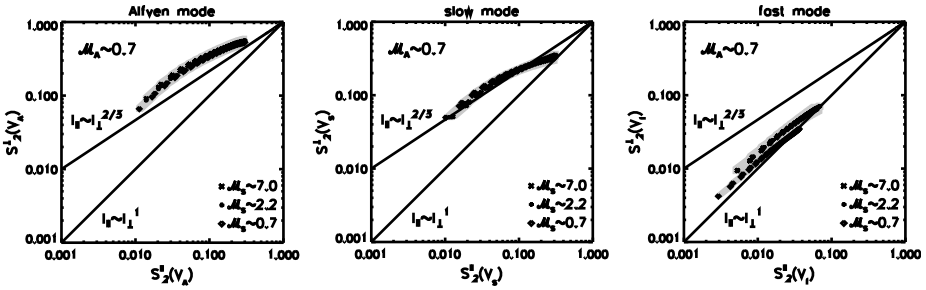

Figure 5.4: Anisotropies of the Alfvén, slow and fast modes. To depict the anisotropy the second-order total structure functions, parallel and perpendicular to the local mean magnetic field were used. Points correspond to the structure function data averaged over several snapshots. The gray areas under points correspond to the degree of variation of the structure functions in time from KL10. Reproduced from [231] with permission of AAS.

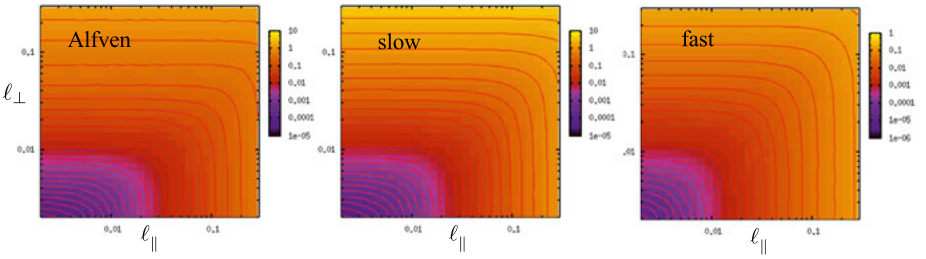

Figure 5.5: Anisotropy of the Alfvén, slow and fast modes as evidenced by the contours of the second-order structure function. Here, we used the new SF decomposition method. The Alfvén and slow mode exhibit scale-dependent anisotropy, while the fast mode is almost isotropic. From [36].

from $M_S = 10$ supersonic simulations used earlier in [37] (see also Section 5.4). The anisotropies of each mode show the same behavior as in the earlier discussed global decomposition method; see Figure 5.2. There are two advantages in using the new decomposition method. First, it is computationally efficient, as the structure functions can be calculated by the Monte-Carlo method, which samples only a fraction of data points. This way, the very high resolution simulations can be processed in a reasonable time. The second advantage is that the structure function is a local measurement, so we can measure spectral characteristics of the modes in a highly inhomogeneous situations. This method has been applied to the decomposition of MHD turbulence obtained in high-resolution cosmological simulation of a galaxy cluster [40]. The cluster environments has been notoriously difficult to analyze due to the strong dependence of all quantities on the distance to the center. The new method was used to calculate the SFs in concentric shells around the cluster center. Among other things, the aforementioned paper estimated the fraction of the fast mode to around 0.25, which is fairly high for subsonic to trans-sonic cluster environment. We hypothesized that

this is due to the way the cluster turbulence is driven—through mergers, which are essentially compressible trans-sonic motions.

5.3 Decomposition into solenoidal and potential modes

To distinguish compressible and incompressible motions, KL10 also used a different decomposition of the velocity field. Using the Hodge generalization of the Helmholtz theorem, one can split an arbitrary vector field $\mathbf{u}$ into three components:

$$\mathbf{u} = \mathbf{u}_p + \mathbf{u}_s + \mathbf{u}_l, \tag{5.6}$$

where components have the following properties:

a) The potential component ($\mathbf{u}_p$) that describes the compressible part of the velocity field is a curl-free component, i. e., $\nabla \times \mathbf{u}_p = 0$. It stems from a scalar potential ϕ:

$$\mathbf{u}_p = \nabla\phi. \tag{5.7}$$

The scalar potential ϕ is defined up to a arbitrary constant.

b) The solenoidal component ($\mathbf{u}_s$) that describes incompressible part of the velocity field is a divergence-free component, i. e., $\nabla \cdot \mathbf{u}_s = 0$. It stems from a vector potential $\mathcal{A}$:

$$\mathbf{u}_s = \nabla \times \mathcal{A}. \tag{5.8}$$

The vector potential $\mathcal{A}$ also defined up to a gradient of the field.

c) The third component is the Laplace one, i. e., ($\mathbf{u}_l$). It is both divergence-free and curl-free. Laplace component comes from a scalar potential and satisfies the Laplace differential equation $\Delta\phi = 0$.

As a result the decomposition can be rewritten in the form:

$$\mathbf{u} = \nabla \times \mathcal{A} + \nabla\phi + \mathbf{u}_l. \tag{5.9}$$

The results of this decomposition are illustrated in Figure 5.6.

One can see that the compressible components of velocity correspond to shocks, while the incompressible part is dominated by GS95-type motions.

Table 5.1 illustrates how turbulent driving changes the distribution of energy for different components of the flow. One can observe that even for highly compressible magnetized supersonic flows most of the energy is residing in the incompressible motions, in particular in Alfvén modes. At the same time, the role of the fast modes increases with the increase of the sonic Mach number.

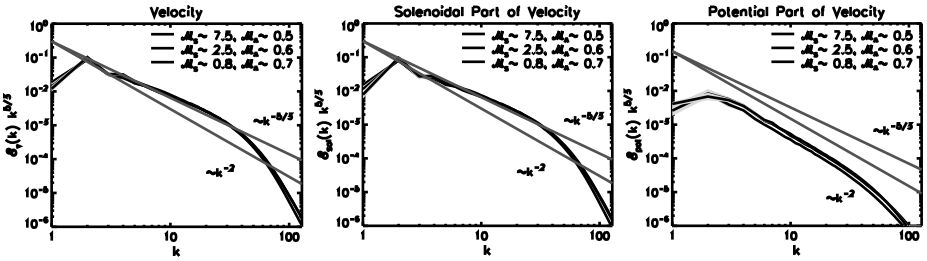

Figure 5.6: Spectra of the solenoidal and potential parts of velocity field for subAlfvénic turbulence from KL10. Reproduced from [231] with permission of AAS.

Table 5.1: Percentage amount of the kinetic energy contained within each velocity component. Errors correspond to a measure of the time variation.

$\mathcal{M}_s$	$\mathcal{M}_A$	$V_{\text{incomp.}}$	$V_{\text{comp.}}$	V_A	V_s	V_f
~ 0.7	~ 0.7	$96.5^{\pm 0.8}$	$3.3^{\pm 0.8}$	$58^{\pm 4}$	$37^{\pm 3}$	$4.8^{\pm 0.7}$
~ 2.2	~ 0.7	$93^{\pm 2}$	$7^{\pm 2}$	$58^{\pm 5}$	$33^{\pm 4}$	$9^{\pm 2}$
~ 7.0	~ 0.7	$92^{\pm 2}$	$7^{\pm 2}$	$56^{\pm 4}$	$36^{\pm 4}$	$8.0^{\pm 0.7}$
~ 0.7	~ 7.4	$95^{\pm 2}$	$5^{\pm 2}$	$52^{\pm 4}$	$42^{\pm 4}$	$6.2^{\pm 0.8}$
~ 2.3	~ 7.4	$86^{\pm 1}$	$14^{\pm 2}$	$47^{\pm 3}$	$37^{\pm 4}$	$16^{\pm 2}$
~ 7.1	~ 7.1	$84^{\pm 2}$	$16^{\pm 2}$	$47^{\pm 4}$	$33^{\pm 4}$	$20^{\pm 2}$

5.4 Density scalings

The properties of random density in supersonic ISM turbulence is of prime interest to astronomers due to its relation to star formation. In view of our earlier decomposition into fundamental MHD modes, the density is related primarily to the slow mode, since this is the mode that perturb density the most in low-beta supersonic fluid. At the same time, the statistics of density is very different from the statistics of the slow mode velocity. In particular, while slow mode exhibit well-pronounced scale-dependent anisotropy (GS95, see also CL03) (see Figure 5.2), the structure function of density at high Mach numbers are almost isotropic; see Figure 5.8.

This puzzling properties of density were first addressed in [37], which shed the light on the dynamics of density in supersonic MHD. It turned out that for density which is distributed approximately log-normally and has high-density tail, the statistics of the second-order structure function is dominated by the contributions from high-density regions or clumps. The measured isotropy, therefore, is the result of this bias. Furthermore, the flat spectrum of density in high Mach number turbulence arises from the same effect, i. e., high-density clumps act as a delta-functions and produce flat spectrum. If we use log-density instead of density, the spectra become steeper and the second-order structure function exhibits well-defined scale-dependent anisotropy as it illustrated in Figure 5.8. In other words, taking logarithm suppresses high peak

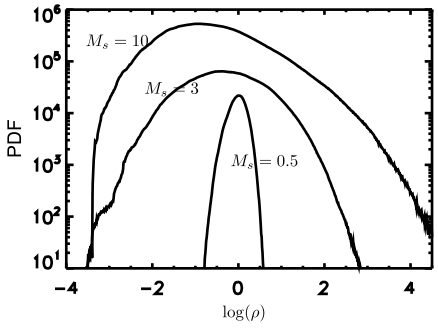

Figure 5.7: Probability density function for a density in direct numerical simulation with Alfvénic Mach number around unity and various sonic Mach numbers. From [37].

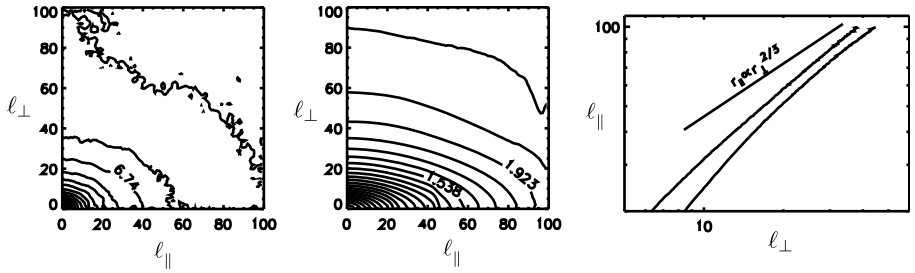

Figure 5.8: Contours of the structure function of density (left), log-density (center), and the anisotropy of log-density (right), solid line represents $M_s \sim 10$, dashed – $M_s \sim 3$ from [37].

contributions and provides quantitative insight into the density distribution that fill most of the volume. Thus way filtered density field has properties similar to the GS95 predictions for velocities corresponding to slow modes. This means that while the perturbations of density, e. g., its log-normal PDF, are created by random slow shocks, the structure of density has an imprint from Alfvénic driving, the same imprint the structure of slow mode velocity has.

5.4.1 Theoretical considerations

It is natural to expect that an analogy exist between the subsonic ($M < 1$) MHD turbulence and its incompressible counterpart, namely, GS95 model. It could be seen, that in the low beta case, i. e., for $P_{\rm mag} > P_{\rm gas}$, density is primary perturbed by the slow mode (CL03). As discussed in GS95, slow modes are sheared by Alfvén turbulence and, as a result, they exhibit Kolmogorov scaling and GS95 anisotropy for low Mach numbers. However, for high Mach numbers shocks are expected to strongly perturb the density.

The problem can be approached by analyzing the underlying hydrodynamic equations. Indeed, there exists a multiplicative symmetry with respect to density

in the ideal flow equations for an isothermal fluid (see, e. g., Passot and Vazquez-Semadeni [353]; henceforth PV98). Therefore, a stochastic process disturbing the density is multiplicative with respect to density, rather than additive. As a result, the distribution for density becomes lognormal, rather that normal. 1D numerical simulations of high-Mach hydrodynamics confirmed that the distribution is approximately log-normal for an isothermal fluid (PV98).

The aforementioned symmetry in the case of magnetized fluid is broken by the magnetic tension. Physically, this corresponds to the higher density regions having lower Alfvén speed, provided that there is no significant correlation between density and magnetic field.[2]

For turbulence with low Mach turbulence, the perturbations of density evolve with the sound speed. For low beta media, such evolution is slow in comparison with shearing induced by Alfvén waves. For turbulence with high sonic Mach number, one expects a considerable amount of shocks to be formed in the fluid. In a sub-Alfvénic case, the turbulent velocities are smaller than the Alfven speed and, therefore, we expect oblique shocks to be disrupted by Alfvénic shearing. The evolution of the weak shocks is also governed by the sonic speed, and structures from shearing as in low Mach case should arise.

We note that shearing does not affect Probability Density Function (PDF) of the density, making magnetized and nonmagnetized turbulence similar as far as the PDFs are concerned. However, this significantly modifies density spectra and structure function scaling. In other words, two distinct physical processes act simultaneously and affect different statistical measures of turbulent density field. The random multiplication of density induced by shocks, affect the PDFs, while the other, Alfvénic shearing, affects anisotropy and scaling of the structure function of the density.

5.4.2 The code

The testing of the theoretical ideas above was performed in BLC05 with data cubes from the 3-dimensional MHD numerical simulations (see CL03). To study highly supersonic turbulence, we performed simulations using a periodic 512^3 Cartesian grid with the average sonic Mach numbers of $\sim$ 10 and $\sim$ 3. It was found that effects of numerical diffusion were significant at the scales of less than 10 grid points. In particular, parallel to the magnetic field, velocities stayed supersonic down to 8 grid units for Mach 10, and 20 grid units for Mach 3. The isothermal equation of state was employed in the simulations and to control the effects of boundaries the turbulence was randomly driven on the scale about 2.5 times smaller than the box size. The driving

2 The case of no density-magnetic field correlation can emerge both to the compression of matter along magnetic field lines and due to reconnection diffusion (see Chapter 9).

corresponded to the Alfvénic Mach number of the order of unity, i. e., the Alfvén velocity was roughly the same as the rms velocity.

5.4.3 Results

In Figure 5.7, we plot the distribution for log-density for various Mach numbers. In all cases, except for the subsonic one, the Alfvénic Mach number M_A is slightly less then unity. This was motivated by the fact, that in a strongly super-Alfvénic fluid, magnetic field will grow through turbulent dynamo (see Chapter 2), eventually approaching the equipartition.

We found that the distribution shows a significant deviation from a lognormal law. The rms deviation of density for a subsonic case is consistent with predicted dependences Mach number for the case of low beta (CL03), and the rms deviation of log-density for supersonic case is around unity independent of the Mach number. The distributions are significantly broader for higher Mach numbers, in agreement with the PDFs observed in hydrodynamic supersonic simulations (see, e. g., [354]).

The dimension of the high-density structures were found to be between 1 and 2, being viewed as a flatted filaments or elongated pancakes. While the lower density structures tend to align along magnetic field, the higher density structures, on the contrary, align perpendicular to magnetic field. The maximum density value in a Mach 10 data cube was $\sim 3 \times 10^3 \rho_0$. Naturally, the density clumps with values of 3–4 orders of magnitude of mean density severely distort power spectrum. Therefore, these clumps with low filling factor can, nevertheless, overshadow small amplitude density structures that fill most of the volume. The spectrum of density for high-Mach is shallow and, unlike the velocity spectrum, it does not follow a well-defined power-law. It is obvious that the randomly distributed high-density clumps dilute any anisotropy originating from small-scale motions.

To overcome the effect of high density clumps and reveal an underlying density scalings of volume-filling fluctuation, we used a logarithm of density normalized density fluctuations instead of normalized density fluctuations.[3] This way we suppress the influence of the high peaks to the spectrum or structure function. Other filtering procedures, e. g., cutting off peaks at some level, gives similar results, but structure function are more distorted, as the procedure of cutting off, or restricting density to some level, introduces artificial structures in the real space.

We know that magnetic field, being perturbed mostly by the Alfvén mode, exhibit anisotropy. While the anisotropy of the density structure function (SF) is not noticeable, SF for log-density exhibit conspicuous anisotropy. In order to test scale-dependent anisotropy of the GS95 type ($r_\parallel \sim r_\perp^{2/3}$), we plotted values of $r_\parallel$ and $r_\perp$ with

3 Normalization is achieved by dividing by the mean density.

equal structure function on Figure 5.8. We observe that magnetic field SF is described by GS95 anisotropy for scales from the driving scales up to 8 grid units. This is consistent with the results of CL04 and the notion that in a sub-Alfvénic case ($M_A < 1$) strong Alfvénic turbulence is marginally affected by compressible motions, despite high sonic Mach number. As to the log-density, its anisotropy is of GS95 type just below the outer scale and it becomes distorted when numerical effects get important, i. e., at the scales around 10 grid units. Incidentally, at the same scales we expect that the Alfen Mach number will be of the order of unity and therefore our simplified model may not be applicable.

We also checked for correlation between density and magnetic field magnitude which was expected from a models of external compression of an ideal MHD fluid. We have not found any significant correlation of this type. Two effects can account for this. One is the compression along the magnetic field lines, another is reconnection diffusion that we discuss in Chapter 9.

5.4.4 Implications

It is a well-known notion that a supersonic turbulence exhibits a lot of shocks. Our driving is incompressible, but the compressible and incompressible motions are expected to be partially coupled at the injection scale when Alfvénic Mach number is of the order of unity (CL03). Therefore, we expect that the driving excites some amount of compressible motions. In fact, our testing showed that the rms velocity, associated with slow mode was of the same magnitude as the rms velocity of the Alfvén mode. Therefore, the resulting flat power spectrum of density is associated with very large perturbation of density from compressible motions that naturally arise at the driving scale. Shocks in isothermal fluid can have very large density contrasts, up to sonic Mach number squared and they can compress density the same was as supernova remnants do in the snowplow phase, namely, they collect matter keeping the total momentum of the shock constant (see [403]). Nevertheless, as we do not see strong shocks near density clumps we believe that in magnetically dominated medium that we deal with the corresponding shocks move material along magnetic field lines the same way that the slow modes do in subsonic case. As the shocks are randomly oriented, the clumpy structure that we observe does not reveal any noticeable anisotropy. The density perturbations associated with such shocks is not correlated with the magnetic field strength enhancement which is analogous to the case of density fluctuations induced by slow modes (see CL03). Our analysis of the data is consistent with this mental picture. At the same time, significant correlations between density and the magnitude of magnetic field were observed in many super-Alfvénic simulations; see, e. g., [347] (compare with 2D sub- and super-Alfvénic simulations by [354]).

If we associate the clumps in simulations with interstellar clouds, in ISM with random driving we would expect the clouds not to have any preferential orientation

in respect to magnetic fields at least until self-gravity does get important. We observed the substantial variation of the gas pressure, up to three orders of magnitude which is consistent with findings in [202]. Flat spectrum of density fluctuations is roughly consistent with some observational data. Needless to say, that a more systematic analysis of data is required and it is interesting, for instance, to test the change of the density spectrum with the Mach number. Testing the anisotropy of density is another interesting direction of study, even though one cannot directly observe log-density and the effects associated with the projection along the line of sight must be considered carefully (see discussion of this in [136]).

Surely, for real molecular clouds self-gravity is important. This effect should make the observed spectrum even flatter, as the density peaks are expected to become higher and more delta-function-like. In addition, cooling should make interstellar gas more pliable to compression compared to the isothermal gas that is studied used in our simulations. This, should result in more density contrast when the original gas is warm. However, in interstellar warm medium the gas has Mach number of the order of unity. At the same time, for molecular clouds for which Mach number can be substantial our isothermal calculations seems to be adequate.

We interpreted the unusual behavior of density fluctuations generalizing the GS95 model of MHD turbulence by considering strong compressions. We used filtering to mitigate the effect of rare strong compression, and succeeded in showing that volume-filling density fluctuations are anisotropic. We found that the range of scales where incompressible turbulent theory is applicable is shortened in numerical simulation with supersonic driving. However, between sub and supersonic scales, there is a region where compressible motions cascade in a way that is yet to be understood.

5.5 Viscosity-dominated regime of MHD turbulence

In hydrodynamic turbulence, energy is injected at a scale L, and cascades down to smaller scales without significant energy losses until it reaches the viscous damping scale l_{dv}. The Kolmogorov energy spectrum is valid for the inertial range, i. e., all scales between L and l_{dv}.

This simple picture above should be modified when we deal with MHD turbulence because there are two dissipation scales—the velocity damping scale l_{dv} and the magnetic diffusion scale l_{dm}, where magnetic structures are dissipated. In fully ionized collisionless plasmas (e. g., the hottest phases of the ISM), l_{dv} is approximately an order of magnitude larger than l_{dm}. However, in partially ionized plasmas (e. g., the warm or cold neutral phase of the ISM), the two dissipation scales are very different and $l_{dv} \gg l_{dm}$. In the cold neutral medium (see [120] for a list of the ISM phases) neutral particle transport leads to viscous damping on a scale which is a fraction of a parsec. In contrast, in these same phases $l_{dm} \sim 100$ km.

This has a significant effect on the energy cascade model in a partially ionized medium. When the energy reaches the viscous damping scale l_{dv}, kinetic energy dissipates there, but the magnetic energy does not. In the presence of a dynamically important magnetic field, Cho, Lazarian, and Vishniac ([88]; hereafter CLV02b) reported a completely new regime of turbulence below the scale l_{dv}. CLV02b showed that at these small scales magnetic fluctuations form a shallow spectrum $E_b(k) \sim k^{-1}$. This spectrum is similar to that of the viscous-convective range of a passive scalar in hydrodynamic turbulence, but a significant difference between the two processes is that magnetic field is far from being passive. In fact, it is dynamically important and at the scales less than l_{dv} its energy is orders of magnitude exceed the kinetic energy.

A higher resolutions numerical study of the viscosity-damped MHD turbulence was presented in CL03 and [91]. The regime was shown to be present in compressible MHD turbulence as well and Figure 5.9 illustrates the results for this regime obtained for compressible and incompressible MHD turbulence.

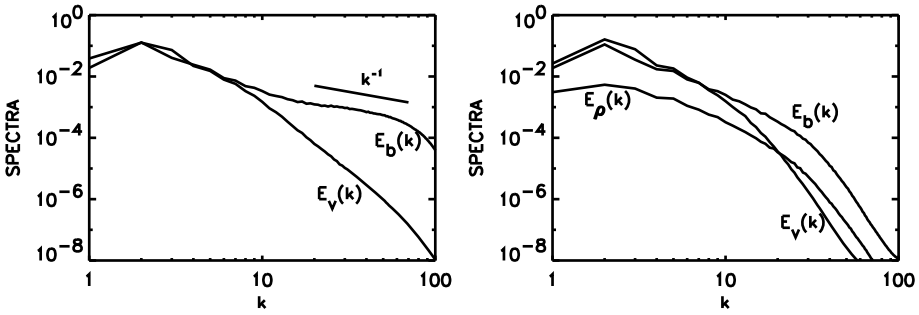

Figure 5.9: Viscous damped regime (viscosity > magnetic diffusivity). Due to large viscosity, velocity damps after $k \sim 10$. (a) *Left:* Incompressible case with 384^3 grid points. Magnetic spectra exhibit a shallower slope ($E_b(k) \propto k^{-1}$) below the velocity damping scale. From CLV02b. (b) *Right:* Compressible MHD 216^3 simulations. Magnetic and density spectra demonstrate structures below the velocity damping scale at $k \sim 10$. The structures are less obvious than the incompressible case as it is harder to achieve small magnetic diffusivity in compressible runs from CL03. Reproduced from [88] with permission of AAS.

Figure 5.10 exhibits structures and spectra in supersonic viscous MHD simulations, emulating conditions in the molecular clouds, where high ambipolar diffusion could result in drag and damping of kinetic motions. Remarkably, the kinetic and magnetic spectra are similar to the incompressible and weakly compressible cases. Nevertheless, the structures, observed in the simulated data are very different. The supersonic structures are dominated by the current sheets, which are also density places of higher density. This is a result of currents sheets having low magnetic pressure which results in gas compression.

Lazarian, Vishniac, and Cho ([280], henceforth LVC04) suggested a theoretical model for viscosity-damped MHD turbulence. In this model, it is taken into account

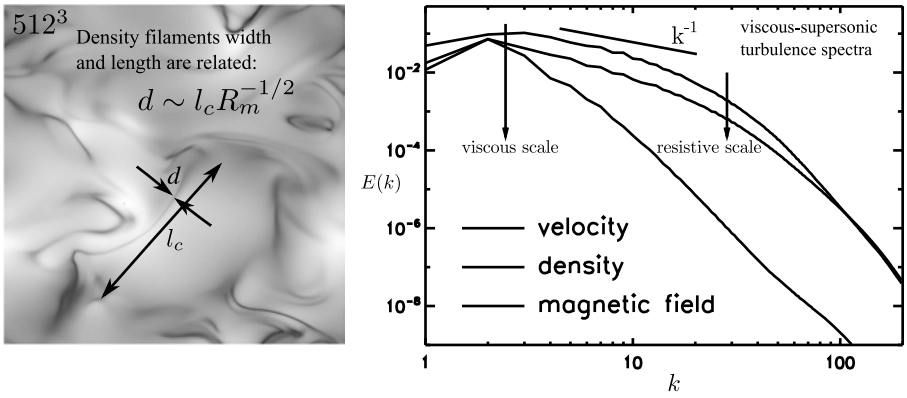

Figure 5.10: Simulations of supersonic, viscously damped MHD turbulence, with high viscosity emulating high drag from ambipolar diffusion in molecular clouds. *Left*: Filaments of density created by magnetic compression of the gas in this regime. Darker regions correspond to higher density. The viscous damping scale l_c is much larger than the current sheet thickness d. This creates large observed density contrasts. *Right*: The spectra of density, velocity, and magnetic field in this case. While the density and magnetic spectra are similar, the velocity spectrum has a cutoff due to high viscosity. Note that the resistive scale in this regime is not L/Rm but $LRm^{-1/2}$. From [36].

that there is no significant velocity fluctuation below l_{dv}, so the time scale for the energy cascade below l_{dv} is fixed at the viscous damping scale. Consequently, the energy cascade time scale $t_{\rm cas}$ is scale-independent below l_{dv}. The requirement for a scale independent energy transfer rate $b_l^2/t_{\rm cas}$ provides

$$b_l \sim \text{constant}, \quad \text{or} \quad E_b(k) \sim k^{-1}, \tag{5.10}$$

where $kE_b(k) \sim b_l^2$.

The curvature of the magnetic field lines is assumed to change slowly in the cascade:

$$k_\parallel \sim \text{constant}. \tag{5.11}$$

This is due to the fact that the cascade is driven by repeated shearing at the same large scale. It is also corresponds to the numerical finding in CLV02b that $k_\parallel$ is constant throughout the viscously damped nonlinear cascade. The wavevector component in the direction of the perturbed field is also approximately constant, so that the increase in k is entirely in the third direction.

The observed structures are intermittent and, therefore, the kinetic spectrum depends on the scaling of intermittency.

5.6 Applying results to collisionless fluids

Some astrophysical magnetized plasmas are collisionless, meaning the typical collision frequency is lower than the gyrofrequency. Therefore, it is important to understand to what extend the results obtained within MHD can also be applied to collisionless environments. The effective collisionality of the medium depends on the collective effects of magnetic scattering of ions. Different instabilities, e. g., mirror, firehose, and gyroresonance instability, induced by large scale compressions produces small scale perturbations that induce efficient scattering of charged particles [380, 263, 383]. This decreases the mean-free path of particles and makes plasmas, effectively, much more collisional. This is not desimilar to the case of a collisionless shock which excite plasma waves and lead to effective particle thermalization.

Furthermore, some subsets of MHD equations, such as reduced or Alfvénic MHD, which we studied in great detail in Sections 3 and 4, are actually applicable to fully collisionless plasmas, because Alfvénic motions are essentially $[\mathbf{E} \times \mathbf{B}]$ drift motions, rely only on magnetic tension and do not require collisions; see, e. g., [382].

A recent study in [374], using a closure for anisotropic plasma pressure, showed that for a reasonable choice of the relaxation term the collisionless fluids behave similar to MHD. The aforementioned work was done in the context of intracluster dynamo. However, similar approach can be applied to other collisionless fluids. More theoretical studies of the problem are given in [378]. Therefore, we expect that both MHD turbulence scaling relations and the results of turbulent dynamo that we discussed in above are applicable to collisionless turbulent astrophysical plasmas above the effective collisional scale. The measurements in the solar wind indicate that the effective MHD scales could be as low as the ion skip depth or the ion Larmor radius.

5.7 Toward understanding of relativistic turbulence

High energy phenomena is frequently associated with astrophysical fluids with relativistic motions. Naturally, the interest to MHD turbulence in relativistic fluids has been growing. Due to advances in numerical techniques, it is now possible to numerically investigate fully relativistic MHD turbulence [468].

When electromagnetic energy density significantly exceeds the rest mass energy density of matter, the electromagnetic fields become essentially force-free, which is described with the so-called relativistic force-free approximation. The examples of such environments include electron-positron pulsar magnetospheres and the inner parsec-scale AGN jets.

MHD turbulence in relativistic force-free regime has been studied first numerically. The calculations are applicable to a many important astrophysical settings, e. g., to the magnetosphere of a pulsar or a black hole. For such systems, the Alfvén speed approaches the speed of light, and we the set of relativistic equations is required to

describe the media. In the flat geometry, this set is

$$\partial_\mu(\rho u^\mu) = 0, \tag{5.12}$$

$$\partial_\mu T^{\mu\nu} = 0, \tag{5.13}$$

$$\partial_t \mathbf{B} = \nabla \times (\mathbf{v} \times \mathbf{B}), \tag{5.14}$$

$$\nabla \cdot \mathbf{B} = 0, \tag{5.15}$$

where u^μ is the fluid four velocity and $T^{\mu\nu}$ is the stress-energy tensor of the fluid and the electromagnetic field. This reduces to

$$\frac{\partial \mathbf{Q}}{\partial t} + \frac{\partial \mathbf{F}}{\partial x^1} = 0, \tag{5.16}$$

where

$$\mathbf{Q} = (S_1, S_2, S_3, B_2, B_3), \tag{5.17}$$

$$\mathbf{F} = (T_{11}, T_{12}, T_{13}, -E_3, E_2), \tag{5.18}$$

$$T_{ij} = -(E_i E_j + B_i B_j) + \frac{\delta_{ij}}{2}(E^2 + B^2), \tag{5.19}$$

$$\mathbf{S} = \mathbf{E} \times \mathbf{B}, \tag{5.20}$$

$$\mathbf{E} = -\frac{1}{B^2}\mathbf{S} \times \mathbf{B}. \tag{5.21}$$

Here, $\mathbf{E}$ is the electric field and $\mathbf{S}$ is the Poynting flux vector. Note that we use units such that the speed of light and π do not appear in the equations [226]. Solving equations first along x^1 direction, one then does this for x^2 and x^3 directions with appropriate rotation of indexes.

Scaling of relativistic Alfvenic turbulence coincides with the GS95. It was proposed by Thompson & Blaes [423] and later numerically tested by Cho [78]. In particular, [78] performed numerical simulations of a decaying relativistic force-free[4] MHD 512^3 cube turbulence and obtained both energy spectrum and, importantly, the anisotropy of eddy structures.[5] The simulation were initiated with only Alfvén modes being present. The left panel of Figure 5.11 shows the evolution of energy spectrum of magnetic field at two different times. Although only large-scale (i. e., small k) Fourier modes were excited at $t = 0$ (not shown), the turbulent cascading produced small-scale (i. e., large k) modes at later times. After $t \sim 3$, the energy spectrum evolves by

4 To obtain the force-free condition from Maxwell's equations and the energy-momentum equation: $\partial_\mu T^{\nu\mu}_{(f)} = -F_{\nu\mu} J^\mu = 0$, where $F^{\nu\mu}$ is the electromagnetic field tensor.

5 We feel that anisotropy is frequently ignored in numerical studies. For instance, as we mentioned earlier, attempts to modify the GS95 theory were motivated by the discrepancy between the expected spectrum and its value in numerical simulations. At the same time, the fact that the GS95 was providing the right scaling of anisotropy, which the theories that were developed to substitute it were failing to reproduce the observed anisotropies was mostly ignored.

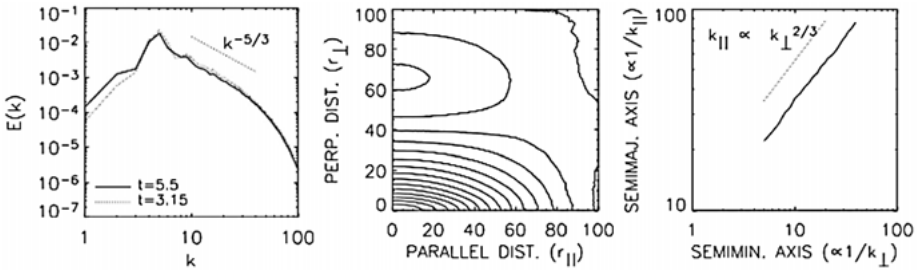

Figure 5.11: Decaying relativistic force-free MHD turbulence. (Left) Energy spectrum is consistent with the GS95 one. (Middle) Eddy shapes, represented by contours, demonstrate scale-dependent anisotropy: smaller eddies are more elongated. (Right) The anisotropy of eddy shape corresponds to GS95 anisotropy. Reproduced from [78] with permission of AAS.

changing the amplitude by not changing its slope. The spectral slope at this stage is very close to a Kolmogorov/GS95 value:

$$E(k) \propto k^{-5/3}. \tag{5.22}$$

Contours of magnetic field iso-correlation in the middle panel of Figure 5.11 depict the shapes of eddies revealed by the second-order structure function. Similar as in non-relativistic studies of reconnection the shape of eddies is measured in a local frame, which, as we discussed earlier, is aligned with the local magnetic field [89, 92, 231]. The contour plot reveals the GS95-type anisotropy with the relation between the semi-major axis ($\sim l_\parallel \sim 1/k_\parallel$) and the semi-minor axis ($\sim l_\perp \sim 1/k_\perp$):

$$k_\parallel \propto k_\perp^{2/3} \tag{5.23}$$

(see the right panel of Figure 5.11). These results confirm the theoretical predictions in [423]. Driven turbulence simulations in [80] provide similar results. Similar to the case of nonrelativistic MHD turbulence the turbulence scaling does not depend on whether the turbulence is decaying or driven turbulence.

As we discussed in Chapter 4, in general the MHD turbulence is at least slightly imbalanced. Our discussion of theories of imbalanced turbulence suggests that the most promising in view of the existing numerical nonrelativistic data is the theory in [30] (henceforth BL08). There is at the moment no theory of relativistic imbalanced MHD turbulence, but appealing to the coincidence of the predictions of GS95 and the theory in [423] the predictions in BL08 should be applicable to the imbalanced nonrelativistic turbulence. This type of turbulence was studied in Cho and Lazarian (2014, [87], henceforth CL14). In fact, those simulations can also be viewed as the test of nonrelativistic theories using relativistic turbulence simulations that we discussed in Section 5.7.1 as the simulations are performed with a completely different code.

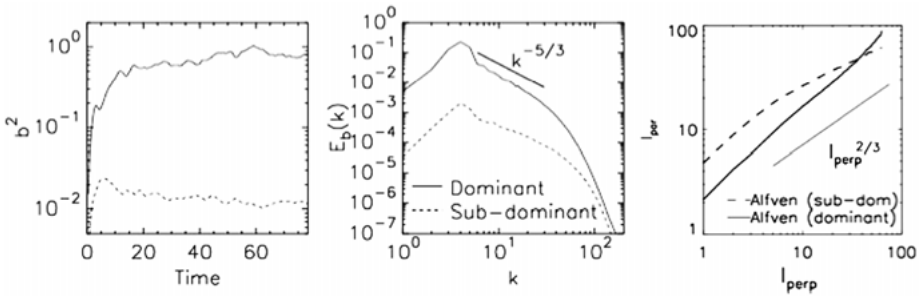

Figure 5.12: Imbalanced relativistic force-free MHD turbulence. (Left) A factor of 4 difference in energy injection rates results in much larger imbalance in energy densities. (Middle) The spectral slopes for the dominant and the subdominant waves are different: the dominant waves have a steeper slope. (Right) The degrees of anisotropy for the dominant and the subdominant waves are different: the dominant waves exhibits weaker anisotropy. Reproduced from [87] with permission of AAS.

The results of the CL14 simulations for 512^3 resolution is presented in Figure 5.12. In the adopted set up, the energy injection rate for Alfvén waves moving in one direction (dominant waves) is 4 times larger than that for waves moving in the other direction (subdominant waves). The left panel of Figure 5.12 demonstrates that, even although the ratio of the energy injection rates is about ~4, the ratio of the energy densities is about significantly larger, i. e., ~100. The middle panel of the figure shows that the spectrum for the dominant waves is a bit steeper than the GS95 one, while that for the subdominant waves is shallower. Figure 5.12 at its right panel shows that the anisotropy of the dominant waves is a weaker than the GS95 prediction, while that of the subdominant waves is stronger. These results can be compared with the BL08 theory in Chapter 4, in particular Figure 4.17 Indeed, it is BL08 prediction that the magnetic spectrum of dominant waves should be steeper than that of subdominant waves and the dominant waves should exhibit anisotropy which is weaker than the GS95 one, while the subdominant waves should exhibit the anisotropy stronger than GS95 one. Thus CL14 concluded that the relativistic imbalanced turbulence corresponds to the BL04 theory. CL14 also showed that the energy density ratio of the dominant to subdominant waves scales in proportion to the ratio of the energy injection rates to the power of n, i. e., $(\epsilon_+\epsilon_-)^n$, where $n > 2$, which is also consistent with the BL08 expectations. Naturally, higher resolution simulations of relativistic imbalanced turbulence would be very advantageous to further testing BL08 theory.

5.7.1 Fully relativistic MHD turbulence

Fully relativistic MHD turbulence has been studied performed in a number of papers [467, 200, 15, 468, 469, 160]. The results in [468, 469] corresponding to the mean lab-

frame Lorentz factor of ~1.67 and performed in 2048^3 cubes confirm that the existence of an inertial spectrum of relativistic velocity fluctuations with a −5/3 spectral index. They also studied the intermittency and found that the scaling exponents of the longitudinal velocity structure functions are consistent with the [392] model. The latter result is not trivial as the simulations for *unmagnetized* relativistic turbulence with the Lorentz factors up to ~1.7 indicate that the relativistic effects enhance intermittency, and, as a result, the scaling exponents for high-order structure functions notably deviate from the prediction of the She–Leveque model [365].

5.7.2 Relativistic compressible turbulence: mode decomposition

The work on imbalanced and balanced relativistic turbulence strongly indicate that the nature of turbulence does not significantly change with the transfer to the relativistic regime. This conclusion is suggestive that the models based on the Goldreich–Sridhar turbulence, e. g., the turbulent reconnection model [278] can be extended to relativistic phenomena (see discussion in [301]).

To what extent compressible relativistic MHD turbulence is different from its nonrelativistic counterpart was tested in Takamoto and Lazarian (2016) [419] henceforth TL16. The procedure adopted for the decomposition was analogous to [81]. Since there is no average velocity in the background flow, the displacement vectors are

$$\hat{\xi}_{\rm slow} \propto k_{||}\hat{\mathbf{k}}_{||} + \left[\frac{u_{\rm slow}^2}{c_{\rm s}^2}\left(\frac{k}{k_{||}}\right)^2 - 1\right]\left[\frac{k_{||}}{k_\perp}\right]^2 k_\perp \hat{\mathbf{k}}_\perp, \tag{5.24}$$

$$\hat{\xi}_{\rm fast} \propto [u_{\rm fast}^2 k^2(1+\sigma) - c_{\rm s}^2 k_\perp^2 - k^2\sigma]\left[\frac{1}{c_{\rm s}k_{||}}\right]^2 k_{||}\hat{\mathbf{k}}_{||} + k_\perp \hat{\mathbf{k}}_\perp, \tag{5.25}$$

where c_s is the relativistic sound velocity, k is the magnitude of the wave vector $\mathbf{k}$, and $u_{\rm fast/slow}$ are the phase velocities of fast and slow modes [10]. As everywhere in the book, $k_{||}$, $k_\perp$ are, respectively, wavevectors the parallel and perpendicular to the magnetic field.

As in the nonrelativistic case, Equations (5.24) and (5.25) provide us with the way to obtain fast and slow mode velocity components by projecting the velocity field on the displacement vectors $\hat{\xi}_{\rm fast/slow}$. Thus the displacement vector of the Alfvén mode velocity component is given as $\hat{\xi}_{\rm A} = \hat{\mathbf{k}}_{||} \times \hat{\mathbf{k}}_\perp$ [303].

We can write the velocity projection onto $\xi_{\{\rm A,fast,slow\}}$ as $\delta v_{\{\rm A,f,s\}}$. Since the form of the linearized mass conservation law and induction equation are the same in relativistic and nonrelativistic cases, the Fourier components of density and magnetic field can be obtained by exactly the same procedure in the non-relativistic case given in [81, 82].

In the nonrelativistic case, the transfer of energy between the modes is marginal and the mode decomposition reveals the distinct cascades of Alfvén, fast, and slow

mode [81]. We will show below that in the case of relativistic turbulence, the coupling increases the decomposition reveals the transfer of energy between the cascades.

The left panel of Figure 5.13 is the ratio of fast to Alfvén mode velocity power at 2 eddy-turnover time in terms of the fast Mach number of the Alfvén component of velocity. In the plot, the fast velocity $c_{f,\perp}$ in the horizontal axis is taken as that in the perpendicular direction to the background magnetic field. The linear increase of the fast mode power with the Mach number corresponds to the non-relativistic case [81, 82]. On the other hand, there is an increase of power with σ.

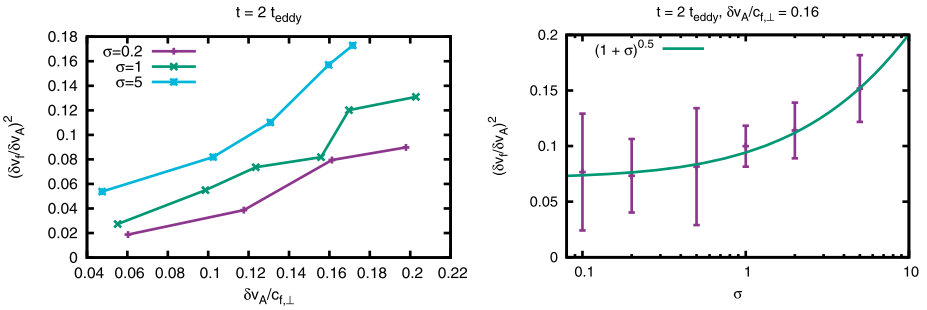

Figure 5.13: Left: The ratio of fast to Alfvén mode velocity power as a function of the Mach number of the Alfvén mode component obtained using 3-velocity. Evidently, the compressible modes become more important with increasing σ-parameter. Right: The ratio of fast to Alfvén mode velocity power in terms of the background σ parameter at $t = 2t_{\rm eddy}$ and $\delta v_{\rm A}/c_{\rm f,\perp} = 0.16$. The ratio is proportional to $\sqrt{1+\sigma}$ for $\sigma > 1$ from TL16. Reproduced from [419] with permission of AAS.

The right panel of Figure 5.13 shows the ratio of fast to Alfvén mode velocity power as a function of the σ value at $t = 2t_{\rm eddy}$ and $\delta v_{\rm A}/c_{\rm f,\perp} = 0.16$. This ratio is nearly independent of the σ-parameter for $\sigma < 1$ in agreement with [81]. On the other hand, it increases approximately by $(1+\sigma)^{1/2}$ when $\sigma > 1$. Therefore, the ratio can be written as

$$(\delta v_{\rm f})^2/(\delta v_{\rm A})^2 \propto (\delta v_{\rm A})/c_{\rm fast,\perp} \qquad (\text{when } \sigma \ll 1), \tag{5.26}$$

$$\propto (1+\sigma)^{1/2}(\delta v_{\rm A})/c_{\rm fast,\perp} \qquad (\text{when } \sigma \gtrsim 1). \tag{5.27}$$

This indicates the exchange of energy between Alfvén and fast mode increases as the electromagnetic field becomes relativistic. This increase of coupling was explained in TL16 by the effect of electric field $|\mathbf{E}| = |-(\mathbf{v}/c)\times\mathbf{B}| \sim |\mathbf{B}|$. Within the quasi-linear theory, that is, taking into account the second-order terms in equations assuming first-order Alfvén mode perturbation, the force term in the equation of motion of RMHD is

$$F_{\rm x} \equiv -\nabla_{\rm x}\left[\frac{B_0^2}{2}\left(1+\frac{c_{\rm A}^2}{c^2}\right)\left(\frac{\delta v_{\rm A}}{c_{\rm A}}\right)^2\right], \tag{5.28}$$

$$F_{\rm y} \equiv -\nabla_y \left[\frac{B_0^2}{2} \left(1 - \frac{c_{\rm A}^2}{c^2} \right) \left(\frac{\delta v_{\rm A}}{c_{\rm A}} \right)^2 \right], \tag{5.29}$$

$$F_{\rm z} \equiv -B_0 \nabla_x \delta B_{\rm A}, \tag{5.30}$$

where the background magnetic field is $\mathbf{B}_0 = B_0 \mathbf{e}_x$ and the Alfvén mode direction in z-direction. It is easy to observe that the z-component drives the usual Alfvén mode, while the anisotropic nature of the electric field gives the weaker force in the y-direction and the stronger force in x-direction, or the parallel direction of the background magnetic field. In the Poynting-dominated regime, $c_{\rm A} \sim c$, the force is only in the direction parallel to the magnetic field direction, and gives rise to better Alfven-fast mode coupling.

Extrapolating our dependences cannot be done for arbitrary large σ and more study of such regime is necessary. One can expect that at $\sigma \sim 24$ the saturation in the exchange of the energy between modes is expected. In this regime, significant changes of Alfvenic turbulence may be expected. In fact, for such strong coupling it may not be possible to talk about separate Alfvenic cascade obeying GS95 relations, but the new regime of coupled Alfven-fast turbulence emerges.

It is important to stress that results in TL16 show that the fast to Alfvén mode power ratio depends on a 3-fast Mach number, not the relativistic 4-fast Mach number. Therefore, in pointing-dominated plasma the transfer of energy to the compressible modes becomes important even for small magnetic field perturbations, which is very different from the nonrelativistic case for which the kinetic energy of turbulence should be comparable to the background magnetic field energy for the conversion to be tangible.[6]

Below we summarize what we know about the relativistic MHD turbulence regime so far:

Alfvén Mode–The top-left panel of Figure 5.14 shows the kinetic energy spectrum of Alfvén mode in terms of the wave vector perpendicular to the background magnetic field.

It is suggestive that for the explored ranges of coupling the spectrum has the Kolmogorov-like slope in the inertial range:

$$E^{\rm A}(k_\perp) \propto k_\perp^{-5/3}, \tag{5.31}$$

which is consistent with the predicted of the nonrelativistic Alfvenic turbulence theory [172].

This result is also consistent with the findings in [468, 469, 365] who performed the Helmholtz decomposition of velocity and showed the Kolmogorov scaling of the incompressible part of the spectrum. The bottom-left panel of Figure 5.14 shows the

6 The enhancement of compressibility effects was mentioned in [365] in the case of relativistic temperatures, but TL16 quantified this effect covering the Poynting-energy dominated regime.

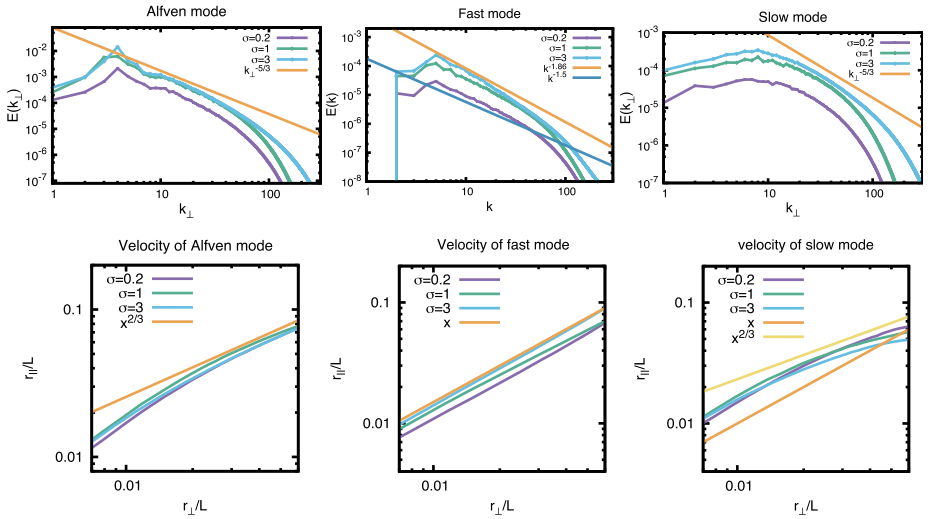

Figure 5.14: Top: Kinetic energy spectra of Alfvén, fast, and slow modes. Bottom: Eddy-scale of Alfvén, fast, and slow modes obtained by a second-order velocity structure function. All the data are measured at 1 eddy-turnover time. The initial Alfvén mode turbulence is injected at wavenumber $k/2\pi = 3/L$ and the velocity dispersion at the injection is $\delta v/c_A = 0.6$ for $\sigma = 0.2, 1$ and $\delta v/c_A = 0.5$ for $\sigma = 3$ from TL16. Reproduced from [419] with permission of AAS.

values of $r_{||}$ and $r_\perp$ with the same second-order structure function for the velocity. The distance $r_{||}$ and $r_\perp$ is determined using the local magnetic field direction following the procedure in [92]. The use of the local system in the relativistic case is as essential as in the nonrelativistic case see more in [278, 92, 303, 89]. The relation between the parallel and perpendicular scales of the eddies correspond to the theoretical expectations of the original Alfvenic turbulence theory [172], and its relativistic counterpart [423].

Fast Mode–The top-middle panel of Figure 5.14 illustrates the kinetic energy spectrum of fast mode. It indicates that the energy spectrum of their inertial region can be written as

$$E^{\rm f}(k) \propto k^{-3/2} \quad (\text{when } \sigma < 1), \tag{5.32}$$

$$\propto k^{-1.86} \quad (\text{when } \sigma > 1). \tag{5.33}$$

The value of the spectrum index 1.86 is similar to that for the potential component $\mathbf{u}_{\rm p} = \nabla\phi$ where ϕ is a scalar function obtained through the Helmgoltz decomposition in [468, 469]. This is not surprising as the fast modes are compressible.

The anisotropy of the fast modes as shown in Figure 5.14 is marginal, i. e., similar to the nonrelativistic modes. An interesting point here is that due to aforementioned Alfven-fast mode coupling, potentially the properties of fast modes can change significantly.

Slow Mode–The top-right panel of Figure 5.14 illustrates the kinetic energy spectrum of slow modes.

The spectrum exhibits the nonpower law behavior even as the resolution is increased from L/512 to L/2024. If we try to fit the power law, it will be $k^{-5/3}$ as in the nonrelativistic case. The deviation from the power law may signify that the energy exchange between slow mode and Alfven that makes the turbulence of the slow mode not self-similar. Further research should clarify this. The correspondence of the anisotropy to that of Alfvenic turbulence indicates that Alfven modes slave and shear the slow modes, exactly as in the nonrelativistic case.

The above study in TL16 was done using adiabatic simulations and, therefore, the temperature was increasing in the simulations. However, the results obtained are similar to the more recent results obtained the same authors with the isothermal code in [420]. The strong coupling of fast and Alfven modes in the relativistic Pointing-dominated plasma was confirmed. However, stronger anisotropy of fast modes was reported. Figure 5.15 shows that the anisotropy of Alfvenic modes is also get modified which means that relativistic turbulence enters a new regime where the fast and Alfven modes cannot be treated separately due to their strong interactions. This suggests that the theory of the Alfven-fast coupled turbulence should be constructed in future to understand turbulence in Pointing-dominated plasmas.

In the relativistic case, we see a more significant change of the properties of the fast modes compared to those of Alfven modes. Therefore, we expect that the theory of Alfvenic modes can stay approximately true even for the relativistic case.

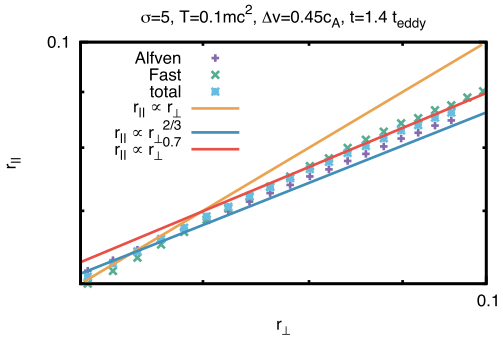

Figure 5.15: Anisotropies of Alfven and fast modes in the case of $\sigma = 5$ and $T = 0.1mc^2$ at $t = 1.4t_{\rm eddy}$. The case with no mode decomposition is also plotted, which shows an intermediate region between isotropic: $r_\parallel \propto r_\perp$ to critical balance case $r_\parallel \propto r_\perp^{2/3}$. The power law index of the anisotropy of MHD turbulence is approximately 0.7 from [420]. Reproduced from Figure 7 from [420].

Unlike Alfven modes, fast modes are likely to create fast shocks and, therefore, the energy transfer in the case pointing-dominated turbulence may be presented as in the schematic in Figure 5.16.

The above results for relativistic turbulence have important astrophysical consequences. For instance, the increase of energy in the form of fast modes means that the second-order Fermi acceleration is expected to become more important. Indeed, fast modes have been identified as the major scattering agent as well as the agent for

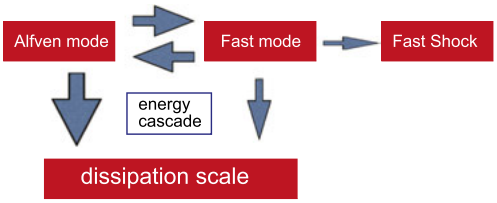

Figure 5.16: A schematic picture of the energy transfer in relativistic Poynting-dominated turbulence from [420]. Reproduced from Figure 8 from [420].

stochastic particle acceleration (see [453]). The insignificant change of the properties of the Alfven modes in relativistic and nonrelativistic turbulence mean that the theories based on the nonrelativistic scaling, e. g., theory of turbulent reconnection [278], are expected to be relevant in the relativistic environments.

6 Intermittency of MHD turbulence

6.1 General considerations

So far, our focus has been on the turbulence self-similarity. This property, which is also called scale-invariance, implies that fluid turbulence is similar at all scales within the inertial range and it can be reproduced by the magnification of some part of it.

At the dissipation scales, the self-similarity fails with turbulence forming non-Gaussian dissipation structures as exemplified, e. g., in [44]. Interestingly enough, self-similarity is not *exactly* true even along the inertial range. Instead, both numerical simulations and experiments show that the fluctuations tend to get increasingly sparse in time and space at smaller scales. This property is termed *intermittency*. Note that the power-law scaling does not by itself guarantee the scale-invariance or absence of intermittency.

One way study intermittency is to investigate the scaling powers of longitudinal velocity fluctuations, i. e., $(\delta V)^p$, where $\delta V \equiv (\mathbf{V}(\mathbf{x}+\mathbf{r}) - \mathbf{V}(\mathbf{x}))\mathbf{r}/r$. The infinite set of powers of $S^p \equiv \langle(\delta V)^p\rangle$, where $\langle\ldots\rangle$ denote ensemble[1] averaging, is equivalent to the p.d.f. of the velocity increments.

For the powers of velocity increments, one can write $S^p(r) = a_p r_p^{\xi}$ to characterize the isotropic turbulent field in its inertial range. While the scaling coefficients a_p are related to the values of the function S^p, e. g., at the injection scale, the scaling exponents ξ_p is more involved. It is possible to show that for a self-similar flow the scaling exponents are linear function of p, i. e., $\xi_p \sim p$. This for Kolmogorov model, $S^1 \sim v_l \sim l^{1/3}$ gives the relation $\xi_p = p/3$. Experimental studies, however, give different values which signifies that the Kolmogorov model does not cover all the complexity of incompressible hydro turbulence.

MHD turbulence, unlike hydro turbulence, deals with both velocity and magnetic fluctuations. The intermittencies of the two fields are not necessarily the same. In addition, MHD turbulence is anisotropic as magnetic field affects motions parallel to the local direction of **B**. This all makes it important to understand the properties of MHD turbulence intermittency.

An interesting and yet not well understood property of structure functions helps to extend the range over which S^p can be studied. Benzi et al. [20] reported that for hydrodynamic turbulence the functions $S^p(S^3)$ exhibit a broader power-law range compared to $S^p(r)$. Rather mysteriously, while for the inertial range a similarity in scaling of the two functions stem from the Kolmogorov scaling $S^3 \sim r$, the power-law scaling of $S^p(S^3)$ protrudes well beyond the inertial range into the dissipation range.[2] In

1 In astrophysics, spatial or temporal averaging is used.

2 In practical terms, this means that instead of obtaining S^p as a function of r, one gets S^p as a function of S^3, which is nonlinear. This, however, corrects for the distortions of S^p.

https://doi.org/10.1515/9783110263282-006

a way, this shows that the dissipation "spoils" different orders of S in the same manner. Therefore, one can use any moment $S^m \sim r^m$ and obtain a good power law of the function $S^p \sim (S^m)^{\xi_p/\xi_m}$ (see [44]).

6.2 She–Leveque model of intermittency

A successful model that reproduces both experimental hydro data and numerical simulations is the She–Leveque model (1994, [392]). Dubrulle [127] derived the corresponding law assuming that the energy from large scale is being transferred to $f < 1$ less intensive eddies and $1 - f$ of more intensive ones. The scaling relations suggested in [392] relates ζ_p to the scaling of the velocity $V_l \sim l^{1/g}$, the energy cascade rate $t_l^{-1} \sim l^{-x}$, and the codimension of the dissipative structures C:

$$\zeta_p = \frac{p}{g}(1 - x) + C\left(1 - (1 - x/C)^{p/g}\right). \tag{6.1}$$

For hydrodynamic incompressible turbulence, these parameters are $g = 3$, $x = 2/3$, and $C = 2$, implying that dissipation happens over 1D structures (e. g., vortices). The She–Leveque scaling was a success in reproducing the intermittency of incompressible hydrodynamic turbulence.

6.3 Intermittency of incompressible turbulence

Muller et al. [329] applied the She–Leveque model to incompressible MHD turbulence. They used Elsässer variables and claimed that their results are indicate that the dissipation happens within 2D structures (e. g., 2D current sheets). The subsequent study in [89] used velocities instead of Elsässer variables and it provided a different answer. In fact, [89] found that the dimension of dissipation structures is the same as in incompressible hydro, i. e., the dissipation structures are 1D. The controversy was addressed in Cho, Lazarian, and Vishniac (2003, [91] henceforth CLV03), where it was noted that, first of all, the measurements in [329] were done in the reference frame related to the *mean* magnetic field, while the measurements in [89] were done in the frame related to the *local* magnetic field. As it follows from our discussion in the previous chapters, the latter is more physically motivated frame, as it is the local magnetic field is the field that is felt by the eddies. Computations in CLV03 confirmed that the dissipation structures that can be identified as velocity vortices in the local magnetic field reference frame look like two-dimensional sheets in terms of Elsässer variables in the mean magnetic field reference frame. This confirms a mental picture where motions perpendicular to magnetic field lines are similar to hydrodynamic eddies. In addition, this sends a warning message about the naive interpretation of the She–Leveque scalings in the MHD turbulence.

6.4 Intermittency of compressible turbulence

The discussion of intermittency above dealt with incompressible fluids; however, this effect carries over to compressible media.

First intermittency studies in compressible MHD turbulence were discussed in Boldyrev (2002 [47]) who assumed that the dissipation there happens in shocks[3] and, therefore, the dimension of the dissipation structures is 2. This does not agree well with the numerical simulations in CL02, CL03, where the dominance of the vortical motions and, therefore, 1D dissipation structures in *sub-Alfvénic* turbulence (i. e., magnetic pressure is larger than the gaseous one) was reported. Nevertheless, numerical simulations in Padoan et al. [344] showed that for *super-Alfvénic* turbulence (i. e., magnetic pressure is less than the gas pressure) the dimension of the dissipation structures changes from one to somewhat higher than two as the Mach number was increasing from 0.4 to 9.5. The very fact that the super-Alfvénic turbulence is different from sub-Alfvénic is not surprising. The difference between the results obtained in [344] at low Mach number and the obtained in incompressible runs in Muller et al. [329] deserves a discussion, however. First of all, the results in [344] are obtained for the velocity, while the results in [329] are obtained for the Elsässer variables. Indeed, CLV03 has shown that the magnetic field and velocity have different intermittencies. It is clear from Figure 6.1 that $\zeta^{\text{magnetic}} < \zeta^{\text{velocity}}$ which means that magnetic field is more intermittent than velocity. An conspicuous feature of super-Alfvénic simulations in Figure 6.1 is that the velocity follows the She–Leveque hydro scaling with vortical dissipation, while magnetic field exhibits a pronounced dissipation in current sheets. Both features are expected if magnetic field is not dynamically important and the turbulence stays essentially hydrodynamic. We also see that the dynamically important magnetic field changes the intermittency. In particular, the flattening of magnetic field scaling can be seen in Figure 6.1.

Another study of intermittency of the velocity field of compressible turbulence was performed in KL10 [231]. In Figure 6.2, we show scaling exponents for the velocity calculated in the mean field reference frame. In the top left plot of Figure 6.2, we see that for the sub-Alfvénic turbulence the scaling exponents of velocity follow the

3 The paper by [47] introduces the model of compressible turbulence which it terms Kolmogorov–Burgers model. Within the model that is suggested in the aforementioned paper, the turbulence goes first along the Kolmogorov scaling and then, rather counterintuitively, at small scales forms shocks. The model was motivated by the low resolution numerical measurements of the turbulence spectrum that indicated the index of supersonic turbulence close to −5/3. This spectrum, however, was shown to be an artifact of numerical simulations. Higher resolution simulations in [240] showed that the slope with −5/3 is the result of the numerical bottleneck and the actual slope of the highly compressible turbulence is getting closer to −2 with the increase of the sonic Mach number, as was expected earlier. In a sense, we claim that the situation is similar with another suggestion in [48, 49], where as we discussed earlier, a theory of MHD turbulence motivated by low resolution numerical simulations is suggested.

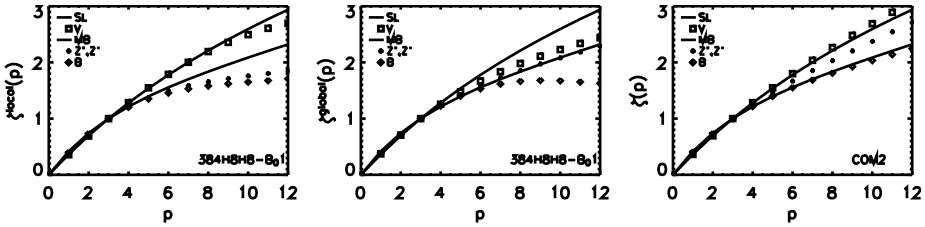

Figure 6.1: *Left panel*: Intermittency exponents for incompressible MHD turbulence in perpendicular directions in the local frame. While the velocity exponents show scalings similar to the She–Leveque model, the scalings of magnetic fields are different. *Central panel*: Intermittency exponents for incompressible MHD turbulence in the frame of the mean magnetic field. The result for $z^{\pm}$ is very similar to the Müller–Biskamp model [329]. *Right panel*: Intermittency exponents for super-Alfvénic compressible turbulence in the mean magnetic field frame from CLV03. Reproduced from [91] with permission of AAS.

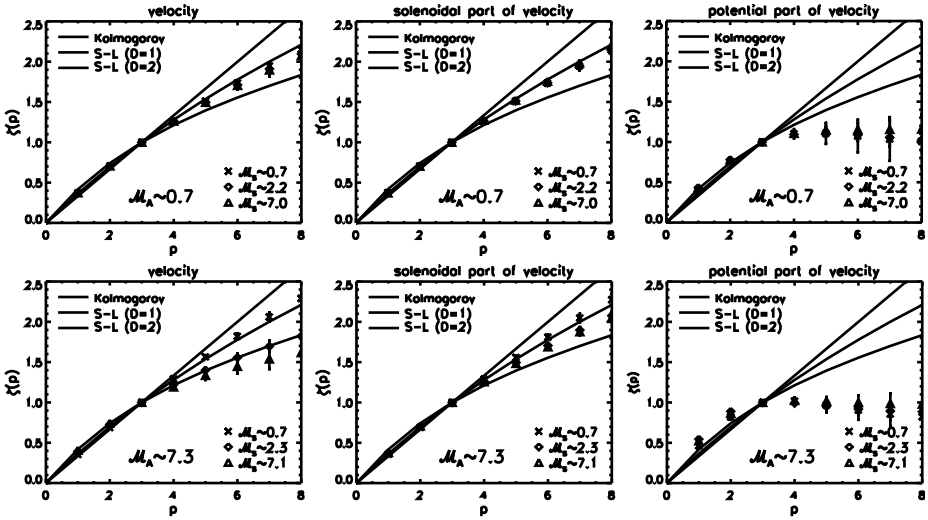

Figure 6.2: Intermittency of compressible turbulence. Scaling exponents of the velocity (left column) and its incompressible and compressible parts (middle and right columns, respectively) for experiments with different sonic Mach numbers in two regimes: sub-Alfvénic (upper row) and super-Alfvénic (lower row) from KL10. Reproduced from [231] with permission of AAS.

She–Lévêque scaling with $D = 1$. This means that most of the dissipative structures are one dimensional. Even though the scalings are not perfectly independent of the value of $\mathcal{M}_s$, since we see somewhat lower values of ζ for higher p, the differences between these values for models with different sonic Mach numbers are within their error bars. Thus the scalings at most only weakly dependent of the values of $\mathcal{M}_s$. At the same time, in the corresponding plot for models with a weak magnetic field we clearly see that the spread of curves for different sonic Mach numbers is much higher than in the previous case. For subsonic simulations, the scaling exponents of velocity

follow well the theoretical curve corresponding to the S-L scaling of one-dimensional dissipation structures. The simulations with $\mathcal{M}_s \sim 2.3$, however, correspond to the S-L scaling of two-dimensional dissipative structures. One can also see that simulations with even higher values of the sonic Mach number have the scaling exponents for $p > 3$ somewhat below the S-L scaling with $D = 2$. These studies suggest that the scaling exponents of the velocity do change with the sonic Mach number in the case of weak magnetic field turbulence. However, the presence of a strong magnetic field significantly reduces these changes and preserves the generation of the dissipative structures with the dimension higher than one.

The scaling exponents can also be calculated after the decomposition of velocity into its incompressible and compressible parts. In the middle and right columns of Figure 6.2, the incompressible and compressible parts of the velocity field are shown, respectively. The incompressible part contains most of the energy and its scaling exponents are very similar to those observed in velocity. This is definitely true in the case of sub-Alfvénic models, and all curves in the middle left plot in Figure 6.2 corresponding to the S-L scaling with $D = 1$. The similarity between the total velocity and its solenoidal part is also evident in the case of super-Alfvénic models for subsonic case, when the role of shocks is strongly diminished. Two sets of supersonic simulations exhibit exponents following a scaling close to the S-L one with $D = 1$, yet still with lower values for $p > 3$.

6.5 Intermittency of viscosity-damped turbulence

In the viscously-damped case, it was proposed in LVC04 [280] that the higher moments of structure functions will scale as $l^{1/2}$ for the first moment and zero for larger moments. In Figure 6.3, we see this general tendency for high p. The correspondence is not precise however the model strongly argues in favor of k^{-1} (which correspond to $\xi(2) = 0$). However, in numerics the spectra are slightly steeper.

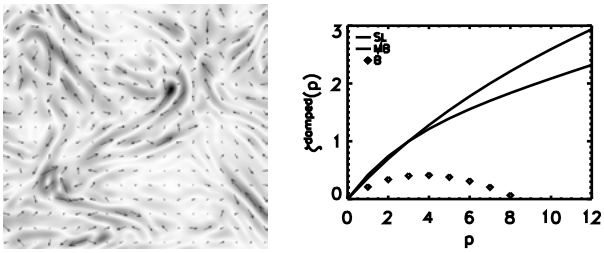

Figure 6.3: The incompressible viscously damped turbulence. *Left*: Magnetic reversals in the plane perpendicular to mean field $\langle \mathbf{B} \rangle$ create current sheets and makes turbulence highly intermittent. Darker regions correspond to higher magnetic field. *Right*: Intermittency indexes in theories SL and MB and numerical data. Reproduced from [91] with permission of AAS.

7 Turbulence and charged particles

One of the consequences of turbulence, whether in laboratory, astrophysical, or laboratory plasmas, is the magnetic field line stochasticity, which plays a crucial role in most key physical processes, such as thermal conduction, reconnection and particle transport. Speaking of laboratory plasmas, the self-excited turbulence in tokamaks results in anomalous transport of particles perpendicular to the field and prevents reaching higher temperatures and densities. MHD turbulence also plays an important role in scattering and accelerating particles in astrophysics as well. The second-order Fermi acceleration can arise directly from the scattering of particles by turbulence because the elementary acts of scattering are produced by MHD waves, which act as a moving scattering centers required for Fermi's second mechanism; see, e. g., [314]. This process is relatively inefficient, being proportional to $(v/c)^2$, compared to first-order's v/c, e. g. diffusive shock acceleration [241, 18, 45]. Properties of MHD turbulence that we discussed above are essential to understanding this process. We refer the reader to [385] for an excellent reading on quasilinear theory (QLT) of particle scattering by stochastic fields. Note that the routine result of the QLT calculation is the second-order particle acceleration coefficient. The second-order process was thought to dominate in turbulence, as opposed to first-order acceleration on discontinuities. As we will show in subsequent sections of this chapter, this may not be necessarily true, i. e., there is an inherent first-order acceleration in turbulent fields as well.

If turbulence is injected at large scales, the anisotropy of Alfvénic modes at small scales makes them inefficient for scattering and acceleration of cosmic rays [70, 453]. In this situation, fast modes were identified as the major scattering and acceleration agent for cosmic rays and energetic particles in the ISM [454]. Turbulent magnetic field in the pre-shock and post-shock environment are important for the first-order Fermi acceleration associated with shocks. In particular, magnetic field enhancement compared to its typical interstellar values is important in the preshock region for the acceleration of high energy particles. Turbulent dynamo that we discussed in Chapter 2 can provide a way of generating magnetic field in the precursor of the shock. In [28], it was shown that the interactions of the density inhomogeneities preexisting in the interstellar medium with the precursor generate strong magnetic fields in the shock precursor. Similarly, magnetic reconnection can act as a converging flow and induce the first-order Fermi acceleration [111, 256].

While particles dynamics in turbulence is a large topic, in this chapter we overview a recent progress on two topics related to particle transport: (1) field line diffusion, in particular diffusion in imbalanced turbulence and (2) first-order acceleration in turbulent fields.

https://doi.org/10.1515/9783110263282-007

7.1 Particle diffusion due to stochastic fields

7.1.1 Richardson's picture of diffusion

Turbulence is now understood as a multiscale phenomenon, by large owing to the pioneering paper of Richardson [369], who studied turbulent diffusion and suggested that for scales less than the injection scale, the diffusion coefficient depends on the scale as $D \sim l^{4/3}$. This is known as Richardson's law. Indeed, if two particles are separated by a distance l, the typical separation speed corresponds to the typical turbulent velocity on scale l, which is, approximately, $\delta v \sim l^{1/3}$ [224]. This suggests that separation between particles grow as $\delta l \sim t^{2/3}$. If turbulence is uniform and characterized only by the dissipation rate per unit mass, ϵ, which has units of $\mathrm{cm}^2/\mathrm{s}^3$, it is natural that the separation between two particles moving with the fluid, $\Delta\mathbf{r}$, conforms to $(\Delta\mathbf{r})^2 = g_0 \epsilon t^3$, where g_0 is a dimensionless number known as Richardson's constant. Richardson's diffusion has been studied extensively by experimental, theoretical, and numerical means [379].

The turbulent diffusion of particles embedded in the MHD fluid received relatively less attention, however, the same type of diffusion is expected in perpendicular direction due to the same scaling $\delta v \sim l^{1/3}$ of strong MHD turbulence [172, 21, 22]. A different and very interesting question is how the magnetic field lines separate from each other in such an environment. This question is crucial because well-magnetized plasmas are often poorly collisional, with the ion Larmor radius being many orders of magnitude smaller that the mean-free path from Coulomb collisions. In particular, the magnetized solar wind features mean-free paths, which are comparable to the distance from the sun. In galaxy clusters, the Coulomb mean-free path is around 10–100 kpc. In most astrophysical environments, there is also a high-energy component, called cosmic rays, for which Coulomb collisions are essentially negligible. Charged particles will, therefore, move along magnetic field lines for great distances and scatter mostly by magnetic perturbations. This will result in parallel diffusion being much larger than the perpendicular diffusion. In the absence of perpendicular momentum, particles will move along magnetic field lines and diffuse only due to the magnetic field line diffusion. The motion of the bulk of the plasma δv that causes ordinary diffusion could be neglected if the ion speed v_i is much larger than δv.[1] For cosmic rays this condition is also very well satisfied, because they move along field lines with the speed comparable to the speed of light c. In other words, at least for short timescales, the fluid is frozen from most particles' perspective.

1 This is equivalent to the condition that the motions in the inertial range are subsonic. While some of the astrophysical turbulence feature supersonic motions on the outer scale, the inertial range motions are normally subsonic.

7.1.2 Field line diffusion

Despite being collisionless, plasmas in many circumstance can be described as fluids on scales larger that the ion Larmor radius [382]. The inertial range of MHD turbulence feature strongly anisotropic perturbations which are much smaller in amplitude that the mean magnetic field. The key component of this turbulence is Alfvenic mode, which is why it is often called Alfvenic turbulence. Due to the fact that the Alfven mode is driven by magnetic tension, not pressure, it is relatively unaffected by the lack of collisions. The presence of slow mode in such highly anisotropic turbulence neither affect dynamics [172, 22], nor influences magnetic field lines, as the anisotropic slow mode perturbation is mostly along the mean field. Therefore, the equations for the Alfvenic components, which are conventionally called reduced MHD (RMHD), are sufficient for studying field lines.

Perturbations in a strong mean magnetic field could be decomposed into backward and forward propagating eigenmodes $\mathbf{w}^{\pm} = \mathbf{v} \pm \mathbf{b}/\sqrt{4\pi\rho}$ called Elsässer variables. Since perturbation sources are not uniform, MHD turbulence is naturally *imbalanced*, i. e., the amplitudes of w^{+} and w^{-} are not equal. This is verified by direct observations in the solar wind, where the dominant always propagates away from the sun [444]. Other astrophysical sources are expected to have strong imbalance, e. g., stellar winds and jets will emit predominantly outward-propagating component. Similarly, AGN jets are expected to have Alfvén perturbations propagating away from the central engine, e. g., due to the black hole spin [46]. The theories of imbalanced Alfvenic turbulence are fairly young and have been verified mostly by comparison with simulations [33, 21], although the solar wind measurements also show some promise. So far, the model most consistent with the data is [30], which correctly explains the ratio of anisotropies and the ratio of energies, given a certain ratio of energy fluxes. Imbalanced relativistic force-free MHD turbulence, supposedly existing in such objects as parsec-scale jets and GRB engines has been simulated recently by [87] and seem to exhibit properties consistent with the [30] model. Since we expect Alfvén mode to survive in low-collisional environments such as jets, pulsar winds, etc., we are particularly interested in the properties of magnetic field line diffusion of Alfvénic turbulence. The study of magnetic field diffusion is also equivalent to the study of charged particle diffusion in the limit of negligible pitch angle scattering, e. g., due to zero perpendicular momentum.

Assuming very strong mean field $\mathbf{B_0}$ pointing in the x direction, the equation for the magnetic field line is

$$\frac{d\mathbf{r}}{dx} = \frac{\mathbf{b}}{B_0}, \tag{7.1}$$

where the magnetic perturbation $\mathbf{b} = \mathbf{B} - \mathbf{B_0}$ is perpendicular to the mean field (Alfvén mode), so that the displacement vector r will only have perpendicular components.

Similarly, particles moving along such a field in one direction will only experience perpendicular diffusion, as $dx \gg |d\mathbf{r}|$.

7.1.3 Limiting cases: very small and very large distances

The nonlinear system's stochasticity is often characterized in terms of the so-called Lyapunov exponents, the separation rates, which are experienced by two close trajectories. It is clear that in the case of field line diffusion the separation on small distances could be obtained by Taylor expansion of the magnetic field, keeping only the linear terms. And the Lyapunov exponents, i. e., the λ in the $r \sim \exp(\lambda x)$ law, will be defined by the diagonal components of the matrix describing perpendicular gradients of the field,

$$\frac{1}{B_0}\frac{\partial B_i}{\partial r_j}. \tag{7.2}$$

After statistical averaging over different initial separations, the positive Lyapunov exponent will dominate, resulting in the growth of separations as

$$\langle \Delta r^2 \rangle \sim \exp(2\lambda|x|). \tag{7.3}$$

Note that this formula is exactly symmetric with respect to the sign of x.

If magnetic field lines separate for a distance much larger than the outer scale of turbulence L, the $\delta\mathbf{b}$ becomes truly random and independent of the separation. In this limit, the magnetic field lines experience random walk, i. e., ordinary diffusion

$$\langle \Delta r^2 \rangle = \frac{B_{\mathrm{rms}}|x|}{LB_0} \tag{7.4}$$

This limit is known as field line random walk (FLRW) and has been used to describe perpendicular diffusion in [204]. Note that the random walk depends only on the RMS of magnetic field and must also be symmetric with respect to the sign of x.

7.1.4 Intertial range distances – hand-waving derivation

Now imagine that we would like to see perpendicular diffusion again as a random walk, i. e., a Markovian process, but now the characteristic RMS would itself depend on the separation distance r. Let us say that we determine such an RMS by calculating first-order perpendicular structure function of $\mathbf{B}$, designate it B_r and assume that it follows Kolmogorov scaling $\delta B_r = Cr^{1/3}$; see, e. g., [25]. By solving $d\Delta\mathbf{r}/ds = \mathbf{B}_r/B_0$, we will find that

$$\langle \Delta r^2 \rangle = \frac{8}{27}C^3\frac{|x|^3}{B_0^3}. \tag{7.5}$$

Here, the diffusion is also symmetric with respect to x. The important limitation of this derivation is that we imagined Markovian process where each step does not depend on the previous steps. In the turbulent diffusion, this is normally not satisfied.

7.1.5 Inertial range distances – Richardson–Alfvén diffusion

Suppose we follow magnetic field lines started from two points, separated by a small initial distance r_0. As the difference between $\mathbf{B}$ scales as $\delta B_l \sim l^{1/3}$, we would expect a stochastic separation of the magnetic field lines in to follow the law:

$$\left\langle (\Delta \mathbf{r})^2 \right\rangle = g_m \epsilon v_A^{-3} |x|^3, \tag{7.6}$$

where ϵ is the dissipation rate per unit mass, as defined above, and $v_A = B_0/\sqrt{4\pi\rho}$ is the Alfvén speed. This expression can be obtained by replacing t in Richardson's formula with the time variable for the Alfven wave, $x/v_A - t$ with $t = 0$.

For the lack of a better term in the literature, we will designate this Richardson–Alfvén diffusion and term the dimensionless constant g_m Richardson–Alfvén constant. Although we call this diffusion by analogy with physical diffusion in time, this is rather a stochastic separation in space. Nevertheless, the term diffusion seems appropriate due to similarity with physical diffusion and relevance of this problem to perpendicular diffusion of particles.

If magnetic field lines separate for a distance much larger than the outer scale of turbulence L, the $\delta\mathbf{b}$ becomes truly random and independent of the separation. In this limit, the magnetic field lines experience random walk, i. e., ordinary diffusion $\langle (\Delta \mathbf{r})^2 \rangle \sim |x|$. This limit is known as field line random walk (FLRW) and has been used to describe perpendicular diffusion in [204]. Note that the random walk must be symmetric with respect to the sign of x.

7.1.6 Numerical results, asymmetric diffusion

We used magnetic field snapshots obtained in simulations of Alfvénic turbulence. These simulations solved the reduced MHD equations with explicit dissipation and driving to achieve statistically stationary state. Further details behind the RMHD rationale, simulation setup, driving, numerical scheme, etc., can be found in [22]. Each simulation represents stationary, strong MHD turbulence with strong mean field. The balanced simulation B1 has been previously reported in [21] and imbalanced simulations I1–6 has been reported in [34]. More details concerning these simulations can be found in the above references. The parameters of the simulations are summarized in Table 7.1, with the defining feature of each imbalance simulation being the ratio of the dissipation rates $\epsilon^{\pm}$ for Elsässer components $\mathbf{w}^{\pm}$.

Table 7.1: Simulation parameters.

Run	Resolution	ϵ^+/ϵ^-	w^+/w^-	$\ell^-_{\parallel *}/\ell^+_{\parallel *}$	g^+_m/g^-_m
B1	1536^3	1	1	1	1
I1	$512 \cdot 1024^2$	1.19	1.16	1.07	1.03
I3	$512 \cdot 1024^2$	1.41	1.37	1.15	1.15
I5	$1024 \cdot 1536^2$	2.00	2.36	1.36	1.31
I6	$1024 \cdot 1536^2$	4.50	6.70	1.78	1.71

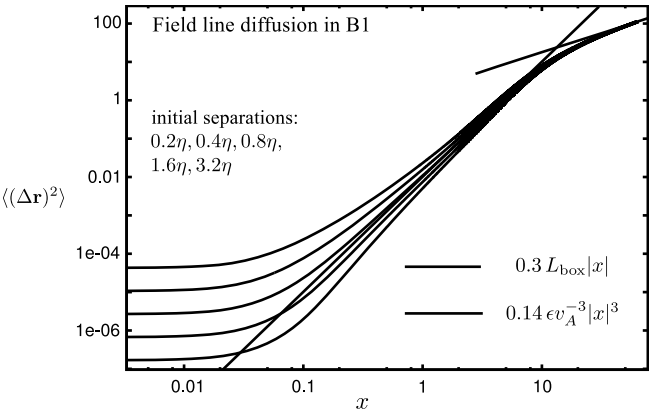

Figure 7.1: Diffusion of magnetic field lines. With initial separations r_0 ($0.2\eta \div 3.3\eta$) two field lines start diffusing apart at $r \sim 12\eta$ by Richardson–Alfvén law with $g_m = 0.14$ and transition to ordinary diffusion with coefficient $0.3L_{\rm box}$ at separations around outer scale of turbulence from [24]. Reproduced from [24] with permission of AAS.

We were tracking the pairs of magnetic field lines started at random positions throughout the box and initially separated by distance r_0 by Equation (7.1). Figure 7.1 shows the tracking results for the B1 simulation. The transition to Richardson's diffusion happens when particles are separated by around twelve Kolmogorov (dissipation) scales η. We chose five initial separations, fractions of η. At large distances, they seem to converge toward Richardson–Alfven diffusion with $g_m = 0.14$. At sufficiently large distances, the field lines started experiencing random walk, i. e., ordinary diffusion with diffusion coefficient of $0.3L_{\rm box}$. We typically used $4 \cdot 10^5$ field line pairs for statistical averaging.

The next tracking experiment involved simulations I1–I6. These also experienced Richardson–Alfvén diffusion, but now the diffusion speed was different depending on whether we track magnetic fields forward or backward (negative or positive dx). We plotted the ratio of forward to backward separations from the simulation I5 on Figure 7.2. It turned out that this ratio is fairly insensitive to the initial separation r_0, when r_0 was varied by a factor of around 16, with most difference being due to statistical error. Different snapshots of the same simulation showed more variation. We

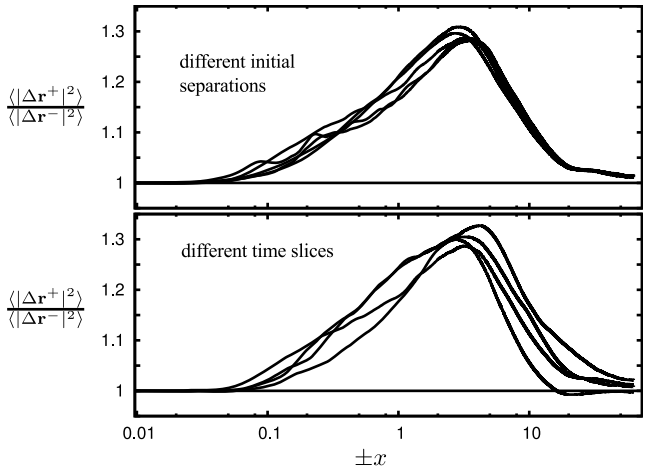

Figure 7.2: The ratio of forward to backward diffusion in datacubes from simulation I5. Upper plot shows five curves from the same datacube with different initial separations, same as on Figure 7.1. Lower plot shows time variability of the ratio. Reproduced from [24] with permission of AAS.

used this variation in time to estimate the error in the diffusion ratio. In the large x limit, this ratio went to unity, consistent with the symmetry of random walk. We estimated the ratio of Richardson–Alfven constants by taking the maximum of the ratio curves, which was also somewhere around the middle of the inertial range in terms of perpendicular separation. The measurements of the ratio g_m^+/g_m^- are presented in Table 7.1 and Figure 7.3.

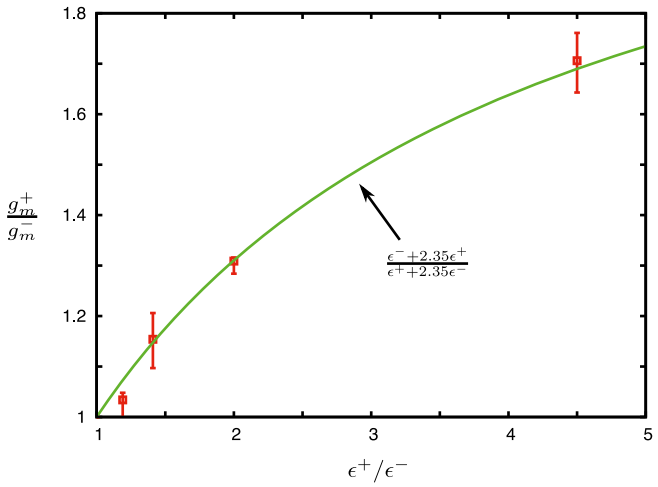

Figure 7.3: The ratio of forward to backward diffusion as a function of imbalance in energy fluxes.

7.1.7 The model of asymmetric diffusion

Hydrodynamic turbulent diffusion forward and backward in time is known to be different by a factor of $a \approx 2$ [42], which is due to fundamental nonreversibility of turbulence. In our case, the diffusion of magnetic field lines comes from the w^+ component, which propagates against mean field and w^- component which propagates along mean field. The diffusion of field lines along the field will be "forward in time" for w^- and "backward in time" for w^+ and vice versa for the opposite direction. Assuming that the diffusion from $b^\pm$ is proportional to the energy flux $\epsilon^\pm$, we can write for the diffusion asymmetry:

$$\frac{g_m^+}{g_m^-} = \frac{\epsilon^- + a_m \epsilon^+}{a_m \epsilon^- + \epsilon^+}, \tag{7.7}$$

where a_m is the time-asymmetry in MHD turbulence. Figure 7.3 indicates that this model agrees with data reasonably well, as long as $a_m = 2.2 \div 2.5$, which is compatible with hydrodynamic time-asymmetry. From the balanced value of $g_m = 0.14$, we can also derive Richardson–Alfven constants forward and backward in time: $g_{t+} = 0.084$, $g_{t-} = 0.196$.

Equation (7.6) looks similar to the critical balance of [172]. Introducing anisotropy constant C_A, critical balance can be written as $\ell_\parallel = C_A v_A \ell_\perp^{2/3} \epsilon^{-1/3}$ [22], where $\ell_\parallel$ is the distance parallel to the field, i. e., analogous to x and $\ell_\perp$ is a perpendicular distance. This is indeed the same functional dependence as Equation (7.6). However, if the assume that these relations are identical, this would imply that $C_A = g_m^{-1/3}$. This is not satisfied, however. The difference is that the measurement of the diverging magnetic fields is quasi-Lagrangian, while the measurement of structure function that lead to anisotropy constant is Eulerian. This difference becomes even more pronounced in the imbalanced case, where each of the $w^\pm$ components has its own anisotropy. The analogy between Richardson–Alfven diffusion and critical balance would suggest that $g^+(\ell_\parallel^+)^3 = g^-(\ell_\parallel^-)^3$. We presented the ratio of parallel scales in the middle of the inertial range in Table 7.1. As we see, the expression above is not satisfied and the ratio of magnetic diffusions cannot be explained by the anisotropy difference. So, despite the similar functional form, Richardson–Alfvén diffusion has no direct relationship to Goldreich–Sridhar anisotropy.

7.1.8 Implications of asymmetric field line wandering for particle transport

Our measurement is the first demonstration of the x^3 superdiffusion of magnetic field lines in simulations of MHD turbulence. Superdiffusion of fast particles in the solar wind has been argued based on observational data [357]. Diffusion of field lines assuming arbitrary scaling of the magnetic spectrum has been first discussed in [204], however derived using Markovian delta-correlated field structure producing exactly

symmetric diffusion, as in Section 7.1.4. Subsequent work employed Goldreich-Sridhar scaling to predict superdiffusion of particles based on superdiffusion of field lines [336, 257]. The reconnection model [278] also used the same scaling for field line diffusion. All of this work predicted summetric diffusion, while the asymmetric superdiffusion was discovered only later in [24]. The earlier measurement of perpendicular diffusion using MHD simulations [41] has been made in the large separation limit and reproduced FLRW, which is symmetric. The measurements of cosmic ray propagation in artificial random fields, such as [163] can, in principle, reproduce superdiffusion, but since artificial fields lack the time-asymmetry of turbulent fields, they cannot reproduce asymmetric diffusion. Based on the similarity between Goldreich–Sridhar anisotropy and Richardson's diffusion [336] suggested that magnetic field lines separate within the Goldreich–Sridhar cone, however, according to the section above, this analogy is misleading, especially in the imbalanced case. Time-asymmetry of turbulence, that we confirmed in this article, have consequences for small-scale dynamo as well [23].

One of the consequences of asymmetric perpendicular diffusion is an induced streaming. Indeed, if we consider two close magnetic field tubes, one of which is filled with isotropically distributed particles and another empty, the asymmetric diffusion into the empty tube will result in an average streaming $\sim (1 - g^+/g^-)$ of the particle's velocity. In particular, for relativistic particles, such as cosmic rays, this will result in streaming velocity of $2c(1 - g^+/g^-)/\pi$, which could easily exceed the threshold for streaming instability, v_A as long as imbalance amplitude $1-w^-/w^+$ exceeds $(3\pi/2)v_A/c$, which is around 10^{-4} in the WISM. Therefore, the induced streaming will be counteracted by streaming instability [244]. Above the threshold for turbulent damping [148, 31, 276], streaming instability will be suppressed and, it can be shown that the weak large-scale streaming should reappear at energies 10^{11} eV and strong streaming is expected above $3 \cdot 10^{13}$ eV, although such energies are already heavily influenced by pitch-angle scattering. The net effect of the streaming instability from particles with energies below $3 \cdot 10^{13}$ eV will be a flux of slab waves which will increase the rate of pitch-angle scattering for these particles.

7.2 Turbulence and particle acceleration

7.2.1 Observational evidence for acceleration different from classic DSA

Magnetically-dominated environments are fairly common in Astrophysics and a sizable fraction of astrophysical objects are made of rarefied plasma. These objects are only visible because they contain a nonthermal particle population, which dominates emission across most of the spectrum. The basic idea that nonthermal emission require particle acceleration has been around for some time. One of the main elements of the explanation of how energy is being transferred to particles is the mechanism of energy dissipation. Indeed, if astrophysical fluids may be considered almost inviscid

and perfectly conducting, how large-scale energy can be lost to thermal and nonthermal particles. Few mechanisms has been suggested: (a) discontinuities in the fluid motion, e. g., shocks, (b) turbulence, and (c) discontinuities in the magnetic field, i. e., current sheets. Following the idea of [151] that collisionless particles can get energy by scattering in fluid motions, especially converging motions, the diffusive shock acceleration (DSA) mechanism has been proposed [241, 18, 302] and has become rather popular in explaining nonthermal electromagnetic emission, as well as cosmic rays—energetic charged particles, detected at Earth. In the DSA, however, the acceleration rate is related to the scattering rate, with the latter being importantly bound by the so-called Bohm limit, which assumes that scattering rate must be lower than Larmor gyration frequency. This makes acceleration progressively slower at higher energies. On the other hand, the observations of many variable astrophysical objects suggested extremely fast acceleration timescales, incompatible with DSA. Few blazar jets powered by supermassive black holes exhibit ~ 10 min variations in TeV emissions, e. g., [2, 5]. Such fast time variabilities, along with other emission region constraints, have been suggested as evidence for mini-jets generated by reconnection [166]. Recent observations of gamma-ray flares from Crab [1] revealed that the impulsive nature of the energy release and the associated particle acceleration might need an alternative explanation as well [100]. It has also been suggested that reconnection plays a crucial role in producing high energy emissions from gamma-ray bursts [464].

In the environments which are known to be magnetically dominated, e. g., the solar corona or the pulsar wind nebula, it is natural to expect the magnetic energy to be the main source. The global energetics of the powerful X-ray flares confirm this natural assumption. Reconnection and associated phenomena has been a active field of study; see, e. g., [425] for a review. It would be interesting to find if there a generic mechanism to transfer magnetic energy into particles and to conceptually understand the nature of recent numerical results that demonstrated that in both MHD fluid simulations [227] and ab-initio plasma simulations [397, 186, 427] of reconnection there is a regular acceleration of particles

Particle acceleration is often classified into "first-order Fermi" mechanism where particles are gaining energy regularly, e. g., by colliding with converging magnetic mirrors and "second-order Fermi" where particles can both gain and lose energy [151]. These two are not mutually exclusive and represent two different terms in the equation for the evolution of the distribution function: the terms describing advection and diffusion in energy space correspondingly. In practical terms, the first-order mechanism usually dominates, if present, as the acceleration rate is proportional to the first order of u/v, where u is the typical velocity of the scatterer and v is the particle velocity. The outcome of the first-order acceleration can be described in terms of the rate at which particle gain energy, acceleration rate, $r_{\rm acc}$, and the rate of particle escaping from the system, $r_{\rm esc}$. If escape is negligible and $r_{\rm acc}$ is constant with energy, the energy of each particle grows exponentially. Also, if $r_{\rm esc}/r_{\rm acc}$ does not depend on energy, the stationary solution for the particle distribution is a power-law, with the power

law index determined by $-1 - r_{esc}/r_{acc}$; see, e. g., [125]. Various environments, such as supernova shocks, were thought to satisfy this condition and produce power-law distributed cosmic rays, which become consistent with observations after being modified by diffusion. Acceleration within many orders of magnitude in energy was regarded as a result of a large-scale physical layout of the acceleration site, e. g., the planar shock can be thought of as a set of large-scale converging mirrors. The very same picture could also be applied to the large-scale reconnection site, where the two sides of the inflow effectively work as converging mirrors [111]. In this chapter, we deviate from this mindset of the problem that achieve scale-free acceleration just because there is only a single scale—the scale of the system. Instead we will try to find regular acceleration over large energy ranges in systems that do not necessarily possess global regular structure; however, they could still be scale-free in statistical sense, such as turbulent systems. Normally, turbulent environments are expected to be regions of second-order acceleration; see, e. g., [385, 85]. In this section, we point to the different mechanism of regular or first-order acceleration. This mechanism is inherently related to a certain statistical measure of energy transfer in turbulence and, therefore, does not rely on a particular geometry and is very robust. As we will show below, the direction of energy transfer from magnetic field to kinetic motions and the sign of curvature drift acceleration are inherently related, so that in systems with the average positive energy transfer from magnetic energy to kinetic motions there is an average positive curvature drift acceleration, while in the opposite case, there is an average curvature drift cooling.

One of the commonly considered cases of magnetically-driven flows is magnetic reconnection. A significant effort was put into understanding on ideal plasma effects that could both cause reconnection and create nonzero parallel component of the electric field [364, 154]. In this section, we apply our model to reconnecting layers which are large-scale in a sense that the current layer is many orders of magnitude thicker than the ion skin depth d_i. In this case, the reconnecting layer may have multiple X-points and while nonideal effects are indeed required for the individual field lines to break and reconnect, their influence is limited to fairly small scales, typically around the ion skin depth d_i. In this section, we instead focus on larger scales and ignore nonideal effects for the following two reasons. First, it has been argued that understanding of global energetics of large-scale reconnection, such as the amount of magnetic energy dissipated per unit time, does not require detailed knowledge on how individual field lines break and reconnect; see Chapter 8 and [278, 143, 297, 27]. These global energetic parameters, as we will show below, could be more important for acceleration to high energies than local nonideal effects. Second, in order to understand high energy particle acceleration, one normally has to consider plasma dynamics on scales much larger than d_i, that is on MHD scales. We do not address here the problem of the acceleration from the thermal pool, for which plasma effects are important. While modern simulations such as [397, 186, 427], are able to reach box sizes of several hundred d_i, some theory work is needed to disentangle acceleration from MHD and the nonideal

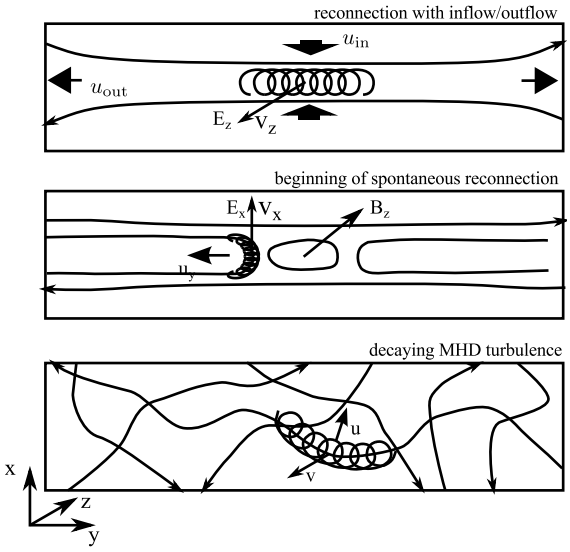

Figure 7.4: Several acceleration mechanisms in the case of magnetic relaxation and/or dissipation The upper panel – reconnection with inflow and outflow. The middle panel – spontaneous reconnection with negligible inflow. The bottom panel – homogeneous decaying MHD turbulence. Reproduced from [38] with permission of AAS.

effects. The particle acceleration produced in the convergent flow of MHD-scale reconnection was discussed in [111, 256] and tested in [227]. This case is conceptually similar to shock acceleration [124]. Below we discuss an alternative mechanism based on curvature drift acceleration which is expected to be efficient in reconnection, as well as other types of magnetically-driven turbulence. Figure 7.4 shows a cartoon of several acceleration mechanisms in magnetized environments. The upper panel depicts reconnection with inflow and outflow where particles can be accelerated regularly due to the gradient drift and the large-scale electric field. The acceleration term is dominated by v_z and E_z. The middle panel depicts initial stages of spontaneous reconnection, which has negligible inflow, therefore, the gradient drift term averages out. In this case, acceleration is mostly driven by contracting field lines which drive fluid motion and at the same time cause the curvature drift of particles. Note that the direction of drift is typically perpendicular to the fluid motion. The dominant acceleration term is associated with E_x and the field curvature of B_y component. The bottom panel depicts the same mechanism in a more homogeneous and isotropic setup of decaying MHD turbulence, which also has contracting field lines. In this situation, all vector components contribute equally.

7.2.2 Statistics of general MHD flows and energy transfer

Well-conductive plasmas can be described on large scales as inviscid and perfectly conducting fluid (ideal MHD). The ideal MHD equations allows for exchange between kinetic and magnetic energies. The Lorentz force density, multiplied by the fluid velocity, $\mathbf{u} \cdot [\mathbf{j} \times \mathbf{B}]/c$ is the amount of energy transferred from magnetic to kinetic energy.

While macroscopic (i. e., kinetic plus magnetic) energy is expected to be conserved in the ideal MHD, it is not the case in real systems which have nonzero dissipation coefficients. This is qualitatively explained by the nonlinear turbulent cascade that brings macroscopic energy to smaller and smaller scales until it dissipates into thermal energy. One of the important examples of this is the spontaneous reconnection where the thin current layer becomes turbulent and starts dissipating magnetic energy at a constant rate. The small scales of these turbulent flows resemble "normal" MHD turbulence, which has equipartition between magnetic and kinetic energies [27]; it is also true that kinetic and magnetic part of the cascade each contribute around half of the total cascade rate. Therefore, if we assume that the turbulent cascade is being fed with magnetic energy, approximately half of the magnetic energy has to be transferred into kinetic energy before equipartition cascade sets in. It follows that the **B** to **v** energy transfer must be *positive on average* and could be approximated by one half of the volumetric energy dissipation rate ϵ, the main parameter of turbulence. The term $\mathbf{u} \cdot [\mathbf{j} \times \mathbf{B}]/c$ is the Eulerian expression for the work done by magnetic tension upon the fluid element. This term can be rewritten as the sum of $-(\mathbf{u} \cdot \nabla)B^2/8\pi$, advection of magnetic energy density by the fluid, and

$$\mathcal{T}_{bv} = \mathbf{u} \cdot (\mathbf{B} \cdot \nabla)\mathbf{B}/4\pi, \tag{7.8}$$

the actual energy transfer between **B** and **v**. For the purpose of future calculations, we will separate the $\mathcal{T}_{bv}$ in the following way:

$$\begin{aligned} \mathcal{T} &= \frac{1}{4\pi}\mathbf{u} \cdot (\mathbf{B} \cdot \nabla)\mathbf{B} \\ &= \frac{1}{4\pi}(\mathbf{u} \cdot \mathbf{B})(\mathbf{b} \cdot \nabla)B + \frac{B}{4\pi}\mathbf{u} \cdot (\mathbf{B} \cdot \nabla)\mathbf{b} = \mathcal{X} + \mathcal{D}, \end{aligned} \tag{7.9}$$

where we designated $\mathbf{b} = \mathbf{B}/B$, a unit magnetic vector. The term $\mathcal{X}$ contains cross helicity density $\mathbf{u} \cdot \mathbf{B}$. We argue that in those systems where $\langle \mathbf{u} \cdot \mathbf{B} \rangle = 0$, which include many physically relevant cases, such as spontaneous reconnection, the whole $\mathcal{X}$ term could average out (see also Figure 7.5). The second term $\mathcal{D}$ contains magnetic field curvature $(\mathbf{B} \cdot \nabla)\mathbf{b}$ and will be important for subsequent calculation of curvature drift.

7.2.3 Acceleration by curvature drift

To explore the implications of magnetic energy transfer in nonthermal particle acceleration, it is instructive to consider the particles motion in slowly-varying electric and magnetic field, which can be described in the so-called drift approximation. The leading drift terms are known as electric, gradient, and curvature drifts. While electric drift, proportional to $[\mathbf{E} \times \mathbf{B}]$, cannot produce acceleration, the other two drifts can. For example, imagine the configuration of the reconnection with the inflow, Figure 7.4 top panel. The gradient drift $\sim [\mathbf{B} \times \nabla B]$ is along $-z$, and so is the electric field in the

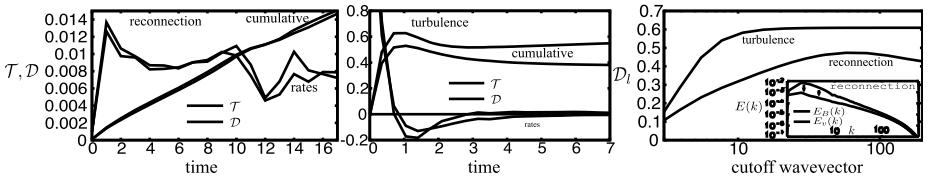

Figure 7.5: A case study of terms related to curvature drift acceleration and energy conversion in spontaneous reconnection and decaying MHD turbulence. Left panel: Case A, volumetrically averaged energy conversion rate $\mathcal{T}$ and curvature acceleration rate $\mathcal{D}$ in MHD simulation with turbulent current layer produced by spontaneous reconnection with setup described in [27]. Right panel: Case B, the same for decaying turbulence generated by random initial field. On both panels, we also show cumulatives $\int \{\mathcal{T}, \mathcal{D}\} dt$. The reconnection case (left panel) is characterized by approximately constant turbulent dissipation rate and it also shows a stable rate of energy conversion $\mathcal{T}$, while $\mathcal{D}$ closely follows $\mathcal{T}$. The decaying turbulence (middle panel) shows a burst of energy conversion rate within a few dynamical times (Alfvénic times). In both cases, the gradient drift acceleration term (not shown) is relatively negligible. Bottom panel shows the scale-dependency of the $\mathcal{D}$ term, by plotting $\mathcal{D}_l$, which is obtained by calculating $\mathcal{D}$ with a coarse-grained dynamical quantities $\mathbf{v}$, $\mathbf{B}$ (Gaussian low pass filter in Fourier space with a cutoff wavenumber $k = 2\pi/l$). $\mathcal{D}_l$ has a physical meaning of all energy transfer B to v accumulated down to scale l, for which reason it asymptotes to a constant at small l or large cutoff wavenumbers. The inset in the right panel shows kinetic and magnetic spectra in case A to demonstrate the range of scales within which magnetic energy is transferred to kinetic—down to $k \approx 30$ with thick arrows depicting the energy transfer. Reproduced from [38] with permission of AAS.

ideal case $E = -[\mathbf{u} \times \mathbf{B}]/c$. Their product will be positive and will result in acceleration which is due to particles being compressed by the converging inflow. This mechanism does not work in the initial, most energetic stages of spontaneous reconnection, which has negligible inflow, Figure 7.4 middle panel [27]. It is this initial stage that has the highest volumetric dissipation rate, however. Figure 7.4 illustrates why curvature drift acceleration is important in this configuration. It also turns out that in any magnetically-driven turbulent environment, such as depicted on the bottom panel of Figure 7.4, curvature drift acceleration will accelerate particles on average.

Let us look carefully at the term which is responsible for acceleration by curvature drift,

$$\frac{d\mathcal{E}}{dt} = -2\frac{\mathcal{E}_\parallel}{B}[\mathbf{u} \times \mathbf{B}] \cdot [\mathbf{b} \times (\mathbf{b} \cdot \nabla)\mathbf{b}], \tag{7.10}$$

(see, e. g., [398]), where $\mathcal{E}_\parallel = v_\parallel p_\parallel/2 = \gamma m v_\parallel^2/2$ is a particle's parallel kinetic energy. With some manipulation, this expression could be equivalently transformed as $2(\mathcal{E}_\parallel/B)\mathbf{u} \cdot (\mathbf{B} \cdot \nabla)\mathbf{b}$. It now becomes clear that this term is related to the transfer rate between magnetic and kinetic energies, in particular it is a fraction of $\mathcal{D}$:

$$\frac{d\mathcal{E}}{dt} = \mathcal{E}_\parallel \frac{8\pi}{B^2}\mathcal{D}. \tag{7.11}$$

The physical meaning of this equation is that, given efficient particle scattering, so that $\mathcal{E}_\parallel = \mathcal{E}/2$, the acceleration rate is determined by the half of the local energy transfer rate $8\pi\mathcal{D}/B^2$, not including the $\mathcal{X}$ term.

7.2.4 Numerical case study of two types of turbulence

We can test the general ideas outlined above in two physical cases that feature turbulent energy transfer from magnetic to kinetic energies. Using spontaneous reconnection and the decaying MHD turbulence simulated numerically, we can directly calculate the discussed terms and compare them. The spontaneous reconnection numerical experiment was started with thin planar current sheet and small perturbations in **u** and **B** and was described in detail in [27], while the decaying MHD turbulence was similar to our previous incompressible driven simulations in [32], except that there was no driving and the initial conditions were set as a random magnetic field with wavenumbers $1 < k < 5$ and zero velocity. Both simulations developed magnetically-driven flows, from which we calculated the average $\mathcal{T}$, $\mathcal{D}$, and $\mathcal{X}$ terms and presented them in Figure 7.5.

The spontaneous reconnection case had fairly stable reconnection rate, this also corresponded to the approximately constant $\mathcal{D}$ integrated over the volume. The $\mathcal{X}$ term did not seem to be sign-definite and contributed relatively little. Gradient drift acceleration was also negligible, possibly due to the absence of global compression. Keeping in mind that all the energy had to come from magnetic energy, and given that the dissipation rate was approximately constant, it was no surprise that the average $\mathcal{D}$ term evolved relatively little. It should be noted, however, that in the spontaneous reconnection experiment the width of the reconnection region was growing approximately linear with time [27], so the $\mathcal{D}$ term magnitude, pertaining to the reconnection region itself was much higher than that of an averaged $\mathcal{D}$ over the total volume. Given the reconnection layer thickness $l(t)$, the local $\mathcal{D}$ could be estimated as $(1/2)v_r(B^2/8\pi)/l(t)$, where v_r is a reconnection rate, which was $v_r \approx 0.015v_A$ in [27] and the 1/2 comes from only half of magnetic energy being transferred into kinetic energy before physically dissipating on very small dissipation scale $\eta \ll l(t)$. This would correspond to acceleration rate of $(1/4)v_r/l(t)$ and can be very high, because the $l(t)$ could be as small as the Sweet-Parker current sheet width or the ion skin depth.

The decaying MHD turbulence experienced two regimes: (1) the initial oscillation when excessive amount of magnetic energy was converted into kinetic energy and the bounce back and partial inverse conversion afterwards, and (2) the self-similar decay stage of MHD turbulence. The first stage had the strongest conversion term which was dominated by $\mathcal{D}$. All terms integrated over time were mostly accumulated within the first 1–2 Alfvénic times.

It is known from turbulence theory that the energy transfer rate $\mathcal{T}$ can be demonstrated to be local in scale, under relatively weak assumptions [9, 23]. The scale-locality means that each scale contributes to the transfer independently. We also know empirically that most of the transfer between magnetic and kinetic energies happens on relatively large scales which are comparable to the outer scale of the system, while below outer scale there is little average transfer due to an approximate equipartition between kinetic and magnetic energies. For example, the reconnecting

turbulent current layer has most of its $\mathcal{T}$ transfer within a factor of a few of the scale of the layer thickness, while in the decaying turbulence problem it is within a factor of a few from the outer scale of the system. Let us designate $\mathcal{T}_l$ as a transfer calculated from quantities which were filtered by low-pass Gaussian filter with a cutoff wavenumber of $1/l$. Keeping in mind of locality, we will conclude that only scales larger than l will contribute to $\mathcal{T}_l$. This means that $\mathcal{T}_l$ will be constant for small l and will start decreasing when l approaches the outer scale of the problem L. In general, we cannot deduce the same for $\mathcal{D}_l$ and $\mathcal{X}_l$, but keeping in mind that $\mathcal{X}_l$ contributes relatively little in two cases that we considered, $\mathcal{D}_l \approx \mathcal{T}_l$ in those cases. Figure 7.5 demonstrates this behavior on the bottom panel, where energy transfer is operating between wavenumbers 2 and 20 in the reconnection case (1/20 is approximately the layer width at this point), and the $\mathcal{D}_l$ mostly changes within the same range of scales. The decaying turbulence case has the transfer more localized around the outer scales.

In terms of drift, the particle with Larmor radius r_L will "feel" magnetic and electric fields on scales larger than r_L, while the scales smaller or equal to r_L will contribute to particle scattering. It follows that the "effective" $\mathcal{D}$ will be $\mathcal{D}_{r_L}$, an implicit function of energy. Combining this with the result obtained above that $\mathcal{D}_l$ goes to a constant for small l, we conclude that the acceleration rate will also go to a constant for particles with r_L smaller than the system size. A similar, more hand-waving argument, is that the term $\mathcal{D}_l$ could be roughly approximated as $B_l^2 v_l / l$, resembles turbulent energy transfer rate, which is scale-independent. Interestingly, starting with scale independent energy transfer in turbulence we arrived at the energy-independent acceleration rates. Given the generality of the arguments presented above, it is not surprising that energy-independent rates were indeed observed in simulations [186].

7.2.5 Expected picture for turbulent acceleration in reconnection

The development of the thin current sheet instability results in turbulence and reconnection in a sense of dissipated magnetic energy. This process will come through two distinct regimes, the regime without significant outflow for times smaller than L/v_A [27] and the stationary reconnection with outflow for larger times [278]. Let us consider the first regime which has larger dissipation rate per unit volume, because the current layer thickness $l(t) = v_r t$ is relatively small. We use v_r for the reconnection rate and t as the time since the beginning of spontaneous reconnection. Let us assume that the current layer thickness is limited from below by the ion skin depth. We will have acceleration rate of $1/(4t)$ for all times larger than d_i/v_r but smaller than L/v_A. The solution for energy, therefore, will be $\mathcal{E} = \mathcal{E}_0 (t v_r / d_i)^{1/4}$ where $\mathcal{E}_0$ is the initial energy, e. g., the thermal energy. The particle's energy will be $\mathcal{E}_{\max} = 0.35 \mathcal{E}_0 (L/d_i)^{1/4}$ given the reconnection rate $v_r = 0.015 v_A$. This, however, is only the maximum energy of accelerated particles, as only a tiny fraction of particles were contained in the original thin current

sheet and started accelerated from initial time d_i/v_r [186]. With proper stochastic treatment and assuming that the escape rate r_{esc} is negligible compared with acceleration rate in this no-outflow problem, we expect to see the power law particle spectrum with the –1 slope and a cutoff at $\mathcal{E}_{max}$.

The subsequent development of an outflow will do three things: first, it will enable the inflow and, therefore, the extra acceleration term associated with gradient drift or converging magnetic mirrors [111]. Second, it will stabilize acceleration rate for the curvature drift acceleration at $v_A/4L$, as the current layer is no longer expanding. Third, it will enable particle escape through the outflow. In this regime, the spectrum will extend from $\mathcal{E}_{max}$ to higher energies, up to Larmor radii of the large scale of the current sheet L. The spectral slope of this extension will be determined by $-1-r_{esc}/r_{acc}$, where r_{acc} should account for all acceleration and cooling mechanisms, such as gradient drift acceleration and outflow cooling. The detailed analysis of this stage will be the subject of a future work.

The electron spectra observed in solar X-ray flares are fitted with the thermal component with temperature of several keV and the steep power law component. This is consistent with our picture, as the rather shallow –1 slope, containing most of its energy near $\mathcal{E}_{max}$, is likely to thermalize. Also, the outflow phase will extend this distribution as a power-law to higher energies.

Magnetic configurations that relax to the lower states of magnetic energy will also regularly accelerate particles, on timescales which are, typically, Alfvénic, but can be much shorter, e. g., in the beginning of spontaneous reconnection. This mechanism of acceleration of collisionless nonthermal particles by MHD electric field should not be confused with the acceleration of the bulk of the plasma by magnetic tension. Indeed, for particles with low energies the drift terms could be neglected, i. e., Equation 7.10 RHS will be trivially zero. In the bulk fluid acceleration, the energy gained by each particle does not depend on its initial energy, while for drift acceleration scenario it is proportional to the particle energy. Another way to understand the difference between plasma heating and our acceleration mechanism is to consider turbulent dynamo where kinetic energy of fluid motions is partially converted into magnetic energy and partially dissipated by the turbulent cascade. In this case, plasma will be heated due to the turbulent cascade, while we expect energetic particles to be cooled or decelerated by the curvature drift, since the $\mathcal{T}$ term will be negative. This means that the relation between energy dissipation and acceleration of particles is not trivial.

Some recent observations, e. g., [2, 1, 5] suggested high energy emission variability could be as fast as variability at lower energies, which is at odds with DSA, which predicts acceleration timescale proportional to diffusion coefficient which is typically a positive power of energy. This has been pointed out as a motivation for reconnection scenario [100, 166, 464].

Particle acceleration during reconnection is a topic under intense study, but the mechanism discussed in this section is distinctly different from the direct acceleration by the reconnecting electric field at the X-line. In fact, we completely ignore non-

ideal effects which produce local $\mathbf{E}\|\mathbf{B}$. Also, our mechanism is not tied to a special X-point, but instead volumetric. An interesting first-order acceleration mechanism in ideal MHD turbulence related to imbalanced turbulence and convergent field lines has been suggested recently by [386].

The regular acceleration due to converging field lines have been suggested in [111], later it was pointed by [124] that an outflow cooling should also be included. In this section, we do not rely on simple transport equation, such as Parker's, therefore, we relax the above approach's requirement that particles need to be almost isotropic. The acceleration in turbulent reconnection has been further numerically studied in [227]. Plasma PIC simulations has also been increasingly used to understand particle acceleration. The emphasis was mostly on the nonideal effects near X-line regions and interaction with magnetic islands [463, 364, 154, 122, 341, 197, 105]. The change of energy due to curvature drift in a single collision of a particle with magnetic island was estimated analytically in [122]. An important question that was left out in that study was whether this term will result in acceleration or cooling, on average. Without understanding this, it was not clear whether this process results in acceleration or deceleration or the second-order effect. In this section, we unambiguously decide this by relating the answer to a certain well-known statistical measure in turbulence—the direction of transfer between magnetic and kinetic energies. We also showed that the curvature drift acceleration does not require particles to be trapped in contracting magnetic islands, so their energy is not limited by this requirement, meaning that the energy cutoff is not related to the island size, instead it is related to the system size; see also [427].

PIC simulations are limited in the range of scales and energies they cover. Recent simulations in [397, 186] demonstrated acceleration up to 100 MeV in electron energies, which is below maximum energy in most astrophysical sources. Theory, therefore, is necessary to supplement conjectures based on the observed PIC distribution tails, explaining the underlying physical mechanism and making predictions for astrophysical systems which often feature gigantic scale separation between plasma scales and the size of the system. The feedback from simulations, nevertheless, was very useful, in particular the recent simulations [186] that reached MHD scales and confirmed the prediction that the curvature drift acceleration will dominate compared to the nonideal electric field acceleration.

8 Reconnection in the presence of MHD turbulence

8.1 The problem of reconnection

This is a chapter that deals with magnetic reconnection in astrophysical environments that are generically turbulent. We discuss how turbulence makes reconnection fast and what this means for many astrophysical systems.

8.1.1 Flux freezing and magnetic topology changes

Magnetic reconnection is a fundamental process that necessarily takes place in turbulent fluids. Indeed, the turbulent fluid motions move magnetic field lines and it is natural question to ask what happens when field lines intersect each other.

It is generally believed that magnetic fields both modify fluid dynamics and being embedded in a highly conductive fluid retain their topology for all time due to the magnetic fields being frozen-in [7, 352]. At the same time, highly conducting astrophysical objects, like stars and galactic disks, show evidence of changes in topology, i. e., "magnetic reconnection" that take place on dynamical time scales [351, 299, 363]. Historically, magnetic reconnection research was motivated by observations of the solar corona [199, 458, 305] and this resulted in attempts to find peculiar conditions conducive for flux conservation violation. Such studies included the search for special magnetic field configurations or special plasma conditions. However, it is clear that reconnection is a ubiquitous process taking place in various astrophysical environments. It is evident that without fast magnetic reconnection, magnetized fluids would behave like Jello or felt, rather than as a fluid.

What makes reconnection enigmatic is that observations indicate that reconnection can be sometimes fast and sometimes slow. Therefore, magnetic reconnection should have some sort of trigger. In what follows, we argue that the trigger is turbulence.

8.1.2 Sweet–Parker model and its generalization to turbulent media

To understand turbulent reconnection, it is a good start with the classical Sweet–Parker model of reconnection depicted in Figure 8.1.

The Sweet–Parker model is first successful analytical model for magnetic reconnection. It was proposed by Parker [349] and Sweet [412].[1] The Sweet–Parker model

1 The basic idea of the model was first discussed by Sweet and the corresponding paper by Parker refers to the model as "Sweet model."

https://doi.org/10.1515/9783110263282-008

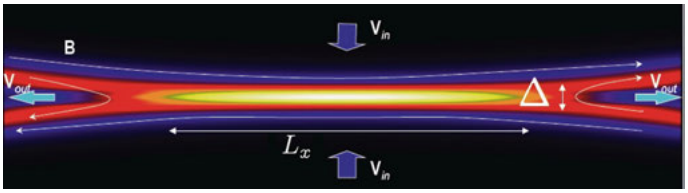

Figure 8.1: Sweet–Parker reconnection. Simulations of laminar reconnection from [233] are used. The current sheet has L_x extension, while the ejection of matter and shared component of magnetic field happens through Δ. The cross-section of the reconnection is shown. Generically, the shared component of magnetic field is directed perpendicular to the picture plane. This component should be also ejected through Δ.

relies on a robust and straightforward geometry (see Figure 8.1). Two regions with uniform *laminar* magnetic fields are separated by thin current sheet. The speed of reconnection is given roughly by the resistivity divided by the sheet thickness Δ, i. e.,

$$V_{\rm rec1} \approx \eta/\Delta. \tag{8.1}$$

One might think that by Δ it is possible increase the reconnection rate. In fact, for *steady state reconnection* the conservation of mass should be fulfilled and the plasma in the current sheet must be ejected at the edge of the current sheet. This enaction happens at the Alfvén speed, V_A and, therefore, the resulting reconnection speed is

$$V_{\rm rec2} \approx V_A\Delta/L_x, \tag{8.2}$$

where L_x is the length of the current sheet. The latter equation requires Δ to be large for a large reconnection speed. But at large Δ the rate annihilation of magnetic field lines prescribed by Equation (8.1) is small. As a result of the two contradictory requirements, the overall reconnection speed is reduced from the Alfvén speed by the square root of the Lundquist number, $S \equiv L_x V_A/\eta$, i. e.,

$$V_{\rm rec,SP} = V_A S^{-1/2}. \tag{8.3}$$

This reconnection speed is a compromise between the fast outflow rate and slow Ohmic diffusion rate. For astrophysical S that can be larger than 10^{16}, the corresponding Sweet–Parker reconnection speed is absolutely negligible.

The Sweet–Parker model is an idealization, as real astrophysical fluids are turbulent. Therefore, it is essential to explore how the Sweet–Parker reconnection is modified in the presence of turbulence. Figure 8.2 illustrates the modification that was suggested in Lazarian and Vishniac (1999) [278]; henceforth, LV99. It is evident from the figure that in the turbulent case in contrast to the Sweet–Parker case, the outflow is not limited by the microscopic region determined by resistivity, but is determined by magnetic wandering. The latter depends on the level of turbulence, e. g., the magnetic Mach number $M_A = u_{\rm inj}/V_A$, where $u_{\rm inj}$ is the turbulence injection velocity. Therefore,

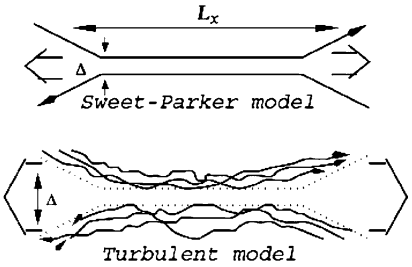

Figure 8.2: *Upper plot*: Sweet–Parker model of reconnection. The outflow is limited to a thin width δ, which is determined by Ohmic diffusivity. The other scale is an astrophysical scale $L_x \gg \delta$. Magnetic field lines are laminar. Modified from [280]. Reproduced by permission of the AAS.

there is no disparity between L_x and Δ, e. g., for trans-Alfvénic turbulence, i. e., for $M_A = 1$ the two scales can be comparable.

To generalize the Sweet–Parker model for the case of turbulence, it is natural to consider M_A which are smaller than one. If the turbulence is injected isotropically at scale L_i with the velocity $u_{\rm inj} < V_A$ gets into the regime of strong turbulence starting with the scale,

$$l_{\rm trans} \sim L_i (u_{\rm inj}/V_A)^2 = L_i M_A^2, \quad M_A < 1. \tag{8.4}$$

The relation between parallel and perpendicular scales in GS95 turbulence in the case of $M_A < 1$ were obtained in LV99:

$$l_\parallel \approx L_i (l_\perp / L_i)^{2/3} M_A^{-4/3} \tag{8.5}$$

Adopting that the field wandering is the cause of the reconnection zone broadening, it is easy to calculate Δ in the regime when the turbulence injection scale L_i is less than L_x. Adopting $l_\parallel = L_i$ in Equation (8.5), one finds that the perpendicular extend of the eddy at the injection scale is $L_i M_A^2$. The transverse contributions from different eddies at the injection scale are not correlated and, therefore, the growth of Δ is random walk with a step of $L_i M_A^2$. The number of the steps along L_x is L_x/L_i, and thus

$$\Delta \approx \left(\frac{L_x}{L_i}\right)^{1/2} L_i M_A^2, \quad L_i < L_x, \tag{8.6}$$

and, therefore,

$$v_{\rm rec,LV99} \approx V_A \left(\frac{L_i}{L_x}\right)^{1/2} M_A^2, \quad L_i < L_x, \tag{8.7}$$

which coincides with the LV99 result in this limit.

LV99 obtained also the result by calculating magnetic field wandering for $L_i > L_x$. The same result can be also obtained using the concept of Richardson dispersion that we have already discussed for MHD turbulence in Chapter 7.

Below we base our presentation on the approach in presented in [143]. Richardson diffusion/dispersion can be illustrated with a simple hydrodynamic model. Consider the growth of the separation between two particles $dl(t)/dt \sim v(l)$, which for

Kolmogorov turbulence is $\sim \alpha_t l^{1/3}$, where α_t is proportional to the energy cascading rate, i. e., $\alpha_t \approx V_L^3/L$ for turbulence injected with super-Alvénic velocity V_L at the scale L. The solution of this equation can be easily obtained:

$$l(t) = \left[l_0^{2/3} + \alpha_t (t - t_0)\right]^{3/2}, \tag{8.8}$$

which at late times leads to Richardson dispersion or $l^2 \sim t^3$ compared with $l^2 \sim t$ for ordinary diffusion. This superballistic behavior, i. e., l^2 increases faster than t^2, follows from the simple fact that for points separated by the distance less than turbulence injection scale, the larger the separation of the points the larger the eddies that induce the point separation.

To obtain the reconnection rates, we consider again the Sweet–Parker reconnection in its original form. In the Sweet–Parker reconnection, magnetic field lines are subject to Ohmic diffusion that induces the mean-square distance between oppositely directed magnetic field lines across the reconnection layer to change with the time

$$\langle y^2(t) \rangle \sim \lambda t, \tag{8.9}$$

where $\lambda = c^2/(4\pi\sigma)$ is the magnetic diffusivity. The plasma is advected out of the sides of the reconnection layer of length L_x at a velocity of order V_A. Thus, the time that the lines can spend in the resistive layer is the Alfvén crossing time $t_A = L_x/V_A$. Therefore, field lines that reconnect are separated by a distance

$$\Delta = \sqrt{\langle y^2(t_A) \rangle} \sim \sqrt{\lambda t_A} = L_x/\sqrt{S}, \tag{8.10}$$

where S is Lundquist number. Combining Equations (8.2) and (8.10), one gets again the Sweet–Parker reconnection scaling, $v_{\rm rec} = V_A/\sqrt{S}$.

In the turbulent case instead of Ohmic diffusion, one should use the Richardson dispersion [143]. In this case, the mean squared separation of particles changes as $\langle |x_1(t) - x_2(t)|^2 \rangle \approx \epsilon t^3$, where t is time, ϵ is the energy cascading rate, and $\langle \ldots \rangle$ denote an ensemble averaging [246]. For sub-Alfvénic turbulence $\epsilon \approx u_L^4/(V_A L_i)$ (see LV99) and, therefore, analogously to Equation (8.10), one can write

$$\Delta \approx \sqrt{\epsilon t_A^3} \approx L_x (L_x/L_i)^{1/2} M_A^2, \tag{8.11}$$

where it is assumed that $L_x < L_i$. Combining Equations (8.2) with (8.11), one obtains

$$v_{\rm rec,LV99} \approx V_A (L/L_i)^{1/2} M_A^2, \quad L_i > L_x, \tag{8.12}$$

that if combined with Equation (8.7) provides the description of the reconnection for turbulent reconnection in the presence of sub-Alfvénic turbulence.

8.1.3 Temporal and spatial Richardson diffusion

The two formally different ways of obtaining LV99 reconnection rates are very much related. In both cases, we are dealing with magnetic field lines stochasticity, but the case of Richardson dispersion considers the time evolution of magnetic fields lines in turbulent fluids, while magnetic field wandering presents the spatial distribution of magnetic field lines for a given moment of time. Because of this connection we may call the dispersion field lines that was quantified in LV99 was termed in [143] the *Richardson dispersion in space*. In Chapter 7 we termed this phenomenon *Richardson-Alfvén diffusion*. As none of the terms is generally accepted for the rest of the presentation we will use a shortcut name "Richardson dispersion" whenever this does not cause confusion.

While it is the incompressible Alfvénic motions that are used to describe the physics of Richardson dispersion, the process also takes place in compressible MHD turbulence. This is due to the fact that Alfvénic turbulence is a part and parcel of compressible MHD turbulence [82]. However, even for turbulence of shocks, i. e., Burgers turbulence, the phenomenon of Richardson diffusion is present, although the exact scaling is different [137].

8.1.4 Turbulent reconnection and violation of magnetic flux freezing

Magnetic flux freezing is a concept that is widely used in astrophysics. It is based on the Alfvén theorem, the proof of which is rather trivial for perfectly conductive laminar fluids. For laminar fluids of finite conductivity, the violation of the Alfvén theorem becomes negligible as fluid conductivity increases. This, however, is not true for turbulent fluids. Turbulent reconnection as we discussed above induces reconnection diffusion. Mathematically, the failure of the flux freezing is discussed in [266]. The numerical proof based on demonstrating of Richardson dispersion of magnetic field lines is in [137].

8.1.5 Turbulent reconnection in compressible media

Compressible turbulence is a rich physical phenomenon. For instance, two new effects become important in compressible media as compared to its incompressible counterpart that we discussed above. The first obvious effect is that the density of plasmas changes in the reconnection region and, therefore, the conservation of mass dictates

$$\rho_{\rm i} v_{\rm rec,comp} L_x = \rho_{\rm s} V_A \Delta, \tag{8.13}$$

where $\rho_{\rm s}$ is the density of plasma in the reconnection layer and $\rho_{\rm i}$ is the density of the incoming plasma far from the reconnection layer.

Another difference arises from the fact that compressible MHD turbulence presents a superposition of three distinct cascades of Alfvenic, fast and slow modes,

while our derivation of the magnetic field wandering rate utilizes only the Alfvénic component of MHD turbulence. As we discussed earlier, the Alfvénic component develops independently from the compressible MHD components in agreement with theoretical considerations in GS95. Therefore, one can estimate the amplitude in incompressible Alfvénic perturbations by subtracting the contribution of the slow and fast modes from the total energy of the turbulent motions

$$u_L^2 \approx V_{\rm total}^2 - V_{\rm comp}^2. \tag{8.14}$$

Using both Equation (8.13) and Equations (8.6) and (8.11), one can obtain the expression for the reconnection rate (compare to Equations (8.12), (8.7)):

$$v_{\rm rec,comp} \approx V_A \frac{\rho_i}{\rho_s} \min\left[\left(\frac{L_i}{L_x}\right)^{1/2}, \left(\frac{L_x}{L_i}\right)^{1/2}\right] \frac{V_{\rm total}^2 - V_{\rm comp}^2}{V_A^2}, \tag{8.15}$$

that can be applied to a compressible fluid.

For the incompressible driving, another form of presenting the reconnection rate is useful. Taking into account the relation between the Alfvénic modes and the generated compressible modes obtained in [81] it is possible to write

$$\frac{V_{\rm comp}^2}{V_{\rm Alf}^2} \approx C_1 \frac{v_{\rm inj}}{V_{\rm Alf}}, \tag{8.16}$$

where C_1 is a coefficient which depends on the media equation of state. Using the relation between the injection velocity and the resulting velocity in weak turbulence given by Equation (8.16), one can rewrite Equation (8.15) as

$$v_{\rm rec,comp} \sim V_A \frac{\rho_i}{\rho_s} \min\left[\left(\frac{L_i}{L_x}\right)^{1/2}, \left(\frac{L_x}{L_i}\right)^{1/2}\right] \frac{v_{\rm inj}^2(1 - C_1(v_{\rm inj}/V_A))}{V_A^2}, \tag{8.17}$$

which presents another form of the expression for the reconnection rate.

8.1.6 Turbulent reconnection in partially ionized gas

If gas is partially ionized, it represents a complex medium where ions coexist with neutrals. However, in view of turbulent reconnection, the distinct feature of the partially ionized gas is that the turbulent motions can be truncated at relatively large scale. Indeed, in partially ionized gas turbulence is subject to damping which arises from both neutral-ion collisions and the viscosity associated with neutrals [280, 451, 449]. Figure 8.3 illustrates the damping of Alfvén modes in a typical environment of molecular cloud. The corresponding damping scales are substantially larger than those in the fully ionized gas. Therefore, it is important to understand how turbulent recon-

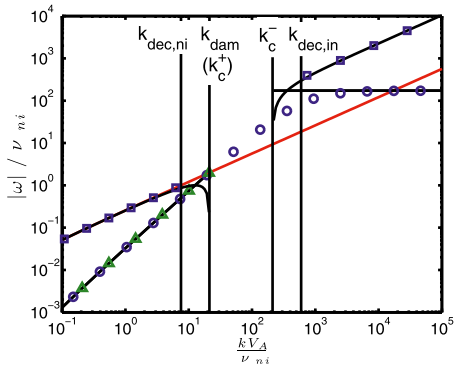

Figure 8.3: Damping of Alfvénic turbulence in low beta partially ionized gas corresponding to molecular cloud conditions. The damping of turbulence happens when the rate of damping (solid line) intersects the dashed line corresponding to the cascading rate from [451].

nection is being modified. This s very practical question, as in many astrophysical settings, e. g., in the case of star formation, one deals with the partially ionized gas.

The reconnection in partially ionized gas can be approached using the concept of the Richardson dispersion in [267]. The essence of such an approach is that on the scales at which Richardson dispersion is applicable, the magnetic fields are not frozen in. This, as we discussed earlier, makes magnetic reconnection fast. As a result, the issue at which scale the reconnection is fast boils down to determining the scale for the onset of the magnetic field wondering that is governed by the Richardson dispersion.

It is easy to see that the magnetic field lines are subject to the Richardson dispersion as soon as the separation of the lines exceeds the size of the smallest turbulence eddy, i. e., the size of the critically damped eddy; what we should find out is when the two essentially coinciding magnetic field lines get separated by this distance.

It is generally accepted that in partially ionized gas the ion-neutral damping or viscosity determines this size. With the eddies are anisotropic, one can associate the damping scale with the parallel scale of the critically eddies $l_{\parallel,\mathrm{crit}}$. Due to the shear induced by the perpendicular motions associated with such eddies, the magnetic field lines which at the initial separation r_{init} are getting separated further and further from each other. This process can be viewed as the evolution in time or in space, similar to the Richardson diffusion. Below we consider this as the evolution in terms of separation growing as we follow the magnetic field lines.

The rate of line separating dr/dl of field lines with the distance l traced along magnetic field lines is proportional to the $r/l_{\perp,\mathrm{crit}}$. The latter is the shear induced by the smallest turbulent eddies of $l_{\perp,\mathrm{crit}}$. Obviously, this provides an exponential rate of separation. It is easy to show that separation becomes equal to $l_{\perp,\mathrm{crit}}$ after the field lines are traced over a distance of

$$L_{RR} \approx l_{\parallel,\mathrm{crit}} \ln(l_{\perp,\mathrm{crit}}/r_{\mathrm{init}}), \tag{8.18}$$

which was introduced by [366] in the framework of "turbulence" with a single scale of driving. In a realistic turbulence with the range of scales, this type of exponential separation is dominated by the smallest eddies which have the greatest shearing rate.

For the partially ionized gas, magnetic field lines do not get dissipated at the scale $l_{\perp,\mathrm{crit}}$. However, ion-neutral interactions damp all the kinetic motions. In this sense, the description of magnetic fields in such a media may be analogous to the description of the media in the high Prandtl number turbulence, i. e., in the turbulence in the fluid with Ohmic resistivity much less than fluid viscosity. For the sake of simplicity, we consider reconnection in such a fluid instead of a more complex realistic partially ionized gas.

In this case, it is natural to associate r_{init} length with the separation of the field lines arising from the action of Ohmic resistivity on the scale of the critically damped eddies

$$r^2_{\mathrm{Ohm}} = \eta l_{\parallel,\mathrm{crit}}/V_A, \tag{8.19}$$

where η is the Ohmic resistivity coefficient. If this scale is less that the Larmor radius of an ion $r_{L,\mathrm{ion}}$, then instead of r_{Ohm} the value of $r_{L,\mathrm{ion}}$ should be used. In other words, $r_{\mathrm{init}} = \min[r_{L,\mathrm{ion}}, r_{\mathrm{Ohm}}]$. For our simplified considerations, we shall assume that $r_{\mathrm{Ohm}} > r_{L,\mathrm{ion}}$. This does not change much in our conclusions.

Taking into account Equation (8.19) and the relation

$$l^2_{\perp,\mathrm{crit}} = \nu l_{\parallel,\mathrm{crit}}/V_A, \tag{8.20}$$

where ν is the viscosity coefficient, one can rewrite Equation (8.18) as

$$L_{RR} \approx l_{\parallel,\mathrm{crit}} \ln \mathrm{Pt}, \tag{8.21}$$

where $\mathrm{Pt} = \nu/\eta$ is the Prandtl number. This equation reflects the fact that for the current sheets much longer than L_{RR}, magnetic field lines are subject to the Richardson dispersion. This, according to [143] means that the reconnection follows the fast reconnection laws established in LV99. At the same time for scales less than L_{RR}, the magnetic reconnection may be stagnating, e. g., follow Sweet–Parker reconnection laws. Incidentally, this can explain the formation of current sheets with the length less than L_{RR}. The compression of matter within these current sheets can explain the density fluctuations on scales of thousands of AU that are observed in the ISM.

There are additional effects, e. g., diffusion of neutrals perpendicular to magnetic field that might potentially influence the reconnection rate [436]. The ions can recombine in the reconnection zone and this can allow the matter to outflow as a flow of neutrals that is not directly constrained by magnetic field. Using this idea, [436] obtained large reconnection rates for laminar magnetic fields provided that magnetic fields are perfectly antiparallel and astrophysical medium for the media of pure ionized hydrogen (see also a numerical study by [190]). The reconnection rates plummet, however, in the presence of the guide field and heavy ions ("metals"). The latter are subject to ionization by the ambient radiation field and, therefore, do not recombine. As a result, the effect of "ambipolar reconnection" is of marginal importance for most of the settings involving realistically turbulent media [280].

8.2 Testing turbulent reconnection

Figure 8.4 presents results of numerical simulations of turbulent reconnection. The turbulence was driven both using wavelets in [233] and in real space in [234] with the results not depending on the driving.

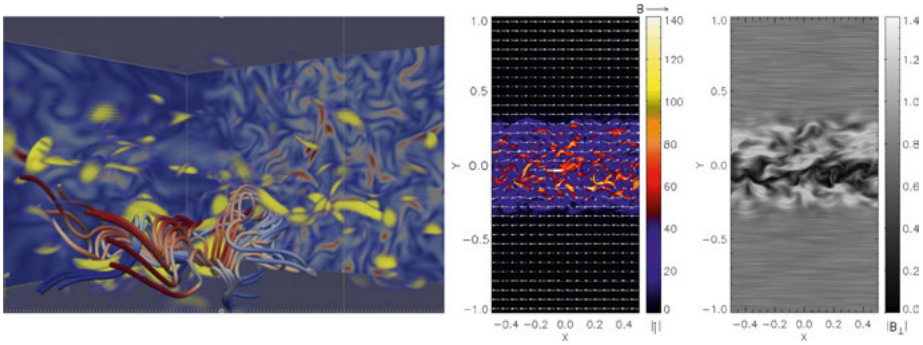

Figure 8.4: Visualization of reconnection simulations in [233, 234]. *Left panel*: Magnetic field in the reconnection region. *Central panel*: Current intensity and magnetic field configuration during stochastic reconnection. The guide field is perpendicular to the page. The intensity and direction of the magnetic field is represented by the length and direction of the arrows. The color bar gives the intensity of the current. *Right panel*: Representation of the magnetic field in the reconnection zone with textures. Reproduced from [233] by permission of the AAS.

As it is shown below, simulations in [233, 234] confirmed the LV99 prediction that turbulent reconnection is a fast reconnection, i. e., its rate does not depend on resistivity. The results provided a good correspondence with the LV99 predictions of the dependence of the reconnection rate on the turbulence injection power.

It is important to explain that in the simulations sub-Alfvénic turbulence was induced, i. e., with the energy of kinetic motions less than the energy of magnetic field. Indeed, according to Equation (8.7), $v_{\mathrm{rec,LV99}} \sim u_l^2$. At the same time for the weak turbulence, the injected power

$$P_{\mathrm{inj}} \sim v_{\mathrm{inj}}^2/\Delta t_{\mathrm{inj}} \tag{8.22}$$

is equal to the cascading power given by Equation (1.2). This delivers a relation

$$v_{\mathrm{rec,LV99}} \sim u_l^2 \sim v_{\mathrm{inj}} \sim P_{\mathrm{inj}}^{1/2}. \tag{8.23}$$

The predicted dependence corresponds well to the testing results, as it is illustrated in Figure 8.5, left panel.

While there exists a good correspondence between the theory and testing, one can also observe some differences from the idealized theoretical predictions. This stems from the idealization in the theoretical constructions. For instance, the injection of

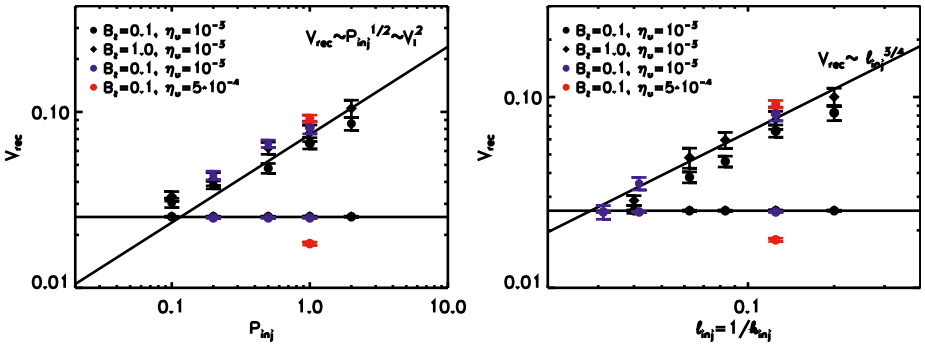

Figure 8.5: *Left panel:* The dependence of the reconnection velocity on the injection power for different simulations with different drivings. The predicted LV99 dependence is shown by dashed line. $P_{\rm inj}$ and $k_{\rm inj}$ are the injection power and scale, respectively, B_z is the guide field strength, and η_u is the value of uniform resistivity coefficient. *Right panel:* The dependence of the reconnection velocity on the injection scale. The LV99 prediction is shown by the dashed line. Dotted line in both panels correspond to the initial laminar Sweet-Parker reconnection. From [234].

energy in LV99 is assumed to happen at a given scale and the effects of the inverse cascade are not considered. Therefore, it is not unexpected that the measured dependence on the turbulence scale differs somewhat from the predictions. In fact, it is a bit more shallow compared to the LV99 predictions (see Figure 8.5, right panel).

Some of the measurement may be seen as intriguing. For instance, the left panel of Figure 8.6 shows the dependence of the reconnection rate on the uniform viscosity obtained from the isothermal simulations of the magnetic reconnection in the pres-

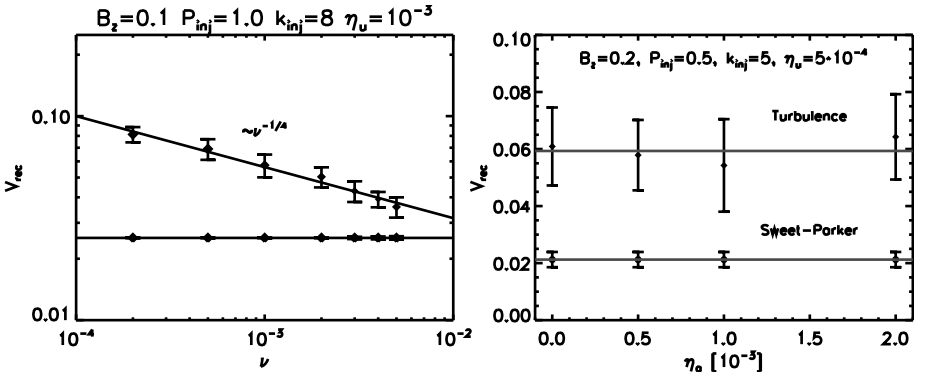

Figure 8.6: *Left panel*: The dependence of the reconnection velocity on uniform viscosity in the 3D isothermal models of Sweet–Parker reconnection (open symbols) and reconnection enhanced by the presence of turbulence (closed symbols) from [234]. *Right panel:* The reconnection rate in models with anomalous resistivity for the Sweet–Parker case (filled circles) and in the presence of turbulence (filled diamonds). We observe no dependence of the reconnection rate on the strength of anomalous effects. Reproduced from [233].

ence of turbulence [234]. The open symbols show the reconnection rate for the laminar case, i. e., with no turbulence driving, while closed symbols correspond to the mean values of the reconnection rate in the presence of turbulence. All parameters in those models are the same, except the uniform viscosity which varied from 10^{-4} to 10^{-2} in the code units. We believe that the dependence on viscosity can be explained as the effect of stemming from the finite inertial range of turbulence. Indeed, for numerical simulations the range of turbulent motions is very limited and any additional viscosity decreases the resulting velocity dispersion and the field wandering. This is expected to affect the reconnection rate.

LV99 predicted that in the presence of turbulence, plasma effects should not play a role, provided that the turbulence is sufficiently strong. One can simulate plasma effects within MHD code by using anomalous resistivity. The results of the corresponding simulations of reconnection are shown in the right panel of Figure 8.6. They confirm that the change of the anomalous resistivity does not change the reconnection rate.

Any numerical study has to address the issue of the numerical effects. The dependence of the reconnection rate on the numerical resolution is shown in Figure 8.7. We observe that the reconnection rate increases with the increase of the resolution. This testifies that the fast reconnection is not due to numerical effects. Indeed, higher numerical diffusivity and, therefore, reconnection would be expected for lower resolution simulations, if the numerical effects rather than turbulence were the cause of fast reconnection.

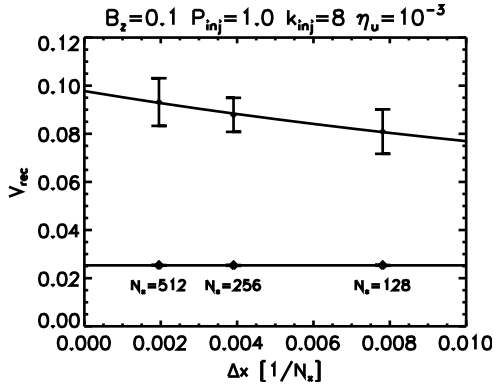

Figure 8.7: Dependence of the reconnection rate on the numerical resolution. If the fast reconnection was due to yet unclear numerical effects on small scales, we would expect to see the increase of the reconnection rate with the decrease of the numerical box. If anything, the actual dependence of the reconnection rate on the box size shows the opposite dependence from [234].

As we discussed above, the LV99 expressions for the reconnection rate can be obtained by applying the concept of Richardson dispersion to a magnetized layer. Therefore, by testing the Richardson diffusion of magnetic field, one can also provide tests of the theory of turbulent reconnection. A successful direct testing of the temporal Richardson dispersion of magnetic field lines was performed in [137]. The study confirmed that

magnetic fields are not frozen in highly conducting fluids providing a strong support for the LV99 theory.

In the LV99 model, current sheets are broad with individual currents distributed widely within the entire three-dimensional volume. The turbulence within the reconnection region is assumed to be similar to the turbulence within a statistically homogeneous volume. Numerically, the structure of the reconnection region was analyzed by [438] using the numerical simulations produced by [233]. The results supported the LV99 model, in particular, that the reconnection region is broad; the magnetic shear is more or less coincident with the outflow zone, and the turbulence within it is similar to turbulence in a homogeneous system.

In the simulations presented above, the turbulence is driven solenoidally to minimize the effects of compression, which does not play a role in the LV99 model. This turbulence driving in a volume corresponds to the case of astrophysical turbulence, which is also volume-driven. An alternative possible driving could be driving at the boundaries. However, the case of the turbulence driven at the box boundaries would produce spatially inhomogeneous imbalanced turbulence [33]. This turbulence does not have a good analytical description and, therefore, predictions of the reconnection rates with the driving of turbulence at the boundaries are problematic. In view of this, it is important to stress that it is not the size of our numerical simulations, but the correspondence of the observed scalings to those predicted in LV99 that makes us confident that the 3D reconnection gets fast in the presence of turbulence.

8.3 Understanding turbulent relativistic reconnection

Recently, it has been recognized that the magnetized relativistic plasmas, i. e., so-called Poynting-dominated plasmas, play an important role for a number of high energy astrophysical processes, e. g., for pulsar winds, relativistic jets, and gamma-ray bursts. The corresponding phenomena are frequently related to a fast rotating strongly magnetized compact object. The energy stored in the magnetic field initially is converted into kinetic and radiation energy to explain the observations. Relativistic turbulent magnetic reconnection is the most probable mechanism for the energy conversion. Then the natural question is whether turbulence in relativistic case also makes magnetic reconnection fast and whether the approach advocated in LV99 for turbulent reconnection can be generalized for getting the understanding of how magnetic fields reconnect in relativistic flows.

As properties of Alfvénic turbulence dominate the LV99 reconnection, it is natural to focus on Alfvenic component for the relativistic case as well. As we discussed above, the properties of relativistic and nonrelativistic MHD turbulence are similar. Therefore, one can hope that the LV99 reconnection model can be generalized to cover the relativistic case. However, it is obvious that effects of compressibility are likely to

be more important in relativistic reconnection compared to its nonrelativistic one. Indeed, the Poynting-flux dominated plasmas, the magnetic field can induce a relativistic velocity in current sheets but the Alfvén velocity is limited by the speed of light, which makes the induced turbulence to stay a trans-Alfvénic one.

The comparison between the theoretical expectations based on the LV99 theory and numerical simulations was performed in [418]. The simulations are performed using the relativistic resistive MHD code developed in [417]. For the initial conditions, the Harris current sheet was adopted with uniform temperature $k_B T/mc^2 = 1$ where k_B, T, m, c are the Boltzmann constant, temperature, rest mass, and light velocity, respectively. The parameters of the relativistic ideal gas, $h = 1 + (p/\rho c^2)(\Gamma/(\Gamma - 1))$ with $\Gamma = 4/3$ where h, p, ρ are the specific enthalpy, gas pressure and rest mass density were adopted. The simulations follow the setup in [233], in particular they use the open boundary in the direction perpendicular to the current sheet and parallel to the magnetic field, which corresponds to the x and z direction. Similarly, the periodic boundary is used in the y direction. The guide field was zero in some runs and not zero in other runs (see Figure 8.11). Turbulence was driven by injecting a randomly determined turbulent flow at a fixed time step. The injected flows had a flat kinetic energy spectra and a characteristic wavelength is distributed around the inverse of sheet width scale (see more in [418]). To quantify the reconnection rate, the approach based on the measurements of the changes of the absolute value of magnetic flux was used. This is the way of the measurements first used in [233]. In the simulations, turbulent reconnection in plasmas with the magnetization parameter from 0.04 (matter dominated) to 5 (Poynting dominated) was investigated.

Figure 8.8 depicts the magnetic field structure and gas pressure profile obtained by the simulations in [418]. The magnetization parameter was chosen to be $\sigma = 5$ and no guide field was used in this particular set-up. The turbulence was induced around the central current sheet region. The figure also illustrates that the magnetic field undergo field wandering that is similar to the nonrelativistic case. This wandering determines the size of outflow region, and thus the reconnection rate in the LV99 theory.

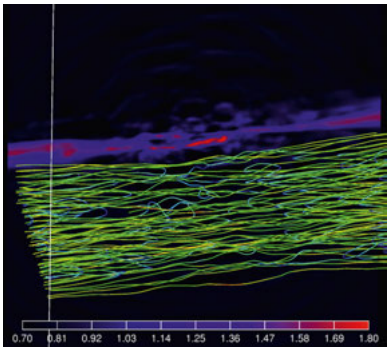

Figure 8.8: Visualization of relativistic reconnection simulations in the case of the magnetization parameter $\sigma = 5$ from [418]. The lines describe the magnetic field lines relating magnetic reconnection. The background plane shows the gas pressure profile in the unit of the upstream magnetic pressure. Similar to the nonrelativistic case, the magnetic field lines are wandering due to the injected turbulence, even in a Poynting-dominated plasma, which results in a wider reconnection exhaust region and large reconnection rate.

Note that the injected turbulence is sub-Alfvénic velocity but it still induces the magnetic field stochasticity.

Simple arguments in [418] provide

$$\frac{\rho_s}{\rho_i} = \frac{1}{(1+\sigma-\gamma_s)\gamma_s}\left[2\sigma\gamma_s^2 - (1+\sigma)\frac{\epsilon_{inj}}{\sqrt{\epsilon t_A^3}}\frac{l_x l_z}{v_s c^2}\right]. \tag{8.24}$$

This shows that the density ratio decreases as $\epsilon^{1/2} \propto v_{inj}$, indicated as Figure 8.9 (left panel). The change of the density is a significant factor to account for the turbulent reconnection rate (see Equation (8.15)).

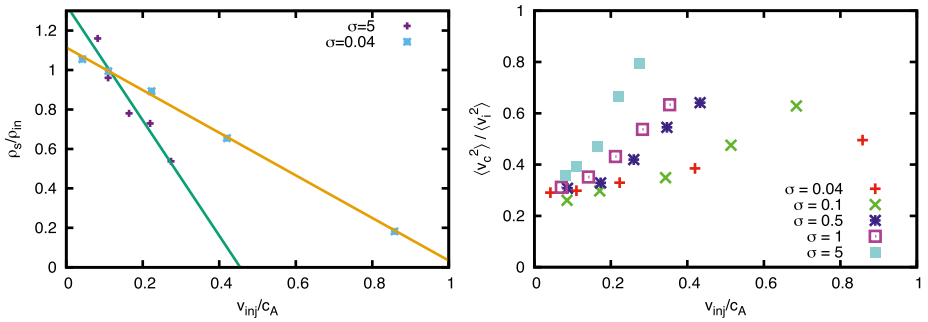

Figure 8.9: *Left panel:* Variations of plasma density in relativistic reconnection. *Right panel:* Generation of compressible modes in relativistic reconnection from [418].

The other factor to account for is the decrease of the energy in Alfvénic turbulence. Indeed, more energy is getting transferred to compressible modes for highly magnetized plasmas as illustrated by Figure 8.9 (right panel). Note that the compressible component is determined there through the Helmholtz decomposition into solenoidal and compressible part. One can observe that the compressible component increases with the increase of the σ-parameter.

Accounting for both effects and guided by the LV99 approach, [418] obtained a good correspondence between the theoretical expectations and numerical results. Figure 8.10 illustrates the dependence of reconnection rate on the power of the injected turbulent energy for different magnetization cases. It shows that the maximal reconnection rate increases with the intensity of driving (cf. Figure 8.5 (left panel)) in the sub-Alfvénic Mach number region. This corresponds to the expectation of the LV99 theory. However, as the injected Alfvén Mach number approaches to trans-Alfvénic region, the turbulence driving gets different, as we discussed. In response to this, the reconnection rate reaches a maximum value and even decreases with injected power. This stems from the fact that the injected turbulence becomes compressible.

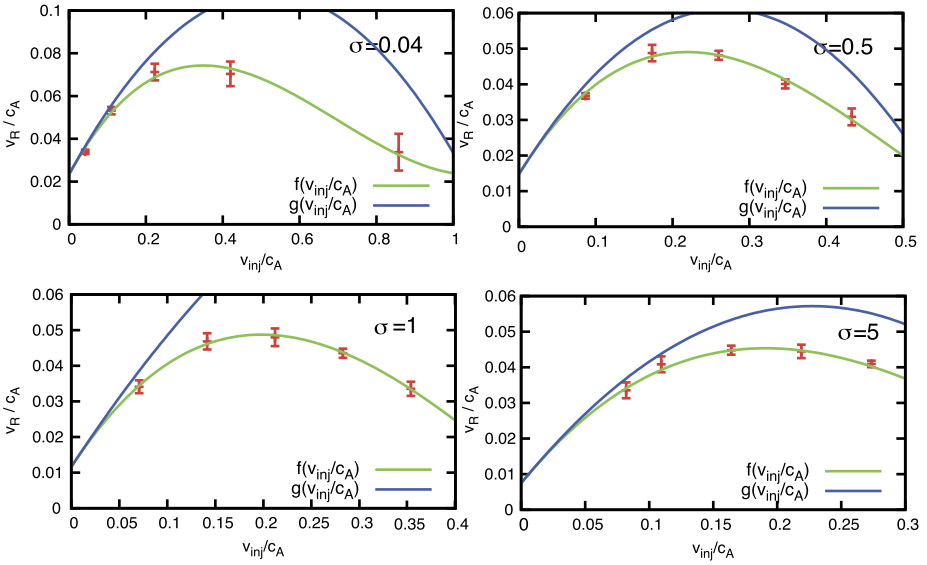

Figure 8.10: Reconnection rate in terms of various magnetization parameters: $\sigma = 0.04, 0.5, 1, 5$. The green dashed curves are the modified turbulent reconnection law taking into account the effect of density decrease and compressible turbulence effects.

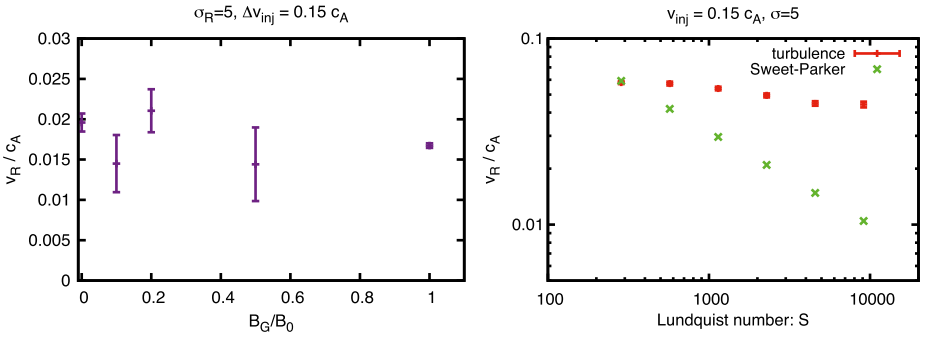

Figure 8.11: *Left panel*: Dependence of the reconnection rate on the guide field. *Right panel*: Dependence of the reconnection rate on resistivity from [418].

The guiding magnetic field is an important parameter in magnetic reconnection. Its effect is depicted in the left panel of Figure 8.11. Similar to [233, 234], we increased the guiding field while fixing the strength of reconnecting the magnetic field component, which resulted in the total σ-parameter increasing with increase of the guide field. Our simulations reveal that the reconnection rate does not depend on the guide field, which is in agreement to the non-relativistic results obtained in [233, 234] presented in Figure 8.5. Thus we conclude that turbulent reconnection in relativistic and non-

relativist cases is rather similar and a compressible generalization of the LV99 theory representing the main features of relativistic reconnection.

Finally, to show that the reconnection is fast, at the right panel of Figure 8.11 the dependence of the reconnection rate on the resistivity is presented. No significant dependence is seen, in agreement with our expectations and non-relativistic simulations.

The obtained results show that the reconnection rate can approach $0.3c$ if we assume a sufficient injection scale l. It is important that this is enough to explain most cases of relativistic reconnection [301]. Note that this result is obtained with pure MHD without appealing to complicated collisionless physics. This manifests that fast relativistic reconnection is a robust process that takes place in various environments irrespectively on the plasma collisionality.

8.4 Generation of turbulence by reconnection

The model of LV99 was formulated assuming that turbulence properties are determined by the external driving. However, magnetic reconnection can also drive turbulence through converting some of the free energy of the reversing magnetic field into turbulent motions. In the context of developed turbulence, this process was discussed in LV99 and [279]. Turbulence in reconnection can appear as a result of instabilities, e. g., resistive tearing [43, 297], the latter demonstrated that the instability becomes faster and not slower with decreasing resistivity above a critical Lundquist number around 10^4. Plasma simulations demonstrated that thin current layers are also unstable [107]. Observing effects of the feedback of the release of magnetic energy in numerics is challenging because currently available 3D MHD numerics are limited by the minimal reconnection rate provided by relatively high resistivity or artificial resistivity of the simulation (which corresponds to Ludquist numbers of several of 10^4). An early work by [252] showed a transfer to fast reconnection in the MHD regime that be interpreted as a process of the transfer from the Sweet–Parker reconnection to the spontaneous turbulent reconnection. The generation of turbulence was also observed in PIC simulations; see, e. g., [108, 216]. In this book, however, we deal with the MHD case and below we will present the results of incompressible simulations [27] and compressible simulations [228]. Similar simulations have also been performed by [340].

Physically, periodic box simulations in [27] correspond to early times in the current sheet disruption when the outflow did not develop. Importantly enough, it did demonstrate fast (resistively-independent) reconnection rates. Simulations with open boundaries in [228] have been performed for a sufficiently long time to allow for the establishment of stationary state. Physically, they correspond to later times in the current sheet evolution, the stationary inflow/outflow reconnection.

8.4.1 Early-time turbulence in the planar current layer

One of the simplest setups to study the development of turbulence in the thin current layer is a periodic setup with the mean field B_{z0} threading the box, reconnecting field $\pm B_{y0}$ changing sign in the x direction; see Figure 8.12. Here, we consider the incompressible case, in which case the dimensionless parameters of the problem are the Lundquist number S and the ratio B_{y0}/B_{z0}. The logic behind using the planar sheet is the attempt to simulate a zoomed-in portion of a very large and unstable Sweet–Parker current layer. We define Lundquist number using the box size, as $S = v_{Ay}L/\eta$, however, we imagine that this is a part of a bigger system with larger system size L_{global}. This setup aims to simulate earlier times, $t < L_{\text{global}}/V_A$, when the global outflow did yet develop. Our setup also assumes that the global Lundquist number determined by the larger system is asymptotically large, so we can ignore gradients from the large-scales. The end time of the simulation is determined by the development of structures with the size comparable to the box size at which point our artificial periodic boundary starts influencing the result.

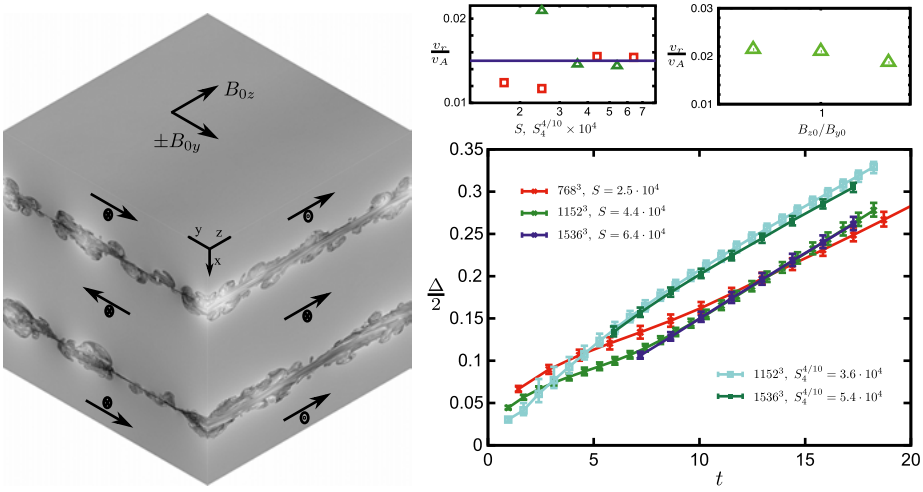

Figure 8.12: Left: The setup of all-periodic reconnection with two current layers. The magnitude of the magnetic field is shown in grayscale. Right: The evolution of the layer width Δ (bottom) and the reconnection rate as a function of the Lundquist number S (top left) and the ratio of B_{z0}/B_{y0} (top right) from [27]. Reproduced from [27] with permission of AAS.

The free energy in the system is the energy density of the opposing fields $B_{y0}^2/8\pi$, which we observe to decline in the turbulent current layer due to dissipation, after $t \approx 0.3L/v_{Az}$ the fraction of dissipated energy w_d becomes approximately constant, around $w_d \approx 0.4$. We inferred the reconnection rate as the speed of growth of the turbulent current layer width Δ, i. e., we define $V_r = d\Delta/dt$. The evolution of d and the inferred reconnection rate are shown on Figure 8.12. V_r was around $0.015v_{Ay}$ for

high Lundquist numbers and is rather insensitive to the imposed mean field B_{z0} (Figure 8.12). The dissipation rate per unit area from both sides of the current sheet can be calculated from w_d and v_r as

$$\epsilon_S = 2w_d v_r (1/2)\rho v_{Ay}^2 \approx 0.006\rho v_{Ay}^3. \tag{8.25}$$

Note that we arrived at the expression not only for "fast reconnection" (independent on resistivity and viscosity), but also for "fast dissipation," the above expression could be obtained by dimensional analysis using basic properties of the layer ρ and v_{Ay}.

The field in the current layer can be analyzed statistically, e. g., with power spectra and structure functions as we demonstrated in Chapter 3. We show the spectrum for one particular simulation at a certain point in time on the left-hand side of Figure 8.13. It should be noted that the peak of the spectrum moves toward smaller wavenumbers, i. e., the outer scale of this turbulence is growing in time, while in the driven turbulence we described in Chapter 3 this scale was fixed and determined by the scale of the outside driving force. Another difference with driven turbulence is that magnetic spectrum dominates over kinetic on large scales, but tend to go to equipartition on smaller scales. This is similar to decaying magnetic turbulence; see, e. g., [44]. We can say that qualitatively reconnection turbulence is very similar to decaying turbulence created by the initial random magnetic field. The scale-locality is an important component of the turbulent reconnection scenario, and these spontaneous reconnection experiments tend to corroborate scale-locality due to the spectral slope of perturbations being within the range between −1 and −3. In real systems, we expect the reconnection rate to be independent of system size as long as ion Larmor radius r_L and ion skip depth d_i are much smaller than the layer width Δ. On the right-hand side, Figure 8.13 shows anisotropy expressed as a ratio of parallel to perpendicular scale $\lambda_\parallel/\lambda_\perp$, obtained by a method we explain in Chapter 3. We can also estimate the interaction strength parameter $\xi = \delta v \lambda_\parallel / v_A \lambda_\perp$ introduced in Chapter 3 and see that for this case

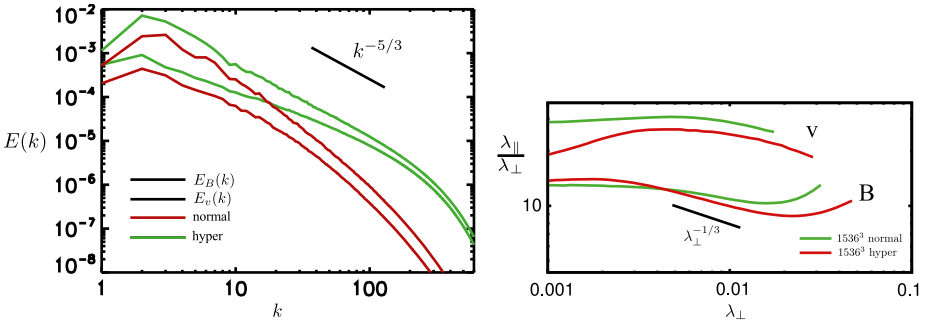

Figure 8.13: Left: The y-z power spectra of velocity and magnetic perturbations of turbulence in the current layer. Right: Anisotropy from the ratio of parallel to perpendicular scales obtained from equating second-order SFs (see Section 3.12). We used simulations with the second as well as fourth-order diffusivities (hyperdiffusitities) to evaluate the effect of the dissipation on the statistics of turbulence in the layer from [27]. Reproduced from [27] with permission of AAS.

it is around unity, i. e., we are dealing with critically balanced strong turbulence. The anisotropy of developed turbulence, $k_\parallel/k_\perp \sim 1/20$ is different from the tangent of the angle of the fastest growing oblique tearing modes ($k_\parallel/k_\perp = B_z/B_y = 1$) which initiate current layer disruption. So turbulence effectively forgets properties of the oblique tearing that started it. From simulations with higher B_z, one can also confirm Alfvén symmetry (see Section 3.3): increasing B_z only increases parallel lengthscale while keeping dynamics essentially unchanged (see also [27]).

8.4.2 Compressible simulations with inflow and outflow of turbulence in the current layer

The simulations in [228] were performed in the presence of initial noise that contributed to the of instabilities of the current sheet layer. This injection was stopped and the later development of the reconnection was going on its own. Nevertheless, the deformation of the current sheet layer were growing, being fed by the continuous energy ejection from the local reconnection events. Those local outflows were estimated to have speeds comparable to the local Alfvénic speeds. The corresponding bending of magnetic field lines is shown in Figure 8.14. In the initial configuration, the magnetic field lines in the upper and bottom half of the domain are antiparallel with a small inclination due to the presence of the guide field. Later a turbulent region is developing around the midplane of the computational box due to the stochastic reconnection taking place there. This region exhibits the magnetic line topology change. In Figure 8.14, the color coding reflects the degree of line alignment with –1 (blue) being perfectly antiparallel and 1 (red) being perfectly parallel to the X direction.

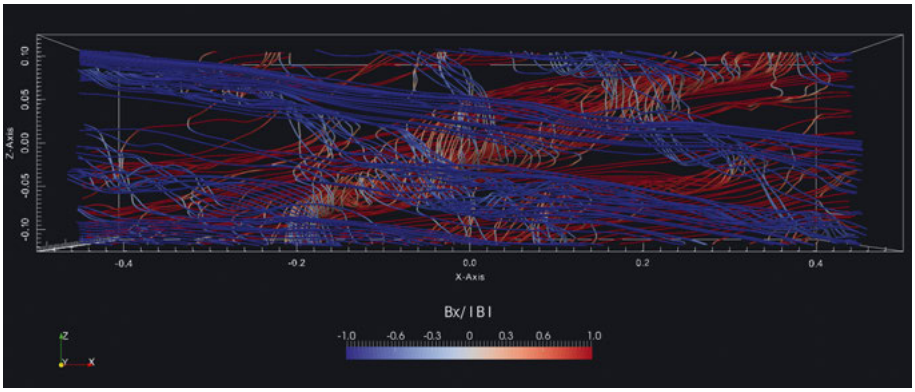

Figure 8.14: Visualization of the magnetic field lines in the reconnection with self-generated turbulence as seen from the below of the current sheet plane. The colors correspond to the line orientation with respect to the X direction with red and blue being parallel and antiparallel to the X axis, respectively. We can recognize the organized field above and below the reconnection region and strongly turbulent flux tubes within the reconnection region from [228].

In the next figure, Figure 8.15, the velocity power spectrum is calculated in two different ways for the snapshot shown in Figure 8.14. The blue line shows the spectrum calculated with the Fourier transform. Since the domain is not periodic (periodicity is enforced only along the Z direction, otherwise the boundaries are open), the other plot is obtained using the second-order structure function. The latter is calculated in the real space and is insensitive to the adopted boundary conditions. Figure 8.15 shows that the power spectrum obtained from the structure function is more regular and approaches the expected GS95/Kolmogorov (dashed lines) slope better. This proves that turbulence is being developed in the setup.

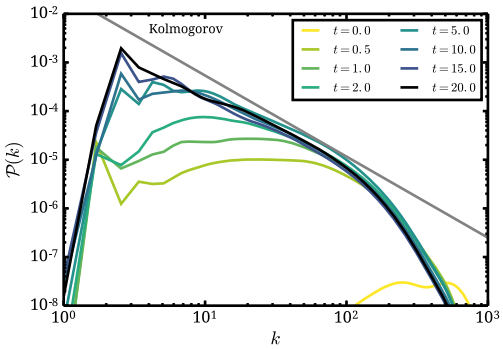

Figure 8.15: Velocity power spectra obtained in a few different ways corresponding to the simulation snapshot shown in the previous figure. We show the power spectrum of the velocity obtained using the fast Fourier transform and the second-order structure function (blue and green lines, respectively). The spectrum from the structure function approaches the Kolmogorov slope (dashed line) better, most probably because it is not sensitive to the type of boundary conditions. For comparison, we show the power spectrum of Z-component (red line) from [228].

For comparison, the red line in Figure 8.15 shows the Fourier power spectrum of the Z-component of the velocity, i. e., in the direction where we impose the periodicity. The power spectrum of this component is has smaller amplitude.

Some other features of the self-generated turbulence like the growth of the turbulence region were presented in [267]. For a more detailed description of these models we refer to [228]. More recent study by Kowal et al (in preparation) based on the $8192 \times 2048 \times 2048$ simulations testify that the tearing instability is mostly suppressed in the 3D reconnection. Instead, the Kelvin-Helmholtz instability was identified as the major source of turbulence in the reconnection layers. These results and conclusions are in agreement with conclusions in [27] and [340].

The spectrum obtained in both in [27] and [228] agrees with the GS95 expectations. This, however sharp contrasts to conclusions in [198] where a much steeper spectrum of magnetic fluctuations $E_B(k) \sim k^{-2.2}$ was reported. A possible cause of this spectrum

could be insufficient time for the turbulence to develop fully. At earlier times of the simulations the spectrum in [230] was also different from that of GS95 theory.[2]

The shortcoming of all the present simulations of reconnection with the self-induced turbulence is that they do not achieve a stationary state with balanced outflows and inflows. These is due to the act that these simulations, except for [230], used closed or periodic boxes. The most advanced simulations, i. e. those in [230] used open boundary conditions in one direction, the axis along which the field lines are annihilated in reconnection. All simulations are high β ones and reconnection velocities measured in the simulations $\sim 10^{-2}$ are expected to grow with the decrease of β.

8.5 Observational testing of turbulent reconnection

LV99 theory is formulated in the MHD regime, which means that the outflow region should be much larger than the ion Larmor radius $\Delta \gg \rho_i$. This condition is satisfied for solar atmosphere, solar wind, but is not satisfied for the magnetosphere. In the latter case, the corresponding scales are comparable and plasma effects are important for reconnection. As a lot of measurements are done in situ for magnetospheric plasmas, this tends to bias the field towards studies of reconnection dominated by plasma physics. At the same time, magnetospheric reconnection is a very peculiar case of reconnection. Below we discuss the situations of reconnection where MHD regime is appropriate.

8.5.1 Solar turbulent reconnection

Solar reconnection was studied by [94] in order to test LV99 theory, in particular, the prediction of thick outflow regions. As we discussed earlier, the driving by magnetic reconnection is not isotropic and, therefore, the turbulence should be accepted to be strong starting from the injection scale. In this case,

$$V_{\rm rec} \approx U_{\rm obs,turb}(L_{\rm inj}/L_x)^{1/2}, \tag{8.26}$$

where $U_{\rm obs,turb}$ is the spectroscopically measured turbulent velocity dispersion. Similarly, the thickness of the reconnection layer is

$$\Delta \approx L_x(U_{\rm obs,turb}/V_A)(L_{\rm inj}/L_x)^{1/2}. \tag{8.27}$$

2 Note, that the steep power spectrum reported in [198] does not preclude the turbulent reconnection from happening. In fact, it was shown in LV99 that turbulent reconnection is possible in turbulence with the wide range of spectral indexes.

The results given by Equations (8.26) and (8.27) should be compared with observations in [94]. There, the widths of the reconnection regions that measured was in the range from $0.08L_x$ up to $0.16L_x$ while the observed Doppler velocities in the units of V_A were of the order of 0.1. These values are in a good agreement with the predictions given by Equation (8.27). We note that the original comparison by [94] employed the expressions in LV99 derived in the assumption of isotropic driving. This driving would induce weak turbulence and somewhat different estimates for the widths of the reconnection regions. Thus the authors concluded that both LV99 and Petschek X-point reconnection are potentially acceptable solutions. In view of our present better understanding of turbulence generation in reconnection layers, the correspondence with LV99 is much better.

We note that the triggering of magnetic reconnection by turbulence generated in adjacent sites is a prediction of LV99 theory. This prediction was successfully tested in [414]. There the authors explained quasi-periodic pulsations in observed flaring energy releases at an active region above the sunspots as being triggered by the wave packets arising from the sunspots.

8.5.2 Solar wind, Parker spiral, heliospheric current sheet

Solar wind reconnection present the case of $\Delta \gg \rho_i$ and, therefore, the magnetic reconnection there is expected to happen in MHD turbulent regime. The evidence supporting this conclusion was obtained by comparing the solar wind and MHD turbulence reconnection data in [249]. There it was concluded that the solar wind reconnection agrees with the predictions of LV99 theory (see Figure 8.16). The general features of the turbulent reconnection observed in MHD simulations were shown to correspond to the features of solar wind reconnection [178].

Similarly, [141] discussed the implications of turbulent reconnection for heliospheric reconnection, in particular the deviations of interplanetary magnetic field from the Parker spiral that is expected in the case of the perfect flux freezing. The deviations were reported by different authors. For instance, [64] found "notable deviations" from the spiral model using Voyager 1 and 2 data at solar distances $R = 1$–5 AU. These conclusions were substantiated by [219], who presented evidence on the breakdown of the Parker spiral model for time- and space-averaged values of the magnetic field from several spacecraft (Helios 2, Pioneer Venus Orbiter, IMP8, Voyager 1) using the measurement from the inner heliosphere at solar distances 0.3–5 AU. In fact, the latter authors interpret their results as the consequence of "a quasi-continuous magnetic reconnection, occurring both at the heliospheric current sheet and at local current sheets." [141] estimated the magnetic field slippage velocities and obtained good quantitative correspondence between measured the deviation and the expectations based on the LV99 reconnection theory. In addition, [141] analyzed the data relevant to the region associated with the broadened heliospheric current sheet (HCS),

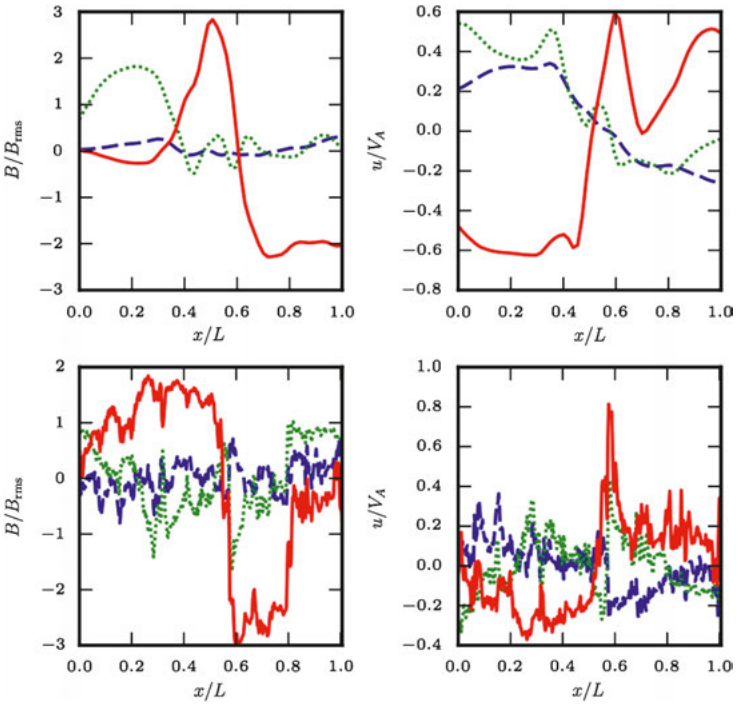

Figure 8.16: Candidate events for turbulent reconnection. *MHD turbulence simulation (top panels) and high-speed solar wind (bottom panels)*. The left panels show magnetic field components and the right panels show velocity components, both rotated into a local minimum-variance frame of the magnetic field. The component of maximum variance in **red** is the apparent reconnecting component, the component of medium variance in green is the nominal guide-field direction, and the minimum-variance direction in blue is perpendicular to the reconnection layer. Reprinted figure with permission from [249]. Copyright (2015) by the American Physical Society.

and provided arguments in favor of the applicability of LV99 magnetic reconnection model to the HCS.

8.5.3 Indirect observational evidence

Magnetic reconnection is an intrinsic process that is difficult to observe directly in generic astrophysical situations. In fact, the observations of the sun and direct measurements of the solar wind are notable exceptions. However, turbulent reconnection is a generic process taking place in turbulent astrophysical plasmas and it opens a possibility to test the properties of reconnection by comparing the theoretical predictions with observations.

For instance, one can argue that the spectrum of turbulent fluctuations observed in astrophysical settings, e. g., in molecular clouds, galactic atomic hydrogen [260] is

indirect evidence in favor of turbulent reconnection. Indeed, the observed statistics is consistent with numerical simulations [231], which are performed in situations when turbulence induces fast reconnection.

Similarly, the processes of efficient magnetic diffusion in turbulent fluids that are mediated by turbulent reconnection presents an indirect, but convincing evidence in favor of the model of turbulent magnetic reconnection. Below we discuss additional examples of processes that are based on turbulent reconnection.

8.5.4 Flares of magnetic reconnection and associated processes

It is evident that the reconnection can make the magnetic field turbulent and turbulence can increase the rate of reconnection. As a result, one gets a *reconnection instability*. A simple quantitative model for the process based on the LV99 model was presented in [279], where it is assumed that since stochastic reconnection is expected to proceed unevenly, with large variations in the thickness of the current sheet, one can expect that some fraction of this energy will generate waves and add energy to the local turbulent cascade.

The possible applications of the theory cover a wide range from solar flares to gamma ray bursts (GRBs). For instance, a model for GRBs based on LV99 reconnection was suggested in [270]. The model was elaborated in [464] and compared with GRB observations in the model where collisions of magnetic slabs were considered. A different version of gamma ray bursts powered by turbulent reconnection proposed by [268] is based on kink instability. It is illustrated in Figure 8.17. The model appeals to the relativistic turbulent reconnection that we described above. Compared to other kink-driven models of GRBs [123, 167, 164, 312], this model takes into account that the kink drives the turbulence [157, 161] and this accelerates the reconnection.

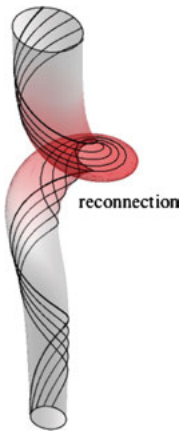

Figure 8.17: In the model by [268, 287], magnetized jet with spiral magnetic field is being ejected. The spiral undergoes kink instability, which results in turbulent reconnection.

The numerical testing of turbulent reconnection within the jets was also attempted in [323]. There 3D relativistic MHD simulations of rotating jets subjected to the kink instabilities were performed for a parameter space that included different density ratios between the jet and the environment, different angular velocities, etc. The simulations show that a complex structure develops in the helical magnetic field developing several regions with large current densities, which are suggestive of intense turbulent reconnection.

Turbulent reconnection is a volume-filling reconnection. The magnetic energy is being released in the volume and can be transferred to energetic particles via both the first- and the second-order Fermi acceleration. Therefore, we believe that magnetic reconnection in the case of AGN jets (see [165]) can be a strong source of high energy particles. This conclusion agrees with the results of numerical simulations in [110].

Particle acceleration induced by magnetic reconnection can take place in the vicinity of black hole of active galactic nuclei (AGNs). In particular, [111], henceforth GL05 proposed that fast turbulent reconnection events could accelerate the particles and produce the observed core radio outbursts in GBHs and AGNs. This model was elaborated in [207] and applied to explaining the gamma-ray flares. This study reported the existence of the correlation between the energy release and the black hole mass that follows from the model of turbulent reconnection. This correlation spans over an enormous range of scales of 10^{10}. This correlation can potentially explain not only the observed radio, but also the gamma-ray emission from GBHs and low luminous AGNs (LLAGNs). For observational testing, 230 sources were used.

The correlations found in [207] as well as in a related study by [396] have motivated further studies of the astrophysical consequences of turbulent reconnection. For instance, [222] have computed the spectral energy distribution (SED) of several GBHs and LLAGNs and found that these match well with the observations, especially at the gamma-ray tail. Importantly, the model also naturally explains the observed very fast variability of the emission. The same model was also applied to explain the high energy neutrinos observed by the IceCube as originating due to LLAGNs [221].

8.6 Comparison of approaches to magnetic reconnection

8.6.1 Turbulent reconnection and numerical simulations

Whether MHD numerical simulations reflect the astrophysical reality depends on magnetic reconnection being correctly presented within these simulations. The problem is not trivial. The astrophysical Lundquist number can be larger than 10^{15} orders than the Lundquist numbers in simulations. Therefore, direct numerical simulation can potentially be completely misleading.

One way to deal with the high Reynolds' numbers in simulations is to use Large Eddy Simulations (LES) [316]. The use of LES for magnetized fluids requires the explicit

parametrization of reconnection rates. For instance, if following the ideas of tearing research we adopt a particular maximal value of reconnection speed is $0.01V_A$. This means that the motions where eddies are moving with velocities larger than this reconnection speed will be constrained by magnetic tension of magnetic field, which cannot reconnect with the speed higher than the given one. In trans-Alfvénic turbulence, this means constraining the motions of eddies on the scales $[10^{-6}L, L]$ if we adopt the usual Kolmogorov $v \sim l^{1/3}$ scaling. If, however, turbulent reconnection provides fast reconnection at all turbulent scales the results of numerical simulations obtained with the above tearing reconnection constraint and astrophysical reality are radically different.

It is possible to claim that from the point of view of the turbulent reconnection theory, a normal MHD code reproduces magnetic reconnection correctly for turbulent regions. Indeed, as for turbulent volumes the reconnection rate does not depend on resistivity and varies with the level of turbulence. In view of the fact that turbulence is the generic state of astrophysical fluids, the regions that are turbulent within numerical studies are correctly represented as far as the magnetic reconnection is concerned. On the contrary, the regions where the turbulence is damped due to numerical diffusivity fail to magnetic reconnection correctly.

8.6.2 Turbulent reconnection versus tearing reconnection

It has been known for a while that Sweet–Parker current sheet is unstable to tearing and this changes the rate of reconnection [415]. This became much more appreciated recently when it was shown numerically that 2D current sheet develops tearing instability starting with a Lundquist number larger than $\sim 10^4$ and this results in reconnection that does not depend on the fluid resistivity [297, 426]. This study of tearing momentarily eclipsed the earlier mainstream research of the reconnection community aimed at explaining fast reconnection through appealing to the collisionless plasma effects stabilizing the Petschek-type X point configuration for reconnection [391, 121, 122]. For most of astrophysical applications, the existence of the X point configurations in the presence of realistic astrophysical forcing was very doubtful (see discussion in LV99). Thus the tearing reconnection is definitely preferred compared to the X-point reconnection. Nevertheless, it is unlikely that tearing provides a generic solution for the astrophysical reconnection.

It is easy to provide arguments suggesting that tearing inevitably transfers to turbulent reconnection for sufficiently large Lundquist numbers S. Indeed, from the mass conservation constraint requirement it follows that in order to have fast reconnection, one has to increase the outflow region thickness Δ in proportion to L_x, as $V_{\rm rec} \approx V_A\Delta/L_x$. While S grows in proportion to L_x, the Reynolds' number Re of the outflow grows as $V_A\Delta/\nu$, where ν is viscosity. Thus $\mathrm{Re} \approx (V_{\rm rec}/V_A)(\eta/\nu)S$. For $V_{\rm rec} \sim 0.01V_A$ and

$\eta \sim \nu$, the increase of S inevitably increase of Re. The outflow gets turbulent for sufficiently large Re. Once the shearing rate introduced by eddies is larger than the rate of the tearing instability growth, the instability should get suppressed. Fortunately, the reconnection, as we showed above become turbulent one with no dependence on tearing.[3]

In addition, the rate prescribed by tearing is incompatible with the requirement of models of MHD turbulence (e. g., GS95), which are based on unconstrained motions of turbulent eddies. Tearing reconnection with its prescribed reconnection rate cannot explain why magnetic reconnection can be sometimes slow and sometimes fast.

8.6.3 Turbulent reconnection: 3D reality versus 2D models

A lot of physical phenomena are very different in 3D and 2D. For instance, 2D turbulence cascade transfers energy to large scales as opposed to the 3D turbulence cascade. In general, whether the physics in the system of reduced dimensions is representative of the physics of the 3D system in such situations is a priori unclear. The correspondence of the physics in the system with reduced dimensions must be theoretically justified and tested. For magnetic reconnection, such a justification faces serious difficulties, e. g., the differences between 2D and 3D magnetic reconnection are stressed, e. g., in Priest (this volume) and also in publications by [51, 52]. There it is shown that an extrapolation from reconnection physics obtained in 2D to 3D is not justified. Below, we provide additional arguments why 2D turbulent reconnection can be a guide for our understanding of the 3D astrophysical reconnection.

[307, 308] studied numerically turbulent reconnection in 2D. The authors emphasized analogies between the magnetic reconnection layer at high Lundquist numbers and homogeneous MHD turbulence. They pointed out various turbulence mechanisms that can enhance reconnection rates in a turbulent fluid, e. g., multiple X-points as reconnection sites, compressibility effects, and motional electromotive force (EMF) of magnetic bubbles advecting out of the reconnection zone. Dealing with 2D models, the authors, however, did not realize the importance of stochastic magnetic field wandering and they did not arrive at an analytical prediction for the reconnection speed. Although they reported the enhancement of the reconnection rate in their numerical study, their setup precluded the calculation of a long-term average reconnection rate. While their study was important in attracting the attention of the community to the possible effects of turbulence, the relation of this study with the LV99 model

3 If one assumes that tearing is the necessary requirement for fast reconnection, this entails the conclusion that tearing should proceed at the critically damped rate, which implies that the Re number and, therefore, Δ cannot increase. This entails, however, the decrease of reconnection rate driven by tearing in proportion $L_x \sim S$. As a result, the reconnection gets dependent on S and, therefore, stops being fast.

is not clear, as the nature of MHD turbulence in 2D is different. In particular, shear-Alfvén waves that play the dominant role in 3D MHD turbulence according to GS95 are entirely lacking in 2D.

The question whether turbulent reconnection is fast in 2D has not been resolved yet if one can judge from the available publications. For instance, in a more recent study by using the approach in [307], i. e., in [442] found no significant effects of turbulence on reconnection. In another study, [389] studied Ohmic electric fields at X-points in homogeneous, decaying 2D MHD turbulence. However, they investigated a case of small-scale magnetic reconnection and their results are not directly relevant to the reconnection of large-scale flux tubes corresponding to high S. Numerical simulations in [298] and [243] came to different conclusions on whether 2D turbulent reconnection is fast in 2D. Irrespectively of the solution of this particular controversy, the results for 2D turbulent reconnection are not likely to be relevant to the understanding of magnetic reconnection in the realistic 3D astrophysical systems.

8.6.4 Turbulent reconnection versus turbulent resistivity

Attempts to describe turbulent reconnection by introducing some sort of turbulent resistivity have been numerous. However, these attempts are misleading. Indeed, it is possible to show that "turbulent/eddy resistivity" description has fatal problems of inaccuracy and unreliability, and this stems from its poor physical foundations. It is true that coarse-graining the MHD equations by eliminating modes at scales smaller than a given length l introduces a "turbulent electric field." This is an effective field acting on the large scales induced by motions of smaller size magnetized eddies. However, it is well known in the fluid dynamics community that the resulting turbulent transport is not well represented by an enhanced diffusivity. Indeed, turbulence lacks the separation in scales to justify such an "eddy-resistivity" description. As a consequence, energy is often not absorbed by the smaller eddies, but supplied by them. The turbulent electric field both creates magnetic flux through turbulent dynamo and destroys it through reconnection. The two processes are not separable in turbulent fluid. The eddy resistivity misses this.

If the turbulent reconnection rate is defined, e. g., by LV99, then an eddy-resistivity can always be tuned to achieve that rate, but this does not have much physical meaning. While the tuned reconnection rate will be correct by construction, other predictions will be in error. The required large eddy-resistivity is expected to smooth out all turbulence magnetic structure below the coarse-graining scale l. In reality, the turbulence will create strong small-scale inhomogeneities, such as current sheets, from the scale l down to the actual microscale. In addition, field-lines in the flow smoothed by eddy-resistivity will not exhibit Richardson-type separation at scales below l and the list of the inconsistencies can be extended. All of this stem from the erroneous

ad hoc concept of "eddy resistivity" being adopted. Note that the aforementioned effects are essential for understanding particle transport/scattering/acceleration in the turbulent reconnection zone. The turbulence with fluid having resistivity corresponding to the value of "turbulent resistivity" must have magnetic field and fluid decoupled on most of its inertia range turbulent scale. In other words, the MHD turbulence should not be affected by magnetic field in gross contradiction with theory, observations and numerical simulations. Magnetic helicity conservation which is essential for astrophysical dynamo is incompatible with the "eddy diffusivity."[4] We can also point out that in the case of relativistic reconnection, turbulent resistivity introduces unphysical noncausal, faster than light propagation effects. The worst feature of the "eddy-resistivity" parametrization is its unreliability: because it has no scientific justification, it cannot be applied with any confidence to astrophysical problems.

The approach that is discussed in this chapter is quite different. It is not based on coarse-graining. The stochasticity of magnetic field-lines is a real and verified physical phenomenon present in magnetized turbulent fluids. Whereas "eddy-resistivity" ideas predict that magnetic flux should be destroyed by turbulence, in fact, turbulent motions constantly change connectivity of magnetic field lines without dissipating magnetic fields. As for relativistic reconnection, being moved by fluid motions the stochastic world-lines in relativistic turbulence remain within the light-cone with no noncausal effects such as produced by "eddy-resistivity" being entailed (see also ELV11).

4 Increasing the resistivity to the values required by LV99 model would make astrophysical dynamos resistive or slow, in gross contradiction to the fact that astrophysical dynamos are know to operate in fluids with negligible resistivity and, therefore, can be only modeled by "fast dynamo" [352].

9 Turbulent transport of magnetic field and heat

Turbulence is known to dramatically change transport processes. In this chapter, we consider how it changes the transport of magnetic field and heat in magnetized plasmas. We consider two problems of astrophysical importance, namely, transport of magnetic field in the problem of star formation in interstellar environments and the problem of heat transport in turbulent plasmas of galaxy clusters. In both cases, the traditional research was based on the implicit assumption that magnetic field are frozen in highly conducting astrophysical fluids, which are the consequences of the Alfven 1942 theorem [7]. With the LV99 model and subsequent studies (e. g., [140, 137, 142]) proving that the magnetic fields are not frozen in turbulent media, the changes of the paradigms of the two aforementioned processes, as well as many other astrophysical processes, are inevitable.

9.1 Important motivation: star formation problem

Star formation is known to be an inefficient process. Indeed, the mass of molecular clouds in our Milky Way galaxy is $M_{\rm MW} \approx 10^9$ solar mass. For the typical interstellar medium (ISM) density of the gas of 50 cm^{-3}, the free fall time is $\tau_{\rm ff} \approx (3\pi/32G\rho)^{1/2} \approx 6\times10^6$ years, which provides a "natural" star formation rate $M_{\rm MW}/\tau_{\rm ff}$ of 200 solar mass per year. At the same time, the measured star formation rate is only $\approx$ 1.3 solar mass per year [332]. A textbook way of explaining this inefficiency appeals to magnetic forces significantly impeding the gravitational collapse (see [326]).

The importance of magnetic fields was suggested as the corner stone of star formation theory (see [315]). While star formation happens due to gravity, but if the matter is strongly magnetized, the magnetic field can prevent such a collapse. If the ratio of the magnetic flux to mass is larger than the critical one,

$$(\Phi/M)_{\rm crit} \approx 1.8 \times 10^{-3} \,{\rm gauss\ cm^2}\, g^{-1} \tag{9.1}$$

magnetic field blocks the cloud collapse (see [119]). Such strongly magnetized clouds are termed *subcritical* and to collapse they have to lose a part of their magnetic flux. As the magnetization of diffuse gas in the Milky Way and in other spiral galaxies corresponds to subcritical value, the compression of matter together with frozen-in magnetic field is expected to result in the formation of subcritical molecular clouds. This is the essence of the magnetically controlled star formation.

The change of the magnetic flux can happen due to the process termed ambipolar diffusion (see [315, 394]). The idea of the ambipolar diffusion can be easily exemplified in the case of gas collapsing to form a protostar. The magnetic field acts on charged particles and it does not directly affect neutrals. Neutrals moving under the gravitational pull get scattered by collisions with ions and charged dust grains. These charged

https://doi.org/10.1515/9783110263282-009

species are coupled with the magnetic field and this transfers the magnetic forces to neutrals. The relative motion of magnetic fields with frozen-in ions in respect to neutrals constitutes the process of ambipolar diffusion. This process gets faster when the ionization ratio drops and, therefore, it is important in weakly ionized cloud cores. As the theory of star formation based on ambipolar diffusion (see [327]) predicts low star formation rates in agreement with observations, it became the textbook theory.

In the opposite case, i. e. when the gravity dominates the magnetic field, i. e., the cloud is supercritical, the gravity induces a collapse dragging magnetic flux with entrained matter into the forming star on the timescales of the free fall. The clouds can be formed supercritical or transfer to the supercritical state via the ambipolar diffusion process. In any case, the magnetic field frozen in the cloud presents a problem. First of all, it is possible to show that if all the magnetic flux is brought together with the material that collapses to form a star in molecular clouds, then the magnetic field in a protostar gets several orders of magnitude higher than the one observed in stars (this is the "magnetic flux problem", see [156] and references therein). For instance, young stars, e. g., T-Tauri stars have a magnetic field $\approx 2 \times 10^3$ Gauss (see [203]), which corresponds to $(\Phi/M) \approx 3 \times 10^{-8}$ Gauss cm^2 g^{-1}. This, however, is a million times smaller that the flux to mass ratio estimated for one solar mass clump in a cloud of density 10^4 cm^{-3} (see [119]). Thus one has to identify ways of efficient magnetic flux removal. A similar problem is present with the magnetic flux through the accretion disk around a forming star. As we discuss later, too strong magnetization is expected to prevent the accretion disks from forming.

We mentioned on several occasions that turbulence is an essential process for interstellar media. Numerical simulations have shown that turbulence can play the dominant role for the formation of the molecular clouds [13]. Moreover, numerical simulations have indicated the ability of turbulence to change the flux to mass ratio within one fluid codes, i. e., with the codes that do not have any ambipolar diffusion effects. These, puzzling from the point of view of the traditional theory, facts were interpreted within the scenario in which compressible turbulence collects matter along magnetic field lines and induces supercritical star formation [430]. A number of researchers claimed that this approach does not require magnetic flux diffusion and that the collapse can be strictly one dimensional. We believe that this scenario is unrealistic (see a discussion in [281]). Instead the role of turbulence for magnetic diffusion must be reevaluated on the basis of the improved understanding of magnetic field dynamics in turbulent medium that we covered in the previous chapter. Indeed, in the presence of turbulent reconnection one cannot assume flux freezing.

As we discuss below, turbulence induces magnetic field diffusion and this diffusion radically changes the star formation paradigm. Because of the important role played by reconnection for the turbulent diffusion in magnetized conducting fluids, the corresponding process introduced in Lazarain (2005) [256] and elaborated in subsequent publications [377, 261, 281] was termed *reconnection diffusion*.

9.2 Diffusion in magnetized turbulent fluid

Turbulent diffusion in hydroturbulence is a well-known process. The examples range from the diffusion of volcanic ashes in atmosphere to mixing sugar in a coffee cup. In all of the cases, the diffusion get incomparably faster compared to the case where only molecular diffusivity takes place.

In MHD turbulence, the magnetic field affects the process of diffusion as the back reaction of magnetic field gets important. The latter was a hotly debated subject in the theory of magnetic field generation, i. e., the dynamo theory (see [352]). There the problem was tackled successfully in the astrophysically meaningless case of infinitesimally weak magnetic field for which backreaction is completely negligible. Evidently, the turbulent eddies can easily bend such magnetic fields at all scales up to the Ohmic dissipation one. This removes the disparity of scales present in the problem of magnetic reconnection that we discussed earlier. In this approximation the magnetic fields are totally passive and dissipate at the small scale without any consequence for the turbulent diffusion processes. This way of reasoning gave rise to the concept of *magnetic turbulent diffusivity* within kinematic dynamo theory. According to this concept, the diffusion of magnetic field is similar to the diffusion of passive scalar in hydrodynamic turbulence. Needless to say that this regime of dynamically unimportant magnetic field is only of academic interest and does not address the actual problem of diffusivity of astrophysical magnetic fields.

The problem of diffusion for dynamically important magnetic fields demands that the magnetic reconnection process should be addressed properly.

As we discuss in the next chapter, the GS95 theory can be viewed as a trubulence of elongated eddies aligned with magnetic field. Indeed, such eddies depend on mixing motions perpendicular to the local direction of magnetic field (see LV99) and the process takes place requires reconnection events happen through every eddy turnover. The latter agrees well with the expectations of the turbulent reconnection theory. Indeed, for small scale eddies magnetic field lines are nearly parallel. Therefore, when they intersect, the pressure gradient is not $V_A^2/l_\parallel$ but rather $(l_\perp^2/l_\parallel^3)V_A^2$. This happens since only the energy of the component of the magnetic field that is not shared is available to drive the outflow. At the same time, the characteristic length contraction of a given field line due to reconnection between adjacent eddies is $l_\perp^2/l_\parallel$. Taken together, this gives an effective ejection rate of $V_A/l_\parallel$. Since the width of the diffusion layer over the length $l_\parallel$ is $l_\perp$, one can write the mass conservation in a form by $V_{\rm rec} \approx V_A(l_\perp/l_\parallel)$. This provides the reconnection rate $V_A/l_\parallel$, which coincides with the nonlinear cascade rate on the scale $l_\parallel$. In fact, if not for the turbulent reconnection, the buildup of unresolved magnetic knots would be unavoidable, significantly flattening the turbulence spectrum compared with the GS95 predictions. This would contradicts both to Solar wind measurements and to all numerical calculations avail-

able.[1] Therefore, we claim that the process of reconnection diffusion (see [256]) is a process that takes place in MHD turbulence.

We first consider the maximal rate allowed by the reconnection diffusion process, i. e., evaluate the diffusivity arising from the eddies at the largest scales. We shall consider all regimes of MHD turbulence, i. e., super-Alfvenic, trans-Alfvenic, and sub-Alfvenic. We start with a super-Alfvenic regime, i. e., $M_A > 1$. Magnetic field becomes dynamically important as soon as its energy density exceeds the kinetic energy of eddies at the Ohmic dissipation scale. In other words, Alfvenic velocity gets larger than the velocity of eddies at the Ohmic dissipation scale or the ion Larmor radius, whichever is larger. For the velocity in Kolmogorov turbulence scaling as $v_l \sim l^{1/3}$, and it is clear that even a weak magnetic field can make a significant difference for the dynamics of sufficiently small eddies. In view of that it is advantageous to introduce a scale at which the magnetic field is dynamically important and the nature of the turbulence changes from hydrodynamic to MHD (see [257]), namely,

$$l_A = L(V_A/V_L)^3 = LM_A^{-3} \tag{9.2}$$

where L and V_L are the injection scale and injection turbulent velocity, respectively. Interestingly enough, if the mean-free path of particles is larger than l_A, the scale l_A may act as an effective mean-free path in terms of particle diffusion along magnetic fields. The corresponding diffusion coefficient coincides with its hydrodynamic counterpart, i. e.,

$$\kappa_{\mathrm{sup}\,A} = 1/3 V_L L \tag{9.3}$$

This happens as the largest eddies of super-Alfvenic turbulence are marginally affected by the magnetic field.

For sub-Aflvenic turbulence, i. e., for low Alfvenic Mach numbers, at large scales $\sim L$ the turbulence is weak (see LV99, [158])) and magnetic fields are only slightly perturbed by propagating Alfven waves. The wave packets in weak turbulence evolve changing their perpendicular scale $l_\perp$, while their scale $l_\parallel$ along the magnetic field stays the same. The diffusion that is being induced by weak turbulence is substantially reduced compared to the case of hydrodynamic turbulence. It is possible to get the diffusion coefficient for the weak turbulence ([257], see also [143] henceforth ELV11)

$$\kappa_{\mathrm{weak}} \sim LV_L(V_L/V_A)^3 \equiv LV_L M_A^3 \tag{9.4}$$

which is smaller than its hydrodynamic counterpart by the factor $M_A^3 \ll 1$.

For sub-Alfvenic turbulence, the additional contribution to diffusivity comes from scales at which magnetic turbulence gets strong. As we discussed earlier, (see

1 If magnetic reconnection were slow then, as was correctly claimed by Don Cox (private communication), the interstellar medium would behave not like a fluid, but more like felt or Jello. This also contradicts to observations.

also [257]) at the scale

$$l_{\rm trans} \sim L(V_L/V_A)^2 \equiv LM_A^2 \tag{9.5}$$

the critical balance condition $l_\parallel/V_A \approx l_\perp/V_l$ is getting satisfied making turbulence strong. One can see that the velocity corresponding to $l_{\rm trans}$ is $V_{\rm trans} \sim V_L(V_L/V_A)$. For strong turbulence, the diffusion

$$\kappa_{\rm strong} \sim V_{\rm trans} l_{\rm trans} \sim LV_L(V_L/V_A)^3 \tag{9.6}$$

which coincides with Equation (9.4), indicating that the diffusivity of smaller eddies in strong MHD turbulence regime can produce is as strong as the diffusivity induced by weak turbulence at the injection scale.

Dealing with sub-Alfvenic turbulence, it is necessary to distinguish between the diffusivity parallel and perpendicular to magnetic field. Magnetic field in a turbulent fluid changes the diffusion of plasma particles moving along magnetic field lines. At the same time, turbulent eddies in the direction perpendicular to the local direction of magnetic field are similar to eddies within the Kolmogorov picture. Indeed, in the presence of fast reconnection magnetic mixing is not inhibited for motions perpendicular to the direction of magnetic field. Note, that in MHD turbulence we deal with motions perpendicular to the local direction of magnetic field. Therefore, for the external observer, the diffusion is isotropic at large scale of super-Alfvenic turbulence.

The trans-Alfvenic case of $M_A = 1$ is the case that the GS95 model in its original formulation deals with. It is the limiting case of both sub-Alfvenic and super-Alfvenic turbulence.

The diffusion at scales less than the injection scale is different. In fact, the diffusion of magnetic field and plasmas at scales smaller than the scales of injection L is subject to Richardson diffusion (see Section 7.1). This is the type of diffusion that gets accelerated with time as well as with scale involved, i. e., "superdiffusion" with superbalistic behavior.[2]

For the sake of simplicity, we discuss the diffusion of magnetetic field from a given clump or a cloud. In this case, one can use the scale and velocity dispersion of the cloud as the proxies of L and V_L. For sub-Alfvenic turbulence, the diffusion coefficient can be approximated as

$$\kappa_{\rm cloud} \sim v_{\rm cloud} l_{\rm cloud} (v_{\rm cloud}/V_A)^3 \tag{9.7}$$

while for the case of turbulence being trans-Alfvenic or super-Alfvenic the same estimate but the M_A^3 factor is absent.[3]

2 For ordinary diffusion $\delta r^2 \sim t$, for ballistic behavior $\delta r^2 \sim t^2$, for the Richardson diffusion $\delta r^2 \sim t^3$.

3 One should be careful with the application of Equation (9.7), however. When the dynamics of magnetic fields is studied at scales less than the injection scale, the magnetic fields obey the Richardson diffusion law and superdiffusion law $\delta r \sim t^{3/2}$ is applicable and the diffusion gets faster with the increase of scale.

9.2.1 Physical picture of reconnection diffusion in the absence of gravity

The description above provides an introduction to the mathematical framework of turbulent diffusivity in a homogeneous magnetized fluid.

The standard theory of star formation is based on the assumption that magnetic field lines preserve their identify and the diffusion of charged particles perpendicular to magnetic field lines is restricted. As a result, the mass loading of magnetic field lines does not change. However, LV99 model and subsequent studies e. g. [143], [137], [142] suggest that the standard assumptions are not applicable if magnetized fluids are turbulent. As a result, in the presence of MHD turbulence, the diffusion of plasma perpendicular to magnetic field is *inevitable*.

We shall illustrate the reconnection diffusion process by demonstration how it allows plasma to move perpendicular to the mean magnetic field (see Figure 9.1). This is relevant to star formation. Consider two magnetic flux tubes with entrained plasmas that intersect each other at an angle. Due to reconnection the identity of magnetic field lines changes. Consider a situation that before the reconnection event the plasma pressures $P_{\rm plasma}$ in the tubes are different, but the total pressure $P_{\rm plasma} + P_{\rm magn}$ is the same for two tubes. This is a situation of a stable equilibrium. If plasmas are partially ionized then ambipolar diffusion, i. e. slow diffusion of neutrals in respect to magnetic field can make gradually smoothen the magnetic field pressure gradients. In the presence of turbulence, a different faster process takes place.

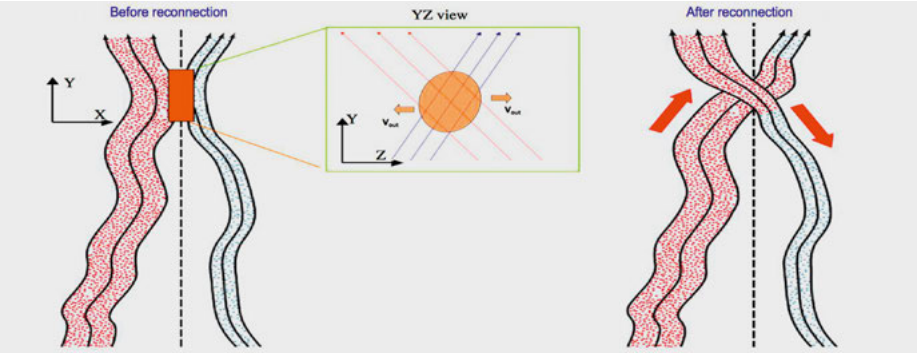

Figure 9.1: Motion of matter in the process of reconnection diffusion. 3D magnetic flux tubes get into contact and after reconnection plasma streams along magnetic field lines. *Left panel*: XY projection before reconnection, upper panel shows that the flux tubes are at angle in the X-Z plane. *Right panel*: after reconnection.

Magnetic field lines in the presence of turbulence are not parallel. Such field lines reconnect all the time in a turbulent flow. The process of reconnection connects magnetic fields with different mass loading and plasma pressures. As a result, plasmas stream along magnetic field lines to equalize the pressure. In the process, the portions of magnetic flux tubes with higher magnetic pressure expand as plasma pressure in-

creases due to the flow of plasma along magnetic field lines. The entropy of the system increases as magnetic and plasma pressures become equal through the volume. As a result a process of the diffusion driven by turbulent reconnection takes place and it is easy to see that this process does not depend on the degree of the ionization of the matter. In the absence of gravity, the outcome of the reconnection diffusion is to make magnetic field and plasmas more homogeneously distributed. Both motions of plasmas along the flux tubes and the exchange of parts of the flux tubes between different eddies contributes to the diffusion.

To get a clear mental picture of what is going on, consider a toy model of two adjacent magnetized eddies (see Figure 9.2). Magnetic flux tubes moving with the eddies reconnect and exchange plasmas and magnetic fields. This induces turbulent diffusion of both magnetic field and plasmas. In the case illustrated by Figure 9.1, the densities of plasma within the flux tubes can be different and the reconnection in Figure 9.2 creates a new flux tubes along which plasma redistributes due to the pressure difference. This process induces the diffusion of plasma perpendicular to the mean magnetic field. In reality, the process above happens at every scale. Therefore, for turbulence with the extended inertial range, the shredding of the columns of plasmas with different density proceeds at all turbulent scales. This makes speed of plasma motion along the magnetic field lines not essential for the diffusion. For the case of strong turbulence, the diffusion of matter and magnetic field is given by Equation (9.6).

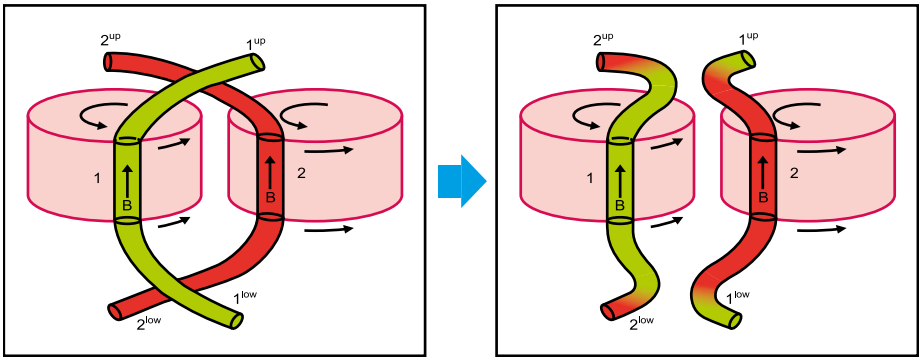

Figure 9.2: Reconnection diffusion: exchange of flux with entrained matter. Illustration of the mixing of matter and magnetic fields due to reconnection as two flux tubes of different eddies interact. Only one scale of turbulent motions is shown. In real turbulent cascade, such interactions proceed at every scale of turbulent motions.

The efficiency of reconnection diffusion depends on the scale of the motions. The process of reconnection diffusion can be illustrated with the diffusion of impurity from a blob of the size a (Figure 9.3). This set up allows us to consider homogeneous turbulence, which simplifies the analysis. Turbulence is characterized by its injection scale $L_{\max}$, its dissipation scale $L_{\min}$ with the inertial range between these scales. Consider

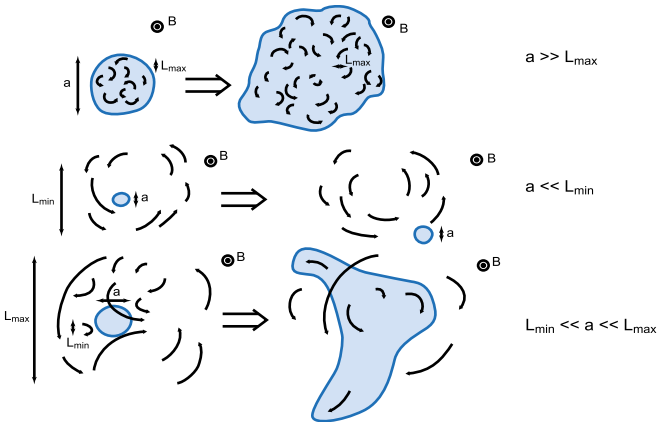

Figure 9.3: Reconnection diffusion depends on the size a of the zone from which the diffusion happens. Different regimes emerge depending on the relation a to the sizes of maximal and minimal eddies present in the turbulence cascade. Eddies perpendicular to magnetic field lines correspond to Alfvenic turbulence. The plots illustrate heat diffusion for different regimes. *Upper* plot corresponds to a being less than the minimal size of turbulent eddies; *Middle plot* corresponds to a being less than the damping scale of turbulence; *Lower plot* corresponds to a within the inertial range of turbulent motions. This is the case of Richardson diffusion.

Alfvenic eddies perpendicular to magnetic field lines. If turbulent eddies are much smaller than a, i. e., $a \gg L_{\rm min}$, they expand the blob acting in a random walk fashion. At the same time, the eddies much larger than the blob, i. e., $a \ll L_{\rm min}$ mostly advect the spot.[4] If a is within the inertial range of turbulent motions, i. e., $L_{\rm min} < a < L_{\rm max}$ then a more complex dynamics of turbulent motions is present. This is the case of Richardson diffusion of superballistic expansion of the blob.

If the blob a is not just an impurity, but its density is different from the density of the surrounding flow, the process of reconnection diffusion depends on the properties of turbulence within and outside the blob. Nevertheless, we may use the idealized schematic in Figure 9.3 to get a qualitative insight. If the blob self-gravitating, as this is relevant to star formation, and is turbulent up to the largest scale the diffusivity of magnetic field from the blob can be roughly estimated as av_a, where v_a is the velocity at the scale a. This estimate assumes that scale a is within the range of strong MHD turbulence. Then the expected diffusion from the volume scales as $a^{4/3}$. If a is in the range of weak turbulence, the reconnection diffusivity is given by Equation (9.7).

The example in Figure 9.3 illustrates the diffusion perpendicular to magnetic field. As we mentioned above, the Alfvenic motions are the most efficient in mixing magnetized fluid perpendicular to the *local* direction of magnetic field. This direction, as we discussed earlier, differs from the mean magnetic field direction. Therefore, in the global system of reference related to the mean magnetic field (and to the external ob-

4 There is also the expansion of the blob arising from the Lyapunov deviation of the flow lines.

server) the diffusion of magnetic field and plasmas is expected to happen both parallel and perpendicular to the mean magnetic field direction. However, the weaker the perturbations of the magnetic field, i. e., the smaller the Alfven Mach number M_A, the more anisotropic the reconnection diffusion is.

9.2.2 Reconnection diffusion in the presence of gravity

In the presence of the gravitational force, the diffusion will also increase the entropy of the system, allowing the "heavy fluid," i. e., gas, to be concentrated and "weightless fluid," i. e., magnetic field, to leave the the gravitational potential. Consider, for instance, the idealized system of plasmas and magnetic field in a uniform directed downwards gravitational field with the acceleration g. In the thermodynamic equilibrium, the plasmas will have the Boltzmann-type distribution with $\rho \exp[-m_i g z/kT_{\rm eff}]$, where the effective "temperature" for supersonic turbulence can be roughly estimated from $kT_{\rm eff} \sim m_{\rm dom} V_L^2/2$, where $m_{\rm dom}$ is the mass of dominant species in the flow. As a result, the weightless fluid, namely, magnetic field, will tend to fill the entire volume to the same pressure. Therefore, the magnetization of the volume in terms of magnetic flux to plasma mass ratio is the lowest at the bottom and highest at the top of the system.

The astrophysical systems the redistribution of the magnetic field is induced by the process of reconnection diffusion. If we have spherical density inhomogeneities, the diameter of these inhomogeneities is acted upon by the parallel scale of Alfvenic eddies $\Lambda_\parallel$. The motions that induce reconnection diffusion are associated with the perpendicular scale of the corresponding eddies $\Lambda_\perp$.

The removal of magnetic field from the cloud is a complex process that for scales less than the injection scale is governed by the law of Richardson diffusion. However, to illustrate the process we consider a toy model of small scale turbulence with the scale of turbulent motions L much smaller than the size of the cloud $L_{\rm cloud}$. For this set-up, the reconnection diffusion process is governed by an ordinary diffusion law. Thus one can obtain the rate of removal of the flux from the gravitational potential U in the simple way. Indeed, the force is given by $F = -dU/dx$ and the diffusion velocity $V_{\rm diff} = \mu F$. Thus one can write the drift flux as

$$J_{\rm drift} = -\rho \mu dU/dx. \tag{9.8}$$

This flux is counteracted by the diffusion flux given by the following relation:

$$J_{\rm diffusion} = -D d\rho/dx. \tag{9.9}$$

For a steady state situation, one gets the total flux being equal to zero and $\rho = \rho_0 \exp(-U/mv_L^2)$. Thus

$$0 = -\rho dU/dx(\mu - D/(mv_L^2)), \tag{9.10}$$

which results in $\mu \approx l/(mv_L)$, which gives result

$$V_{\rm diff} \approx l/v_L(F/m). \tag{9.11}$$

If magnetic field counteracts to gravity $F \sim B^2/(L_{\rm cloud}n)$, where n is the density of particles, which combines with Equation (9.11) gives

$$V_{\rm diff} \sim LB^2/(mv_L L_{\rm cloud}n) = LV_A^2/(v_L L_{\rm cloud}), \tag{9.12}$$

and the diffusion time for the magnetic field is

$$t_{\rm esc} \sim L_{\rm cloud}^2 mv_L n/(LB^2) = L_{\rm cloud}^2 v_L/(V_A^2 L) \tag{9.13}$$

Note, that in the case of sub-Alfvenic turbulence, we should associate the injection scale L with the perpendicular size of eddies at which MHD turbulence gets strong (see Equation (9.5)).

9.3 Reconnection diffusion and the identity of magnetic field lines

The discussion above considered large scale flux tubes. Below we consider the process of reconnection diffusion microscopically, at the level of individual field lines.

9.3.1 Explosive diffusion of magnetic field lines in turbulent flows

A textbook description of magnetic field lines in perfectly conducting fluid assumes that the line always preserves its identity. This is impossible in a turbulent fluid (see ELV11). We shall start by showing how the Richardson diffusion produces rather non-trivial results. Consider the problem of separating particles in hydrodynamic Kolmogorov turbulence that we discussed in Chapter 8. The separation between two particles obeys the equation $dl(t)/dt \sim v(l) \sim \alpha l^{1/3}$, where α is proportional to a cubical root of the energy cascading rate. The solution of this equation is $l(t) = [l_0^{2/3} + \alpha(t - t_0)]^{1/3}$ describes the Richardson diffusion of $l^2 \sim t^3$. However, the interesting feature of this solution is that the provides the type of fast separation even if the initial separation of particles is zero. This means the violation of Laplacian determinism. Mathematically, the above paradox is resolved by accounting to the fact that turbulent field is not differentiable[5] and, therefore, it is not unexpected that the initial value problem does not have a unique solution. In physical settings, the turbulence gets damped at a nonzero scale, which makes the paradox less vivid.

The essential features of the example above carry over to the case of MHD turbulence, as in the plane perpendicular to the local direction of magnetic field, strong

5 The Kolmogorov velocity field is Hölder continuous, i. e., $|v(r_1) - v(r_2)| \le C|r_1 - r_2|^{1/3}$.

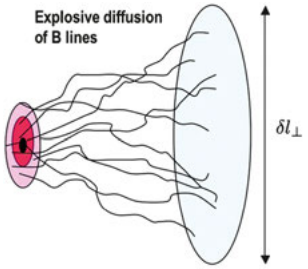

Figure 9.4: Particle tracing magnetic field lines may start at different initial locations shown as coaxial ellipsoids. However, after a period of time the field line spread over a larger volume and the final position of the field lines does not correlate with their initial position.

MHD turbulence satisfies the Kolmogorov description. Figure 9.4 illustrates the loss of the Laplacian determinism for magnetic field lines. In analogy with the example above, the final line spread $l_\perp$ does not depend on the initial separation of the field lines. This is a remarkable effect that provides a microscopic picture of reconnection diffusion based on the description of magnetic field lines rather than on the reconnection of well-organized flux tubes.

We shall trace magnetic field lines in the realistic turbulence with the dissipation scale $l_{\mathrm{min},\perp}$, where, $\perp$ denotes the scale perpendicular to the local magnetic field. A couple relevant points were discussed in ELV11. First of all, resistivity, whatever its nature, introduces stochastic forcing of magnetic field line dynamics. Indeed, the induction equation with the resistive term $\eta\Delta B$ induces stochasticity associated with Ohmic diffusion. Therefore, the definition of the magnetic field line on scales affected by resistivity gets not deterministic. In fact, the magnetic field line motion is a concept defined mostly by convention and not testable experimentally (see [337, 429, 8], ELV11). Thus magnetic field lines may be traced by ions that start at the same field line (see Figure 9.5) For a smooth laminar magnetic field and ideal MHD equations, the motions of ions will reveal magnetic field lines as two ions on the same field line will always remain on the same line. However, the situation is radically different in the presence of turbulence.

In our thought experiment, we shall trace ions moving with the same velocity and separated perpendicular to magnetic field by a Larmor radius ρ_0. Let us assume that the minimal scale of turbulence $l_{\mathrm{min},\perp} > \rho_0$. For this case, the dynamics of ions can be approximated by the dynamics of charged particles of "a single scale MHD turbulence" discussed in [366]. Indeed, the turbulent motions at the critically damped scale $l_{\mathrm{min},\perp}$ are dominant for shearing and steering matter and magnetic field on the smaller scales. The Rechester and Rosenbluth (1978) theory [366] predicts the Lyapunov growth of the perpendicular separation of ions

$$l_\perp \approx \rho_0 \exp(l/l_{\mathrm{min},\parallel}), \tag{9.14}$$

where l is the distance traveled by ions along magnetic field and $l_{\mathrm{min},\parallel}$ is the scale parallel scale of the critically damped eddies with the perpendicular scale $l_{\mathrm{min},\perp}$ (see also [336, 257]). For ions to find themselves in different eddies, they must be separated by $l_\perp$

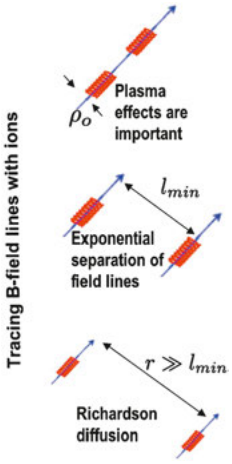

Figure 9.5: *Upper plot:* Ions tracing the same magnetic field line. The diffusion and decorrelation arises from plasma or Ohmic effects as well Rechester–Rosenbluth effect. *Middle plot:* Ions separated by scales much larger than the ion Larmor radius are further separated by the Rechester–Rosenbluth effect. *Lower:* At scales larger than the turbulence damping scale, the Richardson diffusion takes over resulting in explosive separation of field lines.

equal to the perpendicular size of the critically damped eddies $l_{\mathrm{min},\perp}$. Substituting this in Equation (9.14), one easily finds that the ions must travel the so-called Rechester–Rosenbluth distance

$$L_{RR} \approx l_{\mathrm{min},\parallel} \ln(l_{\mathrm{min},\perp}/\rho_0), \tag{9.15}$$

to get into different eddies.

The anisotropic character of turbulence results in the difference between $l_{\mathrm{min},\perp}$ and $l_{\mathrm{min},\parallel}$ which is a point different from the original Rechester–Rosenbluth theory formulated for the idealized toy model of isotropic turbulence. Note, that the distance given by Equation (9.15) is just a few times larger than the scale $l_{\mathrm{min},\parallel}$. As soon as ions get separated over $l_{\mathrm{min},\perp}$, they get into different eddies as their trajectories diverge fast as a result of the Richardson diffusion. Thus after a relatively short period during which ions move in a correlated manner remembering their original position, a stochastic regime takes place. At the latter phase, the initial positions of the ions is completely forgotten. We remind the reader that we used the ions as tracers of magnetic field. Thus we can talk about the stochasticity of magnetic field lines as they these lines are traced by ions.

The smaller the turbulence scale, the larger the effects of stochasticity. For instance, if the turbulence proceeds to the scale ρ_0, the arguments above only get stronger, as from the very beginning the ions may experience stochastic turbulence driving and get uncorrelated. In many cases, for instance, in fully or mostly ionized ISM, the Alfvenic turbulent cascade at ρ_0 gets continued as a whistler cascade involving only electrons. Such cascading provides stochasticity below ρ_0. With the whistler scaling as $v_l \sim l^{2/3}$ (see [86] and references therein) the "whistler-induced" Richardson diffusion should go as $l^2 \sim t^6$, inducing fast separation of magnetic field lines. In this case, the magnetic field lines can be traced by electrons and this induces stochastic perturbations on ion trajectories. If one argues that it is electrons that are current

carrying agents, this does not alter our arguments above. Indeed, one would use the Larmor radius of electron $\rho_{\rm electron}$ instead of ρ_0 in Equation (9.15) and this changes the result by an insignificant factor.

9.3.2 Spontaneous stochasticity of magnetic field lines and reconnection diffusion

The process of magnetic field lines becomes stochastic in turbulent fluids this effect is termed "spontaneous stochasticity" (see ELV11). The common wisdom underlying the star formation research, for instance, is based on the picture of laminar field lines with no spontaneous stochasticity. With such fields, nearby ions stay all the time entrained on the same field line provided that the nonideal effects, e. g., resistivity, are negligibly small. Naturally, this set up is unrealistic for any turbulent astrophysical environment, including star forming molecular clouds.

To proceed with our discussion of the physics of reconnection diffusion, consider two separated turbulent volumes (see Figure 9.6). Each of the volumes has its own set of magnetic field lines. However, as the field lines wander due to the Richardson diffusion, they overlap in the volume $\Delta_{\rm int}$ and their identity as associated with the particular volume is lost (Figure 9.6, left). Magnetic field lines reconnect and the newly formed lines allow plasma exchange between the volumes. If plasma and magnetic field pressures in the volumes were different, this picture based on the diffusion of magnetic field lines is very similar to the picture describing the exchange of plasmas between magnetic flux tubes in Figure 9.1.

Dealing with magnetic reconnection we have discussed the separation of magnetic field lines. Figure 9.6, left, illustrates the spread of magnetic field lines in the

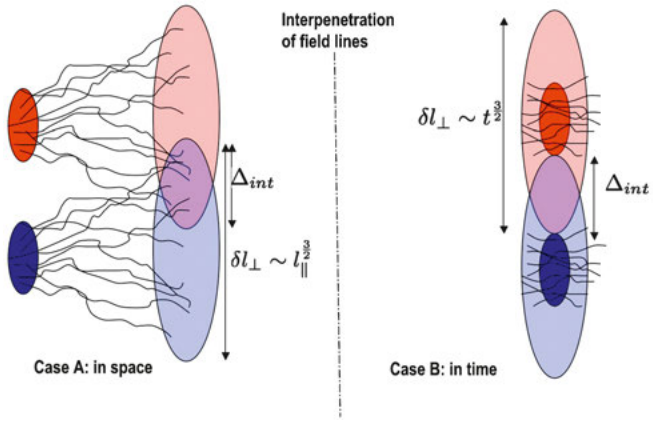

Figure 9.6: Microscopic physical picture of reconnection diffusion. Magnetized plasma from two regions is spread by turbulence and mixed up over $\Delta_{\rm int}$. *Left panel*: Description of the process in terms of field wandering in space. *Right panel*: Description of the spread in time.

perpendicular direction in the situation when magnetic field lines are traced by particles moving along them. Using Equation (7.1), one can get the RMS separation of the magnetic field lines (LV99)

$$\delta l_\perp^2 \approx \frac{l_\parallel^3}{L}\left(\frac{V_L}{V_A}\right)^4, \tag{9.16}$$

i. e., $l_\perp^2$ is proportional to $l_\parallel^3$. This regime is the Richardson diffusion in terms of magnetic field lines. The numerical testing of this prediction of LV99 is shown in Figure 7.1. This is the diffusion in space and Equation (9.16) provides the distance $l_\parallel$ at which the magnetic field lines of regions separated by $l_\perp$ start overlapping.[6]

For the partially ionized gas, the following question is important. Does the Rechester–Rosenbluth length given by Equation (9.15) present a bottleneck for Richardson diffusion on the larger scales? There has not yet been a numerical study of the Richardson diffusion in a partially ionized gas. However, one can argue that the Richardson diffusion makes the latter irrelevant if one considers magnetic diffusion on scales significantly larger than the turbulence damping scale.

We note that magnetic field wandering described in LV99 is an implementation of Richardson diffusion (ELV11). A similar process of field wandering in space has been then used to calculate perpendicular diffusion of CRs and heat transport (see [336, 256, 455]). We considered this important process in the Section 7.1.

9.3.3 Reconnection diffusion in partially ionized gas

Star formation happens in partially ionized gas. It is known that partial ionization does as strong affect fluid conductivity as it affects the damping of the turbulent motions [280, 450]. The analogy between the turbulence and dynamo in partially ionized gas and in fluids with viscosity much larger than resistivity, i. e. with high Prandtl numbers, was discussed in [448].

In high Prandtl number media the GS95-type turbulent motions decay at the scale $l_{\perp,\mathrm{crit}}$, which is much larger than the scale of at which Ohmic dissipation gets important. Thus, over a range of scales less than $l_{\perp,\mathrm{crit}}$ magnetic fields preserve their identity and are being driven by the shear on the scale $l_{\perp,\mathrm{crit}}$ as it is the case in numerical simulations in [88] and the theory in [280]. In view of the findings in ELV11 one should establish the range of scales at which magnetic fields are subject to Richardson diffusion. It is obvious that the transition to the Richardson diffusion happens when field

6 Thus for sufficiently large $l_\parallel$ all parts of the volume of magnetized plasmas get connected. In other words, the entire volume becomes accessible to particles moving along magnetic field lines. Naturally, in this situation the customary for the star formation community notion of flux to mass ratio does not have much meaning.

lines get separated by the perpendicular scale of the critically damped eddies $l_{\perp,\mathrm{crit}}$. The separation in the perpendicular direction starts with the scale r_{init} follows the Lyapunov exponential growth with the distance l measured along the magnetic field lines. Therefore, $r_{\mathrm{init}} \exp(l/l_{\parallel,\mathrm{crit}})$, where $l_{\parallel,\mathrm{crit}}$ corresponds to critically damped eddies with $l_{\mathrm{perp,crit}}$. It seems natural to associate r_{init} with the separation of the field lines arising from Ohmic resistivity on the scale of the critically damped eddies, i. e.

$$r_{\mathrm{init}}^2 = \eta l_{\parallel,\mathrm{crit}}/V_A, \tag{9.17}$$

where η is the value of Ohmic resistivity.

Thus we as in Section 9.3.1 get to the Rechester–Rosenbluth scale,

$$L_{RR} \approx l_{\parallel,\mathrm{crit}} \ln(l_{\perp,\mathrm{crit}}/r_{\mathrm{init}}) \tag{9.18}$$

Accounting for Equation (9.17) and that

$$l_{\perp,\mathrm{crit}}^2 = \nu l_{\parallel,\mathrm{crit}}/V_A, \tag{9.19}$$

where ν is the viscosity coefficient. One can rewrite Equation (9.18)

$$L_{RR} \approx l_{\parallel,\mathrm{crit}} \ln \mathrm{Pt} \tag{9.20}$$

where $\mathrm{Pt} = \nu/\eta$ is the Prandtl number.

If the current sheets are much longer than $L_R R$, then magnetic field lines undergo Richardson diffusion and, according to ELV11, the LV99 turbulent reconnection model is applicable. At the same time, on scales less than L_{RR} magnetic reconnection can be slow.[7]

9.4 Theoretical expectations and numerical simulations of reconnection diffusion

9.4.1 Limitations of numerical simulations

The difference between reconnection in astrophysical situations and in numerical simulations stems from the fact that the Lundquist number.[8] Because of the huge astrophysical length-scales L_x involved, the astrophysical Lundquist numbers are huge,

7 Incidentally, this can explain the formation of density fluctuations on scales of thousands of Astronomical Units, that are observed in the ISM [189].

8 It is different from the magnetic Reynolds' number which is the ratio of the magnetic field decay time to the eddy turnover time. It is defined using the injection velocity v_l as a characteristic speed instead of the Alfvén speed V_A, which is used in the Lundquist number.

e. g., for the ISM they are about 10^{16}. In contrast, present-day MHD simulations correspond to $S < 10^4$. As the numerical efforts scale as L_x^4, where L_x is the size of the box, it is not feasible at present or in the foreseeable future to have simulations with realistic Lundquist numbers. Therefore, the numerical studies of reconnection diffusion in [377, 375] as well as in [176] deal with a very different range of Lundquist numbers. As a result, the theoretical justification why *for a given problem* the difference in the Lundquist numbers is not essential is mandatory. For the case of reconnection diffusion, the turbulent reconnection theory theory (see Chapter 8), predicts that the dynamics of reconnection is independent of the Lundquist number. As a result, one comes to an important conclusion that the reconnection diffusion in the computer simulations *in the presence of turbulence* adequately represents the reconnection diffusion in the astrophysical settings.

Understanding of the nature of reconnection diffusion allows one to simulate this process using the existing 3D MHD codes. Some results of such a simulation is shown in Figure 9.7. We observe that *in the absence of ambipolar diffusion*, the magnetic field escapes the gravitational potential, thus allowing the matter to become concentrated in the center. This process is the essence of star formation. The simulations in [377] were performed for different settings, e. g. starting from equilibrium configurations representing subcritical clouds as well as for collapsing clouds, representing supercritical clouds. In all the cases studied, the efficient removal of magnetic flux from clouds was reported.

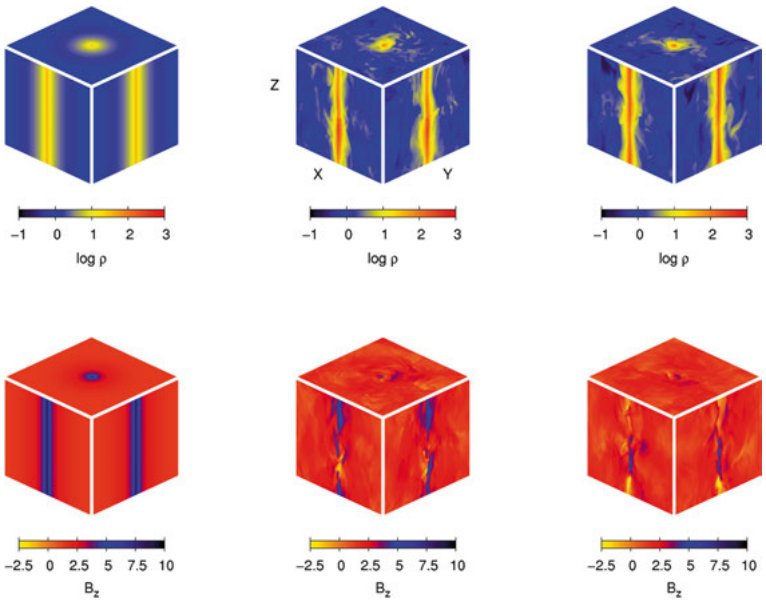

Figure 9.7: Removal of magnetic field via reconnection diffusion from cylindrical models of molecular clouds. In the process of simulations, the density is accumulated at the center of the potential well (*upper raw*), while the magnetic field leaves the center (*lower raw*) from [377].

9.4.2 Reconnection diffusion in circumstellar accretion disks

Circumstellar accretion disks are known to play a fundamental role at the late stages of star formation (see [3]). Observations revealed that embedded magnetic fields in molecular cloud cores are high enough to inhibit the formation of rotationally supported disks. This problem is also known as "magnetic breaking catastrophe." It is established that ambipolar diffusion is not powerful enough to induce the removal of magnetic fields fast enough. This motivated [395] to suggest the effects of enhanced resistivity that can explain the observational data. More recent elaborations of this idea of microscopic resistivity can be found in [237] and [292]. On the contrary, it was argued in [269] that the removal of magnetic field is due to reconnection diffusion.

The numerical studies of reconnection diffusion in disks are similar to the numerical studies of the process in the molecular clouds. Figure 9.8 shows results of the simulations in [375] which, indeed, support the notion that reconnection diffusion is the process responsible for the removal of magnetic fields. The turbulence level within the simulated molecular cloud turbulence is chosen to correspond to observations. The turbulence is *not* driven during the disk formation process.

The benchmark simulations testify, in agreement with earlier studies, that without turbulence the formation of disks is suppressed as the angular momentum of the forming disk is tranformed to the ambient medium. On the contrary the simulations

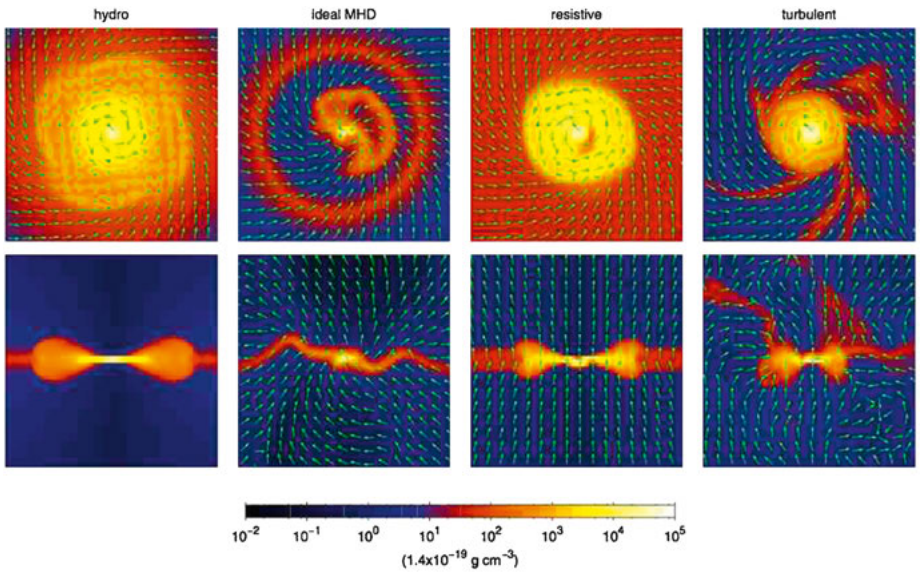

Figure 9.8: Formation of circumstellar disks (from left to right): in hydro simulations, MHD simulations without turbulence, MHD simulations with unrealistically high resistivity and MHD simulations with turbulence at the start of simulations. Reconnection diffusion produces realistic disks from [375].

performed in the presence of turbulence in the initial stage of disk formation established the correspondence of the properties of the disks to observations. The reconnection diffusion was identified as the source of the magnetic field loss. While additional processes may also be present during the simulations, see [388], it is well established that the reconnection diffusion is the process that is definitely present and important.[9]

More recent simulations of the accretion disks in [176] provided additional quantitative evidence in favor of the reconnection diffusion. They also identified turbulent reconnection as the process that converts the initial "split monopole" magnetic field configuration into the dipole configuration. While the initial magnetic field configuration attaches the disk to the surrounding medium, the dipole magnetic field essentially decouples the disk from the surrounding molecular cloud. The corresponding topology change significantly helps in solving the notorious problem of "magnetic breaking catastrophe." These results are illustrated in Figure 9.9.

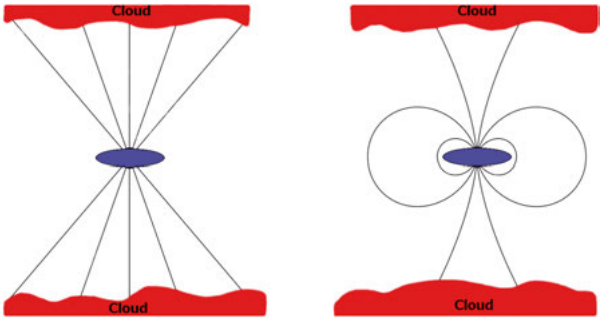

Figure 9.9: Change of the magnetic field configuration from the split monopole on the left to the dipole configuration on the right decreases the degree of coupling of the disk with the surrounding ISM without removing magnetic field from the disk from [68].

9.5 Predictions and tests for reconnection diffusion

Reconnection diffusion is a physical process very different from the textbook-accepted process of ambipolar diffusion. Thus it is not surprising that the star formation controlled by reconnection diffusion is very different from the traditional one. Below we outline a few predictions that the reconnection diffusion entails.

9.5.1 Reconnection diffusion in interstellar diffuse gas

A naive interpretation of magnetic fields frozen in interstellar plasmas suggests that fluctuations of magnetic field and density should be correlated. More considerations

9 The models with enhanced resistivity require resistivities that are not motivated by the known physics. Thus we do not consider them as a solution.

suggest that these correlations may not be perfect, as motions along magnetic field lines that compress only gas are also present, e. g., slow modes in the media with magnetic pressure larger than the pressure of the ionized gas (see [88, 354]). However, observations by [424] demonstrated a very poor correlation between the magnetic field strength and density, which was rather unexpected for many researchers. Indeed, the degree of ionization of the diffuse media is sufficiently large to make the effects of ambipolar diffusion negligible.

At the same time, in view of our earlier discussion, the above result is expected. Indeed, we stressed that the reconnection diffusion tends to make the magnetic energy density uniformly distributed in the volume. In other words, in the presence of reconnection diffusion mixing of density fluctuations by turbulent eddies takes place and this destroys any density-magnetic field correlations arising from simultaneous compression of magnetic field and conducting gas.

Reconnection diffusion can also account for the results of other observations. For instance, [104] analyzed an extensive set of Zeeman measurements and showed that clouds with column densities N_H less than 10^{21} cm^{-2} are subcritical, i. e., magnetically dominated, while at higher densities they get supercritical, i. e., gravity dominated. He noted, that for cold HI clouds with $N_H < 10^{21}$ cm^{-2} the magnetic field is approximately $\sim$ 6 μG, which coincides with the value of magnetic field strength in a much more rarefied warm neutral media. On the basis of our study, we claim that reconnection diffusion presents an appealing solution. Indeed, the efficient diffusion of magnetic field is expected make magnetic field strength the same in cold dense clouds and surrounding warm rarefied medium.

In addition, [104] notes that the kinetic and magnetic energies of low density clouds are approximately in equipartition and larger that the thermal energy. This means that the turbulence is trans-Alfvenic supersonic turbulence and this turbulence is expected to be efficient in driving reconnection diffusion. From the plot presented in [104] (see Figure 9.10), it is evident that the majority of the clouds preserves the magnetic field strength of the order of 6 μG even as the column density gets as high as 10^{23} cm^{-2}. This is the likely consequence of the reconnection diffusion being efficient at those densities. A tendency of the increase of the mean magnetic field for densities larger than 10^{23} cm^{-2} was explained in [281] as the consequence of self-gravity getting dominant. In this situation, the reconnection diffusion fails to remove magnetic field from the contracting clouds fast enough.

In addition, [281] pointed out that the aforementioned independence of magnetic field strength on the cloud density can be related to the empirical Larson relations [253] obtained for interstellar turbulence. Indeed, [253] found that the velocity dispersion is proportional to the square root of the cloud size, i. e., $\sigma_V \sim R^{1/2}$ and that the 3D density of cloud is inversely proportional to cloud size, i. e., $\rho \sim R^{-1}$. For instance, one can assume a rough equality between the kinetic energy and magnetic energy

$$\frac{B^2}{8\pi} \sim \rho\sigma_v^2, \tag{9.21}$$

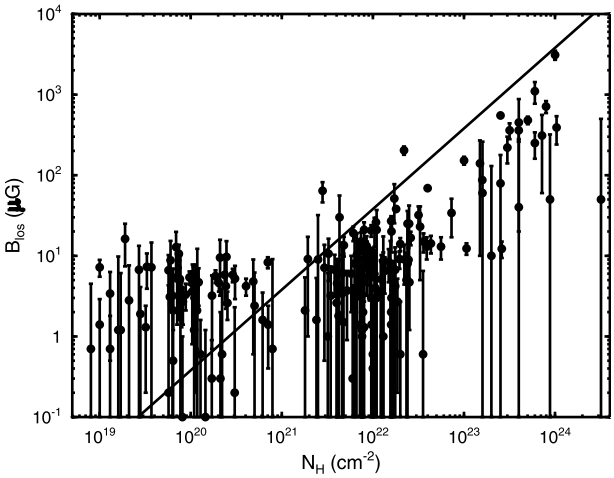

Figure 9.10: HI, OH, and CN Zeeman measurements of line of sight component of magnetic field versus the total column density NH of atomic and molecular hydrogen. The straight line is the critical mass/flux $M/\Phi = 3.8 \times N_H/B$ with subcritical clouds above the line. The two molecular clouds near $N = 10^{22}$ have OH maser contamination in their spectra and the corresponding Zeeman results are not reliable from [104].

which is natural for trans-Alfvenic turbulence. If one also assumes the virialization of a cloud

$$\frac{GM}{R} \sim \sigma_v^2, \tag{9.22}$$

then, combining Equations (9.21) and (9.22) with an estimate of the cloud mass $M \sim \rho R^3$ one gets

$$\sigma_v \sim B^{1/2} R^{1/2} \tag{9.23}$$

and

$$\rho \sim B R^{-1}, \tag{9.24}$$

which reproduces the [253] relations, provided that the reconnection diffusion keeps magnetic field uncorrelated with density. For cloud cores where reconnection diffusion is not sufficiently fast to remove magnetic field on the time of the dynamic collapse [416, 368], the Larson relations fail. This failure at higher densities agrees well with observations and simulations [333].

9.5.2 Reconnection diffusion and extreme cases of star formation

Testing ideas is good in extreme environments, where alternative processes are excluded. For instance, ambipolar diffusion definitely cannot work in the high ionization

media. It was found, for instance, that reconnection diffusion concept provides new ways of approaching the challenge explaining star formation in environments of high ionization, i. e., for instance, in galaxies emitting more than 10^{12} solar luminousities in the far-infrared. These ultra-luminous infrared galaxies or ULIRGs present physical conditions with very high density of cosmic rays [348]. Ambipolar diffusion in these environments is expected to be marginal due to high ionization by cosmic rays. Contrary to the expectations of the star formation theory based on ambipolar diffusion, these environments provide the highest star formation rate which is suggestive of a process which removes magnetic fields irrespectively of the level of ionization. At the same time, reconnection diffusion is such a process.

Similarly, the formation of early stars [77] is a great problem for which the effects of magnetic fields are hotly debated. Reconnection diffusion mitigates the cloud support by magnetic fields and, therefore, decreases the uncertainties associated with the presence of magnetic fields for star formation in early Universe [448].

9.5.3 Intuitive understanding of reconnection diffusion

The idea of magnetic flux freezing is so deeply rooted in astrophysics, that any attempts to challenge it sound heretical. At the same time, we would like to stress that fast reconnection in turbulent magnetized media is very natural. Moreover, a lot of accepted astrophysical ideas implicitly rely on the ability of magnetic field to reconnect fast in turbulent media and, therefore, not to be frozen in the turbulent fluids. Indeed, without turbulent reconnection the intersecting magnetic field flux tubes do not cross each other creating the felt-like strucute. Thus the magnetized turbulent fluid would not behave like a fluid. This automatically would mean that the numerical simulations of interstellar media that show fluid-like behavior are irrelevant to describing the actual interstellar medium dynamics. In other words, unless turbulent reconnection and reconnection diffusion concepts are accepted, all the crop of the present and future numerical simulations of magnetized ISM and other magnetized astrophysical media should be accepted completely irrelevant and useless.

At the same time, if turbulent magnetized fluids preserve fluid-type behavior as it required by GS95 theory of turbulence, one has to accept that turbulent reconnection and reconnection diffusion takes place. In addition, the ideas of magnetic field meandering that have been invoked for decades to understand the observed diffusion of cosmic rays perpendicular to magnetic field (see [350, 204]) are naturally related to the reconnection diffusion concept. The latter is evident from the analysis of the numerical simulations in [137].

The failure of flux freezing in turbulent fluids has important astrophysical consequences for star formation and beyond it. The generic flux freezing violation in turbulent fluids contradicts to the customary accepted point of view that in astrophysical

situations the flux freezing is "nearly" fulfilled and the violations are due to the existing finite nonideal effects. Turbulence makes violates the flux freezing through the entire volume. However, turbulence, unlike resistivity, does not destroy magnetic flux, but makes the magnetic field stochastic. As a result, the charged particles get the possibility of exploring the entire volume, which also means that magnetic field get the ability to diffuse through the volume.

9.5.4 Reconnection diffusion and alternative ideas

Reconnection diffusion is a numerically confirmed and theoretically justified concept. In terms of astrophysical applications, in many cases there is no real alternative way of explaining many existing observations but to appeal to reconnection diffusion. For instance, an alternative way for changing locally the value of the magnetic field flux to mass ratio is to allow the conducting matter to be accumulated along magnetic field lines. This process definitely takes place, but the requirement of one dimensional motion of matter is very restrictive and requires collecting the matter from enormous distances. Indeed, it requires ~ 1 kpc collection of interstellar gas to create an individual star (see [430]). This is definitely not feasible in turbulent environments, as magnetic field wandering is ought to interfere with the required one-dimensional motion. Estimates in [281] show that for typical interstellar medium conditions the spread of magnetic field lines over the distance for the material collection is expected to be so large that only a fraction of matter $\sim 10^{-4}$ could be viewed as collected along the mean field. As for simulations that "supported" the idea forming the clouds by collecting the material along magnetic field lines to form stars, we believe that we deal with the misinterpretation of the numerical results. Indeed, reconnection diffusion is an intrinsic part of the simulations of the turbulent interstellar medium and it should be accounted for in interpreting the results of numerical simulations.

The approach based on reconnection diffusion should also be distinguished from the research on the decorrelation of magnetic field and density within compressible turbulent fluctuations. This decorrelation naturally takes place within the theory of compressible MHD turbulence. Indeed, as follows from 3D numerical simulations in [81, 83] there exist separate turbulent cascades of Alfven and fast modes in strongly driven turbulence as well as a cascade of slow modes driven by Alfvénic cascade. For instance, slow modes in magnetically dominated plasma are associated with density perturbations with marginal perturbation of magnetic fields, while the same is true for fast modes in weakly magnetized or high beta plasmas. Naturally, these compressible modes decorrelate magnetic fields and density on the crossing time of the wave. This was the effect studied in more detail in a one-dimensional setting both analytically and numerically by [354], who pointed out that the enhancements of magnetic field strength and density may correlate and anti-correlate in turbulent interstellar gas

within the fluctuations and this can introduce the dispersion of the mass-to-flux ratios within the turbulent volume. The fluctuations provide a varying in time changes and predict that the decorrelation should vary with the driving compressibility, e. g., related to the Mach number. We are not aware of such a dependence, but instead the decorrelation looks to be complete. This can be explained by the reconnection diffusion which deals with the *permanent* decorrelation of magnetic field and density making magnetic field-density decorrelation irreversible.

Finally, we would like to compare the concept of reconnection diffusion with that of "turbulent ambipolar diffusion" [149, 470]. The latter concept is based on the idea that turbulence can create gradients of neutrals and those can accelerate the overall pace of ambipolar diffusion. The questions that naturally arise are (1) whether this process can proceed without magnetic reconnection and (2) what is the role of ambipolar diffusion in the process. [191] performed numerical simulations with 2D turbulent mixing of a layer with magnetic field perpendicular to the layer and reported fast diffusion that was of the order of turbulent diffusivity number $V_L L$, *independent of ambipolar diffusion coefficient*. However, this sort of mixing can happen without reconnection only in a *degenerate case of 2D mixing* with exactly parallel magnetic field lines. In any realistic 3D case, turbulence will bend magnetic field lines and the mixing process does inevitably involve reconnection. Therefore, the 3D turbulent mixing in magnetized fluid must be treated from the point of view of reconnection theory. If magnetic reconnection does not happen within one eddy rotation time, the process in [191] should come to holt due to the inability of magnetic field lines to freely cross each other. This is in contrast to the 2D case where no such constraints are present. Indeed, slow magnetic reconnection should arrest the 3D mixing and this should make the conclusions obtained in the degenerate 2D case inapplicable to the 3D diffusion. If, however, reconnection is fast as predicted in LV99, then mixing and turbulent diffusion are expected to take place. The resulting turbulent diffusion rate is independent from on the rate of the ambipolar diffusion processes, which is, incidentally, in agreement with results in [191]. The process will proceed with the same rate in partially ionized gas as in fully ionized plasmas.[10]

The previous discussion provide the answers to the questions that we posed in the paragraph above. One has to conclude that turbulent diffusion in partially ionized gas is (1) impossible without fast turbulent reconnection and (2) independent of ambipolar diffusion physics. In this situation, we believe that it is misleading to talk about "turbulent ambipolar diffusion" in any astrophysical 3D setting. In fact, the actual diffusion in turbulent media is controlled by magnetic reconnection and is independent of ambipolar diffusion process.

10 The 2D toy model in [191] does not require reconnection as the magnetic field lines are strictly parallel to each other and perpendicular to the motions of the fluid. The obtained results coinside with the expectations for the reconnection diffusion as LV99 reconnection does not constrain motions of magnetized eddies.

9.5.5 Transport of heat in magnetized fluid

The issue of diffusion in magnetized plasma is also relevant to heat transfer. This process which is relevant to the wide variety of circumstances from mixing layers in the Local Bubble [400] and Milky Way [16] to cooling flows in an intracluster medium (ICM) [144]. The latter issue is related to the absence of evidence of plasma cooling (see [145]). This suggests the existence of heating that replenishes the energy lost via X-ray emission. Heat transfer from hot outer regions is a process to consider in this context.

[336], henceforth NM01, obtained estimates of thermal conductivity by electrons using the GS95 model of MHD turbulence with the velocity V_L at the energy injection scale L that is equal to the Alfven velocity V_A, i. e., the turbulence with the Alfven Mach number $M_A \equiv (V_L/V_A) = 1$. While the work was done in the context in ICM, for actual ICM $M_A > 1$. There are other plasmas, e. g., parts of the interstellar media, for which $M_A < 1$. Below we discuss turbulence for both $M_A > 1$ and $M_A < 1$ and compare the particle diffusion to that by turbulent fluid motions. For heat transfer, we refer to our results in [257, 259].

Let us follow the traditional way of reasoning and initially disregard the dynamics of fluid motions on diffusion, i. e., consider diffusion induced by particles moving along static magnetic fields. As we discussed, magnetized turbulence in the GS95 model is anisotropic with eddies elongated along (henceforth denoted by $\parallel$) the direction of local magnetic field. Consider isotropic injection of energy at the outer scale L and dissipation at the scale $l_{\perp,\min}$, where $\perp$ denotes the direction of perpendicular to the local magnetic field. At smallest scales, less than $l_{\perp,\min}$ the separations of magnetic field lines for $r_0 < l_{\perp,\min}$ are mostly influenced by the motions at the scale $l_{\perp,\min}$, which results in Lyapunov-type growth: $\sim r_0 \exp(l/l_{\parallel,\min})$. This growth is similar to that discussed in toy models of "turbulence" with a single scale of turbulent motions [366, 72]. Indeed, the largest shear that causes field line divergence is provided by the marginally damped motions at the scale around $l_{\perp,\min}$. r_0 can be of the size of the cloud of electrons of the electron Larmor radius $r_{\mathrm{Lar,particle}}$. To get to the scale of $l_{\perp,\min}$ and get into the regime of the Richardson diffusion, the electrons should travel over the distance

$$L_{RR} \sim l_{\parallel,\min} \ln(l_{\perp,\min}/r_{\mathrm{Lar,particle}}). \tag{9.25}$$

We may mention that within the single-scale "turbulence" model $L = l_{\parallel,\min} = l_{\perp,\min}$ and the scale L_{RR} is called Rechester–Rosenbluth distance. For the ICM parameters, the logarithmic factor in Equation (9.25) is of the order of 30, and this causes 30 times decrease of thermal conductivity for the single-scale models.[11] In realistic turbulence

11 If for the single-scale "turbulence" model, $L_{RR} \sim 30L$ [72], the diffusion over distance Δ takes L_{RR}/L steps, i. e., $\Delta^2 \sim L_{RR}L$, which decreases the corresponding diffusion coefficient $\kappa_{\mathrm{particle,single}} \sim \Delta^2/\delta t$ by

with a limited (e. g., a few decades) inertial range, the logarithmic factor stays of the same order but it marginally affects the thermal conductivity, provided that $L \gg l_{\parallel,\min}$. Note that the GS95 model of turbulence takes into account that at small scales with field lines that are sufficiently stiff, i. e., the deviation of the field lines from their original direction is of the order unity at scale L and less for smaller scales.

Diffusion for $M_A > 1$

Consider first the diffusion for $M_A > 1$. We know that turbulence with $M_A > 1$ evolves along hydrodynamic isotropic Kolmogorov cascade, i. e., $V_l \sim V_L(l/L)^{1/3}$ over the range of scales $[L, l_A]$, where

$$l_A \approx L(V_A/V_L)^3 \equiv LM_A^{-3}. \tag{9.26}$$

Making use of the relations between parallel and perpendicular scales

$$l_\parallel \sim L(l_\perp/L)^{2/3}M_A^{-1}, \quad M_A > 1, \tag{9.27}$$

it is possible to calculate heat diffusion arising from electrons streaming along magnetic field lines.

If the mean-free path of particles, e. g., electrons satisfy $\lambda \gg l_A$, they stream freely over the distance of l_A.[12]

For particles initially at distance $l_{\perp,\min}$ to get separated by L, the required travel is the random walk with the step l_A, i. e., the mean-squared displacement of a particle until it enters an independent large-scale eddy $\Delta^2 \sim l_A^2(L/l_A)$, where L/l_A is the number of steps. These steps require time $\delta t \sim (L/l_A)l_A/C_1v_{\rm particle}$, where $v_{\rm particle}$ is electron thermal velocity and the coefficient $C_1 = 1/3$ reflects the 1D character of motion along magnetic field lines. Thus the electron diffusion coefficient is

$$\kappa_{\rm particle} \equiv \Delta^2/\delta t \approx (1/3)l_Av_{\rm particle}, \quad l_A < \lambda, \tag{9.28}$$

which for $l_A \ll \lambda$ reflects a substantial reduction of diffusivity compared to its unmagnetized value $\kappa_{\rm unmagn} = \lambda v_{\rm particle}$. We note, that we assumed in Equation (9.28) that $L \gg 30l_{\parallel,\min}$.

For $\lambda \ll l_A \ll L$, $\kappa_{\rm particle} \approx 1/3\kappa_{\rm unmagn}$ as both the L_{RR} and the additional distance for electrons to diffuse due to the fact that magnetic field is stiff at scales less than l_A are negligible compared to L. For $l_A \to L$, when magnetic field is dynamically important up to the scale L, it gets around 1/5 of the value in unmagnetized medium, according to NM01.

---

the factor of 30. This is a significant decrease of thermal conductivity. This is, however, an artifact of the use of unrealistic model that disregards the existence of the turbulent cascade.

12 Mean-free path in turbulent collisionless plasmas is modified as we discuss in Section 2.2.1.

Note that even dynamically unimportant magnetic fields can influence heat conductivity over short time intervals. For instance, over time interval less than $l_A^2/C_1\kappa_{\rm unmagn}$ the diffusion happens mostly along magnetic field lines and the difference between parallel and perpendicular diffusivities is large. This gives $\langle y^2\rangle^{1/2} \sim \frac{x^{3/2}}{3^{3/2}L^{1/2}}M_A^3$. This allows for the transient existence of sharp small-scale temperature gradients in galaxy clusters.

Diffusion for $M_A < 1$

For $M_A < 1$, turbulence is anisotropic from the injection scale L. In fact, at large scales the turbulence is *weak*[13] (see LV99). For scales less than $l_{\rm trans}$, the turbulence is *strong*, i. e., the relations in LV99 provide $V_l \sim V_L(L/l_\perp)^{-1/3}M_A^{1/3}$ and

$$l_\parallel \sim L(l_\perp/L)^{2/3}M_A^{-4/3}, \quad M_A < 1. \tag{9.29}$$

For $M_A < 1$, magnetic field wandering in the direction perpendicular to the mean magnetic field (along y-axis) can be described by $d\langle y^2\rangle/dx \sim \langle y^2\rangle/l_\parallel$ (LV99), where $l_\parallel$ is expressed by Equation (9.29) and one can associate $l_\perp$ with $2\langle y^2\rangle$,

$$\langle y^2\rangle^{1/2} \sim \frac{x^{3/2}}{3^{3/2}L^{1/2}}M_A^2, \quad l_\perp < l_{\rm trans} \tag{9.30}$$

For weak turbulence, $d\langle y^2\rangle/dx \sim LM_A^4$ (LV99) and, therefore,

$$\langle y^2\rangle^{1/2} \sim L^{1/2}x^{1/2}M_A^2, \quad l_\perp > l_{\rm trans}. \tag{9.31}$$

Equation (9.30) has the factor M_A^2, which reflects the suppression of thermal conductivity perpendicular to the mean magnetic field as the magnetic field gets stronger. Physically, this means that for $M_A < 1$ the magnetic field wonders around the well-defined direction. Thus the diffusivity gets anisotropic with the diffusion coefficient parallel to the mean field $\kappa_{\parallel,\rm particle} \approx 1/3\kappa_{\rm unmagn}$ being larger than coefficient for diffusion perpendicular to magnetic field $\kappa_{\perp,\rm particle}$.

Consider the coefficient $\kappa_{\perp,\rm particle}$ for $M_A \ll 1$. As NM01 showed, particles become uncorrelated if they are displaced over the distance L in the direction perpendicular to the magnetic field. To do this, a particle has first to travel L_{RR} (see Equation (9.18)), where Equation (9.29) relates $l_{\parallel,\rm min}$ and $l_{\perp,\rm min}$. In most cases, the additional travel arising from the logarithmic factor is negligible compared to the overall diffusion distance L. At larger scales, the electron has to diffuse $\sim L$ in the direction parallel to magnetic field to cover the distance of LM_A^2 in the direction perpendicular to magnetic field direction. The diffusion over a distance R is random walk with the step LM_A^2. Therefore, one requires $R^2/L^2M_A^4$ steps. The time of the individual step is $L^2/\kappa_{\parallel,\rm particle}$.

13 The terms "weak" and "strong" turbulence are accepted in the literature, but can be confusing. As we discuss later at smaller scales at which the turbulent velocities decrease, the turbulence becomes *strong*. The formal theory of weak turbulence is given in [158].

Therefore, the perpendicular diffusion coefficient can be estimated as

$$\kappa_{\perp,\text{particle}} = R^2/(R^2/[\kappa_{\parallel,\text{particle}} M_A^4]) = \kappa_{\parallel,\text{particle}} M_A^4, \quad M_A < 1. \tag{9.32}$$

An essential assumption above is that the particles do not trace their way back over the individual steps along magnetic field lines, i. e., $L_{RR} << L$. Note that for M_A of the order of unity this is not accurate and one should account for the actual 3D displacement. This introduces the change by a factor of order unity.

Turbulent diffusivity

Turbulent motions themselves can induce advective transport. In [82], we dealt with the turbulence with $M_A \sim 1$ and estimated

$$\kappa_{\text{dynamic}} \approx C_{\text{dyn}} L V_L, \quad M_A > 1, \tag{9.33}$$

where $C_{\text{dyn}} \sim 0(1)$ is a constant. This constant for hydro turbulence is around 1/3 [291]. If we deal with heat transport in plasmas, we can assume $C_{\text{dyn}} \approx 2/3$ to account for the advective heat transport by both protons and electrons.[14] Thus Equation (9.33) is relevant for the cases of $M_A > 1$ up to $M_A \sim 1$. For weak turbulence, there is diffusivity arising from eddies of strong turbulence at scales less than l_{trans}, i. e., $\kappa_{\text{dynamic}}^{\text{strong}} \approx C_{\text{dyn}} l_{\text{trans}} V_{\text{trans}}$ and the weak turbulence eddies. Both have the same functional form [257], [143] and the total diffusivity is the sum of the two, i. e., for plasma one can write

$$\kappa_{\text{dynamic}} \approx (\beta/3) L V_L M_A^3, \quad M_A < 1, \tag{9.34}$$

where $\beta \approx 4$.

Relative importance: parameter space

It is important to define the parameter space for which electron conduction or turbulent heat advection dominates. The corresponding plot for $\kappa_{\text{particle}} < \kappa_{\text{dynamic}}$ is shown in Figure 9.11, where the Mach number M_s and the Alfven Mach number M_A are the variables. For $M_A < 1$, the ratio of diffusivities arising from fluid and particle motions is $\kappa_{\text{dynamic}}/\kappa_{\text{particle}} \sim \beta\alpha M_S M_A (L/\lambda)$ (see Equations (9.32) and (9.34)), the square root of the ratio of the electron to proton mass $\alpha = (m_e/m_p)^{1/2}$, which provides the separation line between the two regions in Figure 9.11, $\beta\alpha M_s \sim (\lambda/L) M_A$. For $1 < M_A < (L/\lambda)^{1/3}$, the mean free path is less than l_A which results in κ_{particle} being some fraction of κ_{unmagn}, while κ_{dynamic} is given by Equation (9.33). Therefore, $\kappa_{\text{dynamic}}/\kappa_{\text{particle}} \sim \beta\alpha M_s (L/\lambda)$, i. e., the ratio does not depend on M_A (horizontal line in

14 This gets clear if one uses the heat flux equation $q = -\kappa_c \bigtriangledown T$, where $\kappa_c = n k_B \kappa_{\text{dynamic/electr}}$, n is *electron* number density, and k_B is the Boltzmann constant, for both electron and advective heat transport.

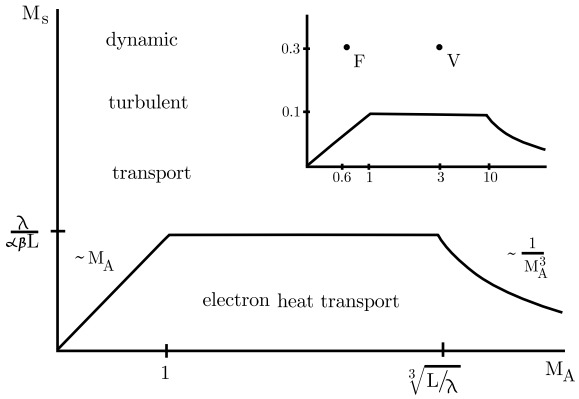

Figure 9.11: Parameter space for particle diffusion or turbulent diffusion to dominate: application to heat transfer. Sonic Mach number M_s is plotted against the Alfven Mach number M_A. The heat transport is dominated by the dynamics of turbulent eddies is above the curve and by thermal conductivity of electrons is below the curve. Here, λ is the mean-free path of the electron, L is the driving scale, and $\alpha = (m_e/m_p)^{1/2}$, $\beta \approx 4$. The panel in the right upper corner of the figure illustrates heat transport for the parameters for a cool core Hydra cluster (point "F"), "V" corresponds to the illustrative model of a cluster core in [130] from [259].

Figure 9.11). When $M_A > (L/\lambda)^{1/3}$, the mean-free path of electrons is constrained by l_A. In this case, $\kappa_{\rm dynamic}/\kappa_{\rm particle} \sim \beta\alpha M_s M_A^3$ (see Equations (9.33) and (9.28)). This results in the separation line $\beta\alpha M_s \sim M_A^{-3}$ in Figure 9.11.

Heat transfer in intracluster medium

It is accepted that Intracluster Medium (ICM) is turbulent. In unmagnetized plasma with the ICM temperatures $T \sim 10^8$ K and density $10^{-3}\,{\rm cm}^{-3}$, the kinematic viscosity $\eta_{\rm unmagn} \sim v_{\rm ion}\lambda_{\rm ion}$, where $v_{\rm ion}$ and $\lambda_{\rm ion}$ are the velocity of an ion and its mean-free path, respectively. This results in the Reynolds' number ${\rm Re} \equiv LV_L/\eta_{\rm unmagn}$ of the order of 30. This is barely enough for the onset of turbulence. For the sake of simplicity, we assume that ion mean-free path coincides with the proton mean-free path and both are $\lambda \approx 3T_3^2 n_{-3}^{-1}\,{\rm kpc}$, where the temperature $T_3 \equiv kT/3\,{\rm keV}$ and $n_{-3} \equiv n/10^{-3}\,{\rm cm}^{-3}$. This provides λ of approximately 0.8–1 kpc for the ICM (see NM01).

It is known, however, that magnetic fields decrease the diffusivity. Assuming the maximal scattering rate of an ion, i. e., scattering every orbit (the so-called Bohm diffusion limit) one gets the viscosity perpendicular to magnetic field $\eta_\perp \sim v_{\rm ion} r_{\rm Lar,ion}$, which is much smaller than $\eta_{\rm unmagn}$, provided that the ion Larmor radius $r_{\rm Lar,ion} \ll \lambda_{\rm ion}$. For the parameters of the ICM, the viscosity is negligible[15] of magnetic lines parallel to each other, e. g., Alfven motions.

15 A *regular* magnetic field $B_\lambda \approx (2mkT)^{1/2}c/(e\lambda)$ that makes $r_{\rm Lar,ion}$ less than λ and, therefore, $\eta_\perp < v_{\rm unmagn}$ is just 10^{-20} G. *Turbulent* magnetic field with many reversals over $r_{\rm Lar,ion}$ does not interact

Below we will use the parameters of the ICM presented in the literature (see Enßlin, Vogt, and Pfrommer (2005), [130] henceforth EVP05, [131], henceforth EV06 and references therein). The estimates of injection velocity V_L varies in the literature from 300 km/s to 10^3 km/s, while the injection scale L varies from 20 kpc to 200 kpc, depending whether the injection of energy by galaxy mergers or galaxy wakes is considered. Let us estimate the minimal boundary for the Reynolds' number. EVP05 considers a model in which the magnetic field with the 10 μG fills 10 % of the volume, while 90 % of the volume is filled with the field of $B \sim 1\,\mu$G. Using the latter number and assuming $V_L = 10^3$ km/s, $L = 100$ kpc, and the density of the hot ICM is 10^{-3} cm^{-3}, one gets $V_A \approx 70$ km/s, i. e., $M_A > 1$. Using these numbers, one can get $l_A \approx 30$ pc for the 90 % of the volume of the hot ICM, which is much less than $\lambda_{\rm ion}$. The diffusivity of ICM plasma gets $\eta = v_{\rm ion} l_A$ which for the parameters above provides Re $\sim 2\times10^3$ at the outer scale L. However, as l_A increases as $\propto B^3$, Re gets around 50 for the field of 4 μG, which is at the border line of exciting turbulence. However, the regions with higher magnetic fields (e. g., 10 μG) can support Alfvenic-type turbulence with the injection scale l_A and the injection velocities resulting from large-scale shear $V_L(l_A/L) \sim V_L M_A^{-3}$.

If $B \sim 1\,\mu$G, the value of l_A is smaller than the mean free path of electrons λ. Equation (9.28) testifies that the value of $\kappa_{\rm electr}$ is 100 times smaller than $\kappa_{\rm Spitzer}$. On the same time, $\kappa_{\rm dynamic}$ for the ICM parameters adopted will be $\sim 30\kappa_{\rm Spitzer}$, which makes the dynamic diffusivity the dominant process. This agrees with the observations in [439]. Figure 9.11 shows the dominance of advective heat transfer for the cool core of Hydra A ($B = 6\,\mu$G, $n = 0.056\,$cm^{-3}, $L = 40\,$kpc, $T = 2.7\,$keV according to EV06), point "F", and for the illustrative model in EVP05, point "V", for which $B = 1\,\mu$G.

We note that our stationary model of MHD turbulence is not directly applicable to transient wakes behind galaxies. The ratio of the damping times of the hydro turbulence and the time of straightening of the magnetic field lines is $\sim M_A^{-1}$. Thus, for $M_A > 1$, the magnetic field at scales larger than l_A will be straightening gradually after the hydro-like turbulence has faded away over time L/V_L. The process can be viewed as the injection of turbulence at velocity V_A but at scales that increase linearly with time, i. e., as $l_A + V_A t$.

9.5.6 MHD and plasma-based descriptions of reconnection diffusion

In the previous section, we proved that LV99 ensures efficient diffusion of matter and magnetic fields in turbulent fluids. One may wonder whether other models of fast reconnection, e. g., collisionless reconnection, can also induce reconnection diffusion.

efficiently with a proton. As a result, the protons are not constrained until l_A gets of the order of $r_{\rm Lar,ion}$. This happens when the turbulent magnetic field is $\sim 2\times10^{-9}(V_L/10^3\,$km/s) G. At this point, the step for the random walk is $\sim 2\times10^{-6}$ pc and the Reynolds' number is of the order of 5×10^{10}.

First of all, we would like to stress that the LV99 model is not in conflict with the studies of magnetic reconnection in collisionless plasmas that have been a major thrust of the plasma physics community [390, 109]. Unlike latter studies, LV99 deals with turbulent environments. It shows, as we discussed in Section 4.1 that local reconnection rates are influenced by plasma effects, e. g., kinetic effects of Hall effects, but the overall or global reconnection rate, i. e., the rate at which magnetic flux tubes reconnect, is determined by the turbulent broadening of the reconnection region. Thus, in the turbulent astrophysical media the rate of reconnection is not going to be affected by additional mechanisms. As a result, the reconnection diffusion will proceed with its maximal rate limited by turbulent motions only.

If, on the contrary, the media that we deal with is not turbulent, reconnection diffusion does not take place even in the presence of fast reconnection. Turbulent mixing is a necessary condition for reconnection diffusion to exist. If other mechanisms of reconnection induce turbulence, this turbulence will induce reconnection diffusion and we return back to the case above.

Plasma effect might be potentially important on a more subtle level, however. As field wandering is essential for reconnection diffusion, one may wonder to what extend the plasma effects can be neglected while describing field wandering. Indeed, the nonideal terms in the Ohms law provide the stochasticity of charge carriers and, therefore, of the magnetic field lines that these charges trace. Consider, for instance, Hall term which is most commonly invoked in the literature of fast reconnection. Hall term was also invoked in a studies of magnetic field loss by circumstellar accretion disks[16] (see [237]). The usual criterion for the Hall term to dominate is that the electron flow velocity is dominated by the current. However, to dominate magnetic field stochasticity the criterion should be different as the correlations of the Hall velocity are short ranged. Assuming the small-scale equipartition of velocity and magnetic field, $B(r)^2/4\pi \sim \rho v(r)^2/2$ and turbulent correlation of velocities $\langle v_i v_j\rangle \sim Cr^y$, one gets for the Hall velocity $V_{\rm Hall} = J/ne = c\nabla \times B/4\pi ne$ correlations

$$\langle V_{{\rm Hall},i} V_{{\rm Hall},j}\rangle \sim \left(\frac{c}{4\pi ne}\right)^2 \Delta\langle B_i B_j\rangle \tag{9.35}$$

The right-hand side of Equation (9.35) can be estimated as $(\frac{c}{4\pi ne})^2 4\pi n\rho C r^{y-2}$, which is much smaller than the correlation of the turbulent velocities if the distance between point of correlation $r \gg c^2 m_i/4\pi ne^2 = \delta_i$, where δ_i is the ion inertial skin depth. This estimate is consistent with a more elaborate one in ELV11. Therefore, even large Hall velocities do not affect meandering of magnetic field lines on the scale much larger that the inertial skin depth. The reconnection diffusion applicable to star formation deals with scales $\gg \delta_i$.

16 To see the effect, the authors had to adopt the Hall term much larger than its value for the adopted parameters of the media.

We should mention that the Hall MHD (HMHD) is frequently presented as a proper way to describe reconnection in astrophysical systems. However, it is shown in ELV11 that HMHD is rarely applicable to the actual astrophysical plasmas. Indeed, the derivation of Hall MHD based on collisionality requires that the ion skin-depth δ_i must satisfy the conditions $\delta_i \gg S \gg \ell_{mfp,i}$, where S is the scale of large-scale variations of magnetic field. The second inequality is needed so that a two-fluid description is valid at the scales of interest, while the first inequality is needed so that the Hall term remains significant at those scales. However, substituting $\delta_i = \rho_i/\sqrt{\beta_i}$ into the expression for the Coulomb collisional frequency yields the result

$$\frac{\ell_{mfp,i}}{\delta_i} \propto \frac{\Lambda}{\ln\Lambda}\frac{v_{\mathrm{th},i}}{c}, \tag{9.36}$$

where $\Lambda = 4\pi\rho n\lambda_D^3$ is the number of particles in the Debye sphere. For weakly coupled astrophysical plasmas, Λ is really large (see the table in EVL11) and, therefore, $\ell_{mfp,i} \gg \delta_i$, unless the ion temperature is extremely low. Thus, Hall MHD is valid only for cold, dense plasmas, e. g., that produced by the MRX reconnection experiment [452], but not in the conditions of the diffuse ISM and molecular clouds where star formation takes place.

A more general discussion of the relative importance of plasma effects and turbulent reconnection is given by Eyink in [142]. There a Generalized Ohm's Law that includes the effects of turbulence was formulated. The analysis has proven that the turbulent reconnection dominates that arising from plasma effects for typical astrophysical situations. An importnant point advocated in [142] is that for the turbulent self-similar cascade the scale-length of the smallest eddy resolved by the observer is completely arbitrary and no objective physics can depend on it. At the same time, the description of the physics must be renormalized by unresolved physics and this effect must be accounted for. In other words, at very small scales, i. e. resistive scales of scales at which plasma effects induce reconnection the traditional Ohm's law is valid. A "blurred" picture of the reconnection at larger scales requires the use "coarse-grained" equations. For these equations the contribution of the traditional Ohm's law terms responsible for microscopic resistivities and plasma effects is negligible and, instead, additional terms related to turbulent motions below the "coarse-graining" scale are dominant. The corresponding formalism provides a mathematical formulation of the concenpt of reconnection diffusion and it explicitly shows that turbulent reconnection is taking place on all scales of turbulent cascade.

The aforementioned notion of the reconnection taking place at every scale of MHD turbulent cascade is in contrast with the one suggested in a series of papers where it is suggested that flux freezing is valid on large scale of turbulent motions and it is only in the vicinity of dissipation scale that the tearing modes induce magnetic reconnection (see, e. g., [297], [296]. The original LV99 model, subsequent publications (see [143]) as well as the latest study in [142] disagree with the notion of flux freezing at any scale

of strong turbulent MHD turbulence cascade. In fact, turbulent reconnection taking place over all scales rather than just the smallest ones is the only viable explanation of the numerical simulations in [137] that demonstrated strong violation of magnetic flux freezing in a turbulent fluid.

10 Extracting properties of astrophysical turbulence from observations

Attempts to study interstellar turbulence from observations date as far back as the 1950s (see [441, 331, 446]). In fact, the initial success of different directions of research was far from uniform (see [214, 115, 254, 11]). Supported by the theoretical understanding of scattering and scintillations (see [177, 335]) the studies of turbulence statistics of ionized media were successful (see [402, 334]) with the discovery of the Big Power Law in the Sky by Armstrong, Rickett, and Spangler (1995) [11] which was the Kolmogorov-type spectrum of plasma density at scales 10^8 – 10^{15} cm. Later using the Wisconsin H_α mapper data, Chepurnov & Lazarian [76] extended this spectrum even further (see Figure 1.1).

Other types of astrophysical turbulence studies were limited to intensities either integrated along the line of sight or within velocity channel maps. The latter type of measurements were erroneously associated with the studies of the density statistics. The effect of mapping of spectral line information to the Position-Position-Velocity (PPV) space as well as the interfering effects of self-absorption, absorption, geometry of observations were not theoretically described and, therefore, the observational studies [102, 185, 406] could not be correctly interpreted in terms of the properties of the underlying ISM turbulence.

For studies of turbulent velocities, a frequently used approach employed velocity centroids, which are first moments of spectral line (see [331, 223, 339, 317]). Later research, in particular, in [132, 134] showed serious problems with using the VC for recovering velocity statistics in supersonic turbulence.

A significant progress in theoretical understanding of the nonlinear mapping of the turbulence statistics from the real space to the PPV space that was initiated by the analytical study in [271] as well as the subsequent studies in [272–274]. The analytical predictions were numerically tested in [75, 62] and productively applied to observations (see [260] for a review) clarifying the meaning of the earlier data and interpreting the new data in terms of the underlying velocity and density statistics of turbulent flows.

The studies of turbulence using synchrotron provided anything, but a universal value of the spectral index of magnetic turbulence. For instance, the angular spectrum of the 408 MHz Haslam map has a slope close to –3: $C_l \propto l^{-3}$ [421, 55]. [247] performed a comprehensive angular power spectrum analysis of all-sky total intensity maps at 408 MHz and 1420 MHz. They found that the slope is close to –3 for high Galactic latitude regions. Other results also show slopes close to –3. For example, using Rhodes/HartRAO data at 2326 MHz [205, 168] obtained a slope of ~ 2.92 for high Galactic latitude regions with $|b| > 20^\circ$. [169] obtained a slope of ~ 3.15 for high Galactic latitude regions with $|b| > 20^\circ$ from the [367] survey at 1420 MHz. [54] also obtained a slope of ~ l^{-3} spectrum from the 1420 MHz map. [79] showed that these results are compatible with the

https://doi.org/10.1515/9783110263282-010

Kolmogorov/GS95 spectrum if a realistic structure of the synchrotron-emitting galactic disk and halo is taken into account.

New ways of study MHD turbulence using fluctuations of polarized synchrotron emission were suggested by Lazarian & Pogosyan [276] on the basis of the analytical description of the statistics of polarized synchrotron affected by the Faraday rotation of the polarized radiation. A way of separating of the contribution of the fast, Alfven and slow modes was suggested in [275] employing the difference of the anisotropies that these modes induce. This opens new ways to study MHD turbulence.

More recently, the approaches to separating turbulent modes in synchrotron were applied to separate the contribution from the fast, Alfven and slow modes using spectral lines. In [208], extended the theory of the PPV statistics to include the effects of anisotropy produce by different modes. In the subsequent publications, this theory was applied for studies using the Velocity Centroids [210] and for studies at optical lines for which dust absorption is important.

Below we discuss these advances in more detail as we believe that a lot of information about realistic interstellar turbulence will be obtained in near future using these techniques.

10.1 Studying turbulence with spectral lines

Several decades ago measurements of spectral profiles were rather challenging. The situation is radically different these days where the challenge is to use productively the enormous wealth of spectroscopic surveys. Naturally, these surveys provide a reliable and cost-effective way of probing interstellar turbulence, provided that we know how to relate the observables, i. e., the Doppler-shifted emission and absorption lines and the underlying turbulence velocity and density statistics.

Traditionally, the information on turbulence spectra is obtained with the measure termed velocity centroids, $\sim \int V_z \rho_s dV_z$, where the integration is taking place over the range of the velocities relevant to the object under study. Usually, the velocity centroids are normalized by the emission intensity at the point (see [407]), but our study in [132] shows that this normalization does not improve the ability of centroids to reflect the velocity statistics. It is easy to see that the velocity centroids are proportional to $\int V_z \rho ds$, where ρ is an actual three dimensional density and the integration is performed along the line of sight (see [265]).

The numerical and analytical analysis in [132] and [134] showed numerically that the velocity centroids fail for studying supersonic turbulence. This provides bad news for the studies of velocity statistics in molecular clouds and diffuse cold ISM (see [115, 317, 322]). The studies for HII regions [339] are less affected, as in most cases, the turbulence there is subsonic. The analytical progress of the information that the velocity centroids can bring was achieved only recently in [210] and on the basis of

the theory of the PPV statistics the foundations of which were laid in [271], henceforth LP00. Therefore, we will start with discussing this study which resulted in the development of two new ways of studying turbulence with spectral lines.

10.1.1 Statistics of the PPV: velocity channel analysis and velocity coordinate spectrum

The most detailed information on turbulent velocity that is observationally available from an emitting or absorbing turbulent volume is a PPV data cube. Evidently, the resolution in the P-P plane is provided by the spatial resolution of the telescope or an interferometer, while the V-resolution requires an adequate spectroscopic resolution.

Astronomers analyzed the distribution of PPV intensities within a particular velocity range or a channel map. This velocity range may be the minimal interval corresponding to the maximum of spectral resolution (see [185] or chosen to be wider, e. g., in order to decrease the noise [406]). In the aforementioned papers, *spatial* spectra were obtained by taking Fourier transform of channel maps had been used to study HI. The relation of the power spectra to the underlying velocity fluctuations was a subject of speculation with claims that the spectral index of channel maps coincides with the spectral index of velocity fluctuation in 2D slices of the actual turbulent volume (see [185] and references therein). It was shown by Lazarian & Pogosyan (2000, [271], henceforth LP00) that the latter claim, as well as other folklore speculations related to the interpretation of the spatial intensity variations within channel maps, are not correct. The analytical relation between the statistics of the intensity fluctuations within the channel maps and the statistics of the underlying velocity and density was established in LP00.

The nontrivial nature of the mapping into the PPV space is illustrated in Figure 10.1. The figure demonstrates the mapping of 3 equal size and equal density eddies, the one with the smallest velocity provides the largest contribution to the PPV intensity.[1] It is also clear that if the channel map or velocity slice of PPV data gets thicker than the velocity extent of the eddy 3, all the eddies contribute to the intensity fluctuations the same way, i. e., in proportion to the total number of atoms within the eddies.

To understand the essence the Velocity Channel Analysis (VCA) formulated in LP00, consider a PPV cube arising from measuring Doppler shifted spectra from a turbulent volume (see Figure 10.2). The channel maps in Figure 10.2 are the velocity slices of the PPV cube. If the medium is optically thin and the velocity is integrated over the

1 Incidentally, this explains the scalings of power spectra in Table 10.2, which indicates that a spectrum of eddies that contain the most of turbulent energy at *large* scales induce the spectrum of thin channel map intensity fluctuations having most of the energy at *small* scales.

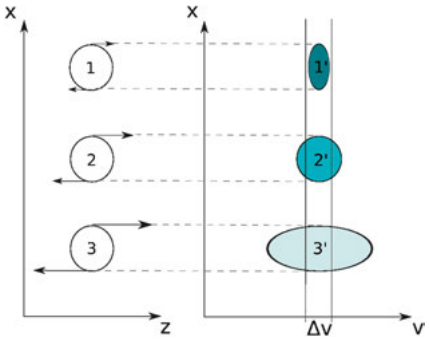

Figure 10.1: An illustration of the mapping from the real space to the PPV space. In the real space, the 3 eddies above have the same spatial size, but different velocities. They are being mapped to the PPV space and there they have the same PP dimensions, but a different V-size. The larger is the velocity of eddies, the larger the V-extent of the eddies, the less density of atoms over the image of the eddy. Therefore, in terms of the intensity of fluctuations in the velocity channel Δv, the largest contribution is coming from the least energetic eddy, i. e., eddy 1, while the most energetic eddy, i. e., eddy 3, contributes the least from [260].

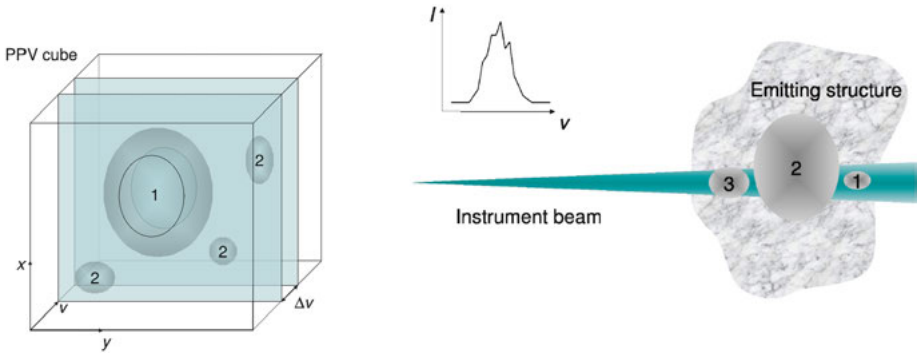

Figure 10.2: *Left panel*: VCA technique. Illustration of the thick and thin velocity slices. The slices are thin for the PPV images of the large eddies, but thick for the images of small ones. *Right panel*: VCS technique. For a given instrument resolution large eddies are in the high resolution limit, while small eddies are in the low resolution limit from [260].

entire spectral line, the fluctuations can depend only on density inhomogeneities. It is also suggestive that the contribution of the velocity fluctuations may depend on whether the images of the eddies under study fit within a velocity slice or if their velocity extent is larger than the slice thickness (see Figure 10.2, left). In the former case, the slice is "thick" for eddies and in the latter case it is "thin." According to LP00, the spectra of fluctuations that correspond to "thin" and "thick" slices are different with the fluctuations induced by turbulent velocity being prominent in thin channels. LP00 shows that by varying the channel thickness it is possible to disentangle the spectra of underlying velocities and densities in a turbulent volume. Note that before the LP00

study spectra were compared for the channel maps of different thickness, which in incorrect claims in the literature.

LP00 dealt with optically thin data. Optically, thick CO data was traditionally delt with by studying total intensities (see [147] with frequently quoted measured spectrum K^{-3}, where K is the plane of sky 2D wavenumber. The origin of such a spectrum and its relation to the underlying velocity and density fluctuations was established in Lazarian and Pogosyan (2004, [272], henceforth LP04) where it was shown that the observed K^{-3} spectrum is universal, i. e., does not depend on the underlying velocity and density spectra of turbulence. Numerically, this prediction in LP04 was first confirmed in [62]. In terms of the techniques of turbulence study, LP04 extends the study of the VCA technique in LP00 to the case of studying turbulence within an emitting turbulent volume in the presence of absorption. Intuitively, results of LP04 are easy to understand. In turbulence, there is a unique statistical relation between the physical scales and the turbulent velocities. LP04 proved that if the thickness of a velocity slice is larger than the dispersion of velocities of the eddies which get optically thick, the effects of self-absorption should be taken into account

A radically new way of analyzing spectroscopic data is presented in Lazarian and Pogosyan (2006, [273], henceforth LP060). There the spectra of intensity fluctuations along the V-axis of the PPV cube are studied (see Figure 10.2, right). The mathematical foundations of the technique we first discussed in LP00, but there the high potential of the new technique which was termed Velocity Coordinate Spectrum (VCS), as the technique was later termed in [255], required further studies. Indeed, it took some time to understand the advantages that the VCS provides for the practical handling of the observational data. The VCS technique was successfully tested in [75]. Note that the VCS technique was extended in Lazarian and Pogosyan (2008, [274], henceforth LP08) to deal with the studies of turbulence using saturated absorption lines. LP08 showed that the saturation of the line acts as a sort of window function in the velocity space. In the presence of this window function, one can still use the unsaturated wings of the line to study turbulence for large wavenumbers.

The VCS technique has a number of advantages. For instance, the VCS allows one to analyze turbulence when spatial information is either not available or sparse. For instance, one can also study turbulence having just a couple of absorption lines, which corresponds to sampling of the PPV volume along a few directions only (see Figure 10.4). Naturally, this stems from the fact that the fluctuations along the V-axis are studied by the VCS. This makes the VCS technique really unique for the velocity turbulence studies. For instance, it allows probing turbulence in the intracluster medium as discussed in [260].

For practical studies of interstellar turbulence, we do not need the lengthy analytical derivations in LP00, LP04, LP06, and LP08, but the summary of the results. The underlying statistics of turbulence are determined by the velocity structure. As only the line of sight component of the velocity is measurable, the z-component of the

turbulent velocity field (i. e., u), we use the structure function

$$D_z(\mathbf{r}) = \left\langle \left(u(\mathbf{x}+\mathbf{r}) - u(\mathbf{x})\right)^2 \right\rangle, \tag{10.1}$$

which for a self-similar power-law turbulent motions provide

$$D_z \sim D(L)(r/L)^m, \tag{10.2}$$

where L is the turbulent injection scale, $D_z(L)$ is the variance of velocity at this scale, m is the scaling exponent, which is $m = 1/3$ for the Kolmogorov turbulence.

The observed signal also may depend on the correlation function of over-density. This function has a constant part that depends on the mean density, as obviously, the fluctuations in the PPV space arising from the effect of velocity crowding should be present even for turbulence with constant density. For instance, for the power-law density spectrum the correlation functions of over-density take the form (see LP06 for the discussion of cases of $\gamma < 0$ and $\gamma > 0$):

$$\xi(r) = \langle \rho \rangle^2 \left(1 + \left[\frac{r_0}{r}\right]^\gamma\right), \tag{10.3}$$

where r_0 has the physical meaning of the scale at which fluctuations are of the order of the mean density (see more in LP06). Obtaining of the values of the indexes m and γ from the analysis of the PPV data was the goal addressed in LP00 and subsequent publications.

To get a feeling how the statistics of velocity and density influence the statistics of intensities in the PPV cubes, one may consider one of the observables, e. g., the structure function of the intensity of emission $I_{\mathbf{X}}(v)$,

$$\mathcal{D}(\mathbf{X}, v_1, v_2) \equiv \left\langle \left[I_{\mathbf{X}}(v_1) - I_{\mathbf{X}}(v_2)\right]^2 \right\rangle, \tag{10.4}$$

where the z-axis component velocity v is measured in the direction defined by the two-dimensional vector $\mathbf{X}$. We distinguish the 2D and 3D vectors by denoting by the capital bold letters the two-dimensional position-position vectors that specify the line of sight. Small bold letters are reserved to describe the vectors of three-dimensional spatial position. The z-axis is chosen to be along the line of sight.

In the case of no absorption, the density of energy in the PPV space

$$\rho_s(\mathbf{X}, v) \sim \int_{-S}^{S} dz \rho(\mathbf{X}, z) \phi_{vz}(\mathbf{X}, z) \tag{10.5}$$

where the emission is coming from the cloud of the $2S$ size and the intensity of emission is assumed to be proportional to the density ρ. The distribution function of the

z-component of velocity is given by ϕ_{vz}. The latter for a z-components of the turbulent u velocity for a finite temperature T gas is

$$\phi_{vz}(\mathbf{x})\mathrm{d}v = \frac{1}{(2\pi\beta)^{1/2}} \exp\left[-\frac{(v-u(\mathbf{x}))^2}{2\beta}\right]\mathrm{d}v, \tag{10.6}$$

where $\beta = \kappa_B T/m_a$, m_a being the mass of emitting atoms/ions. For $T \to 0$, the function ϕ_v converts into a delta-function that depends on regular gas flow and the turbulent velocity u.

Several things follow from Equation (10.5). First of all, both densities and velocities contribute to the energy density in the PPV space, but the velocity and density statistics enters the expression in different ways. Therefore, the final expressions for the statistics of ρ_s will depend differently on the statistics of ρ and u. For instance, the correlation function of the PPV densities ρ_s is (see LP06)

$$\begin{aligned}\xi_s(R,v) &\equiv \langle \rho_s(\mathbf{X_1},v_1)\rho(\mathbf{X_2},v_2)\rangle \\ &\propto \int_{-S}^{S} \mathrm{d}z\left(1-\frac{|z|}{S}\right)\frac{\xi(r)}{D_z^{1/2}(\mathbf{r})}\exp\left[-\frac{v^2}{2D_z(\mathbf{r})}\right],\end{aligned} \tag{10.7}$$

where the correlation function ξ_s is defined in the PPV space, where R is the spatial separation between points in the plane-of-sky and v is the separation along the V-axis. The velocity structure function $D_z(\mathbf{r}) = \langle (v_z(\mathbf{x_1}-v_z(\mathbf{x_2}))^2\rangle$ carries the information about the correlations of the z-component of velocity.

Taking Fourier transform of ξ_s, one gets the PPV spectrum P_s, which is a sum of two terms P_ρ and P_v, namely

$$P_s = P_\rho + P_v, \tag{10.8}$$

and the dominance of the first or the second term depends on how the spectra are obtained. Indeed, the PPV space presents inhomogeneous statistics, which is different along the V-axis and in the PP plane. The analysis of the fluctuations along the V-axis is what the Velocity Correlation Spectrum (VCS) is about, while the analysis of the fluctuations in the PP plane is the domain of the Velocity Channel Analysis (VCA). Different asymptotics of P_s spectrum are presented in Table 10.1.

VCA

The interpretation of the channel maps is the domain of the VCA. Table 10.2 shows how the power spectrum of the intensity fluctuations measured within channels depends on the thickness of the velocity channel. Below we provide quantitative discussion of the VCA. As we mentioned earlier, the notion of thin and thick slices depends on the turbulence scale under study and the same slice can be thick for small scale turbulent

Table 10.1: The short-wave asymptotical behavior of power spectra P_s in PPV space. Results are presented for one-dimensional spectrum of fluctuations along the velocity coordinate $P_s(k_v)$, two-dimensional spectrum of fluctuations $P_s(K)$, three-dimensional anisotropic spectrum of PPV fluctuations $P_s(K, k_v)$. We use the convention that capital letters denote 2D vectors in PP-plane. The adopted convention is that the variables related to spatial coordinates are denoted with capital letters. The component of P_s arising from pure density fluctuations is P_ρ, while the component affected both by the density and velocity fluctuations is P_v. The power-law underlying statistics of density and velocity are assumed: γ is the spectral index of the density correlation function, m is the spectral index of the velocity correlation function. The size of the turbulent cloud is S from LP06.

	1D: $P_s(k_v)$ $k_v D_z^{1/2}(S) \gg 1$	**2D: $P_s(K)$** $KS \gg 1$	**3D: $P_s(K, k_v)$** $k_v^2 D_z(S) \gg (kS)^m$
P_ρ:	$(r_0/S)^\gamma [k_v D_z^{1/2}(S)]^{2(\gamma-1)/m}$	$(r_0/S)^\gamma [KS]^{\gamma+m/2-3}$	$(r_0/S)^\gamma [k_v D_z^{1/2}(S)]^{-2(3-\gamma)/m}$
P_v:	$[k_v D_z^{1/2}(S)]^{-2/m}$	$[KS]^{m/2-3}$	$[k_v D_z^{1/2}(S)]^{-6/m}$

Table 10.2: The VCA asymptotics. *Thin* means that the channel width < velocity dispersion at the scale under study; *thick* means that the channel width > velocity dispersion at the scale under study; *very thick* means that a substantial part of the velocity profile is integrated over from [260].

Slice thickness	**Shallow 3-D density** $P_n \propto k^{-3+\gamma}, \gamma > 0$	**Steep 3-D density** $P_n \propto k^{-3+\gamma}, \gamma < 0$
2-D intensity spectrum for thin slice	$\propto K^{-3+\gamma+m/2}$	$\propto K^{-3+m/2}$
2-D intensity spectrum for thick slice	$\propto K^{-3+\gamma}$	$\propto K^{-3-m/2}$
2-D intensity spectrum for very thick slice	$\propto K^{-3+\gamma}$	$\propto K^{-3+\gamma}$

fluctuations and thin for large scale ones (see Figure 10.2). With this remark in mind, we can consider thin and thick slices.

It is easy to see that the power law index *steepens* with the increase of velocity slice thickness. In the thickest velocity slices, the velocity information is averaged out and we get the density spectral index $-3 + \gamma$. The velocity fluctuations dominate in thin slices, and the index m that characterizes the velocity fluctuation can be obtained using thin velocity slices (see Table 10.1).

Note that the spectrum of intensity in a thin slice gets shallower as the underlying velocity get steeper. This is easy to understand if one considers turbulence in an incompressible optically thin medium. The intensity of emission in a velocity slice is proportional to the number of emitting atoms per velocity interval. The latter is given by the thickness of the slice. Thin slice means that the velocity dispersion induced by the eddies under study is larger than the thickness of a slice. The increase of the velocities of the eddies means that less and less energy is being emitted within the velocity interval corresponding to the slice (see Figure 10.1). Mathematically, this effect results in the dependences in Table 10.2.

VCS

Unlike studies of the fluctuations within channel maps that the observers were doing prior to LP00, the analysis of the fluctuations along the V-axis was first proposed within the Velocity Correlation Spectrum (VCS) technique that was suggested in LP00 and extended and elaborated in LP06.

In the VCS, the spectrum measured is a function of the wave number $k_v \sim 1/v$ along the V-axis. This means that large k_v correspond to small velocity differences, while small k_v correspond to large velocity differences.

The theoretical predictions of the asymptotics of the VCS on the velocity and density spectra are far from being trivial.

Assume that the maximal resolution of a telescope corresponds to resolving the turbulent eddies at scale ΔB of a cloud at the distance $L_{\rm cloud} \gg S$. At this scale, the turbulent velocity is $V_{\Delta B} \equiv \sqrt{D(S)(\Delta B/S)^m}$. It is easy to see that when $k_v^{-1} > V_{\Delta B}$ the beam is resolves the eddies and, therefore, is narrow, while for observations of smaller scales its width is important. The spectrum of fluctuations along the V-coordinate at the scale k_v depends on whether the instrument resolves the correspondent spatial scale $[k_v^2 D_z(S)]^{-1/m} S$. If this scale is resolved, then $P_v(k_v) \propto k_v^{-2/m}$ and $P_\rho(k_v) \propto k_v^{-2(1-\gamma)/m}$. If the scale is not resolved, then $P_v(k_v) \propto k_v^{-6/m}$ and $P_\rho(k_v) \propto k_v^{-2(3-\gamma)/m}$. These results are presented in a compact form in Table 10.3.

Table 10.3: Scalings of VCS for shallow and steep densities for measurements taken with the telescope with a finite beam size from LP06.

Spectral term	$\Delta B < S[k_v^2 D_z(S)]^{-\frac{1}{m}}$	$\Delta B > S[k_v^2 D_z(S)]^{-\frac{1}{m}}$
$P_\rho(k_v)$	$\propto (k_v D_z^{1/2}(S))^{-2(1-\gamma)/m}$	$\propto (k_v D_z^{1/2}(S))^{-2(3-\gamma)/m}$
$P_v(k_v)$	$\propto (k_v D_z^{1/2}(S))^{-2/m}$	$\propto (k_v D_z^{1/2}(S))^{-6/m}$

The transition from the low to the high resolution regimes happens as the velocity scale gets of the order of the turbulent velocity at the minimal spatially resolved scale. As the change of slope is a velocity-induced effect, it is not surprising that the difference in spectral indexes in the low and high resolution limit is $4/m$ for both the P_v and P_ρ terms, i. e., it does not depend on the density. This opens another way of separating the velocity and density contributions. Incidentally, in the situation where the available telescope resolution is not sufficient, i. e., in the case of extragalactic turbulence research, the high spatial resolution VCS can be obtained via studies of the absorption lines from point sources.

Figure 10.3 illustrates that in the case of shallow density both the density and velocity spectra can be obtained. There the left panel corresponds to high amplitude of the density correlations, $r_0 > \Delta B$, i. e., when density effects become dominant at relatively long wavelengths for which the beam is narrow. In the middle panel, the

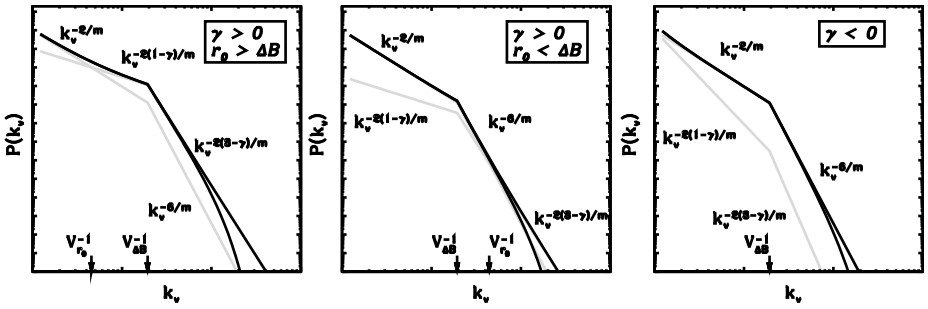

Figure 10.3: Illustrations of the VCS technique. In every panel, light lines show contributions from the ρ-term (density modified by velocity, dashed line) and v-term (pure velocity effect, solid line) separately. The dark solid line shows the combined total VCS spectrum. The dotted line depicts the boundary of the thermal suppression of fluctuations. For the *left* and *middle panels,* the density power spectrum is taken to be shallow, i. e., $\gamma > 0$ from LP06.

amplitude of density correlations is low $r_0 < \Delta B$ and they dominate only the smallest scales which results in the intermediate steepening of the VCS scaling. The *right panel* illustrates the case of the steep density spectrum. Evidently, in this case the density contribution is always subdominant.

Effects of self-absorption

A study of absorption effects in is presented in LP04 and LP06. For the VCA, it was found that for sufficiently thin slices the scaling relations obtained in the absence of absorption still hold provided that the absorption on the scales under study is negligible. Note that the thermal broadening limits to what extent the slice can be thin. This means that in some cases that the underlying turbulent velocity spectrum may not be recoverable. In terms of the VCS, the absorption limits the range of k_v for which the turbulence can be explored. In other words, only measurements for sufficiently large k_v reflect the true turbulence spectrum. The problem is that the thermal dispersion determines the upper range of $k_v < 1/V_{\rm th}$. In terms of practical studies, it means that to get the information in the presence of self-absorption one has to use heavy species in astrophysical flows, e. g., heavy molecules.

The intensities $I_{\mathbf{X}}(v)$ can be affected by absorption. The latter can be studied on the basis the standard equation of radiative transfer

$$dI_\nu = -g_\nu I_\nu ds + j_\nu ds, \tag{10.9}$$

where, for absorption and emissivity coefficients α and $\tilde{\epsilon}$, $g_\nu = \alpha(\mathbf{x})\rho(\mathbf{x})\phi_\nu(\mathbf{x})$, $j_\nu = \tilde{\epsilon}\rho(\mathbf{x})\phi_\nu(\mathbf{x})$, $\mathbf{x}$ is a three-dimensional position vector $(\mathbf{X}, z)$, $\rho(\mathbf{x})$ is the density, and $\phi_\nu(\mathbf{x})$ is the velocity distribution of the atoms.

The criterion for the absorption to be important is $\alpha^2\langle(\rho_s(\mathbf{X},v_1)-\rho_s(\mathbf{X},v_2))^2\rangle \sim 1$, which for $\gamma<0$ results in the critical size of the slice thickness V_c given by (LP06)

$$\begin{aligned} V_c/D_z(S)^{1/2} &\approx (\alpha\bar{\rho}_s)^{\frac{2m}{m-2}}, \quad m>2/3 \\ V_c/D_z(S)^{1/2} &\approx (\alpha\bar{\rho}_s)^{-1}, \quad m<2/3, \end{aligned} \tag{10.10}$$

where $\bar{\rho}_s$ is the mean PPV density.

As we mentioned earlier, the absorption dominates for the slices thicker than V_c. The difference with the case of $\gamma>0$ is that, in the latter case, one should also consider the possibility that the density contribution can be important (see Table 10.4). The criterion above coincides with one for the VCS, if we identify the critical k_v with $1/V_c$. If the resolution of the telescope is low, another limitation applies. The resolved scale should be less than the critical spatial scale that arises from the condition $\alpha^2\langle(\rho_s(\mathbf{X_1},v)-\rho_s(\mathbf{X_2},v))^2\rangle \sim 1$ which for $\gamma<1$ results in $R_c/S \approx (\alpha\bar{\rho}_s)^{\frac{2}{m-2}}$ (LV06). If only scales larger than R_c are resolved, the information on turbulence cannot be recovered.

Note that a few nontrivial effects take place. For instance, it is common knowledge that for optically thin medium the spectral line integration results in intensity fluctuations that reflecting the underlying density statistics. However, LP04 showed that this may not be true for lines affected by absorption. When velocity is dominant, as we mentioned earlier, a *new* very interesting regime for which intensity fluctuations exhibit the power spectrum $P(K)\sim K^{-3}$ emerges. On the contrary, when density is dominant (see Table 10.4), the spectral index of intensity fluctuations is the same as in the case of an optically thin cloud integrated through its volume. This means that for $\gamma>0$, i. e., for the shallow spectrum of density, in the range of parameter space defined in Table 10.4 the measurements of intensity fluctuations of the integrated spectral lines reflect the *actual* underlying density spectrum in spite of the absorption effects.

Table 10.4: Conditions for the impact of density inhomogeneities to the PPV statistics exceeds the velocity contribution. Spectral index of density fluctuations γ must be larger than 0, i. e., the intensity of fluctuations increases with the decrease of scale. For $\gamma<0$, the velocity fluctuations always dominate in creating small-scale ripples in the PPV space from LP06.

Condition	$\gamma>0$
$m\geq\max[\frac{2}{3},\frac{2}{3}(1-\gamma)]$	$v^2<D_z(S)(r_0/S)^m$
$\frac{2}{3}(1-\gamma)<m<\frac{2}{3}$	$v^2<D_z(S)(r_0/S)^{\frac{2/3\gamma m}{m-2/3(1-\gamma)}}$
$m\leq\min[\frac{2}{3},\frac{2}{3}(1-\gamma)]$	$r_0/S>1$

VCS with absorption lines

Strong absorption lines, which are in a saturated regime, can be used for probing turbulence spectra. This problem was addressed in LP08, who analyzed optical depth

fluctuations that correspond to the logarithms of the measured intensities. The analysis was made for the VCS technique and numerical simulations in [75] proved that the sampling along from 5 to 10 directions to absorbing sources, e. g., stars, is enough to recover properly the underlying spectrum of turbulent velocity (see Figure 10.4).

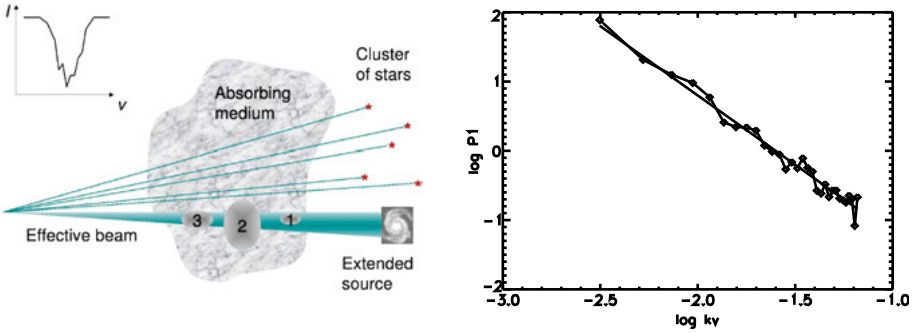

Figure 10.4: Illustration of VCS absorption studies of turbulence. *Left panel*: Schematic of measuring turbulence with absorption lines from point sources, e. g., stars, and extended source, e. g., a galaxy. *Right panel:* Spectrum of turbulence recovered from synthetic observations when the signal is sampled along 10 absorption lines. The solid line corresponds to the underlying spectrum and points correspond to the recovered spectrum from [75].

LP08 study shows that for the range of optical depth less than 10^3, the width of a typical interstellar line is determined by Doppler shifts rather than the atomic constants and this makes the study feasible. In reality, the flat saturated part of the profile is not useful for any statistical study of turbulence and, therefore, the wings of saturated absorption lines should be used for turbulence studies.

The effect of saturation of the absorption line results in limiting the range of k_v at which the information on turbulence is available. If the effect of saturation is approximated with a Gaussian mask of width Δ, that is centered in the middle of the wing, Δ measures the fraction of the line that is available for studies of turbulence. LP08 demonstrated that the recovery of the turbulent spectrum with the VCS was possible for $k_v > 3\Delta^{-1}$, where all the quantities are normalized over the total turbulent velocity dispersion. Naturally, thermal effects provide additional limitations for the range of scales to study. In fact, the range of k_v for studies of asymptotic power-law solutions is limited to $3\Delta^{-1} < k_v < 1/(3\beta)$, where β represents thermal broadening. For k_v beyond this range, the recovery of the turbulence spectrum is still possible, but fitting of the integral expressions, rather than the use of the asymptotical solutions is necessary.

Studies of turbulence with absorption lines can be applied to clusters of galaxies, where the absorption from quasars and distant galaxies can be used. The technique can be applied also to the nearby gas of the local interstellar medium. In the latter case, the lines of sight coming from the telescope are converging. This effect is important for

the VCA rather than to the VCS. For the latter the aforementioned asymptotics of the VCS techninique are applicable.

Synergy of the VCA and the VCS

The VCA and the VCS have their own advantages and, therefore, it is important to search for the synergy of the two techniques. For instance, the VCS is a unique tool that allows studies of astrophysical turbulence even when the instrument does not resolve spatially the turbulent fluctuations. This means that for a turbulent volume with marginal spatial resolution but good spectral resolution, studies of turbulence with the VCS are possible using Doppler shifted spectral lines.

The finite gas temperature affects the techniques differently. For the VCA, gas temperature acts in the same way as the finite width of a channel. Within the VCS, the term with temperature gets factorized and it influences the amplitude of fluctuations as discussed in LP06. One can correct for this term which can provide a new way of estimating the interstellar gas temperature.

Another advantage of the VCS compared to the VCA is that it reveals the spectrum of turbulence directly, while using the VCA the slope of the spectrum is inferred from varying the thickness of the channel. A simultaneous use of the VCA and the VCS makes the turbulence spectrum identification more reliable.

At the same time, the spectral range for the VCS for Kolmogorov-type turbulence is significantly reduced. This calls for fitting of the VCS spectra rather than using the asymptotic solutions (see below).

Interstellar turbulence spectra obtained with the VCA and the VCS

VCA applications

As we discussed earlier, a number of observations that analyzed the statistics of channel maps had been done before the understanding what the statistics of channel maps mean was obtained. Table 10.5 illustrates the results obtained with VCA by different groups. The studies of spectra in channel maps predated VCA (see lines 1, 8, 9 in Table 10.5 as well as [102, 406], but researchers were choosing Δv arbitrarily, making comparisons impossible. For those LP00 and LP04 performed the VCA analysis using the published data. For instance, as we mentioned earlier, LP04 predicted that self-absorption can produce a universal spectrum $\sim K^{-3}$, where K is the observational analog, in the $2D$ plane of the sky, of the wavenumber k. If this spectrum dominates in both thin and thick slices, the only conclusion that can be made is that the density spectrum $E_\rho \sim k^{-\alpha}$ corresponds to $\alpha > 1$ (see lines 3, 6, 7), while the details of the velocity and density spectra are not available. When the spectrum of intensities from absorbing gas in a thick slice is different from K^{-3}, the information about the underlying densities is available (see lines 8, 9). It is encouraging that the observed spectral indexes correspond to those in simulations (see [37, 232]), which show a tendency of having the spectrum of density becoming flatter as the spectrum of velocity

Table 10.5: Selected VCA results from [260]. Superscript "^{g}" denotes galactic objects, "^{e}" – extra-galactic. $P^{\rm thin}_{\rm PPV}$ and $P^{\rm thick}_{\rm PPV}$ are the power law spectrum in thin and thick PPV slices, respectively. "Ref. obs." and "Ref. theor" correspond to papers where the measurement were done and interpreted using VCA, respectively. Indexes in round brackets correspond to substantial observational errors correspond to consistency only. → CygA is used to denote material toward Cygnus A.

N	data	Object	$P^{\rm thin}_{\rm PPV}$	$P^{\rm thick}_{\rm PPV}$	depth	E_v	E_p	Ref. obs.	Ref. theor.
1	HI	Anticenter^g	$K^{-2.7}$	N/A	Thin	$k^{-1.7}$	N/A	[185]	[273]
2	HI	→ CygA	$K^{-(2.7)}$	$K^{-(2.8)}$	Thin	N/A	$k^{-(0.8)}$	[112]	[112]
3	HI	SMC^e	$K^{-2.7}$	$K^{-3.4}$	Thin	$k^{-1.7}$	$k^{-1.4}$	[405]	[405]
4	HI	Center^g	K^{-3}	K^{-3}	Thick	N/A	N/A	[114]	[272]
5	HI	B.Mag.^{g}	$K^{-2.6}$	$K^{3.4}$	Thin	$k^{-1.8}$	$k^{-1.2}$	[328]	[328]
6	HI	Arm^g	K^{-3}	K^{-3}	Thick	N/A	N/A	[220]	[258]
7	HI	DDO 210^e	K^{-3}	K^{-3}	Thick	N/A	N/A	[17]	[17, 258]
8	^{12}CO	L1512	N/A	$K^{-2.8}$	Thick	N/A	$k^{-0.8}$	[410]	[114]
9	^{13}CO	L1512	N/A	$K^{-2.8}$	Thick	N/A	$k^{-0.8}$	[410]	[17]
10	^{13}CO	Perseus	$K^{-(2.7)}$	K^{-3}	Thick	$k^{-(1.7)}$	N/A	[411]	[411]
11	^{13}CO	Perseus	$K^{-2.6}$	K^{-3}	Thick	$k^{-1.8}$	N/A	[345]	[345]
12	C^{18}O	L1551	$K^{-2.7}$	$K^{-2.8}$	Thin	$k^{-1.7}$	$k^{-0.8}$	[413]	[413]

gets steeper. A good quantitative correspondence between the VCA analysis of Perseus data and their numerical simulations was also obtained in [345] as well as in [240].

The LP00 and LP04 theory resolve many otherwise puzzling facts. For instance, studies of turbulence are more involved for the inner parts of the galaxy, where (a) two distinct regions at different distances from the observer contribute to the emissivity for a given velocity and (b) effects of the absorption may be important. Nevertheless, the analysis of the data in Dickey et al. [114] showed that important progress may be made even in those unfavorable circumstances. In particular, [114] reported the steepening of the spectral index with the increase of the velocity slice thickness. They found that the spectral index for strongly absorbing direction to be approaching –3 in accordance with the predictions in LP04. Note, that the effects of optical depths can also explain another set of observations for which the spectral index stayed the same, e. g., –3, while the thickness of the slice was varying (see [220]).

21-cm absorption provides another way of probing turbulence on small scales. The absorption depends on the density to temperature ratio ρ/T, rather than to ρ as in the case of emission. However, in terms of the VCA this change is not important and one would expect to see the emissivity index steepening as velocity slice thickness increases, provided that velocity effects are present. Nevertheless, [112] did not see such steepening. This can be interpreted as the evidence of the viscous suppression of turbulence on the scales less than 1 pc. The fluctuations in this case can be due to density and their shallow spectrum $\sim K^{-2.8}$ either related to damped magnetic structures below the viscous cutoff (see [280] or due to density fluctuations in high Mach number compressible MHD, see [37].)

Historically, the CO data was analyzed after integration over the entire emission line rather than using channel maps. Stutzki et al. [410] presented the power spectra of 12CO and 13CO fluctuations obtained via integrating the intensity over the entire emission line for L1512 molecular cloud. The study found for both isotopes the power spectrum of intensity fluctuations with a similar spectral index. According to LP04, this may correspond to optically thick asymptotics. If the velocity fluctuations dominate, the expected universal spectrum is K^{-3}, while if the density fluctuations dominate the expected spectrum is $K^{-3+\gamma}$. The index measured in [410] is ~ 2.8, which may either correspond to -3 within the experimental errors, or more likely indicate that $\gamma \approx 0.2$, i. e., the density spectrum is shallow. The latter possibility is indirectly supported by ^{18}CO measurement for L1551 cloud by Swift in [413]. The latter study used the VCA and obtained the shallow density spectrum with $\gamma \approx 0.2$, while his measured velocity spectrum was approximately Kolmogorov (the index is -3.72). Padoan et al. [345] successfully tested the VCA with numerical simulations that included radiative transfer and applied the technique to Five College Radioastronomy Observatory (FCRAO) survey of the Perseus molecular cloud complex. The obtained turbulence spectral index for velocity is ~ -3.8.

VCS applications

The direct application of the asymptotic solutions was performed in [346] for the 13CO data. A more sophisticated approach was employed in Chepurnov et al. [76] where the fitting of the data by the integral expressions in LP06 was used. Below we discuss the latter approach.

Figure 10.5 (left) shows the results of our VCS-analysis of galactic high latitude data. Rather than first correcting for the gas thermal broadening, then fitting the

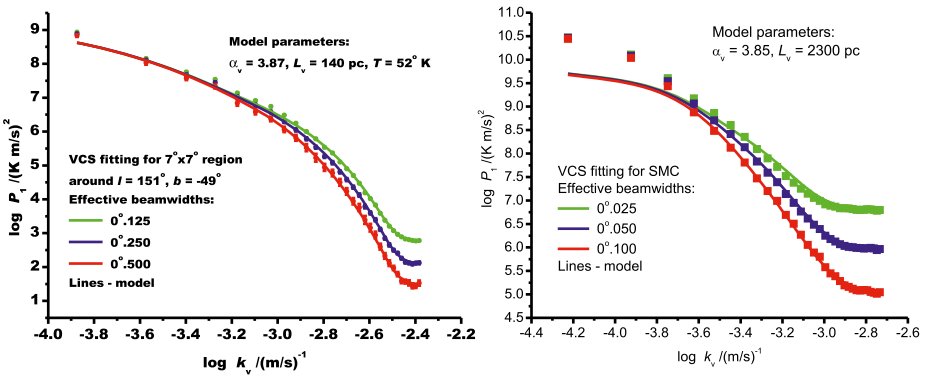

Figure 10.5: Fitting of turbulent models and observational data for different resolutions. *Left panel*: Application of the VCS high latitude HI Arecibo data. The energy injection scale is 94 pc from [76]. *Right panel*: Application of the VCS to Small Magellanic Cloud HI data. The spectral index for velocity is a bit more shallow. The model corresponds to the energy injection at 3 kpc from [74].

asymptotic expressions from LP06 into the observed VCS spectrum as was done in [346, 76] used the analytical expressions analytical expression in LP06 to find the model that fits the data at different spatial resolutions. Thus in this approach the resolutions played for the VCS a role similar to the thickness of slices Δv for the VCA.

An important advantage of the approach based on fitting data to the models is that it opens ways of studying nonpower law turbulence, e. g., turbulence at the injection scales. It allows also studies of turbulence when thermal broadening is important. The application of the technique to GALFA galactic HI data is illustrated in Figure 10.5 (left). Our results show that the model of turbulence with spectrum steeper than Kolmogorov, i. e., with $E_v \sim k^{-3.9}$, the temperature[2] of gas around 130 K and a single injection scale of 100 pc. The density spectrum was estimated to be at the border-line of shallow and steep, i. e., $E_\rho \sim k^{-3}$.

The application of the VCS to HI of the Small Magellanic Cloud (SMC) (see line 3 in Table 10.5) is illustrated in Figure 10.5 (right). The results of the VCS are the following: the spectrum of velocity is similar to the one in the Milky Way, i. e., $E_v \sim k^{-3.85}$, but the density spectrum is steeper than in the Milky Way HI, i. e., $E_\rho \sim k^{-3.3}$, the turbulent velocity is $\sim$ 7 km/s, the sonic Mach number in the cold HI is $\sim$ 6 and the injection scale of around 3 kpc. The latter corresponds to the ideas of exciting turbulence in the SMC during its encounter with its neighbor, the LMC. The offset of the points at small k_v was explained by the regular shear velocity in the SMC that was estimated to be around 50 km/s.

The studies above show a big promise of the VCS technique in obtaining parameters of the turbulent interstellar gas both for Milky Way and neighboring galaxies. Similar analysis is applicable to molecular clouds and individual galactic regions, e. g. supernovae remnants.

Application of the theory to velocity centroids

The analytical machinery developed for statistics spectral line fluctuations in PPV space is at the core of the VCA and the VCS techniques. Recently, it has been applied [210] to obtaining the statistics of velocity centroids. The latter are defined as

$$C(\mathbf{X}) = \int dv v I_v(\mathbf{X}), \tag{10.11}$$

where $I_v(\mathbf{X})$ is the intensity of emission of Doppler broadened line in the direction $\mathbf{X}$ and at velocity v. The centroids are more affected by density fluctuations, which limits their applicability to studies of supersonic turbulence [132, 134]. However, they can efficiently probe turbulence when the thermal line broadening exceeds the turbulent one. In the latter case, the statistics measured by the VCA and the VCS are strongly

2 The analysis in LP06 shows that the contribution of turbulence in warm gas to fluctuations in PPV is exponentially suppressed compared to that in cold gas.

contaminated by the thermal effects, which gives centroids an edge for studying subsonic turbulence.[3]

The effects of absorption also limit the studies of turbulence with centroids. For instance, the universal spectrum K^{-3} is also expected in the presence of strong self-adsorption.

Effects of dust absorption and collisionally excited emission lines

The effect of dust absorption limits the depth to which the turbulence is sampled along the line of sight. This can be described by introducing the length $\Delta(\mathbf{X})$ along the line of sight corresponding to dust optical depth equal unity, i. e., to $\tau(\Delta) = 1$ as discussed in Kandel et al. [210]. In the aforementioned paper, extending the results in LP04 and LP06, a new asymptotic regime was predicted for the spectrum of fluctuations for the scales larger than $\Delta(\mathbf{X})$. The spectrum was shown to be shallower by unity in this regime. This result can be physically understood as the sampling the a thin layer of a turbulent volume.

In addition, the dust absorption was shown to remove the degeneracy inducing the universal K^{-3} spectrum of intensity fluctuations of self-absorbing medium reported in LP04. The effect is easy to understand. The dust absorption limits the depth over which one can sample the turbulent volume. Thus, paradoxically, this decreases the effects of self-absorption.

When emission lines are collisionally excited, the emissivity is proportional to density squared. However, the study [210] showed that this does not change the asymptotic regimes for obtaining the power spectra from observations.

The application of the VCA to the emission data from HII regions in [12] is shown in Figure 10.6. Indeed, it is easy to see that the change of the observed spectral index in channel maps is consistent the theoretical expectations, in particular with the change of the power spectrum by unity at large scales arising from the dust extinction.

10.2 Synchrotron fluctuations

In many instances, the distribution of relativistic electrons is much more uniform compared to magnetic field. Therefore, the fluctuations of the synchrotron emission may be related in many instances directly to the fluctuations of magnetic field.

The first complication in terms of studying turbulence with synchrotron emission arises from the complicated dependence of synchrotron emissivity on the magnetic field. Indeed, if the distribution of relativistic electrons is

$$N_e(\mathcal{E})d\mathcal{E} \sim \mathcal{E}^{\alpha} d\mathcal{E} \tag{10.12}$$

3 The VCA and the VCS can also be used to study subsonic astrophysical turbulence if heavy atoms/molecules with reduced thermal broadening are used to sample the volume observationally.

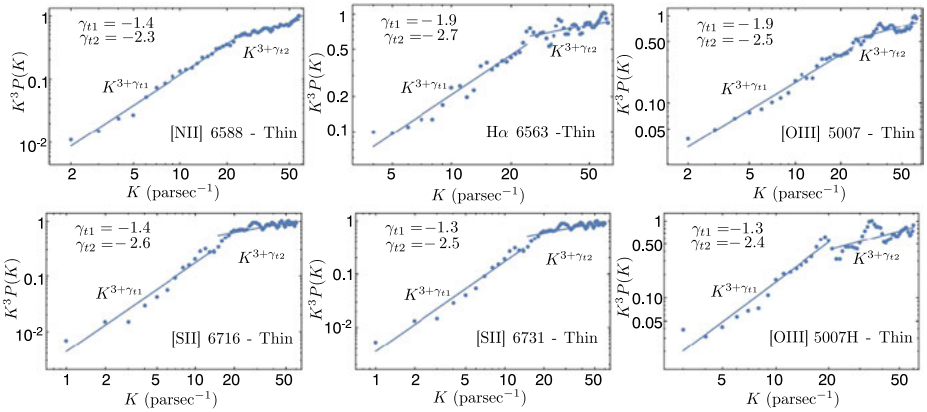

Figure 10.6: Power spectra $K^3P(K)$ of intensity fluctuations for data from HII regions [12] for the thin velocity slice case for different spectral lines. The two regimes with different slopes are observed, with corresponding best-fitting lines. The difference between the slopes is close to the theoretical expectations from [210].

then the intensity of the synchrotron emission is

$$I_{\rm sync}(\mathbf{X}) \propto \int dz H_\perp^\gamma(\mathbf{x}) \tag{10.13}$$

where $\mathbf{X} = (x, y)$ is the 2D position vector in the plane of the sky and $H_\perp = \sqrt{H_x^2 + H_y^2}$ is the amplitude of the perpendicular to the line of sight component of the magnetic field. Note that the index $\gamma = (\alpha + 1)/2$ is generally a fractional power that changes in the range from 1 to 4.

The measures available from observations is the correlation function of the synchrotron intensity

$$\xi_{\rm sync}(\mathbf{R}) \equiv \langle I_{\rm sync}(\mathbf{X_1}) I_{\rm sync}(\mathbf{X_2}) \rangle \propto \int dz_1 dz_2 \langle H_\perp^\gamma(\mathbf{x}_1) H_\perp^\gamma(\mathbf{x}_2) \rangle \tag{10.14}$$

that can be obtained by averaging over an ensemble of the pairs for the measurements at the fixed two-dimensional separation $\mathbf{R} = \mathbf{X_1} - \mathbf{X_2}$. This function is the projection of the three-dimensional correlation of synchrotron emissivity

$$\xi_{H_\perp^\gamma}(\mathbf{R}, z) = \langle H_\perp^\gamma(\mathbf{x}_1) H_\perp^\gamma(\mathbf{x}_2) \rangle, \tag{10.15}$$

which depends on three dimentional separation $\mathbf{x_1} - \mathbf{x_2} = (\mathbf{R}, z)$. The accepted assumption is that the turbulence is homogeneous.

The problems of averaging correlations of the fractional power of magnetic field is intrinsic to dealing with other combinations of the Stocks' parameters and, therefore, presented a challenge for turbulence studies using both intensities and polarization. This challenge was addressed in Lazarian and Pogosyan (2012 [275], henceforth LP12)

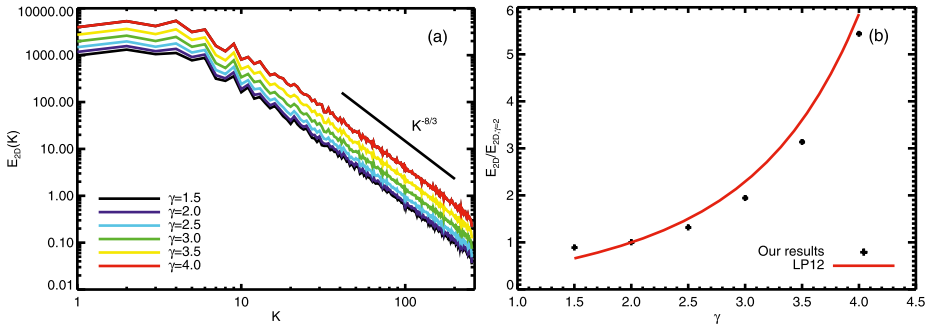

Figure 10.7: Dependence on the power-law index γ. Here, the synchrotron emissivity depends on $B_\perp^\gamma$ and $\gamma = (p+1)/2$, (a) The 1D spectrum of synchrotron emission for $1.5 \le \gamma \le 4$. (b) The comparison between the measured amplitudes of synchrotron emission normalized by $E_{2D,\gamma=2}$ and the theoretical prediction in LP12.

where the formalism of calculating the correlations of the fractional powers of $H_\perp$ was developed.

The analytical predictions in LP12 were successfully tested numerically in [290] and the results are shown in Figure 10.7. The expressions in LP12 allowed to relate the statistics of fluctuations for arbitrary γ to the statistics of fluctuations for $\gamma = 2$, which simplifies further analytical studies. Figure 10.7 confirms LP12 conclusions that the change of γ affects the amplitude of the synchrotron spectrum rather than its slope.

Synchrotron polarization provides more ways to probe magnetic field. Lazarian and Pogosyan (2016, [276], henceforth LP16) considered the fluctuations of the linear polarization

$$P \equiv Q + iU. \tag{10.16}$$

In case of an extended synchrotron source, the polarization of the synchrotron emission at the point of emission can be characterized by the polarized emission density $P_i(\mathbf{X}, z)$, where $\mathbf{X}$ marks the two-dimensional position of the source on a sky and z is a line-of-sight distance. This is different from the polarized intensity detected by an observer performing measurements at wavelength λ:

$$P(\mathbf{X}, \lambda^2) = \int_0^L dz P_i(\mathbf{X}, z) e^{2i\lambda^2 \Phi(\mathbf{X}, z)}. \tag{10.17}$$

is a line-of-sight integral over emission subject to the Faraday rotation of the polarization plane (see [57]). Above L denotes the extent of the source along the line-of-sight and the Faraday rotation measure (RM) is given by

$$\Phi(z) = 0.81 \int_0^z n_e(z') H_z(z') dz' \quad \text{rad m}^{-2}, \tag{10.18}$$

where n_e is the density of *thermal* electrons in cm^{-3}, H_z is the strength of the parallel to the line-of-sight component of magnetic field in μGauss, and the radial distance is in parsecs.

One can easily see that the polarization measured by the observer is affected both by the structure of the perpendicular to the line of sight component of magnetic field that induces the synchrotron emission as well as the parallel to the line of sight component of magnetic field that affects thermal electrons and induces Faraday rotation. The problem is how to separate the statistics of these contributions.

Correlation properties of the RM density at two points in space can be described by the correlation or structure functions

$$\xi_\phi(\mathbf{X_1}-\mathbf{X_2}, z'-z'') \equiv \kappa^2 \langle \Delta(n_e H_z)(\mathbf{X_1}, z') \Delta(n_e H_z)(\mathbf{X_2}, z'') \rangle \tag{10.19}$$

To obtain the spectra of fluctuations, LP16 used the power-law correlation model

$$\xi_\phi(\mathbf{X_1}-\mathbf{X_2}, z'-z'') = \sigma_\phi^2 \frac{{r_\phi}^{m_\phi}}{{r_\phi}^{m_\phi} + (R^2+\Delta z^2)^{m_\phi/2}} \tag{10.20}$$

$$D_\phi(\mathbf{X_1}-\mathbf{X_2}, z'-z'') = 2\sigma_\phi^2 \frac{(R^2+\Delta z^2)^{m_\phi/2}}{{r_\phi}^{m_\phi} + (R^2+\Delta z^2)^{m_\phi/2}} \tag{10.21}$$

where m_ϕ is the scaling slope and r_ϕ is the correlation length of RM density, $R = |\mathbf{X}_1 - \mathbf{X_2}|$ and $\Delta z = z' - z''$.

LP16 showed that models with $m_\phi > 1$ produce the similar asymptotical behavior as $m_\phi = 1$ model, thus the following notation was introduced:

$$\widetilde{m}_\phi = \min(m_\phi, 1). \tag{10.22}$$

The emitted polarized radiation can be described by polarized emission density P_i. The polarized emissivity depends on magnetic field component $\vec{H}_\perp$ and the wavelength λ, $j(\lambda, \mathbf{x}) \propto \lambda^{\gamma-1} |\vec{H}_\perp|^\gamma$. LP16 defined $P_i(\mathbf{x}) \propto \lambda^{1-\gamma} j(\lambda, \mathbf{x})$ to be wavelength independent.

As we mentioned before, the fractional power dependence on the magnetic field $\propto |\vec{H}_\perp|^\gamma$ is the same for the intensity and polarized intensity. The corresponding results γ dependence in LP12 are applicable and the fluctuations of the polarized intensity for the arbitrary index γ can be expressed using the fluctuations of the polarized intensity for $\vec{H}_\perp^2$:

$$\left[\langle P_i(\mathbf{x_1}) P_i^*(\mathbf{x_2})\rangle - \langle P_i\rangle\langle P_i^*\rangle\right]_\gamma \approx A(\gamma)\left[\langle P_i(\mathbf{x_1}) P_i^*(\mathbf{x_2})\rangle - \langle P_i\rangle\langle P_i^*\rangle\right]_{\gamma=2}, \tag{10.23}$$

where $A(\gamma)$ is a factor given by the ratio of the variances $A(\gamma) = \langle P^2\rangle_\gamma / \langle P^2\rangle_{\gamma=2}$ (see LP12).

In terms of Q and U Stokes' parameters, the correlation of emitted polarized radiation at two points is, in general,

$$\xi_i \equiv \langle P_i(\mathbf{x_1}) P_i^*(\mathbf{x_2}) \rangle = \langle Q(\mathbf{x_1})Q(\mathbf{x_2}) + U(\mathbf{x_1})U(\mathbf{x_2}) \rangle + i \langle U(\mathbf{x_1})Q(\mathbf{x_2}) - Q(\mathbf{x_1})U(\mathbf{x_2}) \rangle \tag{10.24}$$

Two parts of the correlation, real and imaginary, are invariants with respect to rotation of the observers frame. The real part is the trace of the polarization correlation matrix obtained in LP12 and imaginary part is the antisymmetric contribution to the correlation. LP16 studied the real part in detail.

The main parameters of the correlations of the emitted synchrotron radiation is the correlation length r_i, the characteristic scaling slope m of its fluctuations, and the relative contribution from the mean and fluctuating polarization. To perform the study of the power spectra, it is convenient to present ξ_i using a power law form

$$\xi_i(\mathbf{X}_1 - \mathbf{X}_2, z' - z'') = \bar{P}_i^2 + \sigma_i^2 \frac{{r_i}^m}{{r_i}^m + (R^2 + \Delta z^2)^{m/2}} \tag{10.25}$$

Above the mean, polarization dominates on all scales if $\bar{P}_i^2 \equiv \langle P_i \rangle \langle P_i^* \rangle > \sigma_i^2$. Otherwise, the mean contribution can be neglected for relatively small separations $R < r_i(\sigma_i^2/\bar{P}_i^2 - 1)^{1/m}$.

After defining separately the statistics of the Faraday rotation and emitted polarized radiation, one can deal with the statistics of the observed polarization. The observed correlation defined in LP16 is

$$\langle P(\mathbf{X_1}, \lambda_1^2) P^*(\mathbf{X_2}, \lambda_2^2) \rangle = \int_0^L dz_1 \int_0^L dz_2 \times \langle P_i(\mathbf{X_1}, z_1) P_i^*(\mathbf{X_2}, z_2) e^{2i(\lambda_1^2 \Phi(\mathbf{X_1}, z_1) - \lambda_2^2 \Phi(\mathbf{X_2}, z_2))} \rangle \tag{10.26}$$

With the mean effect separated, one can write

$$\langle P(\mathbf{X_1}, \lambda_1^2) P^*(\mathbf{X_2}, \lambda_2^2) \rangle = \int_0^L dz_1 \int_0^L dz_2 \, e^{2i\bar{\phi}(\lambda_1^2 z_1 - \lambda_2^2 z_2)} \times \langle P_i(\mathbf{X_1}, z_1) P_i^*(\mathbf{X_2}, z_2) e^{2i(\lambda_1^2 \Delta\Phi(\mathbf{X_1}, z_1) - \lambda_2^2 \Delta\Phi(\mathbf{X_2}, z_2))} \rangle \tag{10.27}$$

which represents the general expression for the correlation function in the Position-Position-Frequency (PPF) data cube.

Observable correlation function in terms of the Stokes' parameters is split again into real and imaginary parts that are separately invariant with respect to frame rotation

$$\langle P(\mathbf{X_1}) P^*(\mathbf{X_2}) \rangle = \langle Q(\mathbf{X_1})Q(\mathbf{X_2}) + U(\mathbf{X_1})U(\mathbf{X_2}) \rangle + i \langle U(\mathbf{X_1})Q(\mathbf{X_2}) - Q(\mathbf{X_1})U(\mathbf{X_2}) \rangle \tag{10.28}$$

In this section, we focus on the symmetric real part $\langle Q(\mathbf{X_1})Q(\mathbf{X_2}) + U(\mathbf{X_1})U(\mathbf{X_2})\rangle$ which is easier to determine and which carries the most straightforward information about the magnetized turbulent medium.

The problem of obtaining underlying turbulence spectra using synchrotron polarization is pretty complex. There are several important dependences, for instance, the correlation length of the Faraday rotation measure r_ϕ, the correlation length of the transverse magnetic field r_i, the line-of-sight size of the emitting region L as well as the separation between two line-of-sight R. In addition, the scaling slopes for RM measure m_ϕ and intrinsic correlations m, amplitude of fluctuations in RM σ_ϕ and intrinsic correlations σ_i, possible mean rotation $\bar{\phi}$ and mean polarization $\bar{P}_i$ of the radiated emission, and the wavelength of observations λ. Among these values, the magnitude of RM, either random σ_ϕ or mean $\bar{\phi}$ together with observation wavelength λ determine the characteristic distance $\mathcal{L}_{\sigma_\phi,\bar{\phi}}$ over which Faraday effect rotates the polarization by one *radian*. As a result, LP12 dealt with five scales, $\mathcal{L}_{\sigma_\phi,\bar{\phi}}$, r_ϕ, r_i, L, R, and two scaling slopes m_ϕ and m, which provided a variety of regimes of turbulence studies.

LP16 introduced two techniques that have similarities with the VCA and the VCS that the authors introduced for studying velocity fluctuations. The Polarization Spacial Analysis (PSA) is an analog of the VCA technique. It correlates the polarization at different spacial points of the PPF space, the latter being an analog of the PPV space we discussed earlier. The other technique is the Polarization Frequency Analysis (PFA) which in some sense is analogous to the VCS, as it analyzes the information along a single line of sight. Unlike the VCS, it is the dispersion of the signal rather than the VCS correlation of intensities at different frequencies that is analyzed.

PSA

The starting equation for the PSA study is

$$\langle P(\mathbf{X}_1)P^*(\mathbf{X}_2)\rangle = \int_0^L dz_1 \int_0^L dz_2\, e^{2i\bar{\phi}\lambda^2(z_1-z_2)} \langle P_i(\mathbf{X}_1,z_1)P_i^*(\mathbf{X}_2,z_2)\rangle e^{-2\lambda^4\langle(\Delta\Phi(\mathbf{X}_1,z_1)-\Delta\Phi(\mathbf{X}_2,z_2),)^2\rangle} \tag{10.29}$$

which provides different regimes depending on the parameters of the media.

PFA

The expression that is employed for the PFA analysis is the one for the dispersion of polarization

$$\langle P^2(\lambda^2)\rangle = \int_0^L dz_1 \int_0^L dz_2\, e^{2i\bar{\phi}\lambda^2(z_1-z_2)} \langle P_i(z_1)P_i^*(z_2)e^{2i\lambda^2(\Phi(z_1)-\Phi(z_2))}\rangle, \tag{10.30}$$

which also provides a variety of regimes.

Table 10.6: Different regimes of synchrotron polarization correlations in Position-Position-Frequency studies from LP16.

PSA, $\xi_P(\mathbf{R})$			
		$\mathcal{L}_{\sigma_\phi,\bar{\phi}} < r_i$	$\mathcal{L}_{\sigma_\phi,\bar{\phi}} > r_i$
$\mathcal{L}_{\sigma_\phi} < \mathcal{L}_{\bar{\phi}}$	$R < r_\phi$	$\sim \mathcal{L}^2_{\sigma_\phi}\, \xi_i(\mathbf{R},0) \mathcal{L}_{\sigma_\phi} r_\phi^{\bar{m}_\phi} / R^{1+\bar{m}_\phi}$	reflects spectrum $H_\perp$
	$R > r_\phi$	$\sim \mathcal{L}^2_{\sigma_\phi}\, \xi_i(\mathbf{R},0)$	
$\mathcal{L}_{\sigma_\phi} > \mathcal{L}_{\bar{\phi}}$		$\sim L\, \mathcal{L}_{\bar{\phi}}\, \xi_i(\mathbf{R},0)$	reflects spectrum $H_\perp$
PFA, $\langle P^2(\lambda^2)\rangle$			
$\mathcal{L}_{\sigma_\phi} < \mathcal{L}_{\bar{\phi}}$		$\propto \lambda^{-2}$	$\propto \lambda^{-2-2am_\phi+2m}$
$\mathcal{L}_{\sigma_\phi} > \mathcal{L}_{\bar{\phi}}$		$\propto \lambda^{-2-2m}$	$\propto \lambda^{-2+2m}$

Table 10.6 summarizes different regimes of turbulence studies with the PSA and the PFA. As we see different regimes emerge when the correlation scale of the magnetic field r_i is larger or smaller, then the characteristic scale over which the Faraday decorrelation happens. The latter is denoted as $\mathcal{L}_{\bar{\phi}}$ when the effect is induced by mean field acting on mean density of thermal electrons and $\mathcal{L}_{\sigma_\phi}$ when turbulent effects dominate the depolarization. Additional differences in the regimes arise depending which of the latter scales is smaller.

Naturally, the study of synchrotron polarization are not limited to the correlations of polarization only. For instance, LP16 introduced a measure that is more sensitive to the fluctuations of Faraday rotation:

$$\left\langle \frac{dP(\mathbf{X}_1)}{d\lambda^2} \frac{dP^*(\mathbf{X}_2)}{d\lambda^2} \right\rangle = \int_0^L dz_1 \int_0^L dz_2 e^{2i\bar{\phi}\lambda^2(z_1-z_2)} \times \left\langle P_i(\mathbf{X}_1,z_1) P_i^*(\mathbf{X}_2,z_2) \Delta\Phi(\mathbf{X}_1,z_1) \Delta\Phi(\mathbf{X}_2,z_2) e^{-2\lambda^2 i(\Delta\Phi(\mathbf{X}_1,z_1)-\Delta\Phi(\mathbf{X}_2,z_2))} \right\rangle \tag{10.31}$$

Numerical calculations in [290] confirm that the measure given by Equation (10.31) can recover the spectrum of Faraday rotation in agreement with the LP12 analytical predictions.

10.2.1 Numerical testing of the synchrotron-based techniques and the application to observations

The theoretical constructions in LP12 and LP16 relate the synchrotron statistics and the underlying turbulence. They were tested in numerical simulations. A number of the theoretical conclusions related to synchrotron intensity fluctuations, i. e., those in LP12, were tested in [192]. In [290] and [466], the LP16 predictions for the PSA tech-

nique have been successfully tested. The LP16 predictions related to the PFA technique have been confirmed in [465].

With the machinery of description of turbulence statistics in both the PPV and the PPF cubes, one can expect a lot of progress in getting the turbulence spectra from observations. As more established the VCA and the VCS techniques have already brought a number of valuable results. The PSA and the PFA techniques are more recent developments. They, nevertheless, already have already resulted in a number of interesting observational studies. For instance, Xu et al. [448], using the machinery in LP16 explained the broken power law corresponding to the structure functions of the galactic Faraday rotation measures. In [187], the technique was successfully applied to explain the depolarization of the optical blazar emission.

10.3 Observational signatures of MHD turbulence modes

10.3.1 Anisotropy arising from Alfvenic turbulence: obtaining magnetic field direction and M_A

The first demonstration to magnetic field direction can be revealed statistically making use of the anisotropy of correlation functions was made by Lazarian in [282]. This was the start of the Correlation Function Analysis (CFA) that employs the Doppler broadened emission lines for magnetic field studies. The first study was performed with synthetic observations obtained with 3D MHD turbulence simulations and it analyzed anisotropies of intensities in channel maps. Later the possibility of determining the magnetic field direction using the CFA was explored with velocity centroids by Esquivel & Lazarian [132]. Further work in [133] revealed that the degree of anisotropy of velocity centroid correlations can be used to determine the Alfven Mach number M_A (see also a more extensive study in [63]). A similar study with the anisotropy of the intensities of thin channel maps was performed in [135]. As we discussed earlier, the statistics of thin channel maps is mostly affected by velocities (LP00) and this explains the similarity of the results obtained with velocity centroids and thin channel maps.

The theoretical foundation of the CFA technique is the anisotropic nature of MHD turbulence. As a result, the correlations of the fluctuations of velocity are also anisotropic. The measurements of 3D velocities are not directly available, but the statistics of the line of sight velocities can be obtained either with velocity centroids or with thin channel maps (see LP00). The turbulence anisotropies are aligned with the magnetic field direction. Therefore, the correlations that are available with the CFA are anisotropic with correlations stronger along the line of sight projected magnetic field. As the distribution of wavevectors in Alfvenic turbulence depends on M_A, the degree of the observed correlation anisotropy also depends on M_A.

Apart from correlation functions, more sophisticated ways of analysis can be used. For instance, [193] proposed to study the anisotropies using the Principal Compo-

nent Analysis (PCA). The comparison of the latter suggestion with the CFA is provided in [461].

10.3.2 Contribution of different MHD turbulence modes

Studies of observational anisotropies is the most evident way of utilizing the anisotropic nature of MHD turbulence. A more sophisticated way of analysis involves studying the contributions arising from fundamental MHD modes, i. e., slow, Alfven and fast. The corresponding analytical study was first performed in LP12 for the case of synchrotron emission. Figure 10.8 illustrates how the properties of turbulent modes change for the case of synchrotron intensities. The ratio of the quadrupole moment of the structure function to the monopole moment is shown. The LP12 shows that the signatures of fast and Alfven modes can be very different, which provides a possibility of distinguishing the contribution of modes using observations. This is very important in view of a radically different effect that fast and Alfven modes have on cosmic ray propagation (see [453]) and on star formation (see [311]).

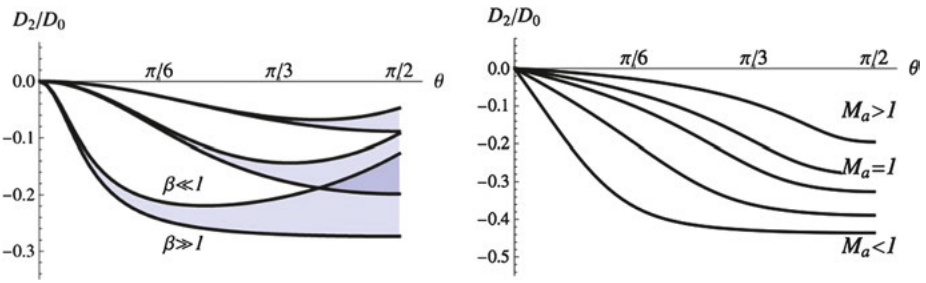

Figure 10.8: The quadrupole to the monopole ratio change versus the angle θ that the mean magnetic field makes with the line-of-sight angle. Left: fast-mode contribution shown in bands, decreasing in magnitude with increased field wandering. Each band corresponds to the range of different plasma β. Right: the same ratio for the mix of Alfven and slow modes in the regime of strong incompressible turbulence. The curves from lower to upper ones correspond to $M_A = 0.1, 0.4, 0.7, 1, 2$ from LP12.

Similar to the synchrotron intensity, the anisotropy of the synchrotron polarization statistics (LP16), as well as the anisotropy of the emission line statistics (see [208, 210]) can be analyzed. The advantages of these compared to the synchrotron intensity include the ability of studying 3D structure of the turbulent mode distribution. Indeed, if synchrotron polarization is used, the Faraday depolarization provides a way to tomographic sampling of the emitting volume along the line of sight ([284]).

Using different spectral lines, one can also sample turbulence at different optical depth. In addition, the use of the galactic rotation curve provides another way to get 3D probing of turbulence at different distances from the observer.

10.4 Relation to CMB foreground studies

The study of dust and synchrotron polarization fluctuations is essential in the context of CMB foregrounds. At angular scales between $10'$ and a few tens of degrees, cosmological B-mode polarization fluctuations created during the epoch of inflation are expected [171]. The gravitational waves produce these modes during the stage of cosmological inflation and the detection of a primordial B-mode polarisation signature is one of the major scientific goals of many CMB experiments. Since the E and B mode signals from inflation are expected to be significantly smaller in amplitude than the fluctuations of foregrounds, accurate modeling of foreground contamination is vital for the reliable measurement of the primordial E and B modes

10.4.1 Polarized CMB foreground

The dominant cosmic microwave background (CMB) foreground at frequencies $\lesssim 100$ GHz comes from synchrotron radiation, which is produced by the interaction of relativistic electrons with the Galactic magnetic field lines, and its polarisation is orthogonal to the plane of sky (POS) magnetic field direction (Ribicki & Lightman 1979). On the other hand, at frequencies $\gtrsim 100$ GHz, the dominant CMB foreground is thermal emission from oblate dust grains, aligned with their longest axes perpendicular to the magnetic field. As the dust emission is higher along its longest axes, a linear polarisation orthogonal to the POS magnetic field direction is produced. The distribution of relativistic electrons is smooth and isotropic compared to that of magnetic field. Therefore the fluctuations of polarised synchrotron emission arise from the magnetic field fluctuations. At the same time the fluctuations of polarised dust emission depend on both the magnetic field and gas dust density fluctuations. The origin of magnetic field and gas density fluctuations is the interstellar MHD turbulence.

To study polarisation properties, it is convenient to decompose a polarisation map into two rotational invariant modes, namely, E, B, as well as T (temperature) modes. The measurements of polarization arising from E and B modes of cosmological origin is the problem of outmost importance. The removal of the polarized galactic foregrounds is essential for the success of such studies, especially for the measurements of elusive B-modes that originate from the gravitational waves in the early universe (see [106]). To know the relative contribution of the foregrounds to the E and B cosmological modes, it is useful to separate the foreground into its own E and B modes. The T (temperature) mode is also important.

For a randomly oriented map, E and B modes are expected to be of equal power. However, observations of dust polarization in the intermediate to high latitude of our galaxy revealed that the power in B mode was half of that in E mode ([358]).

10.4.2 MHD turbulence for foreground studies

As we discussed earlier, the properties of MHD turbulence depend on the degree of magnetization, which can be characterized by the Alfvén Mach number. For super-Alfvénic turbulence, i. e. $M_A \gg 1$, magnetic forces are not important in the vicinity of injection scale, thus at these scales, turbulence statistics are effectively isotropic. For sub-Alfvénic turbulence, i. e. $M_A < 1$, magnetic forces are dominant, and turbulence statistics is highly anisotropic. The compressibility of plasma is described by the plasma β ($\equiv P_{\rm gas}/P_{\rm mag}$) parameter. Naturally, $\beta \to \infty$ corresponds to incompressible regime

The turbulent mode decomposition developed in LP12 can be employed for understanding the nature of the polarized foreground fluctuations arising from dust and synchrotron. In particular, in an important study Caldwell et al. [67] used this decomposition and concluded that there was a problem in describing statistical properties of CMB polarized foregrounds from dust using the accepted MHD turbulence models. In addition, the recent paper [4] suggested the detection of positive value ~ 0.36 for the TE cross-correlation in Planck dust emission maps.

This problem of decomposing foregrounds into modes was revisited in [209, 211] and the conclusion different from that in [67] was reached. In what follows we discuss the approach in [218] as it illustrates how our knowledge of MHD turbulence and description of MHD modes in the global system of reference presented in LP12 can solve problems of understanding the CMB foreground statistics.

For the calculations we assume that the line of sight (LOS) is along the z axis, and the mean field $\boldsymbol{H}_0 = H_0(\sin\theta, 0, \cos\theta)$ is aligned in the $x-z$ plane making an angle θ with the LOS. We describe perturbations using two-dimensional wavevector $\boldsymbol{K} = K(\cos\psi, \sin\psi, 0)$ in the $x-y$ plane of the sky. The angle α between wavevector and magnetic field is defined by $\cos\alpha = \sin\theta\cos\psi$.

On the basis of the study [81] of the power-spectrum of magnetic field turbulence for Alfvén, slow and fast modes it is possible to write expressions for them (LP12, [67])

$$P_{a,H}(k,\alpha) = \frac{1}{a^2} F_a(\alpha) P_a(k)\,, \tag{10.32}$$

$$P_{s,H}(k,\alpha) = \frac{2}{a^2 D_{-+}} \frac{F_s(\alpha) P_s(k)}{(1 + D_{++}^2/D_{--}^2 \tan^2\alpha)}\,, \tag{10.33}$$

and

$$P_{f,H}(k,\alpha) = \frac{2}{a^2 D_{++}} \frac{F_f(\alpha) P_f(k)}{(1 + D_{-+}^2/D_{+-}^2 \tan^2\alpha)}\,, \tag{10.34}$$

where we use the notations adopted in the series of foreground studies e. g. [67, 209], namely, $a \equiv H_0/\sqrt{4\pi\rho_0}$ is the Alfvén velocity and $D_{\pm\pm} = 1 \pm \sqrt{D} \pm \beta/2$, and $D =$

$(1+\beta/2)^2 - 2\beta\cos^2\alpha$. This is intended to help the reader to get more details from the aforementioned papers.

In Eqs. (10.32), (10.33) and (10.34), $P(k)F(\alpha)$ describes anisotropic power, which contains factorized scale dependent part and an angle dependent part. The anisotropic dependence of the power spectrum applicable for Alfvén and slow modes is given by (see LP12)

$$F_{\rm a,s}(\alpha) = \exp\left[-\frac{M_A^{-4/3}|\cos\alpha|}{(\sin^2\alpha)^{1/3}}\right] . \tag{10.35}$$

The power spectrum of fast mode is isotropic and we write use $F_{\rm f}(\alpha) = 1$.

To study dust polarization, we define the power spectrum of the density fluctuations. Alfvén modes do not induce density fluctuations and the only contribution to density fluctuations comes from fast and slow compressible modes. On the basis of the [81] study, the power spectrum of fractional density fluctuations for slow and fast modes can be written as (see [209])

$$P_{s,\rho}(k,\alpha) = \frac{2}{a^2 D_{-+}} \frac{\sin^2 2\alpha\, F_s(\alpha) P_s(k)}{(D_{--}^2\cos^2\alpha + D_{++}^2\sin^2\alpha)} , \tag{10.36}$$

and

$$P_{f,\rho}(k,\alpha) = \frac{2}{a^2 D_{++}} \frac{\sin^2 2\alpha\, F_f(\alpha) P_f(k)}{(D_{+-}^2\cos^2\alpha + D_{-+}^2\sin^2\alpha)} . \tag{10.37}$$

To study dust polarization it is natural to adopt the assumption of magnetic field and density not being correlated. This follows from the theory of turbulent reconnection in LV99 and agrees well with the observations of diffuse media at high galactic latitudes [103].

10.4.2.1 E and B modes arising from dust and synchrotron polarization

Below we present the statistical description of dust and synchrotron polarization fluctuations in terms of E and B modes. Synchrotron emission arises from relativistic electrons moving in magnetic field. due to the motion of relativistic electrons in magnetized regions. The polarized emissivity can be written

$$\epsilon_{\rm sync} = \epsilon_Q + i\epsilon_U = A_{\rm sync} H_\perp^{\gamma_{\rm sync}} (H_x + {\rm i}H_y)^2 , \tag{10.38}$$

where $A_{\rm sync}$ is a normalization constant that depends on the number density of relativistic electrons, $H_\perp$ is the plane-of-sky magnetic field that varies with the 2D position vector on the sky $X = (x, y)$, and $\gamma_{\rm sync}$ is, generally, a fractional power. For the galactic synchrotron emission, $\gamma_{\rm sync}$ is found to take an approximate value of 0 (see [162]; [277]).

Since the synchrotron polarisation axis is perpendicular to the sky projected magnetic field [372], we take $A_{\rm sync} < 0$, and as we will see later, this sign is important for TE cross-correlation.

Dust emission, one the other hand, is thermal emission from aligned dust grains. The direction of polarization is determined by the grain longest dimension that is perpendicular to the magnetic field. The linear polarization from dust emission can be written in a form similar to the one for synchrotron emission

$$\epsilon_P = \epsilon_Q + i\epsilon_U = A_d n_d H^{\gamma_d} (H_x + iH_y)^2 \,. \tag{10.39}$$

For $\gamma_d = -2$, the polarized emission is independent of magnetic field strength. In equation (10.39), n_d is dust density which we take to be proportional to gas density (see [282]), and $A_d 0$ is a constant.

The expressions for E and B synchrotron powers both for dust and synchrotron contributions are presented in [218]. For synchrotron emission and Alfvén modes, we have

$$\langle \tilde{E}^2 \rangle_{{\rm sync},a} \propto (\sin\theta)^{2\gamma_{\rm sync}+2} \cos^2\theta \sin^2\psi \times \left(\frac{2 - \gamma_{\rm sync} \cos 2\psi}{\sin\alpha} \right)^2 P_{a,H}(\alpha) \,, \tag{10.40}$$

and

$$\langle \tilde{B}^2 \rangle_{{\rm sync},a} \propto (\sin\theta)^{2\gamma_{\rm sync}+2} \cos^2\theta \cos^2\psi \times \left(\frac{2 + 2\gamma_{\rm sync} \sin^2\psi}{\sin\alpha} \right)^2 P_{a,H}(\alpha) \,, \tag{10.41}$$

where $P_{a,H}(\alpha)$ is defined in Eq. (10.32). Similarly, the synchrotron emission arising from slow and fast modes results in

$$\langle \tilde{E}^2 \rangle_{{\rm sync},i} \propto (\sin\theta)^{2\gamma_{\rm sync}+4} \sin^4\psi \times \left(\frac{2 - \gamma_{\rm sync} \cos 2\psi}{\sin\alpha} \right)^2 P_{i,H}(\alpha) \,, \tag{10.42}$$

and

$$\langle \tilde{B}^2 \rangle_{{\rm sync},i} \propto (\sin\theta)^{2\gamma_{\rm sync}+4} \sin^2\psi \cos^2\psi \times \left(\frac{2 + 2\gamma_{\rm sync} \sin^2\psi}{\sin\alpha} \right)^2 P_{i,H}(\alpha) \,, \tag{10.43}$$

where $P_{i,H}(\alpha)$ denotes the power spectrum of magnetic field of slow and fast modes, defined in Eqs. (10.33) and (10.34). These expressions get more simple for $\gamma_{\rm sync} = 0$, which, incidentally, is close to what is expected for Galactic synchrotron emission.

Similarly, for dust polarization, the contribution to the E and B powers arising from Alfvén modes are

$$\langle \tilde{E}^2 \rangle_{d,a} \propto \sin^2 2\theta \frac{\sin^2 \psi}{\sin^2 \alpha} P_{a,H}(\alpha) \,, \tag{10.44}$$

and

$$\langle \tilde{B}^2 \rangle_{d,a} \propto \sin^2 2\theta \frac{\cos^2 \psi}{\sin^2 \alpha} P_{a,H}(\alpha) \,. \tag{10.45}$$

Similarly, for slow and fast modes, with the assumption of uncorrelated density and magnetic field, we have

$$\langle \tilde{E}^2 \rangle_{d,i} \propto \frac{\sin^4 \theta (1 - \cos 2\psi (1 + \gamma_{\rm d} \sin^2 \alpha))^2}{\sin^2 \alpha} P_{i,H}(\alpha) + \sin^4 \theta \cos^2 2\psi P_{i,\rho}(\alpha) \,, \tag{10.46}$$

and

$$\langle \tilde{B}^2 \rangle_{d,i} \propto \frac{\sin^4 \theta \sin^2 2\psi (1 + \gamma_{\rm d} \sin^2 \alpha)^2}{\sin^2 \alpha} P_{i,H}(\alpha) + \sin^4 \theta \sin^2 2\psi P_{i,\rho}(\alpha) \,, \tag{10.47}$$

where $P_{i,\rho}(\alpha)$ indicates density power spectrum of slow and fast modes, defined in Eqs. (10.36) and (10.37).

The quantity of interests in terms of CMB polarization studies is the ratio of B to E power. Since Planck studies of both dust and synchrotron foregrounds reveal a rather uniform B/E ratio across the sky, it is meaningful to calculate the angle averaged B/E ratio [67]:

$$R = \frac{\int {\rm d}\Omega \langle \tilde{B}^2 \rangle}{\int {\rm d}\Omega \langle \tilde{E}^2 \rangle} \,, \tag{10.48}$$

where ${\rm d}\Omega = \sin\theta \, {\rm d}\theta \, {\rm d}\psi$.

Since fast and slow modes have different spectra, formally, one has to use the full expressions that are provided in [218]. However, the dependence of the B/E ratio on the wavenumber ℓ is weak, and therefore, one can write

$$R \approx \frac{P_{a,B} + P_{s,B} + P_{f,B}}{P_{a,E} + P_{s,E} + P_{f,E}} \,, \tag{10.49}$$

where $P_{a,E}, P_{a,B}$ are the amplitudes of power of E mode and B mode that arise from Alfvén, fast and slow modes, respectively.

10.4.2.2 TE cross-correlation for synchrotron and dust

The correlation of temperature and E mode, i. e. TE correlation, is another important measure for CMB studies. The fluctuations of brightness temperature of the polarized emission arise from the fluctuations of the magnetic field strength for synchrotron emission. At the same time both fluctuations of the magnetic field strength and the dust density contribute to the fluctuations of , temperature arising from dust.

The results for correlations arising from both aligned dust and synchrotron are provided in [218]. The fluctuation of temperature arising from dust is given by

$$\delta T_{\rm dust} = c_{\rm dust}\delta n\,, \tag{10.50}$$

where $c_{\rm dust}$ is a constant. In the assumption of no magnetic field – density correlations the cross correlation arising from dust is

$$\langle TE\rangle_{d,i} \propto \sin^2\theta\cos 2\psi P_{i,\rho}(\alpha)\,. \tag{10.51}$$

The contribution comes from compressible fast and slow modes, while Alfven modes do not induce the cross-correlation.

For the synchrotron fluctuations, all three MHD modes contribute to the TE cross-correlation. The calculations in [218] provide:

$$\langle TE\rangle_{{\rm sync},a} \propto (\sin\theta)^{2\gamma_{\rm sync}+2}\frac{\cos^2\theta\sin^2\psi}{\sin^2\alpha} \times(2-\gamma_{\rm sync}\cos 2\psi)\,P_{a,H}(\alpha)\,, \tag{10.52}$$

while for compressible fast and slow modes

$$\langle TE\rangle_{{\rm sync},i} \propto (\sin\theta)^{2\gamma_{\rm sync}+4}\frac{\sin^4\psi}{\sin^2\alpha} \times(2-\gamma_{\rm sync}\cos 2\psi)\,P_{i,H}(\alpha)\,. \tag{10.53}$$

The normalised cross-correlation coefficient r_i can be written as

$$r_i = \frac{\int {\rm d}\Omega\,\langle TE\rangle}{\sqrt{\int {\rm d}\Omega\,\langle TT\rangle}\sqrt{\int {\rm d}\Omega\,\langle EE\rangle}}\,. \tag{10.54}$$

and its values can be compared with observations, e. g. by Planck.

10.4.2.3 Comparison with observations

The ratio of the B to E modes is shown in Figure 10.9 for the case of an equal mixture of Alfven and slow modes. This provides a reasonable approximation to the turbulence at high galactic latitudes. For both dust and synchrotron the fluctuations of polarization observed by Planck can be explained if the Alfven Mach number M_A is less than

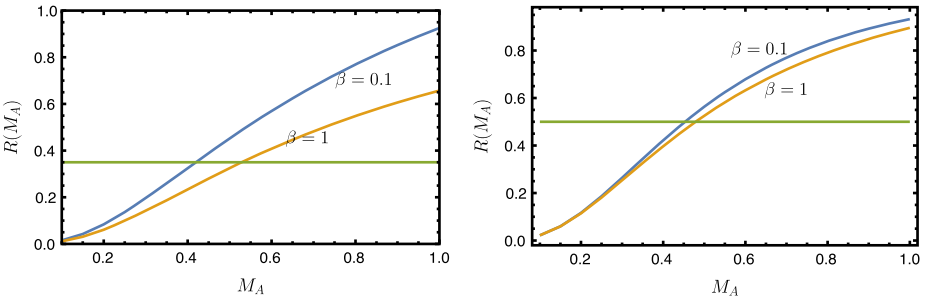

Figure 10.9: Ratio of B to E power for the equal mix of Alfvén and slow modes for: Left panel. Synchrotron polarization fluctuations for $\gamma_{\rm sync} = 0$. The dotted line corresponds to the Planck measured value ≈ 0.35. Right panel. Dust polarization fluctuations.

unity, i. e. turbulence is subAlfvenic. The exact value of M_A is difficult to determine precisely but $M_A < 0.5$ seem to satisfy the existing constrains. Note that it is subAlfvenic turbulence that is expected above the plane of the galaxy.

As for the TE cross-correlation from dust, the positive values shown for slow and fast MHD modes in Figure 10.10 correspond to observations. More details can be found in [218], but here we would like to stress the practical utility of the quantitative analytical treatment of MHD turbulence that we strongly advocated in this book.

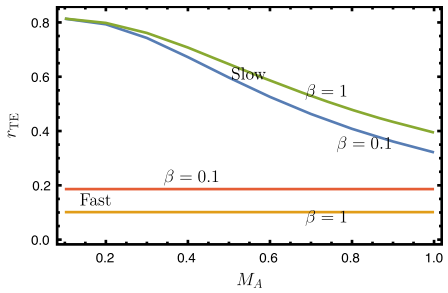

Figure 10.10: Dust TE cross-correlation for fast and slow modes for different values of plasma β.

As for the practical consequences of the study we can state that using the approach in LP12, Kandel et al. [209, 211] established that to account for the measured E/B ratio, the MHD turbulence at high galactic latitudes should have the subAlfven, which is rather natural from what we know about the distribution of turbulent motions in the galactic disk. The TE positive correlation follows naturally if the density and magnetic field are not correlated. The latter is the natural consequence of flux freezing violation in turbulent fluids that we have discussed extensively in this book. This decorrelation is also confirmed by observations by Crutcher [103].

10.5 Gradient technique: utilizing the turbulence knowledge to study magnetic fields

The anisotropic properties of MHD turbulence give rise to the CFA technique that allows one to get magnetic field direction in a statistical way. The required averaging does not allow studies of detailed structure of magnetic field. To address the latter problem, a new technique that we describe below was suggested. This technique utilizes our understanding of MHD turbulence and turbulent reconnection.

10.5.1 Velocity gradients

Basic technique

As we discuss in this book, the velocity fluctuations arising from MHD turbulence are anisotropic. Figure 10.11 shows iso-contours of velocity for sub-Alfvenic turbulence. It is obvious that these contours are elongated along magnetic field. This means that the spatial changes of the velocity amplitude, i. e., *velocity gradients* are perpendicular to the magnetic field.

The question of how accurate is the tracing of magnetic field can be addressed through recalling the properties of MHD turbulence. Indeed, can recall that the picture of strong Alfvenic turbulence can be presented as the turbulence of magnetized eddies. This wave-eddy dualism is a remarkable feature of MHD turbulence that follows from the model of turbulent reconnection. Indeed, LV99 turbulent reconnection theory predicts that the reconnection of magnetic field associated with the eddy takes place within one eddy turnover time. Therefore, magnetic field does not constrain turbulent motions if these motions are happening perpendicular to the magnetic field. Naturally, this magnetic field should be *local* to the eddy. Therefore, from the perspective of the turbulent reconnection the concept of *local* magnetic field (which was missing in the original formulation of the GS95 theory) is pretty trivial. Indeed, the path of

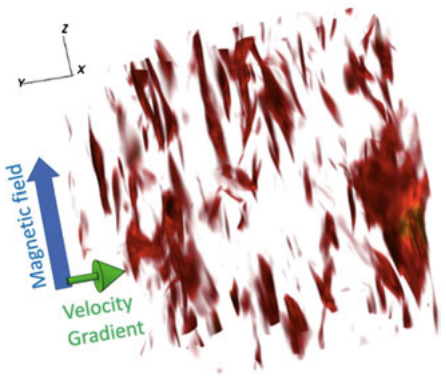

Figure 10.11: 3D velocity iso-contours (red structures) from a sub-Alfvénic simulation aligned with the magnetic field direction (blue arrow shows the mean magnetic field direction). The gradients of velocity amplitude is perpendicular to magnetic field from [285].

least resistance for the turbulent motions correspond to eddies that mix magnetic field lines with the minimal deformation of magnetic field. Incidentally, the Kolmogorov spectrum of perpendicular motions in this picture is a consequence of the aforementioned mixing that is identical to hydrodynamic motions. It is easy to check that the condition of critical balance within this picture is the consequence of finite rigidity of magnetic field lines. Indeed, an eddy creates an Alfven wave with the period equal to its turnover time, i. e., for the $l_\perp/v_\perp \approx l_\parallel/V_A$ and this provides the relation between parallel and perpendicular scales of the eddy, i. e., between $l_\parallel$ and $l_\perp$.

The above physical picture of MHD turbulence and turbulent reconnection that is an inseparabel part of the MHD turbulent cascade helps us to explain why gradients of velocities are reliable tracers of magnetic fields in turbulent plasmas. Indeed, as the eddies trace local directions of magnetic field, the velocity gradients associated with them are perpendicular to the magnetic field. For the expected Kolmogorov scaling of perpendicular motions $v_\perp \sim l_\perp^{2/3}$, the velocity gradients scale as $v_\perp/l_\perp \sim l_\perp^{-1/3}$, i. e., the smallest eddies are producing the largest velocity gradients. These smallest eddies are well aligned with the magnetic field and their gradients well trace the *local* magnetic field. Detailed analysis in Lazarian & Yuen ([285]) shows that the eddies at the resolution of a telescope provide the largest contribution to the observed gradients. In other words, velocity gradients carry the information about the small-scale projected magnetic field.

For practical studies of velocity gradients, either calculating of gradients of velocity centroids [174, 460] and their modifications [285] or calculating of intensities within thin channel maps [285] can be used. Figure 10.12 illustrates the comparison of the magnetic field structure obtained with Velocity Channel Gradients (VChGs) with

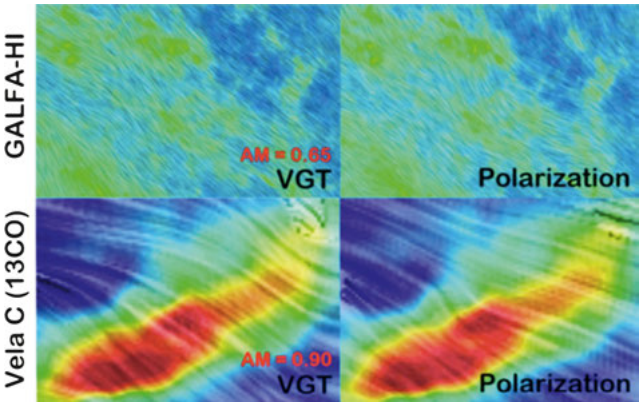

Figure 10.12: Magnetic field textures are created by the line integral convolution method. *Left panels*: VCG technique (gradients are turned 90 degrees) applied to GALFA-H I data (upper panel) and Vela C 13CO data (lower panel). *Right panels*: polarimetric studies of the same regions with PLANCK and BLASTPOL (Fissel et al. (2016)) from [285].

that obtained with dust polarimetry. The

$$AM = \langle \cos^2 \phi - 1/2 \rangle, \tag{10.55}$$

where $\langle \dots \rangle$ denote averaging and ϕ is the angle between the velocity gradients and the direction given by polarization. Both from the value of the *AM* and visually we see that the VCG technique provides a good correspondence to the polarimetric studies of magnetic fields. This is also true for the projected magnetic field in the synthetic observations obtained with 3D MHD simulations and velocity gradients (see [460, 459, 285]). We note that an additional value of velocity gradients that they change their direction 90 degrees in the regions of gravitational collapse. This provides a unique way to study star formation processes.

The practical calculations of gradients are done using Gaussian fitting into the distribution of gradient directions calculated over given block of points [460]. This way provides the gradient direction over the block and the statistical error. Blocks of 20 pixels are frequently sufficient for obtaining a reliable determining of magnetic field with the statistical error less than 10 degrees.

The subblock averaging may be seen like a constrain limiting the resolution of the magnetic field maps. Indeed, this type of averaging is not necessary for polarimetric studies. However, one should keep in mind that the spectral line observations can be done with much higher resolution using ground based intruments. In addition, [285] demonstrated that the direct interferometric output can be successfully used for gradient studies. It is important that the velocity gradient maps can be constructed with interferometer output without the requirement of the single dish input. Therefore, even with the subblock averating, the velocity gradients can provide higher resolution maps as compared with the far infrared polarimetry.

In comparison to far infrared polarimetry the velocity gradient technique can make use of the wealth of spectroscopic surveys. In many cases the corresponding data is already publicly available. In any case, obtaining such data does not require expensive space of balloon-borne missions. Moreover, using velocity gradients it is possible to study magnetic fields both in dense and the surrounding diffuse media, which is not feasible for the present generation of the far infrared polarimeters.

We also note that due to the property of velocity gradients to increase their value with the decrease of the scale, the contribution of the velocity gradients arising from the large scale astrophysical flows is not important. At the same time, in the presence of gravitational collapse the direction of velocity gradients changes by 90 degrees (see [460, 285]). This change is easy to understand in the two limiting cases. In the case of very strong magnetic field, the free fall happens only along magnetic field lines and the velocity gradients get aligned *along* magnetic field. The latter alignment is also present for the case of a weak magnetic field that is taken for a ride by the collapsing matter.

The effect of velocity gradient direction flip provides a unique possibility of detecting the regions of gravitational collapse. It is important that for this purpose the use of polarimetry is not required. The properties of velocity gradient distribution change at the boundary of the collapsing region and this provides an observational signature of the transition from the turbulence-dominated to collapse dominated regions. The pilot studies (Hu et al. 2018, in progress) show that the regions of molecular clouds undergoing the gravitational collapse subtend a small part of the cloud volume. This can be viewed as an indication that the gravitational collapse cannot be the driver of turbulence in molecular clouds.

Obtaining 3D distribution of magnetic field

Galactic rotation curve provides a way to map the distribution of magnetic fields at different distances from the observer if velocity gradients are used. This is an important bonus compared to the far infrared polarimetry which samples magnetic field along the entire line of sight. If applied to 13CO and other molecular species, velocity gradients allow to study magnetic fields within molecular clouds in the galactic disk. For most of these clouds, far infrared polarimetry is useless due to the effect of confusion. Moreover, using different molecular species that exist at different optical depth one can provide tomographic studies of the magnetic field distribution within a given molecular cloud.

The first study of the 3D distribution of magnetic field using velocity gradients was performed in [175]. To test the obtained 3D distribution of magnetic fields, this distribution was used to predict the expected polarization toward a number of stars to which both the distance and polarization were known. A good correspondence[4] of the predicted and measured polarization was obtained (see Figure 10.13. The use of a larger sample of stars with known distances and polarization that is getting available due to GAYA satellite (http://sci.esa.int/gaia/) is going to provide a better testing of the 3D magnetic field structure available with velocity gradients.

Obtaining 3D magnetic field distribution is also important for accounting of the CMB polarized foregrounds. We note that the structure of velocity channel maps arising from MHD turbulence can be studied in different ways. For instance, Clark (see [96]) suggested an empirical technique for tracing magnetic field in diffuse media based on the alignment of intensity filaments in channel maps and the magnetic fields. This alignment was discussed as a way of predicting the foreground polarization from dust in high latitude HI ([97]). From the point of view of theory of PPV statistics the filaments in thin velocity channels should be interpreted as velocity

4 The perfect correspondence of the magnetic field direction obtained with polarimetry and velocity gradients is not expected due to the difference of summing up the Stokes parameters and gradients along the line of sight. This difference is small for subAlfvenic turbulence, but it gets more and more significant as the Alfven Mach number M_A increases.

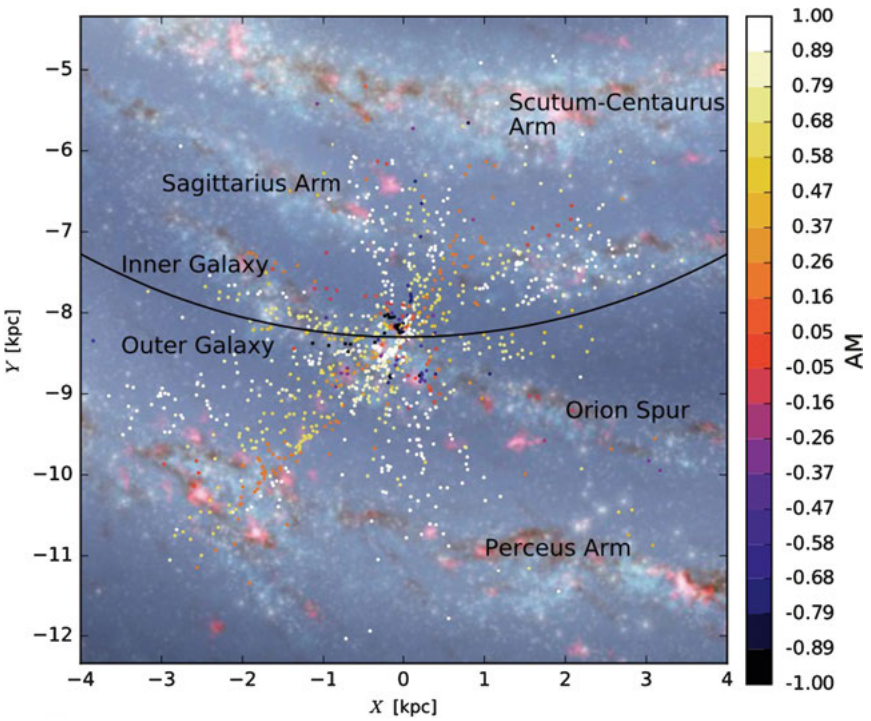

Figure 10.13: Testing of the 3D galactic magnetic field distribution obtained with the VChGs using polarization to the stars with known distances. The white points correspond to the perfect correspondence.

caustics (see [285]). The velocity gradients have better theoretical description and justification compared to filaments. Both numerical research and observations show that the correspondence between the direction of velocity gradients and that determined by polarization is better than the the correspondence between the direction of filaments and the polarization. Therefore it is advantageous to use the velocity gradients to predict the expected foreground polarization from dust.

10.5.2 Synchrotron intensity gradients

It follows from the theory of Alfvenic turbulence that magnetic field fluctuations and velocity fluctuations enter in a symmetric way. Therefore, the magnetic field gradients are expected to trace local direction of magnetic field in a way similar to velocity gradients. LP12 described how synchrotron intensity fluctuations reflect the magnetic field fluctuations. It follows that Synchrotron Intensity Gradients (SIGs) are perpendicular to the projected direction of magnetic field. This conclusion was supported by numerical simulations in [286]. Figure 10.14 shows the comparison of the SIGs direc-

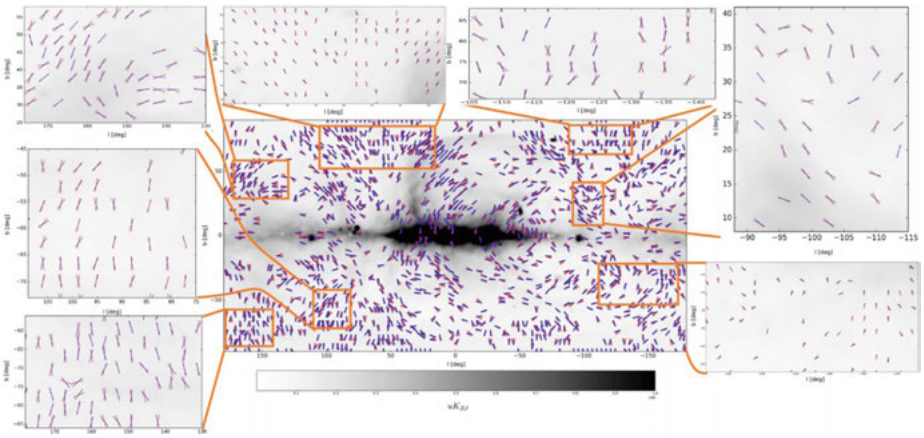

Figure 10.14: SIGs (red) and the B-field traced by synchrotron polarization (blue) from the full-sky PLANCK synchrotron data. The background is the synchrotron intensity map with darker tones corresponding to higher intensity. Seven distinct regions that are away from the galactic plane are zoomed in to show the relative alignment between the SIGs and the magnetic fields from [286].

tions (rotated 90 degrees) and the projected magnetic field directions as revealed by PLANCK map of polarized synchrotron.

The measurements using synchrotron polarization are usually have to be corrected for the Faraday rotation. This requires polarization measurements at multiple frequencies. On the contrary, the SIGs provide magnetic field direction using the measurement of intensity at a single frequency. This discovery opens an avenue for mapping magnetic fields using both existing and future synchrotron intensity maps. If polarisation measurment at low frequency is available, the comparison of the direction of magnetic field obtained with the SIGs and the the polarimation measurement allows one to construct detailed Faraday rotation maps.

10.5.3 Synchrotron polarization gradients

It was shown by Lazarian & Yuen ([283]) that the gradient technique is also applicable to synchrotron polarization, namely, to the measure:

$$P(\mathbf{X},\lambda) = \int_S dz P(\mathbf{X},z) e^{2i\lambda^2 \Phi(\mathbf{X},z)} \tag{10.56}$$

where S is the size of the emitting region along the line of sight, λ is the wavelength and the Faraday rotation measure is given (see [57])

$$\Phi = 081 \int_0^z dz' n_e(z') H_z(z') \,\mathrm{rad\,m^2}, \tag{10.57}$$

where n_e is the electron density and H_z is the z-component of magnetic field.

The Faraday rotation effect causes Faraday depolarization. For the combination of the regular and random field, the effect is described in LP16. Using this theory [285] showed that Synchrotron Polarization Gradients (SIGs) and Synchrotron Polarization Derivative Gradients (SPDGs), i. e., the gradients of $dP/d\lambda^2$ can be used to study 3D distribution of magnetic fields. The corresponding procedure is illustrated in Figure 10.15. Indeed, the measurements of polarization at two sufficiently low radio frequencies sample polarization up to the different physical boundaries L_1 and L_2. This is the consequence of Faraday depolarization effect which for turbulent field is quantified in LP16. As a result one can sample the distribution of plane-of-sky magnetic fields along the line of sight. In particular, by calculating the difference in polarized signal one can get polarized intensity arising from the volume limited by $[L_1, L_2]$ boundaries. The gradients of this polarized intensity provide the direction of the plane-of-sky magnetic field within the volume with $[L_1, L_2]$ boundaries. Combining this information with the Faraday polarization measurements one can obtain the thrue 3D structure of magnetic field as was demonstrated using numerical simulation in ([283]).

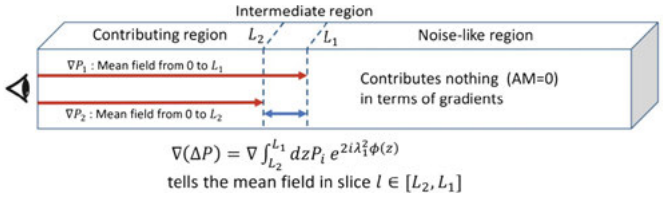

Figure 10.15: An illustration of using SPDGs to map the 3D magnetic field structure. The differences of the gradients and two neighboring frequencies allow the mean magnetic field structure between the slice $[L_2, L_1]$ to be evaluated from [283].

The direction of the SPGs and the SPDGs is perpendicular to the magnetic field direction and it is not affected by the Faraday rotation. Therefore, a reliable 3D restoring of magnetic field structure is possible. This was illustrated in [283] using numerical simulations.

10.5.4 Intensity gradients

As we discussed earlier the statistics of turbulent density does not exhibit robust universal scaling relations [37, 232]. Nevertheless, our study in [37] demonstrated that the change of the density spectra and anisotropy at high sonic Mach numbers M_s happens due to the fact that dense compressed clumps appear in the turbulent volume. At the same time, for the densities in the most of the volume the GS95 scalings are approximately valid. Thus one can expect that within a significant part of the turbulent

volume the density gradients can trace the magnetic field in a way similar to other gradient techniques that we described above. At the same time, density gradients are expected to be much more sensitive to shocks, which provides a way of identification shocks through observations. Indeed, numerical simulations in [459] demonstrated that while the direction of velocity gradients does not change in the presence of the shocks, the density gradients turn from being perpendicular to the magnetic field to being perpendicular to the shock front. This effect is illustrated by Figure 10.16 where both magnetic field and high contrast density enhancements obtained in 3D MHD numerical simulations are shown. It is easy to observe that the density structures are mostly perpendicular to magnetic field. As a result, the density and therefore observed intensity gradients tend to be parallel to magnetic field in supersonic subAlfvenic turbulence.

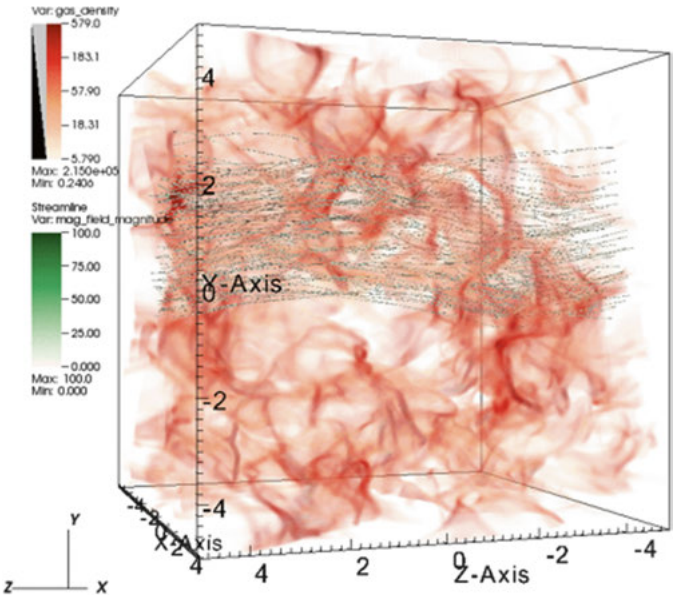

Figure 10.16: Illustration of the structure of magnetic field (black dotted lines) and high contrast density enhancements (red features) within subAlfvenic supersonic 3D MHD turbulence simulations.

In strongly magnetized media, the shocks are formed preferentially perpendicular to magnetic field lines. Thus the 90-degree change of the density gradient directions is expected. This effect is seen in the analysis of the HI observational data in Figure 10.17.

Both density and velocity gradients change their direction ~ 90 degrees in respect to magnetic field in the presence of gravitational collapse. Nevertheless, density gradients quicker react to the gravitational collapse [459]. This shows the synergy of

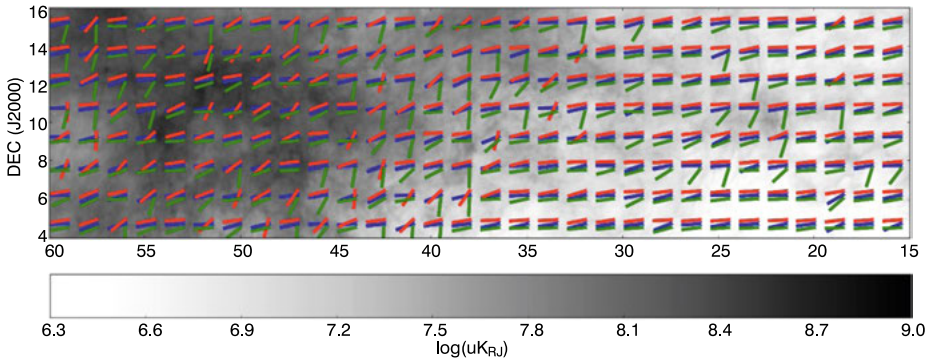

Figure 10.17: Velocity (red) and density (green) gradients obtained using GALFA-HI survey are compared with the Planck polarization data (blue). It is suggestive that the regions corresponding to strong deviations of density gradients from the direction given by velocity gradients correspond to shocks.

the velocity and density gradient studies. In some situations, e. g., in the case of dust emission, density gradients provide the only type of gradients that are available.

Due to the fact that shocks can easily distort the direction of density gradients, in terms of magnetic field tracing we view the Intensity Gradients (IGs)[5] as a suplimentary way of magnetic field tracing in the galactic diffuse and dense media. However, in combination with velocity gradients the IGs provide a powerful way to identify shocks in galactic environments.

10.5.5 Dispersion of gradient directions: obtaining magnetization of the media

As we discussed earlier, the direction of gradients is obtained via the block averaging procedure ([460]). The properties of the Gaussian that is used for fitting the distribution of gradients within the block depend on the Alfven Mach number M_A of the turbulence (see the upper panel of Figure 10.18). The power law dependences of the dispersion of the distribution of gradient orientations were obtained by Lazarian et al. ([285]) and used there to determine the distribution of M_A from observations. The results of the analysis of the GALFA HI data are shown in the lower panel of Figure 10.18. This is the first application of the technique and we expect that the accuracy of it will increase. For instance, the variations of the galactic magnetic field directions that are not arising from turbulence can increase measured M_A as compared to its actual value. This effect can be taken into account to increase the accuracy of the technique.

5 The IGs should be distinguished from the Histograms of Relative Orientation (HRO) technique (see [401]). The latter statitically quantifies the relative alignment of density gradients and polarization and does not present a new way of tracing either magnetic fields of shocks.

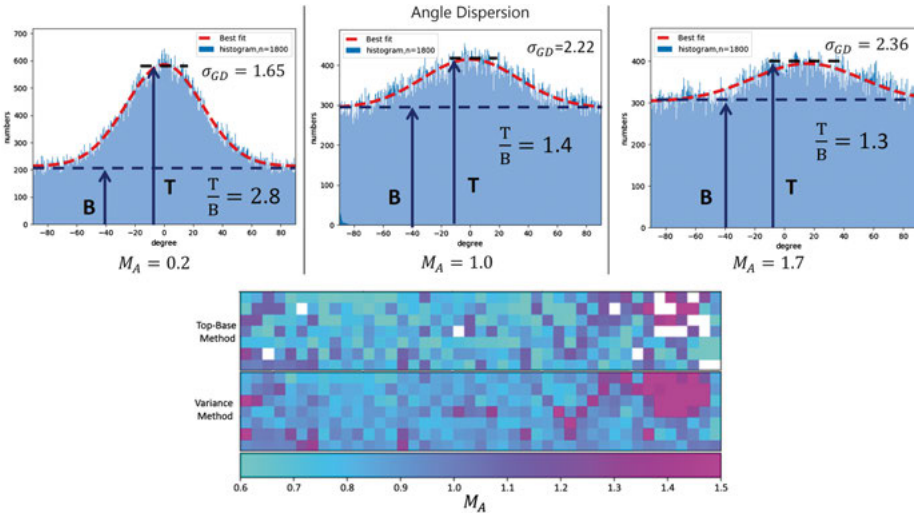

Figure 10.18: *Upper panels*: The panels here show the velocity channel gradients (VChGs) distribution for three numerical cubes with different M_A. Both the angle dispersion of gradients and the top/base, i. e. T/B, ratio are changing with M_A. *Lower panel:* M_A distribution obtained by applying the gradient dispersion technique to HI data from [95, 355]. Reproduced from [285].

The physical basis of the velocity and synchrotron gradient techniques are the same. Therefore the approaches proven with velocity gradients can be applied to synchrotron gradients. Threfore the procedure of using the distribution of velocity gradient to determine M_A can be successfully applied to find the magnetization using distribution of synchrotron intensities and synchrotron polarization gradients. At the same time, we expect the distribution of density gradients to depend both on M_A and on the sonic Mach number M_s.

In the situations when both M_A and the turbulent velocity dispersion δV are known, it is possible to obtain magnetic field strength from the relation $M_A = \delta B/B$. For Alfvenic motions $\delta V = \delta B/(4\pi\rho)^{1/2}$, one can express the plane of the sky magnetic field as $B \approx \sqrt{4\pi\rho}\delta V/M_A$.

10.5.6 Probing magnetic fields with different types of gradients

The gradient technique that we have discussed above is a good illustration of the utility of both understanding the basic properties of MHD turbulence and the ability to describe the observable fluctuations that MHD turbulence induces. Figure 10.19 illustrates the relation between the fundamental MHD theory and the gradient technique.

Interstellar media is complex and the interrelation of magnetic fields in different phases of the ISM is far from trivial. Different types of gradients are biased to preferential probing turbulence and magnetic fields in particular ISM phases. Therefore,

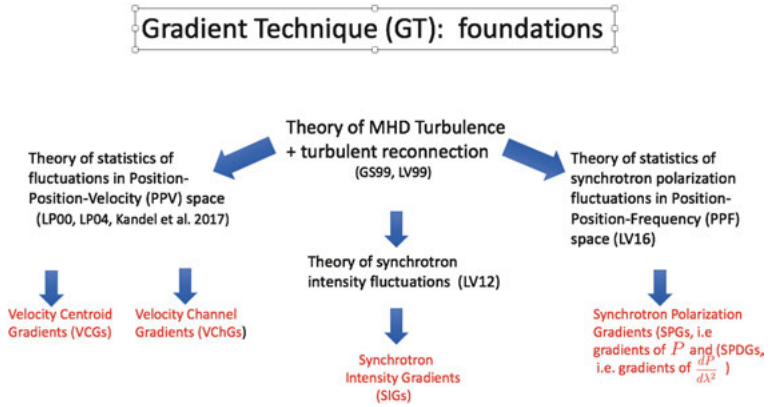

Figure 10.19: The theoretical foundations of the gradient technique. The advances of MHD turbulence theory and understanding of turbulent reconnection as well as the statistical description of observable turbulent fluctuations provide the solid foundations for tracing magnetic fields with velocity and synchrotron gradients.

combining the different types of gradients we expect to get an outlook on magnetized ISM in its complexity.

It is important that both velocity and synchrotron polarization gradients can provide the information about the 3D magnetic field structure. This opens a unique possibility of obtaining the 3D map of galactic magnetic field and explore its role in the galactic ecosystem.

10.6 Synergy of different approaches

We have discussed the ways of studying turbulence spectra, turbulence magnetization, composition of turbulent motions in terms of Alfven, slow and fast modes, as well as the ways of using MHD turbulence properties for mapping magnetic field distribution. Each of these ways provides important information and combining those we can get a global picture how the turbulent ISM works. Correlating properties of magnetic turbulence with other types of data, e. g., the data on the star formation activity, one can address long standing puzzles of astrophysical research. At the same time, obtaining the statistics of astrophysical turbulence from observations can test the properties of MHD turbulence at the extremely large Reynolds and Lundquist numbers that will not be available for numerical simulations in the foreseeable future.

We note that unlike the studies of turbulence in solar wind, which requires very expensive space missions, the analysis of the data that we described in this chapter may employ ground based observations and in many cases can be based on the existing archival data. One should also remember that the observations can probe turbulence

at much larger variety of conditions and scales compared to the in-situ measurements with spacecrafts.

Observational studies of turbulence is an essential component of the efforts to understand astrophysical MHD turbulence and its consequences. Other components include theoretical and numerical efforts as it is illustrated in Figure 10.20. We want to stress the importance of numerics for testing both turbulence theory and simulating observational settings. At the same time, numerics is not a substitution for theory. For instance, a tremendous progress that was initiated by GS95 theory would not be possible using just brute force numerical efforts. Similarly, the understanding of turbulent reconnection, as we discussed earlier, allows to understand what features of numerical simulations correspond to astrophysical reality and what features are just a numerical artifact.

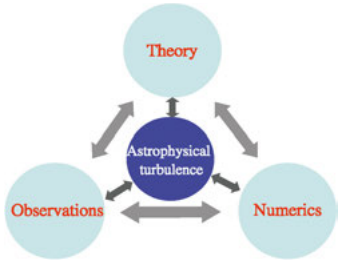

Figure 10.20: Big picture: interrelation between the approaches to studying astrophysical turbulence from [260].

We believe that the synergetic use of theoretical, observational, and numerical approaches in dealing with the complexity of astrophysical turbulence can bring success in this important direction of astrophysical research.

Bibliography

[1] A. Abdo, M. Ackermann, M. Ajello, A. Allafort, L. Baldini, J. Ballet, G. Barbiellini, D. Bastieri, K. Bechtol, R. Bellazzini et al., Gamma-ray flares from the Crab Nebula, *Science* **331** (2011), 739–742.

[2] F. Aharonian et al., Primary particle acceleration above 100 TeV in the shell-type supernova remnant <ASTROBJ>RX J1713.7-3946</ASTROBJ> with deep HESS observations, *Astron. Astrophys.* **464** (2007), 235–243.

[3] Y. Aikawa and H. Nomura, Observations and modeling of gaseous protoplanetary disks, *Phys. Scr. T* **130** (2008), 014011.

[4] Akrami Y., et al., arXiv preprint arXiv:1801.04945 (2018).

[5] J. Aleksić et al., MAGIC discovery of very high energy emission from the FSRQ PKS 1222+21, *Astrophys. J. Lett.* **730** (2011), L8.

[6] A. Alexakis, P. D. Mininni and A. Pouquet, Shell-to-shell energy transfer in magnetohydrodynamics. I. Steady state turbulence, *Phys. Rev. E* **72** (2005), 046301.

[7] H. Alfvén, Remarks on the rotation of a magnetized sphere with application to solar rotation, *Ark. Astron.* **28** (1942), 1–9.

[8] H. Alfven, On frozen-in field lines and field-line reconnection, *J. Geophys. Res.* **81** (1976), 4019–4021.

[9] H. Aluie and G. L. Eyink, Scale locality of magnetohydrodynamic turbulence, *Phys. Rev. Lett.* **104** (2010), 081101.

[10] A. M. Anile, *Relativistic Fluids and Magneto-Fluids*, February 1990.

[11] J. W. Armstrong, B. J. Rickett and S. R. Spangler, Electron density power spectrum in the local interstellar medium, *Astrophys. J.* **443** (1995), 209–221.

[12] S. J. Arthur, S.-N. X. Medina and W. J. Henney, Turbulence in the ionized gas of the Orion nebula, *Mon. Not. R. Astron. Soc.* **463** (2016), 2864–2884.

[13] J. Ballesteros-Paredes, R. S. Klessen, M.-M. Mac Low and E. Vazquez-Semadeni, Molecular cloud turbulence and star formation, in: *Protostars and Planets V*, pp. 63–80, 2007.

[14] A. M. Beck, H. Lesch, K. Dolag, H. Kotarba, A. Geng and F. A. Stasyszyn, Origin of strong magnetic fields in Milky Way-like galactic haloes, *Mon. Not. R. Astron. Soc.* **422** (2012), 2152–2163.

[15] K. Beckwith and J. M. Stone, A second-order Godunov method for multi-dimensional relativistic magnetohydrodynamics, *Astrophys. J. Suppl. Ser.* **193** (2011), 6.

[16] M. C. Begelman and A. C. Fabian, Turbulent mixing layers in the interstellar and intracluster medium, *Mon. Not. R. Astron. Soc.* **244** (1990), 26P–29P.

[17] A. Begum, J. N. Chengalur and S. Bhardwaj, Power spectrum of HI intensity fluctuations in DDO 210, *Mon. Not. R. Astron. Soc.* **372** (2006), L33–L37.

[18] A. R. Bell, The acceleration of cosmic rays in shock fronts. I, *Mon. Not. R. Astron. Soc.* **182** (1978), 147–156.

[19] A. R. Bell, Turbulent amplification of magnetic field and diffusive shock acceleration of cosmic rays, *Mon. Not. R. Astron. Soc.* **353** (2004), 550–558.

[20] R. Benzi, M. V. Struglia and R. Tripiccione, Extended self similarity in numerical simulations of 3D anisotropic turbulence, in: *eprint arXiv:chao-dyn/9509018*, p. 9018, September 1995.

[21] A. Beresnyak, Spectral slope and Kolmogorov constant of MHD turbulence, *Phys. Rev. Lett.* **106** (2011), 075001.

[22] A. Beresnyak, Basic properties of magnetohydrodynamic turbulence in the inertial range, *Mon. Not. R. Astron. Soc.* **422** (2012), 3495–3502.

[23] A. Beresnyak, Universal nonlinear small-scale dynamo, *Phys. Rev. Lett.* **108** (2012), 035002.

https://doi.org/10.1515/9783110263282-011

[24] A. Beresnyak, Asymmetric diffusion of magnetic field lines, *Astrophys. J. Lett.* **767** (2013), L39.
[25] A. Beresnyak, Spectra of strong magnetohydrodynamic turbulence from high-resolution simulations, *Astrophys. J. Lett.* **784** (2014), L20.
[26] A. Beresnyak, On the parallel spectrum in magnetohydrodynamic turbulence, *Astrophys. J. Lett.* **801** (2015), L9.
[27] A. Beresnyak, Three-dimensional spontaneous magnetic reconnection, *Astrophys. J.* **834** (2017), 47.
[28] A. Beresnyak, T. W. Jones and A. Lazarian, Turbulence-induced magnetic fields and structure of cosmic ray modified shocks, *Astrophys. J.* **707** (2009), 1541–1549.
[29] A. Beresnyak and A. Lazarian, Polarization intermittency and its influence on MHD turbulence, *Astrophys. J. Lett.* **640** (2006), L175–L178.
[30] A. Beresnyak and A. Lazarian, Strong imbalanced turbulence, *Astrophys. J.* **682** (2008), 1070–1075.
[31] A. Beresnyak and A. Lazarian, Wave decay in magnetohydrodynamic turbulence, *Astrophys. J.* **678** (2008), 961–967.
[32] A. Beresnyak and A. Lazarian, Comparison of spectral slopes of magnetohydrodynamic and hydrodynamic turbulence and measurements of alignment effects, *Astrophys. J.* **702** (2009), 1190–1198.
[33] A. Beresnyak and A. Lazarian, Structure of stationary strong imbalanced turbulence, *Astrophys. J.* **702** (2009), 460–471.
[34] A. Beresnyak and A. Lazarian, Scaling laws and diffuse locality of balanced and imbalanced magnetohydrodynamic turbulence, *Astrophys. J. Lett.* **722** (2010), L110–L113.
[35] A. Beresnyak and H. Li, Basic Bell-MHD Turbulence, *Astrophys. J.* **788** (2014), 107.
[36] A. Beresnyak and A. Lazarian, MHD turbulence, turbulent dynamo and applications, in: *Magnetic Fields in Diffuse Media* (A. Lazarian, E. M. de Gouveia Dal Pino and C. Melioli, eds.), Astrophysics and Space Science Library 407, p. 163, 2015.
[37] A. Beresnyak, A. Lazarian and J. Cho, Density scaling and anisotropy in supersonic magnetohydrodynamic turbulence, *Astrophys. J. Lett.* **624** (2005), L93–L96.
[38] A. Beresnyak and H. Li, First-order particle acceleration in magnetically-driven flows, *Astrophys. J.* **819** (2016), 90.
[39] A. Beresnyak and F. Miniati, Turbulent amplification and structure of the intracluster magnetic field, *Astrophys. J.* **817** (2016), 127.
[40] A. Beresnyak, H. Xu, H. Li and R. Schlickeiser, Magnetohydrodynamic turbulence and cosmic-ray reacceleration in galaxy clusters, *Astrophys. J.* **771** (2013), 131.
[41] A. Beresnyak, H. Yan and A. Lazarian, Numerical study of cosmic ray diffusion in magnetohydrodynamic turbulence, *Astrophys. J.* **728** (2011), 60.
[42] J. Berg, B. Lüthi, J. Mann and S. Ott, Backwards and forwards relative dispersion in turbulent flow: an experimental investigation, *Phys. Rev. E* **74** (2006), 016304.
[43] D. Biskamp, Magnetic reconnection via current sheets, *Phys. Fluids* **29** (1986), 1520–1531.
[44] D. Biskamp, *Magnetohydrodynamic Turbulence*, Cambridge University Press, Cambridge, September 2003.
[45] R. D. Blandford and J. P. Ostriker, Particle acceleration by astrophysical shocks, *Astrophys. J. Lett.* **221** (1978), L29–L32.
[46] R. D. Blandford and R. L. Znajek, Electromagnetic extraction of energy from Kerr black holes, *Mon. Not. R. Astron. Soc.* **179** (1977), 433–456.
[47] S. Boldyrev, Kolmogorov-Burgers model for star-forming turbulence, *Astrophys. J.* **569** (2002), 841–845.
[48] S. Boldyrev, On the spectrum of magnetohydrodynamic turbulence, *Astrophys. J. Lett.* **626** (2005), L37–L40.

[49] S. Boldyrev, Spectrum of magnetohydrodynamic turbulence, *Phys. Rev. Lett.* **96** (2006), 115002.
[50] A. Bonafede, L. Feretti, M. Murgia, F. Govoni, G. Giovannini, D. Dallacasa, K. Dolag and G. B. Taylor, The Coma cluster magnetic field from Faraday rotation measures, *Astron. Astrophys.* **513** (2010), A30.
[51] A. H. Boozer, Separation of magnetic field lines, *Phys. Plasmas* **19** (2012), 112901.
[52] A. H. Boozer, Tokamak halo currents, *Phys. Plasmas* **20** (2013), 082510.
[53] J. E. Borovsky, Contribution of strong discontinuities to the power spectrum of the solar wind, *Phys. Rev. Lett.* **105** (2010), 111102.
[54] F. R. Bouchet and R. Gispert, Foregrounds and CMB experiments. I. Semi-analytical estimates of contamination, *New Astron.* **4** (1999), 443–479.
[55] F. R. Bouchet, R. Gispert and J.-L. Puget, The mm/sub-mm foregrounds and future CMB space missions, in: *American Institute of Physics Conference Series* (E. Dwek, ed.), American Institute of Physics Conference Series 348, pp. 255–268, 1996.
[56] A. Brandenburg and K. Subramanian, Astrophysical magnetic fields and nonlinear dynamo theory, *Phys. Rep.* **417** (2005), 1–209.
[57] M. A. Brentjens and A. G. de Bruyn, Faraday rotation measure synthesis, *Astron. Astrophys.* **441** (2005), 1217–1228.
[58] G. Brunetti and A. Lazarian, Compressible turbulence in galaxy clusters: physics and stochastic particle re-acceleration, *Mon. Not. R. Astron. Soc.* **378** (2007), 245–275.
[59] G. Brunetti and A. Lazarian, Acceleration of primary and secondary particles in galaxy clusters by compressible MHD turbulence: from radio haloes to gamma-rays, *Mon. Not. R. Astron. Soc.* **410** (2011), 127–142.
[60] G. Brunetti and A. Lazarian, Particle reacceleration by compressible turbulence in galaxy clusters: effects of a reduced mean free path, *Mon. Not. R. Astron. Soc.* **412** (2011), 817–824.
[61] R. Bruno and V. Carbone, The solar wind as a turbulence laboratory, *Living Rev. Sol. Phys.* **2** (2005), 4.
[62] B. Burkhart, A. Lazarian, A. Goodman and E. Rosolowsky, Hierarchical structure of magnetohydrodynamic turbulence in position-position-velocity space, *Astrophys. J.* **770** (2013), 141.
[63] B. Burkhart, A. Lazarian, I. C. Leão, J. R. de Medeiros and A. Esquivel, Measuring the Alfvénic nature of the interstellar medium: velocity anisotropy revisited, *Astrophys. J.* **790** (2014), 130.
[64] L. F. Burlaga, R. P. Lepping, K. W. Behannon, L. W. Klein and F. M. Neubauer, Large-scale variations of the interplanetary magnetic field - Voyager 1 and 2 observations between 1–5 AU, *J. Geophys. Res.* **87** (1982), 4345–4353.
[65] A. Busse, W.-C. Müller and G. Gogoberidze, Lagrangian frequency spectrum as a diagnostic for magnetohydrodynamic turbulence dynamics, *Phys. Rev. Lett.* **105** (2010), 235005.
[66] A. M. Bykov, S. M. Osipov and D. C. Ellison, Cosmic ray current driven turbulence in shocks with efficient particle acceleration: the oblique, long-wavelength mode instability, *Mon. Not. R. Astron. Soc.* **410** (2011), 39–52.
[67] R. R. Caldwell, C. Hirata and M. Kamionkowski, Dust-polarization maps and interstellar turbulence, *Astrophys. J.* **839** (2017), 91.
[68] D. Casanova, A. Lazarian and R. Santos-Lima, *Astrophys. J.*, in press (2015).
[69] G. Cassam-Chenaï, J. P. Hughes, J. Ballet and A. Decourchelle, The blast wave of Tycho's supernova remnant, *Astrophys. J.* **665** (2007), 315.
[70] B. D. G. Chandran, Scattering of energetic particles by anisotropic magnetohydrodynamic turbulence with a Goldreich-Sridhar power spectrum, *Phys. Rev. Lett.* **85** (2000), 4656–4659.
[71] B. D. G. Chandran, Strong anisotropic MHD turbulence with cross helicity, *Astrophys. J.* **685** (2008), 646–658.

[72] B. D. G. Chandran and S. C. Cowley, Thermal conduction in a tangled magnetic field, *Phys. Rev. Lett.* **80** (1998), 3077–3080.

[73] C. Chen, S. Bale, C. Salem and B. Maruca, Residual energy spectrum of solar wind turbulence, *Astrophys. J.* **770** (2013), 125.

[74] A. Chepurnov, B. Burkhart, A. Lazarian and S. Stanimirovic, The turbulence velocity power spectrum of neutral hydrogen in the small magellanic cloud, *Astrophys. J.* **810** (2015), 33.

[75] A. Chepurnov and A. Lazarian, Turbulence spectra from doppler-broadened spectral lines: tests of the velocity channel analysis and velocity coordinate spectrum techniques, *Astrophys. J.* **693** (2009), 1074–1083.

[76] A. Chepurnov and A. Lazarian, Extending the big power law in the sky with turbulence spectra from Wisconsin Hα Mapper data, *Astrophys. J.* **710** (2010), 853–858.

[77] C. Chiappini, U. Frischknecht, G. Meynet, R. Hirschi, B. Barbuy, M. Pignatari, T. Decressin and A. Maeder, Imprints of fast-rotating massive stars in the Galactic Bulge, *Nature* **472** (2011), 454–457.

[78] J. Cho, Simulations of relativistic force-free magnetohydrodynamic turbulence, *Astrophys. J.* **621** (2005), 324–327.

[79] J. Cho, Non-locality of hydrodynamic and magnetohydrodynamic turbulence, *Astrophys. J.* **725** (2010), 1786–1791.

[80] J. Cho, Properties of balanced and imbalanced relativistic Alfvénic magnetohydrodynamic turbulence, *J. Korean Phys. Soc.* **65** (2014), 871–875.

[81] J. Cho and A. Lazarian, Compressible sub-Alfvénic MHD turbulence in low-β plasmas, *Phys. Rev. Lett.* **88** (2002), 245001.

[82] J. Cho and A. Lazarian, Compressible magnetohydrodynamic turbulence: mode coupling, scaling relations, anisotropy, viscosity-damped regime and astrophysical implications, *Mon. Not. R. Astron. Soc.* **345** (2003), 325–339.

[83] J. Cho and A. Lazarian, Compressible MHD turbulence: mode coupling, anisotropies, and scalings, in: *Revista Mexicana de Astronomia y Astrofisica Conference Series* (J. Arthur and W. J. Henney, eds.), Revista Mexicana de Astronomia y Astrofisica Conference Series 15, pp. 293–298, January 2003.

[84] J. Cho and A. Lazarian, The anisotropy of electron magnetohydrodynamic turbulence, *Astrophys. J. Lett.* **615** (2004), L41–L44.

[85] J. Cho and A. Lazarian, Particle acceleration by magnetohydrodynamic turbulence, *Astrophys. J.* **638** (2006), 811–826.

[86] J. Cho and A. Lazarian, Simulations of electron magnetohydrodynamic turbulence, *Astrophys. J.* **701** (2009), 236–252.

[87] J. Cho and A. Lazarian, Imbalanced relativistic force-free magnetohydrodynamic turbulence, *Astrophys. J.* **780** (2014), 30.

[88] J. Cho, A. Lazarian and E. T. Vishniac, New regime of magnetohydrodynamic turbulence: cascade below the viscous cutoff, *Astrophys. J. Lett.* **566** (2002), L49–L52.

[89] J. Cho, A. Lazarian and E. T. Vishniac, Simulations of magnetohydrodynamic turbulence in a strongly magnetized medium, *Astrophys. J.* **564** (2002), 291–301.

[90] J. Cho, A. Lazarian and E. T. Vishniac, MHD turbulence: scaling laws and astrophysical implications, in: *Turbulence and Magnetic Fields in Astrophysics* (E. Falgarone and T. Passot, eds.), Lecture Notes in Physics 614, Springer Verlag, Berlin, pp. 56–98, 2003.

[91] J. Cho, A. Lazarian and E. T. Vishniac, Ordinary and viscosity-damped magnetohydrodynamic turbulence, *Astrophys. J.* **595** (2003), 812–823.

[92] J. Cho and E. T. Vishniac, The anisotropy of magnetohydrodynamic Alfvénic turbulence, *Astrophys. J.* **539** (2000), 273–282.

[93] J. Cho, E. T. Vishniac, A. Beresnyak, A. Lazarian and D. Ryu, Growth of magnetic fields induced by turbulent motions, *Astrophys. J.* **693** (2009), 1449–1461.
[94] A. Ciaravella and J. C. Raymond, The current sheet associated with the 2003 November 4 coronal mass ejection: density, temperature, thickness, and line width, *Astrophys. J.* **686** (2008), 1372–1382.
[95] S. E. Clark, J. C. Hill, J. E. G. Peek, M. E. Putman and B. L. Babler, *Phys. Rev. Lett.* **115** (2015), 241302.
[96] S. E. Clark, *Magnetic fields in the interstellar medium*, Ph.D. thesis, Columbia University, 2017.
[97] S. E. Clark, A new probe of line-of-sight magnetic field tangling, *Astrophys. J. Lett.* **857** (2018), 10.
[98] T. E. Clarke, P. P. Kronberg and H. Böhringer, A new radio-X-ray probe of galaxy cluster magnetic fields, *Astrophys. J.* **547** (2001), L111–L114.
[99] T. E. Clarke, Faraday rotation observations of magnetic fields in galaxy clusters, *J. Korean Astron. Soc.* **37** (2004), 337–342.
[100] E. Clausen-Brown and M. Lyutikov, Crab nebula gamma-ray flares as relativistic reconnection minijets, *Mon. Not. R. Astron. Soc.* **426** (2012), 1374–1384.
[101] S. Corrsin, Estimates of the relations between Eulerian and Lagrangian scales in large Reynolds number turbulence., *J. Atmos. Sci.* **20** (1963), 115–119.
[102] J. Crovisier and J. M. Dickey, The spatial power spectrum of galactic neutral hydrogen from observations of the 21-cm emission line, *Astron. Astrophys.* **122** (1983), 282–296.
[103] R. M. Crutcher, B. Wandelt, C. Heiles, E. Falgarone and T. H. Troland, Magnetic fields in interstellar clouds from zeeman observations: inference of total field strengths by Bayesian analysis, *Astrophys. J.* **725** (2010), 466–479.
[104] R. M. Crutcher, Magnetic fields in molecular clouds, *Annu. Rev. Astron. Astrophys.* **50** (2012), 29–63.
[105] J. T. Dahlin, J. F. Drake and M. Swisdak, The mechanisms of electron heating and acceleration during magnetic reconnection, *Phys. Plasmas* **21** (2014), 092304.
[106] S. Das, S. Mukherjee and T. Souradeep, Revised cosmological parameters after BICEP 2 and BOSS, *J. Cosmol. Astropart. Phys.* **2** (2015), 016.
[107] W. Daughton, V. Roytershteyn, B. Albright, H. Karimabadi, L. Yin and K. Bowers, Transition from collisional to kinetic regimes in large-scale reconnection layers, *Phys. Rev. Lett.* **103** (2009), 65004.
[108] W. Daughton, V. Roytershteyn, H. Karimabadi, L. Yin, B. J. Albright, B. Bergen and K. J. Bowers, Role of electron physics in the development of turbulent magnetic reconnection in collisionless plasmas, *Nat. Phys.* **7** (2011), 539–542.
[109] W. Daughton, J. Scudder and H. Karimabadi, Fully kinetic simulations of undriven magnetic reconnection with open boundary conditions, *Phys. Plasmas* **13** (2006), 072101.
[110] E. M. de Gouveia Dal Pino and G. Kowal, Particle acceleration by magnetic reconnection, in: *Astrophysics and Space Science Library* (A. Lazarian, E. M. de Gouveia Dal Pino and C. Melioli, eds.), Astrophysics and Space Science Library 407, p. 373, 2015.
[111] E. M. de Gouveia dal Pino and A. Lazarian, Production of the large scale superluminal ejections of the microquasar GRS 1915+105 by violent magnetic reconnection, *Astron. Astrophys.* **441** (2005), 845–853.
[112] A. A. Deshpande, K. S. Dwarakanath and W. M. Goss, Power spectrum of the density of cold atomic gas in the galaxy toward Cassiopeia A and Cygnus A, *Astrophys. J.* **543** (2000), 227–234.
[113] P. H. Diamond and M. A. Malkov, Dynamics of mesoscale magnetic field in diffusive shock acceleration, *Astrophys. J.* **654** (2007), 252–266.

[114] J. M. Dickey, N. M. McClure-Griffiths, S. Stanimirović, B. M. Gaensler and A. J. Green, Southern galactic plane survey measurements of the spatial power spectrum of interstellar H I in the inner galaxy, *Astrophys. J.* **561** (2001), 264–271.

[115] R. L. Dickman and S. C. Kleiner, Largescale structure of the taurus molecular complex – Part three – Methods for turbulence, *Astrophys. J.* **295** (1985), 479.

[116] M. Dobrowolny, A. Mangeney and P. Veltri, Fully developed anisotropic hydromagnetic turbulence in interplanetary space, *Phys. Rev. Lett.* **45** (1980), 144–147.

[117] K. Dolag, M. Bartelmann and H. Lesch, Evolution and structure of magnetic fields in simulated galaxy clusters, *Astron. Astrophys.* **387** (2002), 383–395.

[118] K. Dolag, F. Stasyszyn, J. Donnert and R. Pakmor, Magnetic fields and cosmic rays in galaxy clusters and large scale structures, in: *Cosmic Magnetic Fields: From Planets, to Stars and Galaxies* (K. G. Strassmeier, A. G. Kosovichev and J. E. Beckman, eds.), IAU Symposium 259, pp. 519–528, April 2009.

[119] B. T. Draine, *Physics of the Interstellar and Intergalactic Medium*, 2011.

[120] B. T. Draine and A. Lazarian, Magnetic dipole microwave emission from dust grains, *Astrophys. J.* **512** (1999), 740–754.

[121] J. F. Drake, Magnetic explosions in space, *Nature* **410** (2001), 525–526.

[122] J. F. Drake, M. Swisdak, H. Che and M. A. Shay, Electron acceleration from contracting magnetic islands during reconnection, *Nature* **443** (2006), 553–556.

[123] G. Drenkhahn and H. C. Spruit, Efficient acceleration and radiation in Poynting flux powered GRB outflows, *Astron. Astrophys.* **391** (2002), 1141–1153.

[124] L. O. Drury, First-order Fermi acceleration driven by magnetic reconnection, *Mon. Not. R. Astron. Soc.* **422** (2012), 2474–2476.

[125] L. O. Drury, P. Duffy, D. Eichler and A. Mastichiadis, On "box" models of shock acceleration and electron synchrotron spectra, *Astron. Astrophys.* **347** (1999), 370–374.

[126] Y. Dubois and R. Teyssier, Cosmological MHD simulation of a cooling flow cluster, *Astron. Astrophys.* **482** (2008), L13–L16.

[127] B. Dubrulle, Intermittency in fully developed turbulence: log-Poisson statistics and generalized scale covariance, *Phys. Rev. Lett.* **73** (1994), 959–962.

[128] J. A. Eilek and F. N. Owen, Magnetic fields in cluster cores: Faraday rotation in A400 and A2634, *Astrophys. J.* **567** (2002), 202–220.

[129] B. G. Elmegreen and J. Scalo, Interstellar turbulence I: observations and processes, *Annu. Rev. Astron. Astrophys.* **42** (2004), 211–273.

[130] T. Enßlin, C. Vogt and C. Pfrommer, Magnetic fields in clusters of galaxies, in: *The Magnetized Plasma in Galaxy Evolution* (K. T. Chyzy, K. Otmianowska-Mazur, M. Soida and R.-J. Dettmar, eds.), pp. 231–238, June 2005.

[131] T. A. Enßlin and C. Vogt, Magnetic turbulence in cool cores of galaxy clusters, *Astron. Astrophys.* **453** (2006), 447–458.

[132] A. Esquivel and A. Lazarian, Velocity centroids as tracers of the turbulent velocity statistics, *Astrophys. J.* **631** (2005), 320–350.

[133] A. Esquivel and A. Lazarian, Velocity anisotropy as a diagnostic of the magnetization of the interstellar medium and molecular clouds, *Astrophys. J.* **740** (2011), 117.

[134] A. Esquivel, A. Lazarian, S. Horibe, J. Cho, V. Ossenkopf and J. Stutzki, Statistics of velocity centroids: effects of density-velocity correlations and non-Gaussianity, *Mon. Not. R. Astron. Soc.* **381** (2007), 1733–1744.

[135] A. Esquivel, A. Lazarian and D. Pogosyan, Studying the interstellar magnetic field from anisotropies in velocity channels, *Astrophys. J.* **814** (2015), 77.

[136] A. Esquivel, A. Lazarian, D. Pogosyan and J. Cho, Velocity statistics from spectral line data: effects of density-velocity correlations, magnetic field and shear, *Mon. Not. R. Astron. Soc.* **342** (2003), 325–336.
[137] G. Eyink, E. Vishniac, C. Lalescu, H. Aluie, K. Kanov, K. Bürger, R. Burns, C. Meneveau and A. Szalay, Flux-freezing breakdown in high-conductivity magnetohydrodynamic turbulence, *Nature* **497** (2013), 466–469.
[138] G. L. Eyink, Locality of turbulent cascades, *Physica D* **207** (2005), 91–116.
[139] G. L. Eyink, Fluctuation dynamo and turbulent induction at small Prandtl number, *Phys. Rev. E* **82** (2010), 046314.
[140] G. L. Eyink, Stochastic flux freezing and magnetic dynamo, *Phys. Rev. E* **83** (2011), 056405.
[141] G. L. Eyink, Turbulent general magnetic reconnection, *ArXiv e-prints* (2014).
[142] G. L. Eyink, Turbulent general magnetic reconnection, *Astrophys. J.* **807** (2015), 137.
[143] G. L. Eyink, A. Lazarian and E. T. Vishniac, Fast magnetic reconnection and spontaneous stochasticity, *Astrophys. J.* **743** (2011), 51.
[144] A. C. Fabian, Cooling flows in clusters of galaxies, *Annu. Rev. Astron. Astrophys.* **32** (1994), 277–318.
[145] A. C. Fabian, R. F. Mushotzky, P. E. J. Nulsen and J. R. Peterson, On the soft X-ray spectrum of cooling flows, *Mon. Not. R. Astron. Soc.* **321** (2001), L20–L24.
[146] D. Falceta-Gonçalves and G. Kowal, Fast magnetic field amplification in the early universe: growth of collisionless plasma instabilities in turbulent media, *Astrophys. J.* **808** (2015), 65.
[147] E. Falgarone, G. Pineau des Forets and E. Roueff, Chemical signatures of the intermittency of turbulence in low density interstellar clouds, *Astron. Astrophys.* **300** (1995), 870.
[148] A. J. Farmer and P. Goldreich, Wave damping by magnetohydrodynamic turbulence and its effect on cosmic-ray propagation in the interstellar medium, *Astrophys. J.* **604** (2004), 671–674.
[149] M. Fatuzzo and F. C. Adams, Enhancement of ambipolar diffusion rates through field fluctuations, *Astrophys. J.* **570** (2002), 210–221.
[150] L. Feretti, D. Dallacasa, F. Govoni, G. Giovannini, G. B. Taylor and U. Klein, The radio galaxies and the magnetic field in Abell 119, *Astron. Astrophys.* **344** (1999), 472–482.
[151] E. Fermi, On the origin of the cosmic radiation, *Phys. Rev.* **75** (1949), 1169–1174.
[152] C. Ferrari, F. Govoni, S. Schindler, A. M. Bykov and Y. Rephaeli, Observations of extended radio emission in clusters, *Space Sci. Rev.* **134** (2008), 93–118.
[153] U. Frisch, *Turbulence. The legacy of A. N. Kolmogorov.*, Cambridge University Press, 1995.
[154] X. Fu, Q. Lu and S. Wang, The process of electron acceleration during collisionless magnetic reconnection, *Phys. Plasmas (1994-present)* **13** (2006), 012309.
[155] A. Galeev and R. Sagdeev, Theory of neoclassical diffusion, in: *Reviews of Plasma Physics, Volume 7*, p. 257, 1979.
[156] D. Galli, S. Lizano, F. H. Shu and A. Allen, Gravitational collapse of magnetized clouds. I. Ideal magnetohydrodynamic accretion flow, *Astrophys. J.* **647** (2006), 374–381.
[157] K. Galsgaard and Å. Nordlund, Heating and activity of the solar corona. 3. Dynamics of a low beta plasma with three-dimensional null points, *J. Geophys. Res.* **102** (1997), 231–248.
[158] S. Galtier, S. V. Nazarenko, A. C. Newell and A. Pouquet, A weak turbulence theory for incompressible magnetohydrodynamics, *J. Plasma Phys.* **63** (2000), 447–488.
[159] S. Galtier, A. Pouquet and A. Mangeney, On spectral scaling laws for incompressible anisotropic magnetohydrodynamic turbulence, *Phys. Plasmas* **12** (2005), 092310.
[160] D. Garrison and P. Nguyen, Characterization of relativistic MHD turbulence, *ArXiv e-prints* (2015).
[161] C. L. Gerrard and A. W. Hood, Kink unstable coronal loops: current sheets, current saturation and magnetic reconnection, *Sol. Phys.* **214** (2003), 151–169.

[162] G. G. Getmantsev, The determination of the mean dimensions of magnetized clouds of interstellar gas by radioastronomical methods, *Soviet Astronomy* **3** (1959), 415.
[163] G. Giacinti, M. Kachelrieß and D. V. Semikoz, Filamentary diffusion of cosmic rays on small scales, *Phys. Rev. Lett.* **108** (2012), 261101.
[164] D. Giannios, Prompt GRB emission from gradual energy dissipation, *Astron. Astrophys.* **480** (2008), 305–312.
[165] D. Giannios, UHECRs from magnetic reconnection in relativistic jets, *Mon. Not. R. Astron. Soc.* **408** (2010), L46–L50.
[166] D. Giannios, Reconnection-driven plasmoids in blazars: fast flares on a slow envelope, *Mon. Not. R. Astron. Soc.* **431** (2013), 355–363.
[167] D. Giannios and H. C. Spruit, The role of kink instability in Poynting-flux dominated jets, *Astron. Astrophys.* **450** (2006), 887–898.
[168] G. Giardino, A. J. Banday, K. Bennett, P. Fosalba, K. M. Górski, W. O'Mullane, J. Tauber and C. Vuerli, Analysis of CMB foregrounds using a database for Planck, in: *Mining the Sky* (A. J. Banday, S. Zaroubi and M. Bartelmann, eds.), p. 458, 2001.
[169] G. Giardino, A. J. Banday, P. Fosalba, K. M. Górski, J. L. Jonas, W. O'Mullane and J. Tauber, The angular power spectrum of radio emission at 2.3 GHz, *Astron. Astrophys.* **371** (2001), 708–717.
[170] G. Gogoberidze, On the nature of incompressible magnetohydrodynamic turbulence, *Phys. Plasmas* **14** (2007), 022304.
[171] B. Gold, N. Odegard, J. L. Weiland, R. S. Hill, A. Kogut, C. L. Bennett, G. Hinshaw, X. Chen, J. Dunkley, M. Halpern, N. Jarosik, E. Komatsu, D. Larson, M. Limon, S. S. Meyer, M. R. Nolta, L. Page, K. M. Smith, D. N. Spergel, G. S. Tucker, E. Wollack and E. L. Wright, Seven-year Wilkinson Microwave Anisotropy Probe (WMAP) observations: galactic foreground emission, *Astrophys. J.* **192** (2011), 15.
[172] P. Goldreich and S. Sridhar, Toward a theory of interstellar turbulence. 2: strong Alfvenic turbulence, *Astrophys. J.* **438** (1995), 763–775.
[173] B. E. Goldstein, E. J. Smith, A. Balogh, T. S. Horbury, M. L. Goldstein and D. A. Roberts, Properties of magnetohydrodynamic turbulence in the solar wind as observed by Ulysses at high heliographic latitudes, *Geophys. Res. Lett.* **22** (1995), 3393–3396.
[174] D. F. González-Casanova and A. Lazarian, Velocity gradients as a tracer for magnetic fields, *Astrophys. J.* **835** (2017), 41.
[175] D. F. Gonzalez-Casanova and A. Lazarian, Mapping of the structure of the galactic magnetic field with velocity gradients: Test using star light polarization, *ArXiv e-prints* arXiv:1805.10329 (2018).
[176] D. F. González-Casanova, A. Lazarian and R. Santos-Lima, Magnetic fields in early protostellar disk formation, *Astrophys. J.* **819** (2016), 96.
[177] J. Goodman and R. Narayan, Slow pulsar scintillation and the spectrum of interstellar electron density fluctuations, *Mon. Not. R. Astron. Soc.* **214** (1985), 519–537.
[178] J. T. Gosling, Observations of magnetic reconnection in the turbulent high-speed solar wind, *Astrophys. J. Lett.* **671** (2007), L73–L76.
[179] T. Gotoh, D. Fukayama and T. Nakano, Velocity field statistics in homogeneous steady turbulence obtained using a high-resolution direct numerical simulation, *Phys. Fluids* **14** (2002), 1065.
[180] F. Govoni, K. Dolag, M. Murgia, L. Feretti, S. Schindler, G. Giovannini, W. Boschin, V. Vacca and A. Bonafede, Rotation measures of radio sources in hot galaxy clusters, *Astron. Astrophys.* **522** (2010), A105.
[181] F. Govoni, M. Murgia, L. Feretti, G. Giovannini, K. Dolag and G. B. Taylor, The intracluster magnetic field power spectrum in Abell 2255, *Astron. Astrophys.* **460** (2006), 425–438.

[182] R. Grappin, J. Leorat and A. Pouquet, Dependence of MHD turbulence spectra on the velocity field-magnetic field correlation, *Astron. Astrophys.* **126** (1983), 51–58.
[183] R. Grappin and W.-C. Müller, Scaling and anisotropy in magnetohydrodynamic turbulence in a strong mean magnetic field, *Phys. Rev. E* **82** (2010), 026406.
[184] R. Grappin and M. Velli, Waves and streams in the expanding solar wind, *J. Geophys. Res.* **101** (1996), 425–444.
[185] D. A. Green, A power spectrum analysis of the angular scale of Galactic neutral hydrogen emission towards $L = 140$ deg, $B = 0$ deg, *Mon. Not. R. Astron. Soc.* **262** (1993), 327–342.
[186] F. Guo, H. Li, W. Daughton and Y.-H. Liu, Formation of hard power-laws in the energetic particle spectra resulting from relativistic magnetic reconnection, *arXiv:1405.4040* (2014).
[187] X. Guo, J. Mao and J. Wang, Can turbulence dominate depolarization of optical blazars?, *Astrophys. J.* **843** (2017), 23.
[188] N. E. Haugen, A. Brandenburg and W. Dobler, Simulations of nonhelical hydromagnetic turbulence, *Phys. Rev. E* **70** (2004), 016308.
[189] C. Heiles, Tiny-Scale Atomic Structure and the Cold Neutral Medium, *Astrophys. J.* **481** (1997), 193.
[190] F. Heitsch and E. G. Zweibel, Suppression of fast reconnection by magnetic shear, *Astrophys. J.* **590** (2003), 291–295.
[191] F. Heitsch, E. G. Zweibel, A. D. Slyz and J. E. G. Devriendt, Magnetic flux transport in the ISM through turbulent ambipolar diffusion, *Astrophys. Space Sci.* **292** (2004), 45–51.
[192] C. A. Herron, B. Burkhart, A. Lazarian, B. M. Gaensler and N. M. McClure-Griffiths, Radio synchrotron fluctuation statistics as a probe of magnetized interstellar turbulence, *Astrophys. J.* **822** (2016), 13.
[193] M. Heyer, H. Gong, E. Ostriker and C. Brunt, Magnetically aligned velocity anisotropy in the taurus molecular cloud, *Astrophys. J.* **680** (2008), 420–427.
[194] J. C. Higdon, Density fluctuations in the interstellar medium: evidence for anisotropic magnetogasdynamic turbulence. I - Model and astrophysical sites, *Astrophys. J.* **285** (1984), 109–123.
[195] T. S. Horbury, M. Forman and S. Oughton, Anisotropic scaling of magnetohydrodynamic turbulence, *Phys. Rev. Lett.* **101** (2008), 175005.
[196] G. G. Howes, S. C. Cowley, W. Dorland, G. W. Hammett, E. Quataert and A. A. Schekochihin, Astrophysical gyrokinetics: basic equations and linear theory, *Astrophys. J.* **651** (2006), 590–614.
[197] C. Huang, Q. Lu and S. Wang, The mechanisms of electron acceleration in antiparallel and guide field magnetic reconnection, *Phys. Plasmas (1994-present)* **17** (2010), 072306.
[198] Y.-M. Huang and A. Bhattacharjee, Turbulent magnetohydrodynamic reconnection mediated by the plasmoid instability, *Astrophys. J.* **818** (2016), 20.
[199] D. E. Innes, B. Inhester, W. I. Axford and K. Wilhelm, Bi-directional plasma jets produced by magnetic reconnection on the Sun, *Nature* **386** (1997), 811–813.
[200] T. Inoue, K. Asano and K. Ioka, Three-dimensional simulations of magnetohydrodynamic turbulence behind relativistic shock waves and their implications for gamma-ray bursts, *Astrophys. J.* **734** (2011), 77.
[201] P. Iroshnikov, Turbulence of a conducting fluid in a strong magnetic field, *Sov. Astron.* **7** (1964), 566.
[202] E. B. Jenkins, Thermal pressures in neutral clouds inside the local bubble, as determined from C I fine-structure excitations, *Astrophys. J.* **580** (2002), 938–949.
[203] C. M. Johns-Krull, Measurements of magnetic fields on T Tauri stars, in: *Star-Disk Interaction in Young Stars* (J. Bouvier and I. Appenzeller, eds.), IAU Symposium 243, pp. 31–42, May 2007.

[204] J. R. Jokipii, The rate of separation of magnetic lines of force in a random magnetic field, *Astrophys. J.* **183** (1973), 1029–1036.
[205] J. L. Jonas, E. E. Baart and G. D. Nicolson, The Rhodes/HartRAO 2326-MHz radio continuum survey, *Mon. Not. R. Astron. Soc.* **297** (1998), 977–989.
[206] B. B. Kadomtsev and O. P. Pogutse, Nonlinear helical perturbations of a plasma in the tokamak, *Sov. Phys. JETP* **38** (1974), 283.
[207] L. H. S. Kadowaki, E. M. de Gouveia Dal Pino and C. B. Singh, The role of fast magnetic reconnection on the radio and gamma-ray emission from the nuclear regions of microquasars and low luminosity AGNs, *Astrophys. J.* **802** (2015), 113.
[208] D. Kandel, A. Lazarian and D. Pogosyan, Extending velocity channel analysis for studying turbulence anisotropies, *Mon. Not. R. Astron. Soc.* **461** (2016), 1227–1259.
[209] D. Kandel, A. Lazarian and D. Pogosyan, Can the observed E/B ratio for dust galactic foreground be explained by sub-Alfvénic turbulence?, *Mon. Not. R. Astron. Soc.* **472** (2017), L10–L14.
[210] D. Kandel, A. Lazarian and D. Pogosyan, Effects of dust absorption on spectroscopic studies of turbulence, *Mon. Not. R. Astron. Soc.* **470** (2017), 3103–3123.
[211] D. Kandel, A. Lazarian and D. Pogosyan, Statistical properties of galactic CMB foregrounds: dust and synchrotron, *ArXiv e-prints* (2017).
[212] D. Kandel, A. Lazarian and D. Pogosyan, Study of velocity centroids based on the theory of fluctuations in position-position-velocity space, *Mon. Not. R. Astron. Soc.* **464** (2017), 3617–3635.
[213] Y. Kaneda, T. Ishihara, M. Yokokawa, K. Itakura and A. Uno, Energy dissipation rate and energy spectrum in high resolution direct numerical simulations of turbulence in a periodic box, *Phys. Fluids* **15** (2003), L21–L24.
[214] S. A. Kaplan and S. B. Pikelner, *The Interstellar Medium*, 1970.
[215] P. J. Käpylä, M. J. Korpi and A. Brandenburg, Alpha effect and turbulent diffusion from convection, *Astron. Astrophys.* **500** (2009), 633–646.
[216] H. Karimabadi, V. Roytershteyn, H. X. Vu, Y. A. Omelchenko, J. Scudder, W. Daughton, A. Dimmock, K. Nykyri, M. Wan, D. Sibeck, M. Tatineni, A. Majumdar, B. Loring and B. Geveci, The link between shocks, turbulence, and magnetic reconnection in collisionless plasmas, *Phys. Plasmas* **21** (2014), 062308.
[217] A. P. Kazantsev, Enhancement of a magnetic field by a conducting fluid, *Sov. Phys. JETP* **26** (1968), 1031.
[218] D. Kandel, A. Lazarian and D. Pogosyan, *Mon. Not. R. Astron. Soc.* **478**, (2018), 530.
[219] O. Khabarova and V. Obridko, Puzzles of the interplanetary magnetic field in the inner heliosphere, *Astrophys. J.* **761** (2012), 82.
[220] A. Khalil, G. Joncas, F. Nekka, P. Kestener and A. Arneodo, Morphological analysis of H I features. II. Wavelet-based multifractal formalism, *Astrophys. J. Suppl. Ser.* **165** (2006), 512–550.
[221] B. Khiali and E. M. de Gouveia Dal Pino, Very high energy neutrino emission from the core of low luminosity AGNs triggered by magnetic reconnection acceleration, *ArXiv e-prints* (2015).
[222] B. Khiali, E. M. de Gouveia Dal Pino and H. Sol, Particle acceleration and gamma-ray emission due to magnetic reconnection in the core region of radio galaxies, *ArXiv e-prints* (2015).
[223] S. C. Kleiner and R. L. Dickman, Large-scale structure of the Taurus molecular complex. II - Analysis of velocity fluctuations and turbulence. III - Methods for turbulence, *Astrophys. J.* **295** (1985), 466–484.
[224] A. Kolmogorov, The local structure of turbulence in incompressible viscous fluid for very large Reynolds' numbers, *Dokl. Akad. Nauk SSSR* **30** (1941), 301–305.

[225] E. Komatsu, J. Dunkley, M. R. Nolta, C. L. Bennett, B. Gold, G. Hinshaw, N. Jarosik, D. Larson, M. Limon, L. Page, D. N. Spergel, M. Halpern, R. S. Hill, A. Kogut, S. S. Meyer, G. S. Tucker, J. L. Weiland, E. Wollack and E. L. Wright, Five-year Wilkinson microwave anisotropy probe observations: cosmological interpretation, *Astrophys. J. Suppl. Ser.* **180** (2009), 330–376.

[226] S. S. Komissarov, Time-dependent, force-free, degenerate electrodynamics, *Mon. Not. R. Astron. Soc.* **336** (2002), 759–766.

[227] G. Kowal, E. M. de Gouveia Dal Pino and A. Lazarian, Particle acceleration in turbulence and weakly stochastic reconnection, *Phys. Rev. Lett.* **108** (2012), 241102.

[228] G. Kowal, D. A. Falceta-Gonçalves, A. Lazarian and E. T. Vishniac, Statistics of Reconnection-driven Turbulence, *Astrophys. J.* **838** (2017), 13.

[229] G. Kowal, D. A. Falceta-Gonçalves and A. Lazarian, Turbulence in collisionless plasmas: statistical analysis from numerical simulations with pressure anisotropy, *New J. Phys.* **13** (2011), 053001.

[230] G. Kowal, D. A. Falceta-Gonçalves, A. Lazarian and E. T. Vishniac, Statistics of reconnection-driven turbulence, *Astrophys. J.* **838** (2017), 91.

[231] G. Kowal and A. Lazarian, Velocity field of compressible magnetohydrodynamic turbulence: wavelet decomposition and mode scalings, *Astrophys. J.* **720** (2010), 742–756.

[232] G. Kowal, A. Lazarian and A. Beresnyak, Density fluctuations in MHD turbulence: spectra, intermittency, and topology, *Astrophys. J.* **658** (2007), 423–445.

[233] G. Kowal, A. Lazarian, E. T. Vishniac and K. Otmianowska-Mazur, Numerical tests of fast reconnection in weakly stochastic magnetic fields, *Astrophys. J.* **700** (2009), 63–85.

[234] G. Kowal, A. Lazarian, E. T. Vishniac and K. Otmianowska-Mazur, Reconnection studies under different types of turbulence driving, *Nonlinear Process. Geophys.* **19** (2012), 297–314.

[235] R. H. Kraichnan and S. Nagarajan, Growth of turbulent magnetic fields, *Phys. Fluids* **10** (1967), 859–870.

[236] R. Kraichnan, Inertial-range spectrum of hydromagnetic turbulence, *Phys. Fluids* **8** (1965), 1385.

[237] R. Krasnopolsky, Z.-Y. Li and H. Shang, Disk formation enabled by enhanced resistivity, *Astrophys. J.* **716** (2010), 1541–1550.

[238] F. Krause and K. H. Raedler, *Mean- Field Magnethydrodynamics and Dynamo Theory*, Pergamon Press, Oxford, 1980.

[239] A. G. Kritsuk, C. T. Lee and M. L. Norman, A supersonic turbulence origin of Larson's laws, *Mon. Not. R. Astron. Soc.* **436** (2013), 3247–3261.

[240] A. G. Kritsuk, M. L. Norman, P. Padoan and R. Wagner, The statistics of supersonic isothermal turbulence, *Astrophys. J.* **665** (2007), 416–431.

[241] G. F. Krymskii, A regular mechanism for the acceleration of charged particles on the front of a shock wave, *Sov. Phys. Dokl.* **22** (1977), 327.

[242] P. Kuchar and T. A. Enßlin, Magnetic power spectra from Faraday rotation maps. REALMAF and its use on Hydra A, *Astron. Astrophys.* **529** (2011), 13.

[243] K. Kulpa-Dybeł, G. Kowal, K. Otmianowska-Mazur, A. Lazarian and E. Vishniac, Reconnection in weakly stochastic B-fields in 2D, *Astron. Astrophys.* **514** (2010), A26.

[244] R. Kulsrud and W. P. Pearce, The effect of wave-particle interactions on the propagation of cosmic rays, *Astrophys. J.* **156** (1969), 445.

[245] R. M. Kulsrud and S. W. Anderson, The spectrum of random magnetic fields in the mean field dynamo theory of the Galactic magnetic field, *Astrophys. J.* **396** (1992), 606–630.

[246] A. Kupiainen, Nondeterministic dynamics and turbulent transport, *Ann. Henri Poincaré* **4** (2003), 713–726.

[247] L. La Porta, C. Burigana, W. Reich and P. Reich, The impact of Galactic synchrotron emission on CMB anisotropy measurements. I. Angular power spectrum analysis of total intensity all-sky surveys, *Astron. Astrophys.* **479** (2008), 641–654.

[248] R. A. Laing, A. H. Bridle, P. Parma and M. Murgia, Structures of the magnetoionic media around the Fanaroff-Riley Class I radio galaxies 3C31 and Hydra A, *Mon. Not. R. Astron. Soc.* **391** (2008), 521–549.

[249] C. C. Lalescu, Y.-K. Shi, G. L. Eyink, T. D. Drivas, E. T. Vishniac and A. Lazarian, Inertial-range reconnection in magnetohydrodynamic turbulence and in the solar wind, *Phys. Rev. Lett.* **115** (2015), 025001.

[250] L. D. Landau and E. M. Lifshitz, *Fluid Mechanics*, Moscow, 1944.

[251] L. D. Landau and E. M. Lifshitz, *Electrodynamics of Continuous Media*, Pergamon Press, Oxford, 1960.

[252] G. Lapenta, Self-feeding turbulent magnetic reconnection on macroscopic scales, *Phys. Rev. Lett.* **100** (2008), 235001.

[253] R. B. Larson, Turbulence and star formation in molecular clouds, *Mon. Not. R. Astron. Soc.* **194** (1981), 809–826.

[254] A. Lazarian, Diffusion-generated electromotive force and seed magnetic field problem, *Astron. Astrophys.* **264** (1992), 326–330.

[255] A. Lazarian, Obtaining statistics of turbulent velocity from astrophysical spectral line data, in: *Penetrating Bars Through Masks of Cosmic Dust* (D. L. Block, I. Puerari, K. C. Freeman, R. Groess and E. K. Block, eds.), Astrophysics and Space Science Library 319, p. 601, January 2004.

[256] A. Lazarian, Astrophysical implications of turbulent reconnection: from cosmic rays to star formation, in: *Magnetic Fields in the Universe: From Laboratory and Stars to Primordial Structures* (E. M. de Gouveia dal Pino, G. Lugones and A. Lazarian, eds.), American Institute of Physics Conference Series 784, pp. 42–53, September 2005.

[257] A. Lazarian, Enhancement and suppression of heat transfer by MHD turbulence, *Astrophys. J. Lett.* **645** (2006), L25–L28.

[258] A. Lazarian, Turbulence spectra from Doppler-shifted spectral lines, in: *Spectral Line Shapes: XVIII* (E. Oks and M. S. Pindzola, eds.), American Institute of Physics Conference Series 874, pp. 301–315, November 2006.

[259] A. Lazarian, SINS of viscosity damped turbulence, in: *SINS - Small Ionized and Neutral Structures in the Diffuse Interstellar Medium* (M. Haverkorn and W. M. Goss, eds.), Astronomical Society of the Pacific Conference Series 365, p. 324, July 2007.

[260] A. Lazarian, Obtaining spectra of turbulent velocity from observations, *Space Sci. Rev.* **143** (2009), 357–385.

[261] A. Lazarian, Fast reconnection and reconnection diffusion: implications for star formation, *ArXiv e-prints* (2011).

[262] A. Lazarian, Reconnection diffusion in turbulent fluids and its implications for star formation, *Space Sci. Rev.* **181** (2014), 1–59.

[263] A. Lazarian and A. Beresnyak, Cosmic ray scattering in compressible turbulence, *Mon. Not. R. Astron. Soc.* **373** (2006), 1195–1202.

[264] A. Lazarian, A. Beresnyak, H. Yan, M. Opher and Y. Liu, Properties and selected implications of magnetic turbulence for interstellar medium, local bubble and solar wind, *Space Sci. Rev.* **143** (2009), 387–413.

[265] A. Lazarian and A. Esquivel, Statistics of velocity from spectral data: modified velocity centroids, *Astrophys. J. Lett.* **592** (2003), L37–L40.

[266] A. Lazarian, G. L. Eyink, E. T. Vishniac and G. Kowal, Magnetic reconnection in astrophysical environments, in: *Astrophysics and Space Science Library* (A. Lazarian, E. M. de Gouveia Dal Pino and C. Melioli, eds.), Astrophysics and Space Science Library 407, p. 311, 2015.

[267] A. Lazarian, G. L. Eyink, E. T. Vishniac and G. Kowal, Turbulent reconnection and its implications, *ArXiv e-prints* (2015).

[268] A. Lazarian and M. V. Medvedev, *preprint* (2015).
[269] A. Lazarian and M. Opher, A model of acceleration of anomalous cosmic rays by reconnection in the heliosheath, *Astrophys. J.* **703** (2009), 8–21.
[270] A. Lazarian, V. Petrosian, H. Yan and J. Cho, Physics of gamma-ray bursts: turbulence, energy transfer and reconnection, *ArXiv Astrophysics e-prints* (2003).
[271] A. Lazarian and D. Pogosyan, Velocity modification of H I power spectrum, *Astrophys. J.* **537** (2000), 720–748.
[272] A. Lazarian and D. Pogosyan, Velocity modification of the power spectrum from an absorbing medium, *Astrophys. J.* **616** (2004), 943–965.
[273] A. Lazarian and D. Pogosyan, Studying turbulence using Doppler-broadened lines: velocity coordinate spectrum, *Astrophys. J.* **652** (2006), 1348–1365.
[274] A. Lazarian and D. Pogosyan, Studying velocity turbulence from Doppler-broadened absorption lines: statistics of optical depth fluctuations, *Astrophys. J.* **686** (2008), 350–362.
[275] A. Lazarian and D. Pogosyan, Statistical description of synchrotron intensity fluctuations: studies of astrophysical magnetic turbulence, *Astrophys. J.* **747** (2012), 5.
[276] A. Lazarian and D. Pogosyan, Spectrum and anisotropy of turbulence from multi-frequency measurement of synchrotron polarization, *Astrophys. J.* **818** (2016), 178.
[277] A. L. Lazarian and V. R. Shutenkov, Correlation functions of the random magnetic field obtained from observations of intensity variations of the background radio emission of the Galaxy, *Pism'a Astron. Ž.* **16** (1990), 690–698.
[278] A. Lazarian and E. T. Vishniac, Reconnection in a weakly stochastic field, *Astrophys. J.* **517** (1999), 700–718.
[279] A. Lazarian and E. T. Vishniac, Model of reconnection of weakly stochastic magnetic field and its implications, in: *Revista Mexicana de Astronomia y Astrofisica Conference Series*, Revista Mexicana de Astronomia y Astrofisica 36(27) , pp. 81–88, August 2009.
[280] A. Lazarian, E. T. Vishniac and J. Cho, Magnetic field structure and stochastic reconnection in a partially ionized gas, *Astrophys. J.* **603** (2004), 180–197.
[281] A. Lazarian, L. Vlahos, G. Kowal, H. Yan, A. Beresnyak and E. M. de Gouveia Dal Pino, Turbulence, magnetic reconnection in turbulent fluids and energetic particle acceleration, *Space Sci. Rev.* (2012), 86.
[282] A. Lazarian and H. Yan, Grain dynamics in magnetized interstellar gas, *Astrophys. J. Lett.* **566** (2002), L105–L108.
[283] A. Lazarian and K. H. Yuen, Tracing 3D distribution of magnetic fields with gradients of synchrotron polarization, *ArXiv e-prints* (2018).
[284] A. Lazarian and K. H. Yuen, Gradients of Synchrotron Polarization: Tracing 3D distribution of magnetic fields, *ArXiv e-prints* (2018).
[285] A. Lazarian and K. H. Yuen, Tracing magnetic fields with spectroscopic channel maps, *Astrophys. J.* **853** (2018), 96.
[286] A. Lazarian, K. H. Yuen, H. Lee and J. Cho, Synchrotron intensity gradients as tracers of interstellar magnetic fields, *Astrophys. J.* **842** (2017), 30.
[287] A. Lazarian, B. Zhang and S. Xu, Gamma-ray Bursts Induced by Turbulent Reconnection, *arXiv e-prints* (2018).
[288] M. R. M. Leão, E. M. de Gouveia Dal Pino, R. Santos-Lima and A. Lazarian, The collapse of turbulent cores and reconnection diffusion, *Astrophys. J.* **777** (2013), 46.
[289] R. J. Leamon, C. W. Smith, N. F. Ness, W. H. Matthaeus and H. K. Wong, Observational constraints on the dynamics of the interplanetary magnetic field dissipation range, *J. Geophys. Res.* **103** (1998), 4775.
[290] H. Lee, A. Lazarian and J. Cho, Polarimetric studies of magnetic turbulence with an interferometer, *Astrophys. J.* **831** (2016), 77.

[291] M. Lesieur, *Turbulence in Fluids: Stochastic and Numerical Modeling*, 2nd revised and enlarged edition, NASA STI/Recon Technical Report A **91** (1990).

[292] H.-B. Li and T. Henning, The alignment of molecular cloud magnetic fields with the spiral arms in M33, *Nature* **479** (2011), 499–501.

[293] Y. Lithwick and P. Goldreich, Compressible magnetohydrodynamic turbulence in interstellar plasmas, *Astrophys. J.* **562** (2001), 279–296.

[294] Y. Lithwick and P. Goldreich, Imbalanced Weak Magnetohydrodynamic Turbulence, *Astrophys. J.* **582** (2003), 1220–1240.

[295] Y. Lithwick, P. Goldreich and S. Sridhar, Imbalanced strong MHD turbulence, *Astrophys. J.* **655** (2007), 269–274.

[296] N. F. Loureiro, R. Samtaney, A. A. Schekochihin and D. A. Uzdensky, Magnetic reconnection and stochastic plasmoid chains in high-Lundquist-number plasmas, *Phys. Plasmas* **19** (2012), 042303.

[297] N. F. Loureiro, A. A. Schekochihin and S. C. Cowley, Instability of current sheets and formation of plasmoid chains, *Phys. Plasmas* **14** (2007), 100703.

[298] N. F. Loureiro, D. A. Uzdensky, A. A. Schekochihin, S. C. Cowley and T. A. Yousef, Turbulent magnetic reconnection in two dimensions, *Mon. Not. R. Astron. Soc.* **399** (2009), L146–L150.

[299] R. V. E. Lovelace, Dynamo model of double radio sources, *Nature* **262** (1976), 649–652.

[300] Q. Y. Luo and D. J. Wu, Observations of anisotropic scaling of solar wind turbulence, *Astrophys. J. Lett.* **714** (2010), L138–L141.

[301] M. Lyutikov and A. Lazarian, Topics in microphysics of relativistic plasmas, *Space Sci. Rev.* **178** (2013), 459–481.

[302] M. A. Malkov and L. O'C. Drury, Nonlinear theory of diffusive acceleration of particles by shock waves, *Rep. Prog. Phys.* **64** (2001), 429–481.

[303] J. Maron and P. Goldreich, Simulations of incompressible magnetohydrodynamic turbulence, *Astrophys. J.* **554** (2001), 1175–1196.

[304] J. Mason, F. Cattaneo and S. Boldyrev, Dynamic alignment in driven magnetohydrodynamic turbulence, *Phys. Rev. Lett.* **97** (2006), 255002.

[305] S. Masuda, T. Kosugi, H. Hara, S. Tsuneta and Y. Ogawara, A loop-top hard X-ray source in a compact solar flare as evidence for magnetic reconnection, *Nature* **371** (1994), 495–497.

[306] W. H. Matthaeus, M. L. Goldstein and D. A. Roberts, Evidence for the presence of quasi-two-dimensional nearly incompressible fluctuations in the solar wind, *J. Geophys. Res.* **95** (1990), 20673–20683.

[307] W. H. Matthaeus and S. L. Lamkin, Rapid magnetic reconnection caused by finite amplitude fluctuations, *Phys. Fluids* **28** (1985), 303–307.

[308] W. H. Matthaeus and S. L. Lamkin, Turbulent magnetic reconnection, *Phys. Fluids* **29** (1986), 2513–2534.

[309] W. H. Matthaeus and D. Montgomery, Selective decay hypothesis at high mechanical and magnetic Reynolds numbers, *Ann. N.Y. Acad. Sci.* **357** (1980), 203–222.

[310] D. J. McComas, B. L. Barraclough, H. O. Funsten, J. T. Gosling, E. Santiago-Munoz, R. M. Skoug, B. E. Goldstein, M. Neugebauer, P. Riley and A. Balogh, Solar wind observations over Ulysses' first full polar orbit, *J. Geophys. Res. Space Phys.* **105** (2000), 10419–10433.

[311] C. F. McKee and E. C. Ostriker, Theory of star formation, *Annu. Rev. Astron. Astrophys.* **45** (2007), 565–687.

[312] J. C. McKinney and D. A. Uzdensky, A reconnection switch to trigger gamma-ray burst jet dissipation, *Mon. Not. R. Astron. Soc.* **419** (2012), 573–607.

[313] B. R. McNamara and P. E. J. Nulsen, Heating hot atmospheres with active galactic nuclei, *Annu. Rev. Astron. Astrophys.* **45** (2007), 117–175.

[314] D. B. Melrose, *Plasma Astrohysics. Nonthermal Processes in Diffuse Magnetized Plasmas – Vol. 1: The Emission, Absorption and Transfer of Waves in Plasmas; Vol. 2: Astrophysical Applications*, Gordon and Breach, New York, 1980.

[315] L. Mestel and L. Spitzer, Jr., Star formation in magnetic dust clouds, *Mon. Not. R. Astron. Soc.* **116** (1956), 503.

[316] M. S. Miesch, W. H. Matthaeus, A. Brandenburg, A. Petrosyan, A. Pouquet, C. Cambon, F. Jenko, D. Uzdensky, J. Stone, S. Tobias, J. Toomre and M. Velli, Large-eddy simulations of magnetohydrodynamic turbulence in astrophysics and space physics, *ArXiv e-prints* (2015).

[317] M. S. Miesch, J. Scalo and J. Bally, Velocity field statistics in star-forming regions. I. Centroid velocity observations, *Astrophys. J.* **524** (1999), 895–922.

[318] F. Miniati and A. Beresnyak, Self-similar energetics in large clusters of galaxies, *Nature* **523** (2015), 59–62.

[319] F. Miniati, The Matryoshka run: a Eulerian refinement strategy to study the statistics of turbulence in virialized cosmic structures, *Astrophys. J.* **782** (2014), 21.

[320] F. Miniati, The Matryoshka run. II. Time-dependent turbulence statistics, stochastic particle acceleration, and microphysics impact in a massive galaxy cluster, *Astrophys. J.* **800** (2015), 60.

[321] F. Miniati, T. W. Jones, H. Kang and D. Ryu, Cosmic-ray electrons in groups and clusters of galaxies: primary and secondary populations from a numerical cosmological simulation, *Astrophys. J.* **562** (2001), 233–253.

[322] M.-A. Miville-Deschênes, G. Joncas, E. Falgarone and F. Boulanger, High resolution 21 cm mapping of the Ursa Major Galactic cirrus: power spectra of the high-latitude H I gas, *Astron. Astrophys.* **411** (2003), 109–121.

[323] Y. Mizuno, C. Singh and E. M. de Gouveia Dal Pino, in preparation, *preprint* (2015).

[324] A. S. Monin and A. M. Iaglom, *Statistical Fluid Mechanics: Mechanics of Turbulence. Volume 2*, revised and enlarged edition, MIT Press, Cambridge, Mass., 1975.

[325] D. Montgomery and L. Turner, Anisotropic magnetohydrodynamic turbulence in a strong external magnetic field, *Phys. Fluids* **24** (1981), 825–831.

[326] T. C. Mouschovias and L. Spitzer, Jr., Note on the collapse of magnetic interstellar clouds, *Astrophys. J.* **210** (1976), 326.

[327] T. C. Mouschovias, K. Tassis and M. W. Kunz, Observational constraints on the ages of molecular clouds and the star formation timescale: ambipolar-diffusion-controlled or turbulence-induced star formation?, *Astrophys. J.* **646** (2006), 1043–1049.

[328] E. Muller, S. Stanimirović, E. Rosolowsky and L. Staveley-Smith, A statistical investigation of H I in the Magellanic Bridge, *Astrophys. J.* **616** (2004), 845–856.

[329] W.-C. Müller and D. Biskamp, Scaling properties of three-dimensional magnetohydrodynamic turbulence, *Phys. Rev. Lett.* **84** (2000), 475–478.

[330] W.-C. Müller and R. Grappin, Spectral energy dynamics in magnetohydrodynamic turbulence, *Phys. Rev. Lett.* **95** (2005), 114502.

[331] G. Münch, Internal motions in the Orion Nebula, *Rev. Mod. Phys.* **30** (1958), 1035–1041.

[332] N. Murray and M. Rahman, Star formation in massive clusters via the Wilkinson microwave anisotropy probe and the Spitzer Glimpse survey, *Astrophys. J.* **709** (2010), 424–435.

[333] F. Nakamura and Z.-Y. Li, Clustered star formation in magnetic clouds: properties of dense cores formed in outflow-driven turbulence, *Astrophys. J.* **740** (2011), 36.

[334] R. Narayan, The physics of pulsar scintillation, *Philos. Trans. R. Soc. Lond. Ser. A* **341** (1992), 151–165.

[335] R. Narayan and J. Goodman, The shape of a scatter-broadened image. I - Numerical simulations and physical principles., *Mon. Not. R. Astron. Soc.* **238** (1989), 963–1028.

[336] R. Narayan and M. V. Medvedev, Thermal conduction in clusters of galaxies, *Astrophys. J. Lett.* **562** (2001), L129–L132.
[337] W. A. Newcomb, Motion of magnetic lines of force, *Ann. Phys.* **3** (1958), 347–385.
[338] M. L. Norman and G. L. Bryan, Cluster turbulence, in: *The Radio Galaxy Messier 87: Proceedings of a Workshop Held at Ringberg Castle*, Springer, Berlin Heidelberg, pp. 106–115, 1999.
[339] C. R. O'dell and H. O. Castaneda, Evidence for turbulence in H II regions, *Astrophys. J.* **317** (1987), 686–692.
[340] J. S. Oishi, M.-M. Mac Low, D. C. Collins and M. Tamura, Self-generated turbulence in magnetic reconnection, *Astrophys. J.* **806** (2015), 12.
[341] M. Oka, T.-D. Phan, S. Krucker, M. Fujimoto and I. Shinohara, Electron acceleration by multi-island coalescence, *Astrophys. J.* **714** (2010), 915.
[342] K. T. Osman and T. S. Horbury, Multi-spacecraft measurement of anisotropic power levels and scaling in solar wind turbulence, *Ann. Geophys.* **27** (2009), 3019–3025.
[343] E. C. Ostriker, J. M. Stone and C. F. Gammie, Density, velocity, and magnetic field structure in turbulent molecular cloud models, *Astrophys. J.* **546** (2001), 980–1005.
[344] P. Padoan, R. Jimenez, M. Juvela and Å. Nordlund, The average magnetic field strength in molecular clouds: new evidence of super-Alfvénic turbulence, *Astrophys. J. Lett.* **604** (2004), L49–L52.
[345] P. Padoan, M. Juvela, A. Kritsuk and M. L. Norman, The power spectrum of supersonic turbulence in Perseus, *Astrophys. J. Lett.* **653** (2006), L125–L128.
[346] P. Padoan, M. Juvela, A. Kritsuk and M. L. Norman, The power spectrum of turbulence in NGC 1333: outflows or large-scale driving?, *Astrophys. J. Lett.* **707** (2009), L153–L157.
[347] P. Padoan and Å. Nordlund, A super-Alfvénic model of dark clouds, *Astrophys. J.* **526** (1999), 279–294.
[348] P. P. Papadopoulos, W.-F. Thi, F. Miniati and S. Viti, Extreme cosmic ray dominated regions: a new paradigm for high star formation density events in the Universe, *Mon. Not. R. Astron. Soc.* **414** (2011), 1705–1714.
[349] E. N. Parker, Sweet's mechanism for merging magnetic fields in conducting fluids, *J. Geophys. Res.* **62** (1957), 509–520.
[350] E. N. Parker, The passage of energetic charged particles through interplanetary space, *Planet. Space Sci.* **13** (1965), 9–49.
[351] E. N. Parker, The generation of magnetic fields in astrophysical bodies. I. The dynamo equations, *Astrophys. J.* **162** (1970), 665.
[352] E. N. Parker, *Cosmical Magnetic Fields: Their Origin and Their Activity*, 1979.
[353] T. Passot and E. Vázquez-Semadeni, Density probability distribution in one-dimensional polytropic gas dynamics, *Phys. Rev. E* **58** (1998), 4501–4510.
[354] T. Passot and E. Vázquez-Semadeni, The correlation between magnetic pressure and density in compressible MHD turbulence, *Astron. Astrophys.* **398** (2003), 845–855.
[355] J. E. G. Peek, B. L. Babler, Y. Zheng et al., *Astrophys. J. Lett.* **234** (2018), 2.
[356] J. C. Perez and S. Boldyrev, Role of cross-helicity in magnetohydrodynamic turbulence, *Phys. Rev. Lett.* **102** (2009), 025003.
[357] S. Perri and G. Zimbardo, Ion superdiffusion at the solar wind termination shock, *Astrophys. J. Lett.* **693** (2009), L118–L121.
[358] Planck Collaboration, Planck intermediate results. XXXVIII. E- and B-modes of dust polarization from the magnetized filamentary structure of the interstellar medium, *Astron. Astrophys.* **586** (2016), A141.
[359] J. J. Podesta, Dependence of solar-wind power spectra on the direction of the local mean magnetic field, *Astrophys. J.* **698** (2009), 986–999.

[360] H. Politano and A. Pouquet, von Kármán–Howarth equation for magnetohydrodynamics and its consequences on third-order longitudinal structure and correlation functions, *Phys. Rev. E* **57** (1998), R21–R24.

[361] A. Pouquet, U. Frisch and J. Léorat, Strong MHD helical turbulence and the nonlinear dynamo effect, *J. Fluid Mech.* **77** (1976), 321–354.

[362] A. Pouquet, P. L. Sulem and M. Meneguzzi, Influence of velocity-magnetic field correlations on decaying magnetohydrodynamic turbulence with neutral X points, *Phys. Fluids* **31** (1988), 2635–2643.

[363] E. R. Priest and T. G. Forbes, The magnetic nature of solar flares, *Astron. Astrophys. Rev.* **10** (2002), 313–377.

[364] P. Pritchett, Relativistic electron production during guide field magnetic reconnection, *J. Geophys. Res. Space Phys. (1978–2012)* **111** (2006), 10212.

[365] D. Radice and L. Rezzolla, Universality and intermittency in relativistic turbulent flows of a hot plasma, *Astrophys. J. Lett.* **766** (2013), L10.

[366] A. B. Rechester and M. N. Rosenbluth, Electron heat transport in a Tokamak with destroyed magnetic surfaces, *Phys. Rev. Lett.* **40** (1978), 38–41.

[367] P. Reich and W. Reich, A radio continuum survey of the northern sky at 1420 MHz. II, *Astron. Astrophys. Suppl. Ser.* **63** (1986), 205–288.

[368] M. Reiter, Y. L. Shirley, J. Wu, C. Brogan, A. Wootten and K. Tatematsu, Evidence for inflow in high-mass star-forming clumps, *Astrophys. J.* **740** (2011), 40.

[369] L. Richardson, Atmospheric diffusion shown on a distance-neighbour graph, *Proc. R. Soc. Lond. Ser. A* **110** (1926), 709.

[370] M. A. Riquelme and A. Spitkovsky, Nonlinear study of Bell's cosmic ray current-driven instability, *Astrophys. J.* **694** (2009), 626–642.

[371] I. Rogachevskii, N. Kleeorin, A. Brandenburg and D. Eichler, Cosmic-ray current-driven turbulence and mean-field dynamo effect, *Astrophys. J.* **753** (2012), 6.

[372] G. B. Rybicki and A. P. Lightman *Radiative Processes in Astrophysics*, John Wiley & Sons, 2008.

[373] D. Ryu, H. Kang, J. Cho and S. Das, Turbulence and magnetic fields in the large-scale structure of the Universe, *Science* **320** (2008), 909.

[374] R. Santos-Lima, E. M. de Gouveia Dal Pino, G. Kowal, D. Falceta-Gonçalves, A. Lazarian and M. S. Nakwacki, Magnetic field amplification and evolution in turbulent collisionless magnetohydrodynamics: an application to the intracluster medium, *Astrophys. J.* **781** (2014), 84.

[375] R. Santos-Lima, E. M. de Gouveia Dal Pino and A. Lazarian, The role of turbulent magnetic reconnection in the formation of rotationally supported protostellar disks, *Astrophys. J.* **747** (2012), 21.

[376] R. Santos-Lima, E. M. de Gouveia Dal Pino and A. Lazarian, Disc formation in turbulent cloud cores: is magnetic flux loss necessary to stop the magnetic braking catastrophe or not?, *Mon. Not. R. Astron. Soc.* **429** (2013), 3371–3378.

[377] R. Santos-Lima, A. Lazarian, E. M. de Gouveia Dal Pino and J. Cho, Diffusion of magnetic field and removal of magnetic flux from clouds via turbulent reconnection, *Astrophys. J.* **714** (2010), 442–461.

[378] R. Santos-Lima, H. Yan, E. M. de Gouveia Dal Pino and A. Lazarian, Limits on the ion temperature anisotropy in the turbulent intracluster medium, *Mon. Not. R. Astron. Soc.* **460** (2016), 2492–2504.

[379] B. L. Sawford, P. Yeung and J. F. Hackl, Reynolds number dependence of relative dispersion statistics in isotropic turbulence, *Phys. Fluids* **20** (2008), 065111.

[380] A. A. Schekochihin and S. C. Cowley, Turbulence, magnetic fields, and plasma physics in clusters of galaxies, *Phys. Plasmas* **13** (2006), 056501.
[381] A. A. Schekochihin and S. C. Cowley, Turbulence and magnetic fields in astrophysical plasmas in: *Magnetohydrodynamics*, Springer, p. 85, 2007.
[382] A. A. Schekochihin, S. C. Cowley, W. Dorland, G. W. Hammett, G. G. Howes, E. Quataert and T. Tatsuno, Astrophysical gyrokinetics: kinetic and fluid turbulent cascades in magnetized weakly collisional plasmas, *Astrophys. J. Suppl. Ser.* **182** (2009), 310–377.
[383] A. A. Schekochihin, S. C. Cowley, R. M. Kulsrud, M. S. Rosin and T. Heinemann, Nonlinear growth of firehose and mirror fluctuations in astrophysical plasmas, *Phys. Rev. Lett.* **100** (2008), 081301.
[384] A. A. Schekochihin, S. C. Cowley, S. F. Taylor, J. L. Maron and J. C. McWilliams, Simulations of the small-scale turbulent dynamo, *Astrophys. J.* **612** (2004), 276–307.
[385] R. Schlickeiser, *Cosmic Ray Astrophysics*, Springer, Berlin, 2002.
[386] R. Schlickeiser, First-order distributed Fermi acceleration of cosmic ray hadrons in non-uniform magnetic fields, *Mod. Phys. Lett. A* **24** (2009), 1461–1472.
[387] A. Schlüter and I. Biermann, Interstellare magnetfelder, *Z. Naturforsch. Teil A* **5** (1950), 237.
[388] D. Seifried, R. Banerjee, R. E. Pudritz and R. S. Klessen, Disc formation in turbulent massive cores: circumventing the magnetic braking catastrophe, *Mon. Not. R. Astron. Soc.* **423** (2012), L40–L44.
[389] S. Servidio, W. H. Matthaeus, M. A. Shay, P. Dmitruk, P. A. Cassak and M. Wan, Statistics of magnetic reconnection in two-dimensional magnetohydrodynamic turbulence, *Phys. Plasmas* **17** (2010), 032315.
[390] M. A. Shay and J. F. Drake, The role of electron dissipation on the rate of collisionless magnetic reconnection, *Geophys. Res. Lett.* **25** (1998), 3759–3762.
[391] M. A. Shay, J. F. Drake, R. E. Denton and D. Biskamp, Structure of the dissipation region during collisionless magnetic reconnection, *J. Geophys. Res.* **103** (1998), 9165–9176.
[392] Z.-S. She and E. Leveque, Universal scaling laws in fully developed turbulence, *Phys. Rev. Lett.* **72** (1994), 336–339.
[393] J. V. Shebalin, W. H. Matthaeus and D. Montgomery, Anisotropy in MHD turbulence due to a mean magnetic field, *J. Plasma Phys.* **29** (1983), 525–547.
[394] F. H. Shu, Ambipolar diffusion in self-gravitating isothermal layers, *Astrophys. J.* **273** (1983), 202–213.
[395] F. H. Shu, D. Galli, S. Lizano and M. Cai, Gravitational collapse of magnetized clouds. II. The role of ohmic dissipation, *Astrophys. J.* **647** (2006), 382–389.
[396] C. B. Singh, E. M. de Gouveia Dal Pino and L. H. S. Kadowaki, On the role of fast magnetic reconnection in accreting black hole sources, *Astrophys. J. Lett.* **799** (2015), L20.
[397] L. Sironi and A. Spitkovsky, Relativistic reconnection: an efficient source of non-thermal particles, *Astrophys. J. Lett.* **783** (2014), L21.
[398] D. V. Sivukhin, Motion of charged particles in electromagnetic fields in the drift approximation, *Rev. Plasma Phys.* **1** (1965), 1.
[399] J. Skilling, I. McIvor and J. A. Holmes, On cosmic ray diffusion and anisotropy, *Mon. Not. R. Astron. Soc.* **167** (1974), 87P.
[400] R. K. Smith and D. P. Cox, Multiple supernova remnant models of the local bubble and the soft X-Ray background, *Astrophys. J. Suppl. Ser.* **134** (2001), 283–309.
[401] J. D. Soler and Planck Collaboration, The role of the magnetic field in the formation of structure in molecular clouds as revealed by Planck, in: *American Astronomical Society Meeting Abstracts #225*, American Astronomical Society Meeting Abstracts 225, 2015.
[402] S. R. Spangler and C. R. Gwinn, Evidence for an inner scale to the density turbulence in the interstellar medium, *Astrophys. J. Lett.* **353** (1990), L29–L32.

[403] L. Spitzer, *Physical Processes in the Interstellar Medium*, 1978.
[404] K. Sreenivasan, On the universality of the Kolmogorov constant, *Phys. Fluids* **7** (1995), 2778.
[405] S. Stanimirović and A. Lazarian, Velocity and density spectra of the small magellanic cloud, *Astrophys. J. Lett.* **551** (2001), L53–L56.
[406] S. Stanimirovic, L. Staveley-Smith, J. M. Dickey, R. J. Sault and S. L. Snowden, The large-scale HI structure of the small magellanic cloud, *Mon. Not. R. Astron. Soc.* **302** (1999), 417–436.
[407] L. G. Stenholm, Molecular cloud fluctuations. II - Methods of analysis of cloud maps, *Astron. Astrophys.* **232** (1990), 495–509.
[408] J. M. Stone, E. C. Ostriker and C. F. Gammie, Dissipation in compressible magnetohydrodynamic turbulence, *Astrophys. J. Lett.* **508** (1998), L99–L102.
[409] H. R. Strauss, Nonlinear, three-dimensional magnetohydrodynamics of noncircular tokamaks, *Phys. Fluids* **19** (1976), 134–140.
[410] J. Stutzki, F. Bensch, A. Heithausen, V. Ossenkopf and M. Zielinsky, On the fractal structure of molecular clouds, *Astron. Astrophys.* **336** (1998), 697–720.
[411] K. Sun, C. Kramer, V. Ossenkopf, F. Bensch, J. Stutzki and M. Miller, A KOSMA 7 deg^2 ^{13}CO 2-1 and ^{12}CO 3-2 survey of the Perseus cloud. I. structure analysis, *Astron. Astrophys.* **451** (2006), 539–549.
[412] P. A. Sweet, The neutral point theory of solar flares, in: *Electromagnetic Phenomena in Cosmical Physics* (B. Lehnert, ed.), IAU Symposium 6, p. 123, 1958.
[413] J. J. Swift, *An Ecological Case Study of Low-Mass Star Formation in Taurus*, Ph.D. thesis, University of California, Berkeley, 2006.
[414] R. Sych, V. M. Nakariakov, M. Karlicky and S. Anfinogentov, Relationship between wave processes in sunspots and quasi-periodic pulsations in active region flares, *Astron. Astrophys.* **505** (2009), 791–799.
[415] S. I. Syrovatskii, Pinch sheets and reconnection in astrophysics, *Annu. Rev. Astron. Astrophys.* **19** (1981), 163–229.
[416] M. Tafalla, D. Mardones, P. C. Myers, P. Caselli, R. Bachiller and P. J. Benson, L1544: a starless dense core with extended inward motions, *Astrophys. J.* **504** (1998), 900–914.
[417] M. Takamoto and T. Inoue, A new numerical scheme for resistive relativistic magnetohydrodynamics using method of characteristics, *Astrophys. J.* **735** (2011), 113.
[418] M. Takamoto, T. Inoue and A. Lazarian, Turbulent reconnection in relativistic plasmas and effects of compressibility, *Astrophys. J.* **815** (2015), 16.
[419] M. Takamoto and A. Lazarian, Compressible relativistic magnetohydrodynamic turbulence in magnetically dominated plasmas and implications for a strong-coupling regime, *Astrophys. J. Lett.* **831** (2016), L11.
[420] M. Takamoto and A. Lazarian, Strong coupling of Alfvén and fast modes in compressible relativistic magnetohydrodynamic turbulence in magnetically dominated plasmas, *Mon. Not. R. Astron. Soc.* **472** (2017), 4542–4550.
[421] M. Tegmark and G. Efstathiou, A method for subtracting foregrounds from multifrequency CMB sky maps**, *Mon. Not. R. Astron. Soc.* **281** (1996), 1297–1314.
[422] H. Tennekes and J. L. Lumley, *First Course in Turbulence*, MIT Press, Cambridge, MA, 1972.
[423] C. Thompson and O. Blaes, Magnetohydrodynamics in the extreme relativistic limit, *Phys. Rev. D* **57** (1998), 3219–3234.
[424] T. H. Troland and C. Heiles, Interstellar magnetic field strengths and gas densities observational and theoretical perspectives, *Astrophys. J.* **301** (1986), 339–345.
[425] D. A. Uzdensky, Radiative magnetic reconnection in astrophysics, *ArXiv:1510.05397* (2015).
[426] D. A. Uzdensky, N. F. Loureiro and A. A. Schekochihin, Fast magnetic reconnection in the plasmoid-dominated regime, *Phys. Rev. Lett.* **105** (2010), 235002.

[427] D. A. Uzdensky and S. Rightley, Plasma physics of extreme astrophysical environments, *Rep. Prog. Phys.* **77** (2014), 036902.
[428] S. Vainshtein and Y. Zeldovich, Origin of magnetic fields in astrophysics (turbulent "dynamo" mechanisms), *Phys. Usp.* **15** (1972), 159–172.
[429] V. M. Vasyliunas, Nonuniqueness of magnetic field line motion, *J. Geophys. Res.* **77** (1972), 6271.
[430] E. Vázquez-Semadeni, R. Banerjee, G. C. Gómez, P. Hennebelle, D. Duffin and R. S. Klessen, Molecular cloud evolution - IV. Magnetic fields, ambipolar diffusion and the star formation efficiency, *Mon. Not. R. Astron. Soc.* **414** (2011), 2511–2527.
[431] E. Vázquez-Semadeni, G. C. Gómez, A. K. Jappsen, J. Ballesteros-Paredes, R. F. González and R. S. Klessen, Molecular cloud evolution. II. From cloud formation to the early stages of star formation in decaying conditions, *Astrophys. J.* **657** (2007), 870–883.
[432] F. Vazza, M. Brüggen, C. Gheller and P. Wang, On the amplification of magnetic fields in cosmic filaments and galaxy clusters, *Mon. Not. R. Astron. Soc.* **445** (2014), 3706–3722.
[433] F. Vazza, G. Brunetti, C. Gheller, R. Brunino and M. Brüggen, Massive and refined. II. The statistical properties of turbulent motions in massive galaxy clusters with high spatial resolution, *Astron. Astrophys.* **529** (2011), 17.
[434] J. Vink and J. M. Laming, On the magnetic fields and particle acceleration in Cassiopeia A, *Astrophys. J.* **584** (2003), 758–769.
[435] E. T. Vishniac and J. Cho, Magnetic helicity conservation and astrophysical dynamos, *Astrophys. J.* **550** (2001), 752–760.
[436] E. T. Vishniac and A. Lazarian, Reconnection in the interstellar medium, *Astrophys. J.* **511** (1999), 193–203.
[437] E. T. Vishniac, A. Lazarian and J. Cho, Problems and progress in astrophysical dynamos, in: *Turbulence and Magnetic Fields in Astrophysics* (E. Falgarone and T. Passot, eds.), Lecture Notes in Physics 614, Springer Verlag, Berlin, pp. 376–401, 2003.
[438] E. T. Vishniac, S. Pillsworth, G. Eyink, G. Kowal, A. Lazarian and S. Murray, Reconnection current sheet structure in a turbulent medium, *Nonlinear Process. Geophys.* **19** (2012), 605–610.
[439] L. M. Voigt and A. C. Fabian, Thermal conduction and reduced cooling flows in galaxy clusters, *Mon. Not. R. Astron. Soc.* **347** (2004), 1130–1149.
[440] H. J. Völk, E. G. Berezhko and L. T. Ksenofontov, Magnetic field amplification in Tycho and other shell-type supernova remnants, *Astron. Astrophys.* **433** (2005), 229–240.
[441] S. von Hoerner, Eine Methode zur Untersuchung der Turbulenz der interstellaren Materie. Mit 10 Textabbildungen, *Z. Astrophys.* **30** (1951), 17.
[442] P. G. Watson, S. Oughton and I. J. D. Craig, The impact of small-scale turbulence on laminar magnetic reconnection, *Phys. Plasmas* **14** (2007), 032301.
[443] R. T. Wicks, T. S. Horbury, C. H. K. Chen and A. A. Schekochihin, Power and spectral index anisotropy of the entire inertial range of turbulence in the fast solar wind, *Mon. Not. R. Astron. Soc.* **407** (2010), L31–L35.
[444] R. T. Wicks, T. S. Horbury, C. H. K. Chen and A. A. Schekochihin, Anisotropy of imbalanced Alfvénic turbulence in fast solar wind, *Phys. Rev. Lett.* **106** (2011), 045001.
[445] R. T. Wicks, A. Mallet, T. S. Horbury, C. H. K. Chen, A. A. Schekochihin and J. J. Mitchell, Alignment and scaling of large-scale fluctuations in the solar wind, *Phys. Rev. Lett.* **110** (2013), 025003.
[446] O. C. Wilson, G. Minich, E. Flather and M. F. Coffeen, Internal kinematics of the Orion Nebula, *Astrophys. J. Suppl. Ser.* **4** (1959), 199.
[447] H. Xu, F. Govoni, M. Murgia, H. Li, D. C. Collins, M. L. Norman, R. Cen, L. Feretti and G. Giovannini, Comparisons of cosmological magnetohydrodynamic galaxy cluster simulations to radio observations, *Astrophys. J.* **759** (2012), 40.

[448] S. Xu and A. Lazarian, Turbulent dynamo in a conducting fluid and a partially ionized gas, *Astrophys. J.* **833** (2016), 215.
[449] S. Xu and A. Lazarian, Magnetohydrodynamic turbulence and turbulent dynamo in partially ionized plasma, *New J. Phys.* **19** (2017), 065005.
[450] S. Xu, A. Lazarian and H. Yan, The line width difference of neutrals and ions induced by MHD turbulence, *Astrophys. J.* **810** (2015), 44.
[451] S. Xu, H. Yan and A. Lazarian, Damping of MHD turbulence in partially ionized plasma: implications for cosmic ray propagation, *ArXiv e-prints* (2015).
[452] M. Yamada, R. Kulsrud and H. Ji, Magnetic reconnection, *Rev. Mod. Phys.* **82** (2010), 603–664.
[453] H. Yan and A. Lazarian, Scattering of cosmic rays by magnetohydrodynamic interstellar turbulence, *Phys. Rev. Lett.* **89** (2002), B1102.
[454] H. Yan and A. Lazarian, Cosmic-ray scattering and streaming in compressible magnetohydrodynamic turbulence, *Astrophys. J.* **614** (2004), 757–769.
[455] H. Yan and A. Lazarian, Cosmic-ray propagation: nonlinear diffusion parallel and perpendicular to mean magnetic field, *Astrophys. J.* **673** (2008), 942–953.
[456] P. K. Yeung, S. B. Pope and B. L. Sawford, Reynolds number dependence of Lagrangian statistics in large numerical simulations of isotropic turbulence, *J. Turbul.* **7** (2006), 58.
[457] P. K. Yeung and Y. Zhou, Universality of the Kolmogorov constant in numerical simulations of turbulence, *Phys. Rev. E* **56** (1997), 1746–1752.
[458] T. Yokoyama and K. Shibata, Magnetic reconnection as the origin of X-ray jets and Hα surges on the Sun, *Nature* **375** (1995), 42–44.
[459] K. H. Yuen and A. Lazarian, Tracing interstellar magnetic field using the velocity gradient technique in shock and self-gravitating media, *ArXiv e-prints* (2017).
[460] K. H. Yuen and A. Lazarian, Tracing interstellar magnetic field using velocity gradient technique: application to atomic hydrogen data, *Astrophys. J. Lett.* **837** (2017), L24.
[461] K. H. Yuen, J. Chen, Y. Hu, K. W. Ho, A. Lazarian, V. Lazarian, B. Yang, B. Burkhart, C. Correia, J. Cho, B. Canto and J. R. De Medeiros, Statistical tracing of magnetic fields: comparing and improving the techniques, *ArXiv e-prints* (2018).
[462] G. P. Zank and W. H. Matthaeus, Nearly incompressible fluids. II - Magnetohydrodynamics, turbulence, and waves, *Phys. Fluids* **5** (1993), 257–273.
[463] S. Zenitani and M. Hoshino, The generation of nonthermal particles in the relativistic magnetic reconnection of pair plasmas, *Astrophys. J. Lett.* **562** (2001), L63.
[464] B. Zhang and H. Yan, The internal-collision-induced magnetic reconnection and turbulence (ICMART) model of gamma-ray bursts, *Astrophys. J.* **726** (2011), 90.
[465] J.-F. Zhang, A. Lazarian, H. Lee and J. Cho, Studying magnetohydrodynamic turbulence with synchrotron polarization dispersion, *Astrophys. J.* **825** (2016), 154.
[466] J.-F. Zhang, A. Lazarian and F.-Y. Xiang, Spectral properties of magnetohydrodynamic turbulence revealed by polarization synchrotron emission with Faraday rotation, *Astrophys. J.* **863** (2018), 197.
[467] W. Zhang, A. MacFadyen and P. Wang, Three-dimensional relativistic magnetohydrodynamic simulations of the Kelvin-Helmholtz instability: magnetic field amplification by a turbulent dynamo, *Astrophys. J. Lett.* **692** (2009), L40–L44.
[468] J. Zrake and A. I. MacFadyen, Numerical simulations of driven relativistic magnetohydrodynamic turbulence, *Astrophys. J.* **744** (2012), 32.
[469] J. Zrake and A. I. MacFadyen, Spectral and intermittency properties of relativistic turbulence, *Astrophys. J. Lett.* **763** (2013), L12.
[470] E. G. Zweibel, Ambipolar drift in a turbulent medium, *Astrophys. J.* **567** (2002), 962–970.

Index

De Gruyter Studies in Mathematical Physics

Volume 47
Eugene Stefanovich
Elementary Particle Theory: Volume 3: Relativistic Quantum Dynamics, 2018
ISBN 978-3-11-049090-9, e-ISBN (PDF) 978-3-11-049322-1,
e-ISBN (EPUB) 978-3-11-049139-5

Volume 46
Eugene Stefanovich
Elementary Particle Theory: Volume 2: Quantum Electrodynamics, 2018
ISBN 978-3-11-049089-3, e-ISBN (PDF) 978-3-11-049320-7,
e-ISBN (EPUB) 978-3-11-049143-2

Volume 45
Eugene Stefanovich
Elementary Particle Theory: Volume 1: Quantum Mechanics, 2018
ISBN 978-3-11-049088-6, e-ISBN (PDF) 978-3-11-049213-2,
e-ISBN (EPUB) 978-3-11-049103-6

Volume 44
Vladimir V. Kiselev
Collective Effects in Condensed Matter Physics, 2018
ISBN 978-3-11-058509-4, e-ISBN (PDF) 978-3-11-058618-3,
e-ISBN (EPUB) 978-3-11-058513-1

Volume 43
Robert F. Snider
Irreducible Cartesian Tensors, 2017
ISBN 978-3-11-056363-4, e-ISBN (PDF) 978-3-11-056486-0,
e-ISBN (EPUB) 978-3-11-056373-3

Volume 42
Javier Roa
Regularization in Orbital Mechanics: Theory and Practice, 2017
ISBN 978-3-11-055855-5, e-ISBN (PDF) 978-3-11-055912-5,
e-ISBN (EPUB) 978-3-11-055862-3

Volume 41
Esra Russell, Oktay K. Pashaev
Oscillatory Models in General Relativity, 2017
ISBN 978-3-11-051495-7, e-ISBN (PDF) 978-3-11-051536-7,
e-ISBN (EPUB) 978-3-11-051522-0, Set-ISBN 978-3-11-051537-4

www.degruyter.com